



UNIVERSITÀ DEGLI STUDI DI PALERMO

Dottorato in Ingegneria dell'Innovazione Tecnologica

Dipartimento di Ingegneria

Settore Scientifico Disciplinare (ING-IND/26)

**ELECTRICAL ENERGY STORAGE DEVICES
BASED ON pH AND SALINITY GRADIENTS:
MODELLING, EXPERIMENTS AND PILOTING**

**IL DOTTORE
ANDREA CULCASI**

**IL COORDINATORE
PROF. SALVATORE GAGLIO**

**IL TUTOR
PROF. GIORGIO MICALE**

**I CO TUTOR
PROF. I. DAVID. L. BOGLE
DOTT. ING. A. TAMBURINI**

**CICLO XXXIII
ANNO CONSEGUIMENTO TITOLO 2021**

Table of Content

| | |
|--|-----|
| List of Figures..... | vi |
| List of Tables..... | xxi |
| Introduction..... | 1 |
| 1 Energy storage systems..... | 3 |
| 1.1 Electrochemical storage devices..... | 5 |
| 1.2 Flow Batteries..... | 6 |
| 1.3 Performance metrics of the energy storage systems..... | 6 |
| 1.4 Modelling of the energy storage devices..... | 9 |
| 2 Bipolar Membranes: fundamentals..... | 10 |
| 2.1 Bipolar membranes: historical developments and working principle | 10 |
| 2.2 Water dissociation in bipolar membranes..... | 10 |
| 2.3 Acid/Base neutralization in bipolar membranes..... | 13 |
| 2.4 Thickness of the transition region of a Bipolar Membrane..... | 18 |
| 2.5 Preparation of bipolar membranes..... | 18 |
| 2.6 Properties of bipolar membranes and how to assess them..... | 19 |
| 2.7 Modelling of the bipolar membranes..... | 24 |
| 3 Bipolar Membrane Electrodialysis processes..... | 26 |
| 3.1 Conventional Electrodialysis: General overview and working principle | 26 |
| 3.2 Bipolar Membrane Electrodialysis..... | 27 |
| 3.2.1 Configurations of BMED units..... | 29 |
| 3.3 Modelling of the Bipolar membrane electrodialysis: state of the art | 30 |
| 3.4 Industrial applications of the BMED process..... | 33 |
| 3.5 Description of the multi-scale model of BMED..... | 34 |
| 3.5.1 Lowest scale: Channel model..... | 37 |

| | | |
|-------|--|-----|
| 3.5.2 | Lowest scale: Bipolar Membrane model..... | 39 |
| 3.5.3 | Middle low scale: Triplet model..... | 41 |
| 3.5.4 | Middle-high scale: Stack model | 48 |
| 3.5.5 | Evaluation of the process performance..... | 53 |
| 3.6 | Steady-state model validation..... | 54 |
| 3.6.1 | Comparison between experimental data and model predictions . | 56 |
| 3.7 | Simulations of industrial scale BMED units | 61 |
| 3.7.1 | Current density analysis..... | 62 |
| 3.7.2 | Mean channel flow velocity analysis..... | 66 |
| 4 | Bipolar Membrane Reverse Electrodialysis..... | 71 |
| 4.1 | Conventional Reverse electrodialysis: general overview and working principle | 71 |
| 4.2 | Bipolar Membrane Reverse Electrodialysis..... | 74 |
| 4.2.1 | State of the art..... | 78 |
| 4.3 | Acid/Base neutralization of waste streams and production of energy | 80 |
| 4.4 | Modelling of the bipolar membrane reverse electrodialysis: state of the art | 82 |
| 4.5 | Description of the multi-scale model..... | 83 |
| 4.5.1 | Lowest scale: Channel model..... | 83 |
| 4.5.2 | Lowest scale: Bipolar Membrane model..... | 83 |
| 4.5.3 | Middle-low scale: Triplet model..... | 86 |
| 4.5.4 | Middle-high scale: Stack model | 86 |
| 4.5.5 | Figures of merit of BMRED processes | 87 |
| 4.6 | Steady-state model validation..... | 88 |
| 4.6.1 | Comparison between experimental data and model predictions . | 89 |
| 4.6.2 | Energy density and prospective Cost analysis..... | 98 |
| 4.7 | Performance analysis of BMRED in different scenarios | 101 |
| 4.7.1 | Sensitivity on current density..... | 103 |
| 4.7.2 | Sensitivity on mean channel flow velocity | 106 |

| | | |
|-------|---|-----|
| 4.7.3 | Sensitivity on inlet acid/base concentrations | 107 |
| 4.7.4 | Sensitivity on inlet salt concentration..... | 110 |
| 4.8 | Example of an industrial BMRED scheme for energy recovery from waste streams..... | 111 |
| 5 | Ionic shortcut currents in electro-membrane processes..... | 113 |
| 5.1 | Literature review and working principle..... | 113 |
| 5.2 | Modelling of the shortcut currents: state of the art..... | 117 |
| 5.3 | Ionic shortcut currents model description..... | 118 |
| 5.3.1 | Performance parameters of the shortcut currents..... | 123 |
| 5.4 | Ionic shortcut model validation..... | 124 |
| 5.4.1 | Ionic shortcut RED model validation results | 126 |
| 5.4.2 | Ionic shortcut BMRED model validation results..... | 131 |
| 5.4.3 | Ionic shortcut model capabilities..... | 133 |
| 5.5 | Simulation analysis of the ionic shortcut currents..... | 135 |
| 5.5.1 | Conventional RED analysis..... | 135 |
| 5.5.2 | Conventional ED analysis..... | 141 |
| 5.5.3 | BMRED analysis..... | 145 |
| 5.5.4 | BMED analysis..... | 149 |
| 6 | Acid/Base Flow Battery..... | 153 |
| 6.1 | General Overview..... | 153 |
| 6.2 | The Acid/Base Flow Battery: working principle | 154 |
| 6.3 | Mathematical modelling of the Acid/Base Flow Battery..... | 157 |
| 6.3.1 | Highest scale: External hydraulic circuit and tanks model..... | 159 |
| 6.3.2 | Performance parameters of the Acid/Base flow battery..... | 160 |
| 6.3.3 | Battery configurations..... | 161 |
| 6.4 | AB-FB dynamic model validation..... | 163 |
| 6.4.1 | Closed-loop model validation..... | 164 |
| 6.4.2 | Yo-Yo model validation | 171 |
| 6.5 | Sensitivity analysis of the AB-FB..... | 177 |

| | | |
|-------|--|-----|
| 6.5.1 | Energy spent on pumping..... | 179 |
| 6.5.2 | Concentration polarization effects | 180 |
| 6.5.3 | Ionic shortcut currents effect..... | 181 |
| 6.5.4 | Multiple battery-cycles effect | 184 |
| 6.6 | Comparison of acid/base flow battery operational modes | 185 |
| 6.6.1 | Closed-loop vs Yo-Yo operations:..... | 185 |
| 6.6.2 | Simulations of multi-stage cases..... | 190 |
| 7 | Acid/Base Flow Battery optimization..... | 196 |
| 7.1 | Literature review..... | 196 |
| 7.2 | Optimization method..... | 198 |
| 7.3 | Optimization results | 202 |
| 7.4 | Results of the Yo-Yo configuration at the Pareto frontier closed-loop conditions | 209 |
| | Conclusions | 211 |
| | Nomenclature..... | 215 |
| | Appendix A –..... | 221 |
| | List of ISI publications..... | 222 |
| | Abstracts at international conferences..... | 224 |
| | References | 225 |
| | Acknowledgements..... | 250 |

List of Figures

| | |
|---|----|
| Figure 1. PhD thesis graphical outline..... | 2 |
| Figure 2. Electrical energy storage capacity installed worldwide for different technologies (From [7])...... | 4 |
| Figure 3. Graph of a typical bipolar membrane voltage-current curve under reverse bias..... | 11 |
| Figure 4. Scheme of the neutral layer a) and the abrupt junction b) models. Blue lines represent the AEL and CEL physical boundaries. Dashed black lines refer to the transition region. | 12 |
| Figure 5. Graph of a typical bipolar membrane voltage-current curve under reverse and forward bias. | 14 |
| Figure 6. Scheme of the bipolar membrane and the adjacent channels | 16 |
| Figure 7. Electromotive force as a function of protons concentration at different process temperatures. | 17 |
| Figure 8. Experimental set-up for the determination of the ion permeabilities of a bipolar membrane..... | 21 |
| Figure 9. a) Imposed electric current and voltage response as functions of time for a typical chronopotentiometry of a bipolar membrane in b) sub-limiting region and c) over-limiting region. Adapted from [64]. | 23 |
| Figure 10. Schematic of a CED unit..... | 27 |
| Figure 11. Schematic of a Bipolar Membrane ElectroDialysis (BMED) unit. | 28 |
| Figure 12. Scheme of the multi-scale model. | 36 |
| Figure 13. Net spacer provided with gasket. The computational domains used in the CFD simulations of the inlet/outlet regions are highlighted. | 38 |
| Figure 14. Scheme of the triplet (with an additional CEM). All the possible fluxes of ions and water through the membranes are listed. The membrane-solution interfaces in each channel are indicated as “sol,1” (on the left) and “sol,2” (on the right), “sol” being either salt (s), base (b) or acid (a) solution..... | 41 |
| Figure 15. Scheme of the hydraulic circuit for one of the three solutions. Vertical lines represent the channels, where pressure drops occur in the inlet/outlet regions (continuous vertical lines) and in the region with developed flow (dashed lines) Horizontal lines represent the manifolds, i.e. distributor and collector, connecting the channels. | 49 |
| Figure 16. Scheme of the equivalent electric circuit of the BMED stack. | 50 |
| Figure 17. Electric resistances scheme along the flow direction within the channels. | 52 |
| Figure 18. Scheme of the adopted experimental set-up..... | 55 |

Figure 19. Inlet-outlet pressure losses in a single spacer-filled channel flow cell as a function of the fluid velocity. Experimental data taken are from a previous work [141]. The main spacer features are: woven filaments, thickness of 480 μm , angle between filament of 90° , flow attack angle of 45° , pitch to height ratio of 2.42, flow path length of 10 cm (excluding divergent and convergent regions at inlet/outlet), width of 10 cm, and three inlet/outlet holes with diameter of 8.5 mm. 56

Figure 20. Voltage-current curves by varying the number of triplets for the first set of experiments (i.e. without the presence of salt background), in $10 \times 10 \text{ cm}^2$ stacks with Fumatech membranes (FAB, FKB, FBP) and with spacers provided with 3 inlet/outlet holes (diameter of 8 mm). Mean flow velocity of the electrolyte solutions in each channel equal to 1 cm s^{-1} . Symbols refer to experimental data, continuous lines to the model predictions. Inlet concentrations: 0.2M HCl and NaOH in the acid and base channels respectively and 0.25M NaCl in the salt channel. Areal blank resistance: $72 \Omega \text{ cm}^2$ 57

Figure 21. Voltage-current curves by varying the number of triplets for the second set of experiments (i.e. with the presence of salt background), in $10 \times 10 \text{ cm}^2$ stacks with Fumatech membranes (FAB, FKB, FBP) and with spacers provided with 3 inlet/outlet holes (diameter of 8 mm). Mean flow velocity of the electrolyte solutions in each channel equal to 1 cm s^{-1} . Symbols refer to experimental data, continuous lines to the model predictions. Inlet concentrations: 0.2MHCl and NaOH in the acid and base channels respectively with the presence of 0.25M NaCl (salt background) and 0.25M NaCl in the salt channel. Areal blank resistance: $72 \Omega \text{ cm}^2$ 58

Figure 22. Parity plots for the comparison of model outcome and experimental results for the concentration values at the stack outlet (i.e. downstream tank inlet) of BMED tests with single-pass: a) Outlet HCl concentration in the acid tank, b) Outlet NaOH concentration in the base tank and c) Outlet NaCl concentration in the salt tank. 60

Figure 23. Conversion rate of hydrochloric acid as a function of the current density for the three cases (A, B and C) of active area (75×75 , 50×50 and 25×25), with a fixed mean channel flow velocity of 1 cm s^{-1} 63

Figure 24. Outlet hydrochloric acid concentration as a function of the current density for the three cases (A, B and C) of active area (75×75 , 50×50 and 25×25), with a fixed mean channel flow velocity of 1 cm s^{-1} 63

Figure 25. Specific Energy Consumption per kilogram of produced acid as a function of the current density for the three cases (A, B and C) of active area (75×75 , 50×50 and 25×25), with a fixed mean channel flow velocity of 1 cm s^{-1} 64

Figure 26. a) Specific Energy Consumption per kilogram of produced acid as a function of the conversion rate and b) Specific Energy Consumption per cubic meter

of produced acid solution as a function of the inlet-outlet concentration difference of HCl for the three cases (A, B and C) of active area (75×75, 50×50 and 25×25), with a fixed mean channel flow velocity of 1 cm s⁻¹..... 65

Figure 27. Current efficiency as a function of the conversion rate for the three cases (A, B and C) of active area (75×75, 50×50 and 25×25), with a fixed mean channel flow velocity of 1 cm s⁻¹..... 65

Figure 28. Current efficiency as a function of current density for the three cases (A, B and C) of active area (75×75, 50×50 and 25×25), with a fixed mean channel flow velocity of 1 cm s⁻¹..... 66

Figure 29. Conversion rate of hydrochloric acid as a function of the mean flow velocity for the three cases (A, B and C) of active area (75×75, 50×50 and 25×25), with a fixed applied current density of 300 A m⁻²..... 67

Figure 30. Specific Energy Consumption per kilogram of produced acid as a function of the mean flow velocity for the three cases (i.e. SEC A, SEC B and SEC C), with a fixed applied current density of 300 A m⁻²..... 67

Figure 31. Outlet hydrochloric acid concentration as a function of the mean flow velocity for the three cases (A, B and C) of active area (75×75, 50×50 and 25×25), with a fixed applied current density of 300 A m⁻²..... 68

Figure 32. Current efficiency as a function of mean flow velocity for the three cases (A, B and C) of active area (75×75, 50×50 and 25×25), with a fixed applied current density of 300 A m⁻²..... 68

Figure 33. Gross and Net Specific Energy Consumption as a function of the mean channel flow velocity for the three cases (A, B and C) of active area (75×75, 50×50 and 25×25), with a fixed applied current density of 300 A m⁻². Continuous lines: gross SEC_m. Dashed lines: net SEC_m. 69

Figure 34. Schematic drawing of a RED stack. The large red arrow from the anode to the cathode indicates the desired direction of the electric current; the other large pink arrows indicate the electrical parasitic pathways (shortcuts) via manifolds in the concentrate hydraulic circuit. 72

Figure 35. Scheme of an entire Bipolar Membrane Reverse Electrodialysis (BMRED) module (with 7 repeating units, acid: HCl, base: NaOH). The inset on the right shows an enlarged view of the repeating unit (triplet) with an additional anion-exchange membrane (AEM) along with the ions and water main fluxes. 74

Figure 36. Theoretical energy density (mixing free energy per unit volume of one solution) as a function of the strong acid/base concentration (e.g. HCl and NaOH)..... 75

Figure 37. EMF contributions for a BMRED triplet. Blue and green areas refer to BPM and MPMs contributions respectively. Inlet concentrations: 0.2 M or 1 M

HCl/NaOH with or without the presence of 0.25M NaCl of background salt in the acid and base compartments. Salt stream: 0.25 M NaCl. 77

Figure 38. Scheme of the equivalent electric circuit of BMRED stacks. 86

Figure 39. Voltage-current curves by varying the number of triplets, in 10×10 cm^2 stacks with Fumatech membranes (FAB, FKB, FBP) and with spacers provided with 3 inlet/outlet holes (diameter of 8 mm). Mean flow velocity of the electrolyte solutions in each channel equal to 1 cm s^{-1} . Symbols refer to experimental data, continuous lines to the model predictions. Inlet concentrations: 0.2M HCl and NaOH in the acid and base channels respectively and 0.25M NaCl in the salt channel. Areal blank resistance: $72 \text{ } \Omega \text{ cm}^2$ 90

Figure 40. Voltage-current curves by varying the number of triplets, in 10×10 cm^2 stacks with Fumatech membranes (FAB, FKB, FBP) and with spacers provided with 3 inlet/outlet holes (diameter of 8 mm). Mean flow velocity of the electrolyte solutions in each channel equal to 1 cm s^{-1} . Symbols refer to experimental data, continuous lines to the model predictions. Inlet concentrations: 0.6M HCl and NaOH in the acid and base channels respectively and 0.25M NaCl in the salt channel. Areal blank resistance: $72 \text{ } \Omega \text{ cm}^2$ 91

Figure 41. Voltage-current curves by varying the number of triplets, in 10×10 cm^2 stacks with Fumatech membranes (FAB, FKB, FBP) and with spacers provided with 3 inlet/outlet holes (diameter of 8 mm). Mean flow velocity of the electrolyte solutions in each channel equal to 1 cm s^{-1} . Symbols refer to experimental data, continuous lines to the model predictions. Inlet concentrations: 1 M HCl and NaOH in the acid and base channels respectively and 0.25M NaCl in the salt channel. Areal blank resistance: $72 \text{ } \Omega \text{ cm}^2$ 92

Figure 42. Voltage-current curves by varying the number of triplets, in 10×10 cm^2 stacks with Fumatech membranes (FAB, FKB, FBP) and with spacers provided with 3 inlet/outlet holes (diameter of 8 mm). Mean flow velocity of the electrolyte solutions in each channel equal to 1 cm s^{-1} . Symbols refer to experimental data, continuous lines to the model predictions. Inlet concentrations: 0.2M HCl and NaOH in the acid and base channels respectively with the presence of salt background and 0.25M NaCl in the salt channel. Areal blank resistance: $72 \text{ } \Omega \text{ cm}^2$ 93

Figure 43. Voltage-current curves by varying the number of triplets, in 10×10 cm^2 stacks with Fumatech membranes (FAB, FKB, FBP) and with spacers provided with 3 inlet/outlet holes (diameter of 8 mm). Mean flow velocity of the electrolyte solutions in each channel equal to 1 cm s^{-1} . Symbols refer to experimental data, continuous lines to the model predictions. Inlet concentrations: 0.6M HCl and NaOH in the acid and base channels respectively with the presence of salt background and 0.25M NaCl in the salt channel. Areal blank resistance: $72 \text{ } \Omega \text{ cm}^2$ 94

Figure 44. Voltage-current curves by varying the number of triplets, in 10×10 cm^2 stacks with Fumatech membranes (FAB, FKB, FBP) and with spacers provided with 3 inlet/outlet holes (diameter of 8 mm). Mean flow velocity of the electrolyte solutions in each channel equal to 1 cm s^{-1} . Symbols refer to experimental data, continuous lines to the model predictions. Inlet concentrations: 1 M HCl and NaOH in the acid and base channels respectively with the presence of salt background and 0.25M NaCl in the salt channel. Areal blank resistance: $72 \Omega \text{ cm}^2$ 95

Figure 45. Parity plots for the comparison of model outcome and experimental results for the concentration values at the stack outlet (i.e. downstream tank inlet) of BMRED tests with single-pass: a) Outlet HCl concentration in the acid tank, b) Outlet NaOH concentration in the base tank and c) Outlet NaCl concentration in the salt tank. 97

Figure 46. Schematic representation of the multi-stage process analysed for the estimation of the Gross Energy Density..... 98

Figure 47. Gross Power Density as a function of the current density for the reference and improved scenarios with a fixed mean flow velocity of 1 cm s^{-1} , an inlet acid/base concentration of 1 M and an inlet salt concentration of 0.25 M.. 103

Figure 48. Gross Energy Density per unit mass as a function of the current density for the reference and improved scenarios with a fixed mean flow velocity of 1 cm s^{-1} , an inlet acid/base concentration of 1M and an inlet salt concentration of 0.25M..... 104

Figure 49. Conversion rate as a function of the current density for the reference and improved scenarios (i.e. τ reference, τ improved) with a fixed mean flow velocity of 1 cm s^{-1} , an inlet acid/base concentration of 1M and an inlet salt concentration of 0.25M..... 105

Figure 50. Current efficiency as a function of the current density for the reference and improved scenarios (with a fixed mean flow velocity of 1 cm s^{-1} , an inlet acid/base concentration of 1 M and an inlet salt concentration of 0.25 M.. 105

Figure 51. GPD (black lines) and NPD (red lines) as a function of the mean flow velocity for the reference and improved scenarios with a fixed current density of 100 A m^{-2} , an inlet acid/base concentration of 1M and an inlet salt concentration of 0.25 M..... 106

Figure 52. Conversion rate as a function of the mean flow velocity for the reference and improved scenarios with a fixed current density of 100 A m^{-2} , an inlet acid/base concentration of 1M and an inlet salt concentration of 0.25M..... 107

Figure 53. GPD as a function of the inlet acid/base concentration for the reference and improved scenarios with a fixed current density of 100 A m^{-2} , a mean flow velocity of 1 cm s^{-1} and an inlet salt concentration of 0.25 M..... 108

| | |
|---|-----|
| Figure 54. GED_m as a function of the inlet acid/base concentration for the reference and improved scenarios with a fixed current density of 100 A m^{-2} , a mean flow velocity of 1 cm s^{-1} and an inlet salt concentration of 0.25 M | 108 |
| Figure 55. Conversion rate as a function of the inlet acid/base concentration for the reference and improved scenarios with a fixed current density of 100 A m^{-2} , a mean flow velocity of 1 cm s^{-1} and an inlet salt concentration of 0.25 M | 109 |
| Figure 56. Current efficiency as a function of the inlet acid/base concentration for the reference and improved scenarios with a fixed current density at 100 A m^{-2} , a fixed mean flow velocity of 1 cm s^{-1} and an inlet salt concentration of 0.25 M | 110 |
| Figure 57. Scheme of the multi-stage BMRED process. | 112 |
| Figure 58. Simplified diagrams of the electric currents flowing inside the stack in a RED/BMRED process. a) with parasitic currents, b) without parasitic currents. | 114 |
| Figure 59. Simplified diagrams of the electric currents flowing inside the stack in an ED/BMED process. a) with parasitic currents, b) without parasitic currents. | 115 |
| Figure 60. Scheme of the equivalent electric circuit of a conventional RED stack. | 119 |
| Figure 61. Scheme of the equivalent electric circuit of a BMRED stack..... | 119 |
| Figure 62. Schematic representation of the electrical resistances along the longitudinal direction in the spacer-filled channel. Grey regions are out of the membrane active area. | 122 |
| Figure 63. Open Circuit Voltage (OCV) as a function of the cell pairs number in $10 \times 10 \text{ cm}^2$ stacks with Fujifilm Type 10 membranes and with spacers provided with 4 inlet/outlet holes (diameter of 6 mm). Mean flow velocity of the electrolyte solutions in each channel equal to 1 cm s^{-1} . Symbols refer to experimental data, continuous lines to the model predictions, and broken lines to the ideal (i.e. no shunt currents) OCV. Inlet solution concentrations (NaCl): a) $0.017 \text{ M} - 5 \text{ M}$; b) $0.05 \text{ M} - 5 \text{ M}$. Areal blank resistance: a) $72 \text{ } \Omega \text{ cm}^2$, b) $60 \text{ } \Omega \text{ cm}^2$ | 127 |
| Figure 64. Gross Power Density (GPD) produced with an applied voltage equal to $OCV/2$ as a function of the cell pairs number in $10 \times 10 \text{ cm}^2$ stacks with Fujifilm Type 10 membranes and with spacers provided with 4 inlet/outlet holes (diameter of 6 mm). Mean flow velocity of the electrolyte solutions in each channel equal to 1 cm s^{-1} . Symbols refer to experimental data, continuous lines to the model predictions. Inlet concentrations (NaCl): a) $0.017 \text{ M} - 5 \text{ M}$; b) $0.05 \text{ M} - 5 \text{ M}$. Areal blank resistance: a) $72 \text{ } \Omega \text{ cm}^2$, b) $60 \text{ } \Omega \text{ cm}^2$ | 128 |
| Figure 65. Comparison between the present model predictions and data by Veerman et al. [110] as functions of the cell pairs number in stacks with 1 inlet/outlet hole (diameter of a1, a2) 10 mm and b1, b2) 8 mm). Dotted line refers to the ideal | |

(i.e. no shunt currents). Mean flow velocity of the electrolyte solution in each channel equal to 1 cm s^{-1} . a1) Open Circuit Voltage and a2) Maximum Gross Power for stacks provided with Ralex membranes (0.65 mm thick) and spacers 1 mm thick [Stack named R1.0]; b1) Open Circuit Voltage and b2) Maximum Gross Power for stacks provided with Fumasep membranes (0.2 mm thick) and spacers 0.082 mm thick [Stack named F0.2]. Inlet concentrations (NaCl): $1 \text{ g l}^{-1} - 30 \text{ g l}^{-1}$ (0.017 M – 0.513 M). Areal blank resistance: a1, a2) $262 \Omega \text{ cm}^2$, b1, b2) $12 \Omega \text{ cm}^2$ 130

Figure 66. Comparison between the predictions of the model and the experimental data as functions of the triplets number. Dotted line refers to the ideal (i.e. no shunt currents). Mean flow velocity of the electrolyte solution in each channel equal to 1 cm s^{-1} . a) Open Circuit Voltage and b) Gross Power Density producible with external current density fixed at 29 A m^{-2} . Inlet solution concentrations: acid and base 0.2M of HCl and NaOH and salt: 0.25M of NaCl..... 131

Figure 67. Comparison between the predictions of the model and the experimental data as functions of the triplets number. Dotted line refers to the ideal (i.e. no shunt currents). Mean flow velocity of the electrolyte solution in each channel equal to 1 cm s^{-1} . a) Open Circuit Voltage and b) Gross Power Density producible with external current density fixed at 29 A m^{-2} . Inlet solution concentrations: acid and base 0.6M of HCl and NaOH and salt: 0.25M of NaCl..... 132

Figure 68. Comparison between the predictions of the model and the experimental data as functions of the triplets number. Dotted line refers to the ideal (i.e. no shunt currents). Mean flow velocity of the electrolyte solution in each channel equal to 1 cm s^{-1} . a) Open Circuit Voltage and b) Gross Power Density producible with external current density fixed at 29 A m^{-2} . Inlet solution concentrations: acid and base 1M of HCl and NaOH and salt: 0.25M of NaCl. 133

Figure 69. Comparison between the predictions of the present model and those of the model by Veerman et al. [110] as functions of the cell pairs number. Dotted line refers to the ideal (i.e. no shunt currents). Mean flow velocity of the electrolyte solution in each channel equal to 1 cm s^{-1} . a1) Open Circuit Voltage and a2) Gross Power Density producible with an applied voltage equal to OCV/2 in 10 cm long and 50 cm wide stacks; b1) Open Circuit Voltage and b2) Gross Power Density producible with an applied voltage equal to OCV/2 in $50 \times 50 \text{ cm}^2$ stacks. Spacers provided with 12 inlet/outlet holes (diameter of 1 cm). Fujifilm Type 10 membranes. Inlet solution concentrations (NaCl): 0.017 M - 5 M. Areal blank resistance: $72 \Omega \text{ cm}^2$ 134

Figure 70. Predicted profiles of cell current (I_k) at different values of the external voltage for $10 \times 10 \text{ cm}^2$ stacks equipped with 50 cell pairs, with Fujifilm Type 10 membranes and with spacers provided with 4 inlet/outlet holes (diameter of 6

mm), fed by 0.017 M - 5 M solutions. Mean flow velocity of the electrolyte solution in each channel equal to 1 cm s^{-1} . Areal blank resistance: $72 \Omega \text{ cm}^2$ 136

Figure 71. Predicted profiles of the longitudinal current flowing along the lower branch of the a) concentrate channels *idown, c, k* and b) diluate channels *idown, d, k* at different values of the external voltage for $10 \times 10 \text{ cm}^2$ stacks equipped with 50 cell pairs, with Fujifilm Type 10 membranes and with spacers provided with 4 inlet/outlet holes (diameter of 6 mm), fed by 0.017 M - 5 M solutions. Mean flow velocity of the electrolyte solution in each channel equal to 1 cm s^{-1} . Areal blank resistance: $72 \Omega \text{ cm}^2$ 137

Figure 72. Predicted profiles of current along the lower (distributor) a) concentrate manifolds *Idistributor, c, k* and b) diluate manifolds *Idistributor, d, k* at different values of the external voltage for $10 \times 10 \text{ cm}^2$ stacks equipped with 50 cell pairs, with Fujifilm Type 10 membranes and with spacers provided with 4 inlet/outlet holes (diameter of 6 mm), fed by 0.017 M - 5 M solute. Mean flow velocity of the electrolyte solution in each channel equal to 1 cm s^{-1} . Areal blank resistance: $72 \Omega \text{ cm}^2$ 138

Figure 73. Predicted Open Circuit Voltage (OCV) as a function of the cell pairs number in $50 \times 50 \text{ cm}^2$ stacks with Fujifilm Type 10 membranes and with spacers provided with 12 inlet/outlet holes (diameter ranging from 2 mm to 14 mm). The dashed black line refers to the OCV predicted by the model neglecting the shunt currents. Inlet concentrations (NaCl): 0.017 M - 5 M. Mean flow velocity of the electrolyte solution in each channel equal to 1 cm s^{-1} . Areal blank resistance: $72 \Omega \text{ cm}^2$ 139

Figure 74. Predicted a) Gross Power Density (GPD) producible with an applied voltage equal to $\text{OCV}/2$ and b) corresponding % loss due to parasitic currents (ψp) as functions of the cell pairs number in $50 \times 50 \text{ cm}^2$ stacks with Fujifilm Type 10 membranes and with spacers provided with 4 inlet/outlet holes (diameter from 2 mm to 14 mm). The dashed line refers to the predictions of the model neglecting the shunt currents. Inlet concentrations (NaCl): 0.017 M - 5 M. Mean flow velocity of the electrolyte solution in each channel equal to 1 cm s^{-1} . Areal blank resistance: $72 \Omega \text{ cm}^2$ 140

Figure 75. Cell current efficiency as a function of the cell position for different feeds, in $10 \times 10 \text{ cm}^2$ stacks equipped with 50 cell pairs, with Fujifilm Type 10 membranes and with spacers provided with 4 inlet/outlet holes (diameter of 6 mm). Mean flow velocity of the electrolyte solution in each channel equal to 1 cm s^{-1} . Areal blank resistance: $72 \Omega \text{ cm}^2$ 141

Figure 76. % current loss due to parasitic currents as functions of the cell pairs number in $44 \times 44 \text{ cm}^2$. Inlet concentrations (NaCl): 0.513 M..... 142

Figure 77. Equivalent electric circuit for a stack provided with n-blocks of 31 cell pairs..... 143

Figure 78. Diluate outlet concentration a) and parasitic loss of current b) as functions of the external current density for an ED stack of 496 cell pairs with 44x44 cm² of membrane active area. Manifolds area 440x5mm². Inlet concentrations: 0.513M..... 143

Figure 79. Cell current a) and parasitic current via the main manifold b) for an ED stack of 496 cell pairs with 44x44 cm² of membrane active area. Manifolds area 440x5mm². Inlet concentrations: 0.513M. 144

Figure 80. Diluate outlet concentration a) and parasitic loss b) for ED stacks with 10x10 cm² of membrane active area. Manifolds area 100x5mm². Inlet concentrations: 0.513M. Red line: 31 cell pairs. Black line: 496 cell pairs. Dashed line: No presence of parasitic currents..... 145

Figure 81. a) Gross Energy Density per kilogram of consumed acid and b) % GED_m loss due to parasitic currents as functions of the triplets number. Mean channel flow velocity: 1 cm s⁻¹. Fixed external current density: 150 A m⁻². Inlet concentrations: 1M HCl and NaOH in the acid and base channels respectively with the presence of 0.25M NaCl as salt background, and 0.25M NaCl in the salt channel. 146

Figure 82. a) Current efficiency and b) % η_c loss due to parasitic currents as functions of the triplets number. Mean channel flow velocity: 1 cm s⁻¹. Fixed external current density: 150 A m⁻². Inlet concentrations: 1M HCl and NaOH in the acid and base channels respectively with the presence of 0.25M NaCl as salt background, and 0.25M NaCl in the salt channel. 146

Figure 83. Gross power density curves for a 500 triplets stack with and without the presence of shunt currents. Mean channel flow velocity: 1 cm s⁻¹. Inlet concentrations: 1M HCl and NaOH in the acid and base channels respectively with the presence of 0.25M NaCl as salt background, and 0.25M NaCl in the salt channel. 147

Figure 84. a) outlet HCl concentration in the acid tank and b) % parasitic loss as functions of the triplets number. Mean channel flow velocity: 1 cm s⁻¹. Fixed triplets number: 500 triplets. Inlet concentrations: 1M HCl and NaOH in the acid and base channels respectively with the presence of 0.25M NaCl as salt background, and 0.25M NaCl in the salt channel. 148

Figure 85. a) Cell current and b) triplet efficiency as functions of the triplet position for different applied current densities (i.e. 50, 150 and 250 A m⁻²). Mean channel flow velocity: 1 cm s⁻¹. Fixed triplets number: 500 triplets. Inlet concentrations: 1M HCl and NaOH in the acid and base channels respectively with

| | |
|---|-----|
| the presence of 0.25M NaCl as salt background, and 0.25M NaCl in the salt channel. | 148 |
| Figure 86. a) Specific Energy Consumption per kilogram of produced acid and b) % SEC loss due to parasitic currents as functions of the triplets number. Mean channel flow velocity: 1 cm s ⁻¹ . Fixed external current density: 300 A m ⁻² . Inlet concentrations: 0.05M HCl and NaOH in the acid and base channels respectively with the presence of 0.25M NaCl as salt background, and 1M NaCl in the salt channel..... | 149 |
| Figure 87. a) Current efficiency and b) % η_c loss due to parasitic currents as functions of the triplets number. Mean channel flow velocity: 1 cm s ⁻¹ . Fixed external current density: 300 A m ⁻² . Inlet concentrations: 0.05M HCl and NaOH in the acid and base channels respectively with the presence of 0.25M NaCl as salt background, and 1M NaCl in the salt channel..... | 150 |
| Figure 88. a) outlet HCl concentration in the acid tank and b) % parasitic loss as functions of the triplets number. Mean channel flow velocity: 1 cm s ⁻¹ . Fixed triplets number: 500 triplets. | 151 |
| Figure 89. a) Cell current and b) triplet efficiency as functions of the triplet position for different applied current densities (i.e. 100, 300 and 500 A m ⁻²). Mean channel flow velocity: 1 cm s ⁻¹ . Fixed triplets number: 500 triplets. | 152 |
| Figure 90. Acid/Base Flow Battery scheme. | 155 |
| Figure 91. Charging a) and discharging b) operation of the Acid/Base Flow Battery..... | 155 |
| Figure 92. Multi-scale model scheme. The dark blue boxes indicate the four dimensional scales of the model, which interact each other and are integrated in a single tool. Light blue boxes indicate sub-models. Orange boxes report the main input parameters. Correlations for flow and mass transfer characteristics coming from Computational Fluid Dynamics (CFD) simulations are used as input for the triplet simulation and the stack hydraulic sub-model..... | 159 |
| Figure 93. Closed-loop operation..... | 162 |
| Figure 94. Open-loop operation..... | 162 |
| Figure 95. Scheme of the yo-yo operation, based on the open-loop multiple passages process mode..... | 163 |
| Figure 96. Comparison between experimental results and model predictions of the external voltage as a function of time in the charge phase. Process configuration: closed-loop. Fixed current density: 100 A m ⁻² . Inlet conditions: distillate in the acid and base tanks, 1 M NaCl in the salt tank. Mean flow velocity: 0.2 cm s ⁻¹ . Blank resistance: 72 ohm cm ² | 165 |
| Figure 97. Comparison between experimental results and model predictions of a) HCl concentration in the acid tank and b) NaOH concentration in the base tank as | |

a function of time in the charge phase. Process configuration: closed-loop. Fixed current density: 100 A m^{-2} . Inlet conditions: distillate in the acid and base tanks, 1 M NaCl in the salt tank. Mean flow velocity: 0.2 cm s^{-1} . Blank resistance: 72 ohm cm^2 .
 166

Figure 98. Comparison between experimental results and model predictions of the external voltage as a function of time in the charge phase. Process configuration: closed-loop. Fixed current density: 200 A m^{-2} . Inlet conditions: distillate in the acid and base tanks, 2 M NaCl in the salt tank. Mean flow velocity: 0.2 cm s^{-1} . Blank resistance: 72 ohm cm^2 .
 166

Figure 99. Comparison between experimental results and model predictions of a) HCl concentration in the acid tank and b) NaOH concentration in the base tank as a function of time in the charge phase. Process configuration: closed-loop. Fixed current density: 200 A m^{-2} . Inlet conditions: distillate in the acid and base tanks, 1 M NaCl in the salt tank. Mean flow velocity: 0.2 cm s^{-1} . Blank resistance: 72 ohm cm^2 .
 167

Figure 100. Comparison between experimental results and model predictions of the external voltage as a function of time in the discharge phase. Process configuration: closed-loop. Fixed current density: 29 A m^{-2} . Inlet conditions: 0.8 M HCl and NaOH in the acid and base tanks respectively, 0.1 M NaCl in the salt tank. Mean flow velocity: 0.2 cm s^{-1} . Blank resistance: 72 ohm cm^2 .
 168

Figure 101. Comparison between experimental results and model predictions of a) HCl concentration in the acid tank and b) NaOH concentration in the base tank as a function of time in the discharge phase. Process configuration: closed-loop. Fixed current density: 29 A m^{-2} . Inlet conditions: 0.8 M HCl and NaOH in the acid and base tanks respectively, 0.1 M NaCl in the salt tank. Mean flow velocity: 0.2 cm s^{-1} . Blank resistance: 72 ohm cm^2 .
 169

Figure 102. Comparison between experimental results and model predictions of the external voltage as a function of time in the discharge phase. Process configuration: closed-loop. Fixed current density: 29 A m^{-2} . Inlet conditions: 1 M HCl and NaOH in the acid and base tanks respectively, 0.1 M NaCl in the salt tank. Mean flow velocity: 0.2 cm s^{-1} . Blank resistance: 72 ohm cm^2 .
 170

Figure 103. Comparison between experimental results and model predictions of a) HCl concentration in the acid tank and b) NaOH concentration in the base tank as a function of time in the discharge phase. Process configuration: closed-loop. Fixed current density: 29 A m^{-2} . Inlet conditions: 1 M HCl and NaOH in the acid and base tanks respectively, 0.1 M NaCl in the salt tank. Mean flow velocity: 0.2 cm s^{-1} . Blank resistance: 72 ohm cm^2 .
 170

Figure 104. Comparison between experimental results and model predictions of the external voltage as a function of time in the charge phase. Process configuration:

Yo-Yo. Fixed current density: 100 A m^{-2} . Inlet conditions: 0.1 M HCl and NaOH in the acid and base tanks, 1 M NaCl in the salt tank. Mean flow velocity: 0.2 cm s^{-1} . Blank resistance: 72 ohm cm^2 171

Figure 105. Comparison between experimental results and model predictions of a) HCl concentration in the acid tank and b) NaOH concentration in the base tank as a function of the stage number in the charge phase. Process configuration: Yo-Yo. Fixed current density: 100 A m^{-2} . Inlet conditions: 0.1 M HCl and NaOH in the acid and base tanks respectively, 1 M NaCl in the salt tank. Mean flow velocity: 0.2 cm s^{-1} . Blank resistance: 72 ohm cm^2 172

Figure 106. Comparison between experimental results and model predictions of the external voltage as a function of time in the charge phase. Process configuration: Yo-Yo. Fixed current density: 200 A m^{-2} . Inlet conditions: 0.1 M HCl and NaOH in the acid and base tanks, 1 M NaCl in the salt tank. Mean flow velocity: 0.2 cm s^{-1} . Blank resistance: 72 ohm cm^2 173

Figure 107. Comparison between experimental results and model predictions of a) HCl concentration in the acid tank and b) NaOH concentration in the base tank as a function of the stage number in the charge phase. Process configuration: Yo-Yo. Fixed current density: 200 A m^{-2} . Inlet conditions: 0.1 M HCl and NaOH in the acid and base tanks respectively, 1 M NaCl in the salt tank. Mean flow velocity: 0.2 cm s^{-1} . Blank resistance: 72 ohm cm^2 174

Figure 108. Comparison between experimental results and model predictions of the external voltage as a function of time in the discharge phase. Process configuration: Yo-Yo. Fixed current density: 29 A m^{-2} . Inlet conditions: 0.8 M HCl and NaOH in the acid and base tanks, 0.1 M NaCl in the salt tank. Mean flow velocity: 0.2 cm s^{-1} . Blank resistance: 72 ohm cm^2 175

Figure 109. Comparison between experimental results and model predictions of a) HCl concentration in the acid tank and b) NaOH concentration in the base tank as a function of the stage number in the discharge phase. Process configuration: Yo-Yo. Fixed current density: 29 A m^{-2} . Inlet conditions: 0.8 M HCl and NaOH in the acid and base tanks respectively, 0.1 M NaCl in the salt tank. Mean flow velocity: 0.2 cm s^{-1} . Blank resistance: 72 ohm cm^2 175

Figure 110. Comparison between experimental results and model predictions of the external voltage as a function of time in the discharge phase. Process configuration: Yo-Yo. Fixed current density: 29 A m^{-2} . Inlet conditions: 1 M HCl and NaOH in the acid and base tanks, 0.1 M NaCl in the salt tank. Mean flow velocity: 0.2 cm s^{-1} . Blank resistance: 72 ohm cm^2 176

Figure 111. Comparison between experimental results and model predictions of a) HCl concentration in the acid tank and b) NaOH concentration in the base tank as a function of the stage number in the discharge phase. Process configuration: Yo-Yo.

Fixed current density: 29 A m^{-2} . Inlet conditions: 1 M HCl and NaOH in the acid and base tanks respectively, 0.1 M NaCl in the salt tank. Mean flow velocity: 0.2 cm s^{-1} . Blank resistance: 72 ohm cm^2 177

Figure 112. Average gross power density (GPD) and net power density (NPD) for charge a) and discharge b) as functions of the mean flow velocity in the channels for stacks equipped with 40 cell triplets, spacer with inlet/outlet holes diameter of 6 mm. Charge external current of 100 A m^{-2} and discharge external current of 30 A m^{-2} . The distance between the two curves represents the pumping power density (PPD). 179

Figure 113. Variation of triplet electromotive force due to concentration polarization in the boundary layers for the 1st triplet at the initial point of charge (SOC=0%) or discharge (SOC=100%), as a function of the non-dimensional coordinate along the channel. Stack equipped with 40 cell triplets, spacer with inlet/outlet hole diameter of 6 mm. Charge external current of 100 A m^{-2} and discharge external current of 30 A m^{-2} 180

Figure 114. Ratio between the manifolds currents and cell currents as a function of the cell-triplet position within the stack for an external current density of 30 A m^{-2} a), 100 A m^{-2} b), 150 A m^{-2} c) and 200 A m^{-2} d) during charge. I_k is the cell-triplet current, $I_{d,a,k}$, $I_{d,b,k}$, $I_{d,s,k}$ are the acid, base and salt electric currents along the distributors, $I_{c,a,k}$, $I_{c,b,k}$, $I_{c,s,k}$ are the acid, base and salt electric currents along the collectors. 40 cell triplets, spacer with inlet/outlet hole diameter 6 mm..... 181

Figure 115. Ratio between the manifolds and cell currents as a function of the cell-triplet position within the stack for open circuit conditions a), an external current density of 30 A m^{-2} b), maximum power c) and short-circuit d) during discharge. I_k is the cell-triplet current, $I_{d,a,k}$, $I_{d,b,k}$, $I_{d,s,k}$ are the acid, base and salt electric currents along the distributors, $I_{c,a,k}$, $I_{c,b,k}$, $I_{c,s,k}$ are the acid, base and salt electric currents along the collectors. 40 cell triplets, spacer with inlet/outlet hole diameter 6 mm. 182

Figure 116. Contour map of percentage of RTE loss due to the parasitic currents via manifolds as function of the discharge and charge external current densities. 40 cell triplets, spacer with inlet/outlet hole diameter of 6 mm. 183

Figure 117. Round trip efficiency as a function of the manifolds diameter for a stack mounting 40 cell triplets a), and of the number of triplets for a manifolds diameter of 6 mm b). Charge external current of 100 A m^{-2} and discharge external current of 30 A m^{-2} 184

Figure 118. a) Voltage, Coulombic and Round Trip efficiencies and b) discharge energy density and discharge efficiency over a sequence of 15 cycles for a stack with 40 cell triplets. Charge external current of 100 A m^{-2} and discharge external current of 30 A m^{-2} 184

| | |
|---|-----|
| Figure 119. Charge energy density and the % Energy lost as functions of the current density. Mean flow velocity: 0.5 cm s ⁻¹ | 187 |
| Figure 120. Discharge energy density and the % Energy gain as functions of the current density. Mean flow velocity: 0.5 cm s ⁻¹ | 188 |
| Figure 121. Charge energy density and the % Energy lost as functions of the mean flow velocity. External current density: 100 A m ⁻² | 189 |
| Figure 122. Discharge energy density and the % Energy gain as functions of the mean flow velocity. External current density: 30 A m ⁻² | 190 |
| Figure 123. Model predictions of the effect of number of stages on acid-base flow battery. a) Charge and discharge current density fixed equal for all stages; b) Profiles of charge/discharge external voltage at each sequential AB-FB stage; c) Average charge/discharge gross power density (GPD) and (discharge) gross energy density (GED); d) Coulombic efficiency (CE), voltage efficiency (VE), and round-trip efficiency (RTE). Each stage is simulated as an AB-FB stack with a membrane active area of 0.5×0.5 m ² | 193 |
| Figure 124. Discharge power as a function of the total membrane area for 4-stage (<i>Ns</i> = 4) and 17-stage (<i>Ns</i> = 17) AB-FB system. Each stage is simulated an AB-FB stack with a membrane active area of 0.5×0.5 m ² | 195 |
| Figure 125. Pareto frontier of gross RTE as a function of the average discharge GPD. Decision variables: <i>ic</i> , <i>id</i> | 202 |
| Figure 126. Pareto frontier of net RTE as a function of the average discharge NPD. Decision variables: <i>ic</i> , <i>id</i> , <i>uch</i> , <i>c</i> and <i>uch</i> , <i>d</i> | 203 |
| Figure 127. Pareto frontier of net RTE as a function of the average discharge NPD. Decision variables: <i>ic</i> , <i>id</i> , <i>uch</i> , <i>c</i> , <i>uch</i> , <i>d</i> , <i>Ctarget,c</i> and <i>Ctarget,d</i> . Lower limit of <i>Ctarget,c</i> =600 mol m ⁻³ | 204 |
| Figure 128. Comparison between the Pareto frontiers of net RTE as a function of the average discharge NPD. Decision variables: <i>ic</i> , <i>id</i> , <i>uch</i> , <i>c</i> , <i>uch</i> , <i>d</i> , <i>Ctarget,c</i> and <i>Ctarget,d</i> . Black line: Lower limit of <i>Ctarget,c</i> =600 mol m ⁻³ . Red dashed line: Lower limit of <i>Ctarget,c</i> =500 mol m ⁻³ | 205 |
| Figure 129. Pareto frontier of net RTE as a function of the average discharge NPD. Decision variables: <i>ic</i> , <i>id</i> , <i>uch</i> , <i>c</i> , <i>uch</i> , <i>d</i> , <i>Ctarget,c</i> , <i>Ctarget,d</i> , <i>L</i> and <i>b</i> . Lower limit of <i>Ctarget,c</i> =500 mol m ⁻³ | 206 |
| Figure 130. Decision variables profiles as functions of the average discharge NPD. Decision variables: <i>ic</i> , <i>id</i> , <i>uch</i> , <i>c</i> , <i>uch</i> , <i>d</i> , <i>Ctarget,c</i> , <i>Ctarget,d</i> , <i>L</i> and <i>b</i> . Lower limit of <i>Ctarget,c</i> =500 mol m ⁻³ | 207 |
| Figure 131. Comparison between the Pareto frontiers of net RTE as a function of the average discharge NPD. Decision variables: <i>ic</i> , <i>id</i> , <i>uch</i> , <i>c</i> , <i>uch</i> , <i>d</i> , <i>Ctarget,c</i> , <i>Ctarget,d</i> , <i>L</i> and <i>b</i> . Black line: volumes ratio 1:1:6 and initial <i>Ct, NaCl, s, out</i> =500 | |

mol m⁻³. Dashed red line: volumes ratio 1:1:1 and initial $C_{t,NaCl,s,out}=100$ mol m⁻³. Limit of $C_{target,c}=500$ mol m⁻³..... 208

Figure 132. Comparison between the Pareto frontiers of net RTE as a function of the average discharge NPD. Decision variables: $i_c, i_d, u_{ch,c}, u_{ch,d}, C_{target,c}, C_{target,d}, L$ and b . Black line: Reference membrane properties. Red line: Improved membrane properties. Limit of $C_{target,c}=500$ mol m⁻³. Volumes ratio = 1:1:6. Initial $C_{t,NaCl,s,out}=500$ mol m⁻³. 209

Figure 133. Comparison between the closed-loop configuration and the Yo-Yo configuration simulated by imposing the conditions of the Pareto frontier of the closed-loop operation with 8 decision variables and volumes ratio= 1:1:1..... 210

List of Tables

| | |
|---|-----|
| Table 1. List of the main performance metrics of the studied electrical energy storage systems. Euro-to-dollar conversion rate 1.18 as of 09/09/2020. | 8 |
| Table 2. List of the main characteristics of BMED models presented in literature..... | 30 |
| Table 3. Summary of the used inlet concentrations in the stack (i.e. outlet concentrations from the tanks) and applied current densities in 10×10 cm ² stacks with Fumatech membranes (FAB, FKB, FBP) and with spacers provided with 3 inlet/outlet holes (diameter of 8 mm). Mean flow velocity of the electrolyte solutions in each channel equal to 0.2 cm s ⁻¹ . Areal blank resistance: 72 Ω cm ² | 59 |
| Table 4. Average (over five tests) model discrepancy of the HCl, NaOH and NaCl outlet concentrations in 10×10 cm ² stacks with Fumatech membranes (FAB, FKB, FBP) and with spacers provided with 3 inlet/outlet holes (diameter of 8 mm). Mean flow velocity of the electrolyte solutions in each channel equal to 0.2 cm s ⁻¹ . Areal blank resistance: 72 Ω cm ² | 60 |
| Table 5. Inputs of the multi-scale model for the simulations of scaled-up BMED units..... | 61 |
| Table 6. Summary with the used inlet concentrations in 10×10 cm ² stacks with Fumatech membranes (FAB, FKB, FBP) and with spacers provided with 3 inlet/outlet holes (diameter of 8 mm). Mean flow velocity of the electrolyte solutions in each channel equal to 1 cm s ⁻¹ | 96 |
| Table 7. Average model discrepancy of the HCl, NaOH and NaCl outlet concentrations for each compartment for the BMRED process. | 97 |
| Table 8. List of the P regression coefficients and inlet-outlet mean concentration differences..... | 99 |
| Table 9. Comparison between experimental data and model outcome for GED and BMRED efficiency for the three cases A, B and C..... | 99 |
| Table 10. Perspective economic analysis of the BMRED process..... | 101 |
| Table 11. Inputs of the multi-scale model for the simulations of BMRED units. | 102 |
| Table 12. List of the membrane properties for the improved membrane properties scenario. | 103 |
| Table 13. Main results of the sensitivity on inlet salt concentrations, with a fixed current density at 100 A m ⁻² , a fixed mean flow velocity of 1 cm s ⁻¹ and inlet acid and base concentration of 1 M..... | 110 |
| Table 14. Initial composition and concentrations – example of industrial BMRED scheme..... | 111 |

Table 15. Summary of the main differences of the equivalent electrical circuits of the investigated processes..... 119

Table 16. Fujifilm type 10 membranes characteristics from [58]..... 125

Table 17. Fumatech membranes characteristics from [224]..... 125

Table 18. Comparison between model outcomes and experimental results of the diluate and concentrate outlet conductivities for a 10×10 cm² stack with Fujifilm Type 10 membranes and with spacers provided with 4 inlet/outlet holes (diameter of 6 mm), equipped with 50 cell pairs, fed by 0.05 M – 5 M inlet concentrations. Mean flow velocity of the electrolyte solutions in each channel equal to 1 cm s⁻¹. Areal blank resistance: 60 Ω cm²..... 129

Table 19. Membrane diffusivities used for AB-FB dynamic model calibration. 164

Table 20. Inputs of the multi-scale model for the sensitivity analysis..... 178

Table 21. Inputs of the multi-scale model for the Closed-loop vs Yo-Yo operations comparison..... 185

Table 22. Overview of main input parameters used in the sensitivity analysis. 190

Table 23. List of the decision variables with their respective lower and upper bounds. 199

Table 24. List of the optimization scenarios. 200

Table 25. Model inputs of the reference case for the optimization study..... 201

Introduction

Electrical energy storage devices allow issues related to the production and the demand of electricity to be overcome. Particularly, in the absence of storage devices, the electricity generated from power supply must be used at the time of production. Therefore, a close match between the time of production and the time of the energy consumption is inherently required. Actually, an imbalance between supply and demand typically occurs, especially when intermittent energy sources are adopted. Moreover, electricity is always produced far from the places in which it is actually used. As a consequence, there is the need to build suitable infrastructures to convey the electricity through several hundreds of kilometers. Furthermore, the total passage towards the production of electricity entirely from renewable sources such as solar and wind is one of the corner posts for future development. The increased production from these intermittent sources has established the imperative for storage of surplus energy, which can then be used when necessary at subsequent times. Moreover, the energy storage should be sustainable and should possess characteristics of modularity and scalability in order to be integrated easily in local micro-grids. Electrochemical batteries are the most suitable devices to this aim. Among them, Acid/Base flow batteries are the most innovative and promising ones. This battery is a non-conventional Electrical Energy Storage (EES) device. The Acid/Base flow battery stores electricity in chemical energy, specifically in the form of pH and salinity gradients. This technology is based on two membrane processes called Bipolar Membrane Electrodialysis (BMED) during the charge phase and its opposite, the Bipolar Membrane Reverse Electrodialysis (BMRED), during the discharge phase of the battery.

The present PhD thesis is devoted to exploring the features and the technical feasibility of this battery, by investigating this technology in every aspect.

Particularly, the present PhD thesis is divided in 7 different chapters which are briefly described in the following.

Chapter 1 is devoted to providing a thorough overview of EES devices including their main features and challenges. In Chapter 2, a review of bipolar membranes, focusing on main production and characterization methods, is reported and critically discussed. Chapter 3 deals with Bipolar Membrane Electrodialysis, which is the process driving the charge phase of the Acid/Base flow battery. Particularly, a novel comprehensive mathematical multi-scale model is there described. This model was validated under steady-state tests. Chapter 4 is devoted to Bipolar Membrane Reverse

Electrodialysis (BMRED) which represents the discharge phase of the battery. A BMRED model is shown in this chapter: this model was developed by adapting the BMED model described in Chapter 3. Here too, the model validation was performed by steady-state experiments. Chapter 5 focuses on the parasitic phenomenon of ionic shortcut currents via manifolds, which affects electro-membrane processes, particularly when highly conductive electrolyte solutions are used. More precisely, in this chapter this parasitic phenomenon was investigated for four different membrane technologies: conventional and bipolar electrodialysis (ED and BMED) and their opposite processes (RED and BMRED). In chapter 6, the fundamentals and features of the Acid/Base flow battery are described, by assessing its performance and the potential in several scenarios. Finally, Chapter 7 reports the optimization study performed for the Acid/Base Flow Battery (AB-FB) system, particularly of the prototype which will be installed and tested in Pantelleria island (Italy), within the framework of the European H2020 project BAoBaB ([1]), which this PhD work is a part of.

A graphical outline of the thesis chapters is depicted in Figure 1.

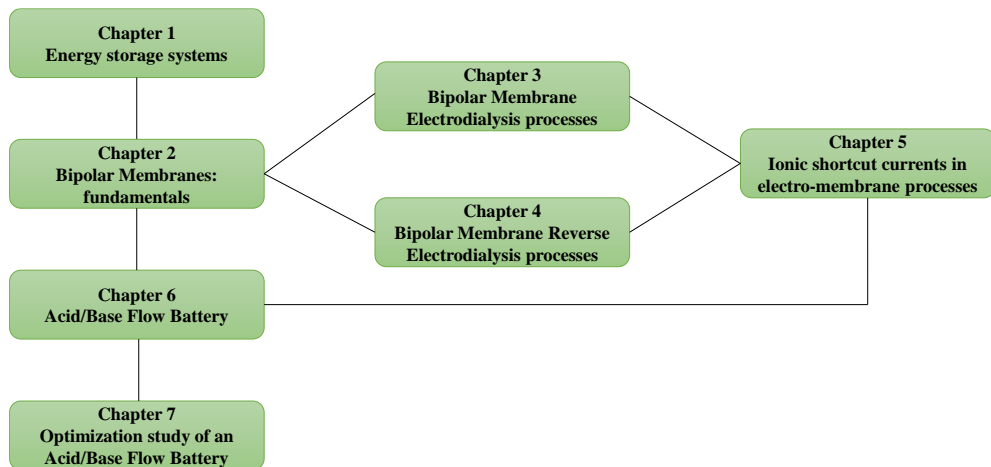


Figure 1. PhD thesis graphical outline

1 Energy storage systems

In the last few years, there has been an increasing need for sustainable development [2]. This was determined by the continuous threat of climate change. Particularly, one of the major problems lies in energy production systems, which currently follow production schemes that are no longer sustainable. As a matter of fact, electricity production typically takes place in a centralized way. Therefore, the electrical energy is produced far from the places in which it is actually used. This is made possible by the construction of complex infrastructures which are able to convey it even thousands of kilometres away with high environmental impact. This also causes the congestion of the grid which leads to an increase of the electricity price. One of the solutions most used by electrical companies is to provide electrical energy at different tariffs as a function of time, for example using three different prices, which are the so called ToU tariffs [3]. On the basis of these tariffs, consumers are lead to use electric energy during the cheaper moments of the day. It is clear that consumers, particularly the industrial ones, cannot decide a priori the time for electricity consumption, thus being compelled to pay more for the energy consumed in the peak hours (which may reach even 4 times the cost of the off-peak energy). In order to reduce costs but also in the absence of electricity from the grid, industries prefer to auto-produce electrical energy by the use of diesel generators with the consequent increase of environmental pollution. The sustainable development policy may be effective only in the presence of collective action and with focus on long-term plans [2]. One of the objectives of EU Commission is to cut greenhouse gas emissions by 80-95% by the year 2050. This ambitious goal may be reached with the technological and social development which aim at a green society. With this respect, renewable energies may represent a way to tackle the problem. This scenario is the one which was outlined by the Decarbonisation Roadmap 2050, with the objective of a gradual passage towards electricity production from renewable sources. The major renewable sources, which are solar and wind, have an intermittent nature, which is difficult to predict [4]. Renewable sources in fact are practically uncontrollable and clearly they may influence the quality of the power grid along with its stability and reliability. It is obvious that these energy sources may not directly supply the same inertial response as the one provided by the classical power generators. Moreover, the supply and demand of renewable energy often do not correspond. All of this represents a current limit on moving towards a 100% renewable society. In order to pursue this goal, the management of the renewable energies with effective storage methods is of crucial importance. Moreover, thanks to storage systems, it is possible to deal with the mismatch between electricity demand and generation from the renewables. Furthermore, the use of storage

technologies may limit the inefficiencies linked to the distribution network and transmission of energy. Particularly, the use of local networks or stand-alone microgrids may somehow help the efficient use of the renewable energies [5]. Microgrids are in simple terms a localized group of electricity sources and storage systems which operate in synergy with the main grid. A user which owns an accumulation system is the basis of the practice of *prosumerism* [6]. It is evident that a storage system should have particular characteristics, as an electricity network may also be damaged depending on the charge/discharge cycles as well as by the used electric currents and the operational time. An effective system, should also be able to reduce the power peaks by the so called “Peak-shaving” strategy [6]. This refers to the discharge of the battery when a certain threshold of the energetic demand is reached. When a limit value is detected, the “shave” of the peak is made possible. These peaks are common throughout the day [6]. This strategy prevents the peaks of demand being transferred to the grid, thus meaning they do not have a negative impact on it. This may be made possible using an appropriate energy storage capacity, to meet the average electricity demand instead of the peaks.

Currently, the most used techniques for the energy storage are the Pumped hydro storage (*PHS*) and Compressed air energy storage (*CAES*). The former consists, in simple words, of water reservoirs placed at different heights for producing hydroelectric energy when it is needed. Conversely, the latter stores energy by compressing air in underground cavities or inside aboveground tanks. These electrical energy storage techniques are the most used worldwide as reported in Figure 2.

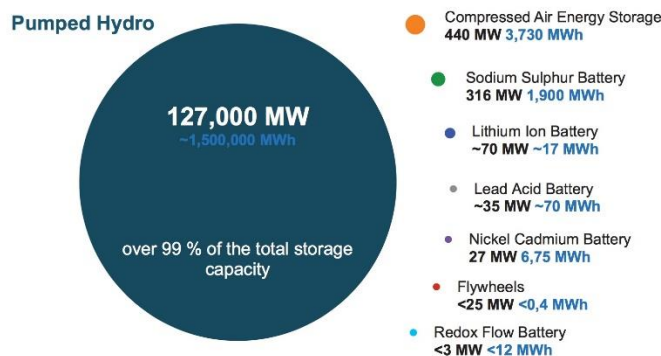


Figure 2. Electrical energy storage capacity installed worldwide for different technologies (From [7]).

Due to their nature, these storage methods have important geographic constraints which lead to difficulties in using these technologies in decentralized

places, unless we have infrastructures characterized by complex electricity distribution networks. In fact, in the case of *PHS* it is necessary that the plant sites contain standing or dammed-up water reservoirs. Conversely, *CAES* needs large underground cavities as natural aquifers or also depleted natural gas reservoirs. In addition, these technologies have some limitations in terms of discharge time and they are suitable for large scale electrical production. However, in the scenario outlined by European Commission about the passage towards the total production of electricity from renewable sources, there is a widespread revival of interest in decentralized accumulation systems based on electrochemical technologies.

1.1 *Electrochemical storage devices*

The electrochemical storage devices are typically made up of two or more cells in a series or parallel fashion depending on the required voltage and current. There are many batteries of this type. In the following, an overview of the four main commercialized categories is reported.

Lead-acid batteries represent a mature, cost-competitive and robust technology. They date back to 1859, the year in which these batteries were invented [8]. They represent the most used rechargeable battery worldwide. A typical lead-acid battery consists of metallic lead and lead oxide electrodes, with the electrolyte based on a sulphuric acid solution at a high concentration. In the case of overcharging, there is a risk of hydrogen evolution, possible explosions and acid release [9]. Moreover, the presence of lead, which is known to be toxic for humans and is also an environmental pollutant, is one of its major drawbacks.

Nickel-Cadmium batteries represent a mature and cost-competitive technology as well [10]. These batteries contain cadmium, which is highly toxic for humans and ecosystems [11]. As concerns performances, Nickel-Cadmium batteries are characterized by a low cell electrical potential of about 1.3V and a limited lifespan. Finally, the “self-discharged” phenomenon is quite significant meaning that these batteries may discharge over the course of a month [12].

Molten salt batteries is another category. Among the batteries of this type, sodium and sulfur one (NaS) is the most adopted [12]. It exhibits many advantages such as the high cyclability, powerful modularity and a very limited self-discharge. The latter is very important for steady-state applications for which a constant power is necessary and particularly in the time frame of hours. This battery operates at high temperatures in the region of 300°C, therefore it needs an extra operating time for the pre-heating process. Moreover, it contains corrosive materials that, together with the high temperatures, imply severe safety issues.

Li-ion batteries are based on the lithium ion transfer from the anode to the cathode during the charge and the opposite process during the discharge [13]. The positive electrode consists of lithium metal oxides, while the negative electrode is based on graphitic carbon. The electrolyte is made up of lithium salts dissolved in alkyl-carbonates. Li-ion batteries represent the most popular battery worldwide. Since the use of lithium in electronics as well as in hybrid vehicles is rapidly increasing, the production of large scale electrical devices may be potentially very expensive. Moreover, Li-ion batteries present some safety limits due to the risk of possible fires and explosions. For these reasons, lithium ion batteries need at least a temperature control, which is also used to increase the efficiency of these devices.

1.2 Flow Batteries

Flow batteries are typically divided in two different types: redox and hybrid [8]. Among the redox flow batteries, Vanadium Redox Flow Battery (VRFB) is the most popular [14]. It makes use of two tanks containing the electrolyte reserves. The electrolytes are then conveyed towards special electrochemical cells which include the electrodes (i.e. anode and cathode) and a membrane separator. Even though VRFB is generally perceived as safe, the vanadium may lead to dramatic environmental issues if accidentally released [15]. Furthermore, the electrolyte in the VRFBs is expensive [16]. Conversely, hybrid flow batteries are equipped with a single external reservoir because the second electrolyte is maintained inside the electrochemical device. Zinc Bromine is the most common example of hybrid flow batteries [17]. The potential toxicity of the bromine is one of the Zinc Bromine battery drawbacks [18]. Overall, flow batteries are very versatile and guarantee a high level of scalability. In fact, since they store energy in a chemical form in the electrolytes [17], their energetic capacity depends on the size, composition, and concentration of the electrolytes, while the nominal power that they may provide depends directly on the dimensions of the electrochemical conversion unit.

1.3 Performance metrics of the energy storage systems

The energy storage technologies are characterized as functions of many parameters and figures of merit [19]. The most used are summarized below.

The energy density is typically expressed in kWh m⁻³ and it represents the nominal energy stored per m³ of electrolyte solution or total electrolytes. The energy storage capacity (in kWh) is the total quantity of energy which can be stored by the system. Power density (in W l⁻¹ or W kg⁻¹) is, in the language of accumulation systems, the maximum power available per unit volume (or mass). The charge and

discharge cycle duration is simply the time necessary for a complete battery cycle. The typical power output (MW) is the power which is discharged on average by the battery. The response time is a parameter linked to the inertia of the system and its capacity to start and reach the nominal power. Lifetime is expressed in terms of number of cycles or the total operational time of the battery. A very important figure of merit is the Round Trip Efficiency (RTE) which is the ratio between the discharge energy over the charge energy for a single charge/discharge cycle. Finally, to have a cost estimation, typically capital costs are reported per unit of discharge power ($\$ \text{kW}^{-1}$) or per unit of energetic capacity ($\$ \text{kWh}^{-1}$). Another cost parameter is the Levelized Cost of Storage (LCOS), which is defined as the discounted cost per unit of discharged electrical energy [20].

In the following, a comparative table of the main electrical storage devices is shown. This table reports the main performance parameters as well as the figures of merit.

Energy storage systems

Table 1. List of the main performance metrics of the studied electrical energy storage systems. Euro-to-dollar conversion rate 1.18 as of 09/09/2020.

| | Energy density kWh m ⁻³ | Energy capacity MWh | Power density W l ⁻¹ | Typical power output MW | RTE | Lifetime cycles | Cycle duration | Response time | Capital cost \$ kWh ⁻¹ |
|--------------|---------------------------------------|------------------------|------------------------------------|----------------------------|---------------|------------------|--------------------|-------------------------|--------------------------------------|
| PHS | 0.13-2 [12] | <8 k [12,19] | 0.01-1.5 [12] | 1-5 k [12] | 65-85% [12] | >10 k [12,19] | Hours [19] | Seconds-minutes [12,19] | 5-250 [12,19] |
| CAES | 0.4-20 [12] | 0.01-1 k [12,19] | 0.04-10 [12] | 3-400 [12] | 42-89% [12] | >8 k [12,19] | Hours [19] | Minutes [12] | 2-265 [12] |
| Lead acid | 25-90 [12] | 0-40 [12] | 10-400 [12] | 0-100 [12,19] | 63-90% [12] | 200-2 k [12] | Hours [19] | < seconds [12,19] | 50-640 [12] |
| NiCd | 15-150 [12] | ≈6.75 [12] | 38-600 [12] | 0-40 [12] | 60-90 [12] | 1.5 k-3.5 k [12] | Minutes – day [17] | milliseconds [12] | 425-2.55 k [12] |
| NaS | 150-345 [12] | 0.4-245 [12] | 1.3-180 [12] | 0.05-34 [12] | 75-92% [12] | 1 k-40 k [12,19] | Hours [19] | Milliseconds [12] | 125-570 [12,19] |
| Li-ion | 94-500 [12] | 0.004-10 [12] | 56-10 k [12] | 0-100 [12] | 75-≈100% [12] | 1 k-20 k [12] | Minutes-Hours [19] | <Seconds [12,19] | 240-4 k [12] |
| VRFB | 16-90 [12] | <60 [12] | 0-33.4 [12] | 0.03-100 [12] | 65-85% [12] | >1.5 k [12,19] | 2-8 h [19] | < seconds [12,19] | 160-1060 [12] |
| Zinc Bromine | 5.2-70 [12] | 0.1-4 [12] | 0-25 [12] | 0.05-10 [12] | 65-75% [12] | 1.5 k-3.5 k [12] | -hours-month [17] | Milliseconds [12] | 160-1060 [12] |

*k refers to 1000.

1.4 Modelling of the energy storage devices

The modelling of a battery is a very important way to evaluate and predict its performance and potential. Moreover, simulation tools allow us to investigate, by the use of software, the response of a battery to several different operating conditions during the battery phases, i.e. charge and discharge, as well as the effect of system parameters such as the temperature. It is clear that different design features lead to performance variation. As a matter of fact, wrong design and operating choices may negatively affect the efficiency of the system by exacerbating the detrimental phenomena. The performance evaluation as well as the simulation of the battery operations is a matter of interest especially where batteries are installed in microgrids [21]. The modelling tools may be simple mathematical systems of equations which aim to simulate simplified electrical circuits. However, such tools could only simulate the qualitative trends of the main performance parameters. A more complex electrochemical-model is needed in order to simulate more accurately the behaviour of the battery both qualitatively and quantitatively.

2 Bipolar Membranes: fundamentals

Bipolar membranes belong to the class of special Ion Exchange Membranes (IEMs). They consist of a layered ion-exchange structure which is, in simple terms, made of one Anion Exchange Layer (AEL) and one Cation Exchange Layer (CEL) stacked together. The zone between the CEL and AEL is referred to as interlayer. Bipolar membranes are typically produced via casting method and are used especially in electrodialysis processes to perform the dissociation reaction of water, thus producing inorganic and organic acid and base solutions. The BPM-layers are typically manufactured with added catalyst to promote the water dissociation. Bipolar membranes may also be used for performing the opposite reaction, which is the acid/base neutralization with the conversion of chemical energy into electricity. The discovery of these special membranes is comparable in importance with the invention of semi-conductor p-n junctions because the bipolar membranes have led to new separation processes, especially in chemical and biochemical industries as well as in environmental protection. In this chapter, the bipolar membranes will be described in detail. Particularly, the possible reaction mechanisms will be shown both in reverse and forward current bias. The main preparation techniques will be discussed as well as the major properties and characterization methods.

2.1 *Bipolar membranes: historical developments and working principle*

A bipolar membrane comprises a cation- and an anion-exchange layer, one on top of the other [22]. The possibility to have layered membranes dates back to the work of Sollner et al. [23]. Later on, Frilette et al. [24] were the first who referred to these layered membranes as bipolar membranes. Later, a few patents about BPMs production were published and the first industrial use involved nitric and hydrofluoric acid regeneration from pickling liquor [25].

The functioning of a bipolar membrane may be compared with the p-n junctions. Specifically, under reversal current bias the water dissociation reaction occurs, while under forward current bias the acid/base neutralization reaction takes place [26].

2.2 *Water dissociation in bipolar membranes*

Under the reversal current bias the water dissociation reaction occurs in the so-called bipolar junction or transition region. This process is typically promoted by the presence of a catalyst in the BPM-layers.

By applying an electric field to a bipolar membrane, a current-voltage curve is obtained. The current-voltage curve presents the well-known shape illustrated in Figure 3.

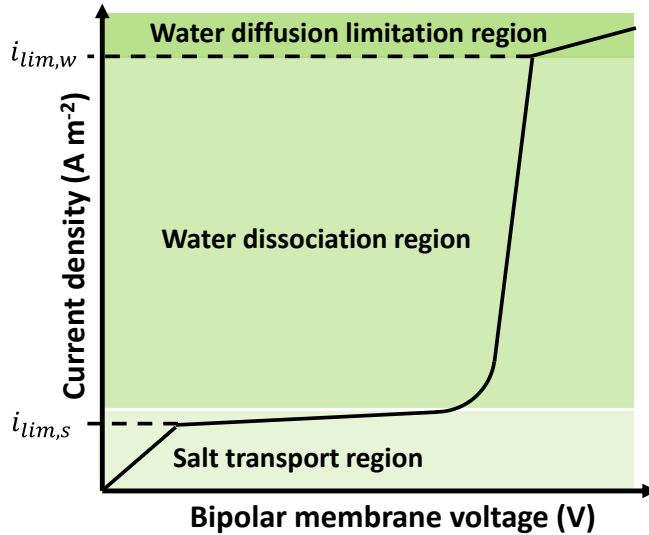


Figure 3. Graph of a typical bipolar membrane voltage-current curve under reverse bias.

Particularly, starting with an equal NaCl concentration in both the channels right next to the two sides of the membrane, the operating current falls within the *Salt transport region* (Figure 3) and it reaches a plateau by increasing the applied voltage. This first limiting current density ($i_{lim,s}$) is related to the NaCl transport from the interlayer to the feed-water channels. Once all the sodium and chloride ions are depleted from the BPM-interlayer, the water dissociation starts and the operating current enters the *Water dissociation region*. The I-V curve (Figure 3) shows a rapid growth of the slope, which delineates the beginning of the proton and hydroxide ions production. Eventually, a second limit current density ($i_{lim,w}$) is reached due to a limitation in the water supply towards the BPM-interlayer, and at that point, the operating current enters the *Water diffusion limitation region*.

The BPM-interlayer has the key-role in the auto-ionization of water. The most proposed structures of the BPM-interlayer are based on the neutral-layer [27] and the abrupt junction [28] approaches (Figure 4).

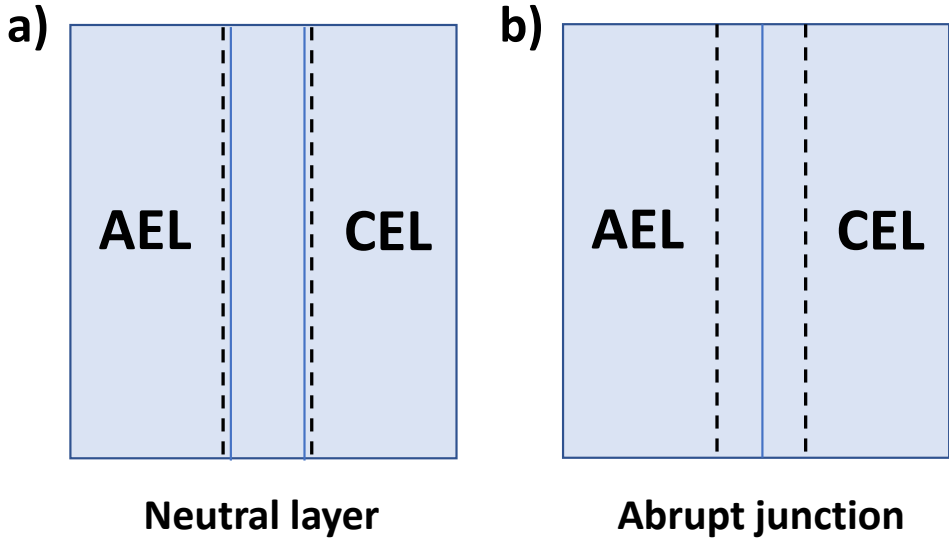


Figure 4. Scheme of the neutral layer a) and the abrupt junction b) models. Blue lines represent the AEL and CEL physical boundaries. Dashed black lines refer to the transition region.

The former assumes the presence of a water meatus between the BPM-layers, while the latter places the transition region in the membrane phase within an area next to the contact-surface between the CEL and AEL.

The water dissociation mechanism is explained by two main currents of thought: the Second Wien Effect (SWE) and the Chemical Reaction Model (CHR). The Second Wien Effect (SWE) explains the acceleration of the water dissociation reaction due to the enhancing effect of the electric field on the forward kinetic constant of the self-ionization reaction of water [29]. Particularly, this theory explains the rapid growth of the proton and hydroxide productions with a high rate constant for water dissociation, i.e. 7-fold higher than the one obtainable in free solution [30]. Conversely, Simons [31] proposed that the water dissociation is due to protonation-deprotonation reactions between the fixed charge included in the BPM-layers and the water molecules. This mechanism is also known as the Chemical Reaction Model (CHR) [32]. A possible reaction mechanism of the water dissociation in the BPM transition region was developed by Strathmann et al. [33] by utilizing the results of Simons. In particular, the water dissociation is caused by protonation-deprotonation reactions of weak basic groups in AEL (Eq. 1-2) and of weak acidic groups in CEL (Eqs. 3-4), as follows,





in which B is the weak base and AH a weak acid.

The production of H_3O^+ and OH^- originate in the membrane phase as follows from the reactions reported in Eqs. 1 and 2, in which water reacts with amino groups, and reactions reported in Eqs. 3 and 4, in which AH is a neutral acid, in the case of phenol, as in the scheme reported by Simons [31].

Afterwards, others [33] adopted a hybrid approach combining the Second Wien Effect and the protonation-deprotonation mechanism.

The nature of the fixed groups of the BPM-layers affects the water dissociation reaction kinetics. Indeed, the formation rate of proton and hydroxide ions may vary with the functional groups. This hypothesis was first proposed by Greben [34] and then by Simons. It was observed that the pKa value of the functional groups and the voltage difference over the bipolar membrane are related to each other. Moreover, the functional ionic groups may be of two types: weak or strong groups. Depending on which of them is present, different proton and hydroxide ion fluxes can be obtained. Furthermore, the performance of bipolar membranes may be improved by including a catalyst in the BPM-layers. Up to now, several different catalysts have been studied [35]. The catalysts investigated in the literature have been divided into two groups: catalysts with organic and inorganic chemistry. Organic catalysts are mainly made of polymeric materials [36], while the inorganic catalysts are typically made of metal compounds [37]. The presence of metallic ions such as magnesium and calcium allows an increase of the proton and hydroxide formation rates. Additionally, Simons studied the effect of metal salts for their catalytic ability to enhance the rate of the water dissociation reaction [38]. The most promising catalysts have been developed recently and are based on graphene [39], ionic liquids [40] or silica [41].

2.3 Acid/Base neutralization in bipolar membranes

By reversing the electric field over the bipolar membrane, i.e. under forward current bias, the opposite process occurs, thus performing the acid/base neutralization in the interlayer of the bipolar membrane. This process is similar to the one occurring in the p-n junctions when electrons and holes are directed towards the n-type and p-type materials respectively. This may happen in two ways: by

inverting the electrodes polarity (with respect to the reversal bias mode) or by assembling the stack with the CELs and AELs facing the anode and cathode respectively. Compared to the reversal bias, the bipolar membrane has lower electrical resistance in the forward mode [35], due to the higher ion concentrations at the BPM-junction. Unlike the I-V curve under reversal current bias, under forward current bias the voltage over the BPM shows a linear trend when varying the electric current as in Figure 5 (dotted line).

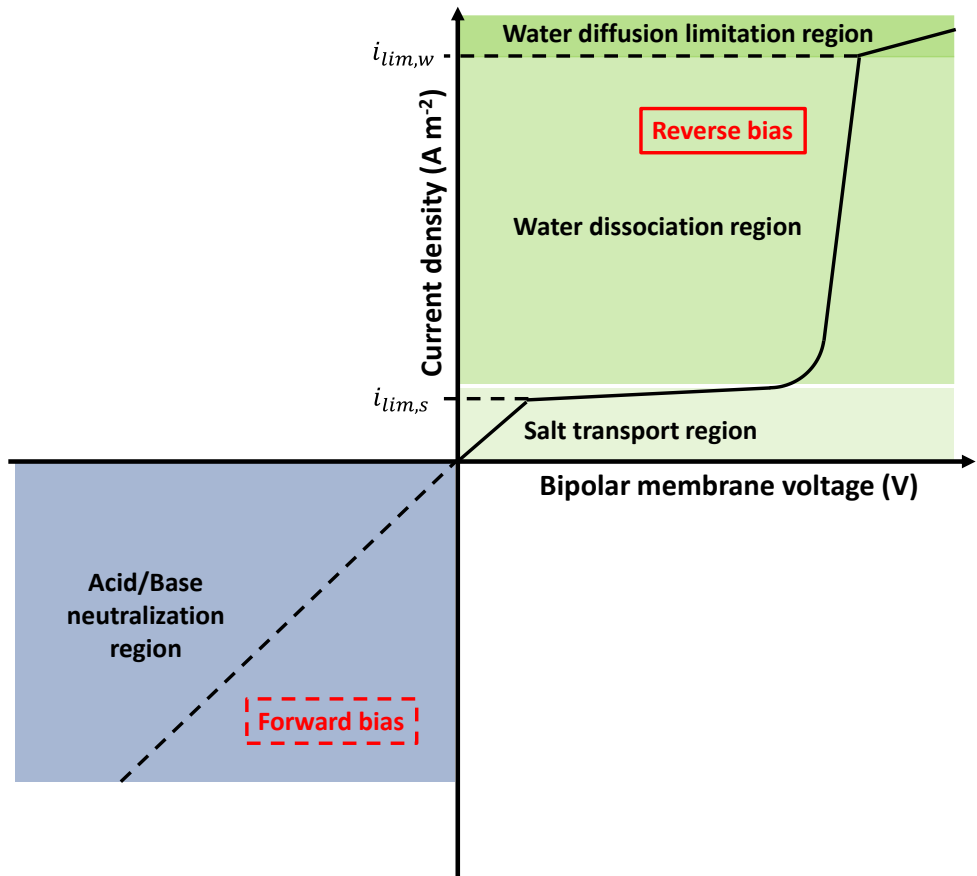


Figure 5. Graph of a typical bipolar membrane voltage-current curve under reverse and forward bias.

The electric current under forward bias has limitations due to the possible delamination of the CEL and AEL, which leads the membrane to irreversible damage: during the acid/base neutralization process, particularly at high electric currents, high amounts of water molecules are generated at the bipolar junction.

These formed water molecules should be able to diffuse out of the junction fast enough to avoid water accumulation at the junction and the consequent delamination of the bipolar membrane layers. Therefore, the formed water molecules should be drained through the CEL and AEL towards their respective adjacent channels. When using commercial bipolar membranes, the electric current under forward bias is limited by this phenomenon, in order to prevent from the detachment between the ion exchange layers.

Moreover, even in ideal process conditions, large quantities of water fluxes occur. Moreover, even disregarding the presence of the neutralization reaction, it is necessary to consider the water fluxes due to osmosis and electro-osmosis. The former occurs when an osmotic pressure difference exists between the two solutions straddling a BPM-layer, and the latter is dependent on the ion migration through CEL and AEL and, particularly, it is caused by the water molecules that are dragged along with the solvation shells of the ions. Therefore, the direction of the water flux across the BPM-layers is mainly dependent on the solution composition and concentrations, as well as the direction of the electric field. Moreover, the bipolar membrane and in particular their layers are in direct contact with acidic and alkaline solutions. Therefore, even in the absence of current, the acid/base neutralization may occur because of diffusion of acid and base molecules through the CEL and AEL. Therefore, in order to operate under forward current bias, bipolar membranes need increased mechanical properties, e.g. high adhesion between CEL and AEL. This may reduce the probability of the delamination phenomenon. However, the bipolar membranes so far available on the market have been designed specifically for the sole reverse current bias mode, to perform the Bipolar Membrane Electrodialysis Process (BMRED). The forward bias mode may be used e.g. for controlling the reaction of acid/base neutralization for industrial applications. Recently, the use of the bipolar membrane was proposed for energy storage purposes and in particular for the construction of innovative flow batteries which store energy in the form of pH gradients. Specifically, BPMs may be used under reversal bias during the charge phase, while the forward bias during the discharge phase. The driving force during the discharge is the neutralization reaction.



By assuming that the whole chemical energy is converted into electrical work, the Gibbs enthalpy (ΔG) is given by,

$$\Delta G = z_e \times F \times EMF \quad (6)$$

in which z_e is electron charge, F is Faraday's constant (96485 C mol^{-1}) and EMF (V) is electromotive force.

The electromotive force over the BPM may be assessed as

$$EMF = \frac{R_g T}{zF} \ln \frac{C_{H^+}|_{ac} \times C_{OH^-}|_{ba}}{K_w} \quad (7)$$

where C is ion activity, R_g is universal gas constant ($8.314 \text{ J mol}^{-1} \text{ K}^{-1}$), T is temperature, z is ion oxidation number, K_w is the self-ionization constant of water and ac and ba refer to the acidic solution/CEL interface, and the alkaline solution/AEL interface, respectively (Figure 6). The ionization constant of water K_w can be calculated by solving the following equations [42].

$$pK_w = -2n_c \left[\log_{10}(1 + Q) - \frac{Q}{Q+1} \rho (\beta_0 + \beta_1 T^{-1} + \beta_2 \rho) \right] + \quad (8)$$

$$pK_w^G + 2 \log_{10} \frac{m^0 M_w}{G}$$

$$Q = \frac{\rho}{\rho^0} \exp \left(\alpha_0 + \alpha_1 T^{-1} + \alpha_2 T^{-2} \rho^2 \right) \quad (9)$$

$$pK_w^G = \gamma_0 + \gamma_1 T^{-1} + \gamma_2 T^{-2} + \gamma_3 T^{-3} \quad (10)$$

where M_w is the molar mass of water (g mol^{-1}), m^0 is the standard molality ($= 1 \text{ mol kg}^{-1}$), n_c is the ion coordination number ($= 6$), G is a constant ($= 1000 \text{ g kg}^{-1}$), $\alpha_0, \alpha_1, \alpha_2, \beta_0, \beta_1, \beta_2, \gamma_0, \gamma_1, \gamma_2, \gamma_3$ are empirical parameters reported in [42].

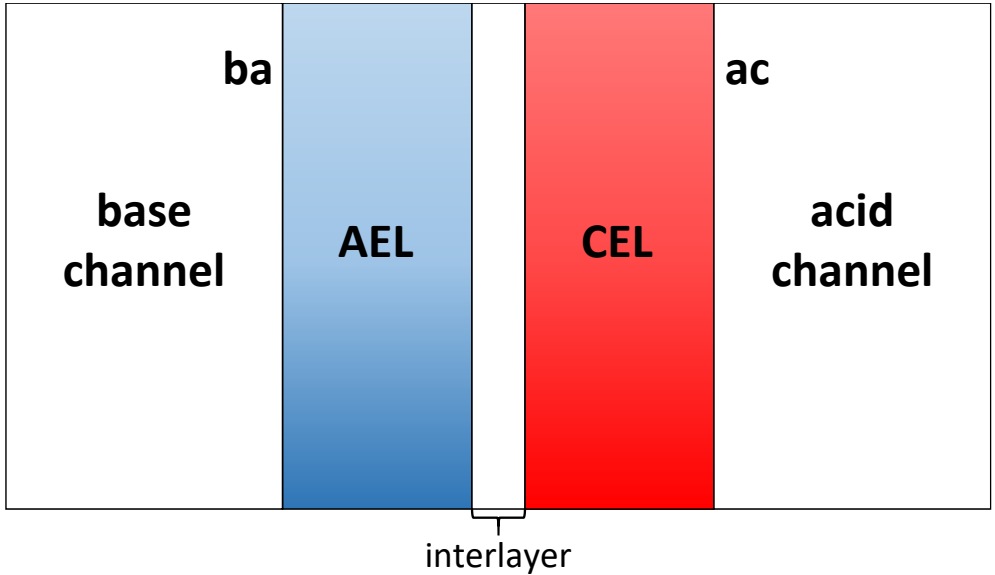


Figure 6. Scheme of the bipolar membrane and the adjacent channels

In Eq. 7 the temperature dependence is both explicitly present in the first fraction, but it is also included in K_w .

By way of example, Figure 7 shows the effect of concentration of protons (fixed equal to the hydroxide ions concentration) and temperature on the EMF .

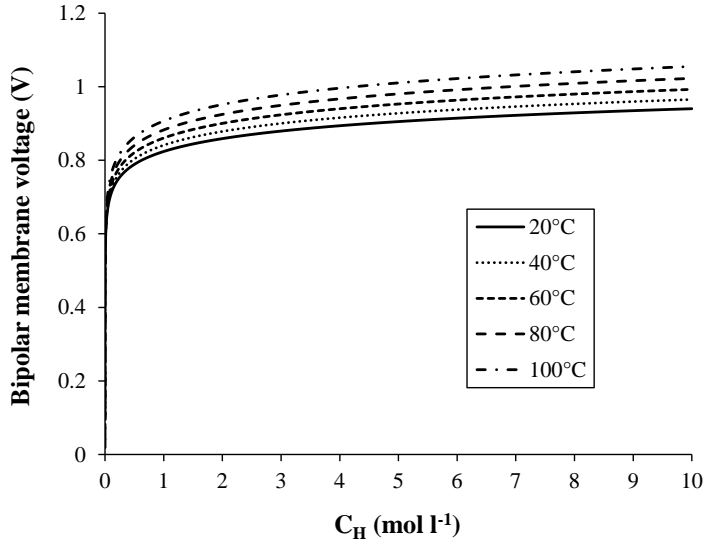


Figure 7. Electromotive force as a function of protons concentration at different process temperatures.

Figure 7 shows that, regardless of the protons concentration, by increasing the temperature from 20°C to 100°C, the average relative difference between the EMF curves is $\approx 11\%$. This suggests that the process may be made more efficient by using increased process temperatures, eventually increasing the electromotive force of the bipolar membrane. In this respect, the recovery of waste heat for this purpose might be a very interesting option.

From Eq.7, the energy density (GED) can be evaluated as

$$GED = F \int_{10^{-7}}^{C_H} EMF dC_H \quad (11)$$

in which C_H is the proton ion concentration (equal to the hydroxide ion concentration). From Eq.11 it follows that the energy density may be very promising, even at low concentrations. For example, by using 1M of HCl and NaOH electrolyte solutions in the two compartments adjacent to the bipolar membrane, an energy density of 24 kWh m⁻³ of acid solution may theoretically be obtained. It is possible to use bipolar membranes under forward bias in combination with the homopolar

membranes, thus performing the Bipolar Membrane Reverse Electrodialysis process. This technology will be discussed thoroughly in Chapter 4.

2.4 *Thickness of the transition region of a Bipolar Membrane*

Regarding the electrical behaviour of bipolar membranes, it may be considered as represented by three resistances in series, which are related to the cation-exchange layer (CEL), the anion-exchange layer (AEL) and the transition region. The CEL and AEL may be considered as homopolar ion exchange membranes, so their electric resistance may be estimated in the range of 0.5-5 ohm cm². The estimation of the electrical resistance of the transition region follows from the measured resistance of the whole bipolar membrane minus the resistances of CEL and AEL. Thus, the transition region has been determined to be in the order of ≈ 5 ohm cm² [33].

The thickness of the transition region may be calculated by adopting the Strathmann approach [33]. Therefore, regardless of the theoretical structure (i.e. neutral layer or abrupt junction), the thickness may be estimated starting from the expected solution conductivity in the transition region. The solution conductivity can be calculated once the composition of the electrolyte solution has been noted. Indeed, the solution conductivity is a function of the ion mobilities. These are, in turn, function of the ion concentrations. During the BPM operation in reversal current bias and particularly during the water dissociation, it is assumed that the transition region is depleted of the salt ions. Therefore, the only ions that are present in the transition region are the proton and hydroxide ions, as follows from the water dissociation equilibrium. From this estimation, the transition region is believed to be in the order of a few nanometres [33].

2.5 *Preparation of bipolar membranes*

In recent decades, many different methods have been developed to produce bipolar membranes [43,44]. For instance, it is possible to differentially functionalize the two faces of a polymeric material sheet, to make one side selective to cations and the other selective to anions. Other methods are based on the adhesion of the two membranes (selectively functionalized) through applying heat and pressure. Eventually, a binder component can be used to improve the adhesion between the two layers. Casting process is the method mostly used. However, while using this method, the interpenetration of the two layers must be avoided because it may result in worse performance of the BPM, e.g. increased electrical resistance of the bipolar membrane, which can then lead to a consequent high voltage drop in forward bias or large applied electric potential in reverse bias. Bauer et al. [22] prepared bipolar

membranes by using mono-sheets through the casting process. The BPMs thereby produced showed improved properties when compared with the commercial membranes produced by lamination, thus resulting in better performance such as, among other things, lower electrical resistances. Chlanda et al. [45] developed bipolar membranes in which the anion exchange layer included a specific cross-linked reaction product, thus obtaining lower interpenetration grades and, as a result, better process performance. Other lesser-used preparation methods are radiation-induced grafting [46] and electro-spinning [47].

2.6 *Properties of bipolar membranes and how to assess them*

Hereafter, the main properties of the bipolar membranes are reported.

Selectivity

Selectivity refers to the membrane's ability to selectively permeate cations or anions through the CEM/CEL or AEM/AEL respectively. Consequently, the performance of membranes strongly depends on their capability to exclude co-ions and allow the passage of counter-ions [48].

Specifically, perm-selectivity is a property that is linked to the affinity between cations or anions and their corresponding membranes [49]. Furthermore, it is associated with the variation in migration speed that the ions have in the membrane phase. A membrane is said to be perfectly permselective if it allows the passage of counter-ions only [48]. The transport of the co-ions through the IEMs can occur by diffusion of the ions from the compartments with a higher concentration towards those with a lower concentration, or the transport can occur by migration [48]. Some works have shown how perm-selectivity decreases as the bonding affinity between counter-ion and fixed charges of the membrane increases [50]. Unlike with counter-ions, the relationship between co-ion properties and perm-selectivity is less clear. In particular, the relationship between co-ions and perm-selectivity has been associated with co-ion hydrated radius, co-ion polarizability, co-ion Stokes radius as well as the Gibbs free energy of hydration [50], but there are few general conclusions. The perm-selectivity of a membrane is given by the transport numbers of the ions in the membrane phase [51].

The transport numbers of the ions in the membrane are generally calculated following two approaches: the Hittorf's method and the ElectroMotive Force (EMF) method [52]. The EMF method is based on the measure of a membrane's potential, with an electrolyte solution used on either side of the membrane. Particularly, the same electrolyte is used on both sides of the membranes, but it has a different

concentration [53]. Regarding the Hittorf's method, it would allow a reliable evaluation of transport numbers as it is based on the measurement of ion fluxes in a channel formed by two membranes: one auxiliary and one under investigation [51]. However, Hittorf's method, as well as its modifications, are rather laborious and, thus, the EMF method is the most commonly used [54]. Nevertheless, a single measurement of the membrane potential allows the calculation of the transport number in binary electrolyte solutions. In the presence of ternary electrolyte solutions, an experimental procedure involving multiple measurements would be needed. Even so, including for non-binary solutions, an apparent potentiometric transport number is obtained, with the system being assumed to behave like a binary electrolyte solution [54]. Compared to the monopolar membranes, the bipolar membranes present a higher apparent perm-selectivity since the proton and hydroxide ions transport numbers are within the range of 0.90-0.96 at a definite interval of current density [55]. Moreover, it was found that the perm-selectivity of the BPM diminishes at higher product concentrations [56].

A possible mathematical approach for calculating transport numbers in multi-ion systems will be described in chapters 3 and 4 for both monopolar and bipolar membranes.

Electrical resistance

Several different methods may be used to evaluate the electrical resistance of the bipolar membranes. One of them, which is the most commonly used, is conductivity measurements in a two-chambered cell with stirrers. Particularly, the membrane resistance is evaluable by subtracting the electrolyte resistance of the cell without the membrane from the electrolyte resistance with it. [22]. Another way to obtain the electrical resistance of the membrane is by using the Electrochemical Impedance Spectroscopy (EIS) [35]. This method consists of the recording of the electrochemical impedance spectra of the membrane, typically on AC (Alternating Current) at a particular frequency. The obtained spectra from this method provides a graph of the imaginary part of the impedance as a function of its real part. Particularly, when the frequency is taut to infinite, the bipolar membrane resistance corresponds to the real part of the impedance [57].

BPM water splitting capacity

The water splitting capacity of the bipolar membrane can be evaluated by using a 6-compartment electro dialytic cell. At a fixed applied current density, the pH variation from the inlet to the outlet of the acid and base compartments is measured by titration of the electrolyte solutions [22]. In such a system, the BPM water splitting

capacity is determined as the ratio between the measured pH and the total current passing through the cell.

Solute and solvent permeability

Another important characteristic is the permeability to the solvent and the solutes. The water permeability is an important property both in reverse and forward bias mode. As previously stated, under reverse bias, the water permeability should be high enough to increase the second limiting current of Figure 3. In fact, when the dissociation rate of water is too high with respect to the capacity of the water to diffuse towards the transition region, the dissociation rate becomes approximately constant even when increasing the applied voltage. On the other hand, under forward bias, the permeability should be high to allow the diffusion of water molecules from the interlayer to the acid and base compartments, thus avoiding the risk of membrane layers delamination (irreversible damage).

To assess the permeability to the salt, a simple diffusion cell, with two stirred compartments and with no electrical potential applied across it, may be employed (Figure 8).

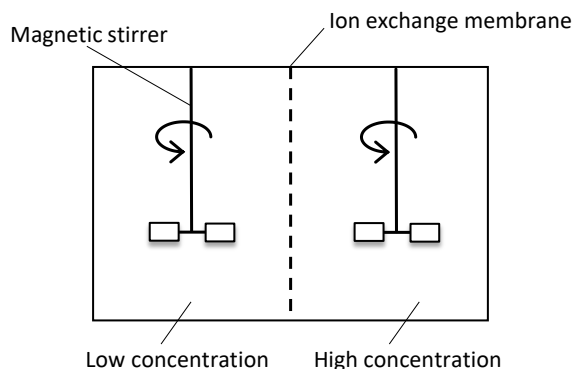


Figure 8. Experimental set-up for the determination of the ion permeabilities of a bipolar membrane.

In this way, the ions have the ability to diffuse through the membrane. Importantly, in order to easily observe the diffusion process, two different solution concentrations must be used on the two sides of the membrane. Before each test, the membrane should be properly conditioned with the solutions to be tested [58].

A simple diffusive permeability (i.e. an apparent diffusivity, whose concentration gradient refers to the solution phase and not to the membrane phase) may be obtained. However, for a more specific estimation of the ion diffusivity in the membrane phase for multi-electrolyte solutions, more complex calculations are

required. These calculations should adopt a multi-ion model approach, taking into consideration the presence of all the ions in the solutions. An example of a multi-ionic mathematical approach involving such ion membrane diffusivities will be shown in Chapter 4 for the bipolar membrane.

Chemical and thermal stability

Thermal and chemical stability is another important property of the bipolar membranes. This property is very important because of the demanding operating conditions that the bipolar membrane may be exposed to. In fact, high acid and base concentrations may be used on both sides of the membrane and, additionally, high process temperatures may be applied to enhance the electromotive force.

Moreover, the stability of the membrane also depends on the solvent being used. By way of example, by using alcohol instead of water, the lifetime of the bipolar membrane is limited to only three days [59]. Some measurements of membrane stability with water as solvent were performed in the work of Bauer [22].

Ion-exchange capacity

The ion-exchange capacity (IEC) is directly related to the concentration of fixed groups of the anion and cation exchange layers of the BPM. As reported in [60], IEC is obtained by exchange of ionic species. Particularly, the tested membrane is brought in equilibrium with a first ionic species, rinsed with demineralized water, and then leached with another salt solution. The amount of ion exchanged are measured by titration: specifically, a solution of NaOH is used for the negatively charged layer and HCl for the positively charged layer. IEC is typically expressed in meq per gram or cm^3 of dried membrane.

Swelling degree

The swelling degree is an important membrane property which can be evaluated as the relative difference between the weight of the wet and dried bipolar membrane [61,62]. This parameter may have some influence on the membrane electrical resistance and ion selectivities. Furthermore, it is a measure of the physical stability of the membrane. In this regard, the most significant mechanical properties are the tensile and bursting strengths measured by the Schopper's tension and Mullen testers respectively [63].

One of the most important aspects of a bipolar membrane is the voltage profile as a function of the current (I-V curves), namely the polarization curve, or the voltage profile as function of time, called chronopotentiometry. Both refer to the electric potential over the whole bipolar membrane, without distinguishing between the two BPM-layers. The polarization curve has already been shown and discussed in section

2.2 for the sole reverse bias and in section 2.3 for both the process modes. The chronopotentiometry instead refers to the measurements of the electric potential over time by applying a fixed electric current for a certain time interval: a typical chronopotentiometry graph is depicted in Figure 9.

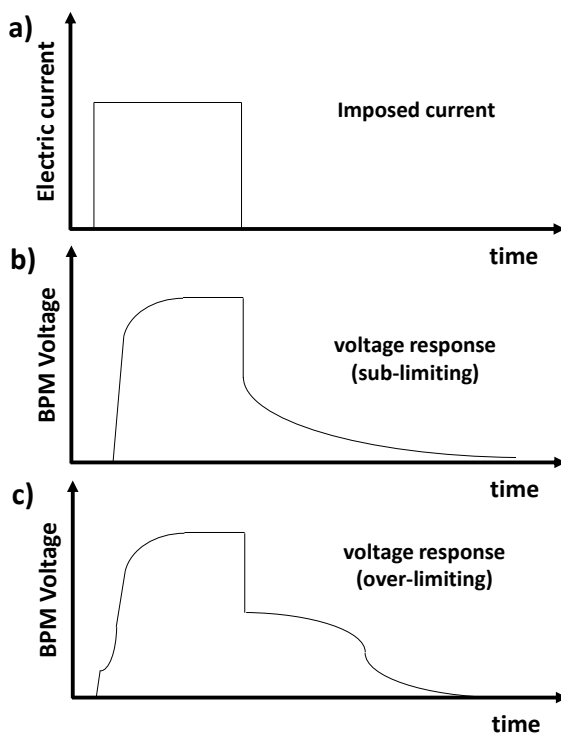


Figure 9. a) Imposed electric current and voltage response as functions of time for a typical chronopotentiometry of a bipolar membrane in b) sub-limiting region and c) over-limiting region. Adapted from [64].

Therefore, the time evolution of the electric potential gives important insights into the response of the bipolar membrane, in both the so-called “sub-limiting” and “over-limiting” regions [64]. Sub-limiting (Figure 9b) and over-limiting (Figure 9c) regions refer to the operation of the bipolar membrane at current densities below or above the salt limiting current density respectively. When the electric current is switched on, the voltage difference values are directly related to the ohmic energy loss and, in turn to the electrical resistances. In addition, the discharge time is associated with the selectivity of the bipolar membrane. Finally, the composition and concentrations of the solutions surrounding the bipolar membrane influence the electromotive force and, thus, the voltage curves. Therefore, these voltage curves represent an important performance indicator, not only giving information regarding

the nature of the bipolar membrane itself, but also demonstrating the outcomes when varying the operating conditions.

2.7 *Modelling of the bipolar membranes*

Due to the complexity of simulating a bipolar membrane, the first modelling attempts tried to focus only on the qualitative mechanisms of solvent transport and water dissociation [65]. The application of the Nernst-Planck equation to describe the ion-transport in the bipolar membrane [66] has been generally accepted, despite being strictly valid in infinite dilution condition [67]. Besides the Nernst-Planck equation, a rigorous approach should also take into account the Poisson's equation to describe the potential profile across the BPM [68]. However, it is not a trivial task to resolve the Poisson's equation without applying any simplifying assumptions [69]. The salt limiting current density is mainly related to bipolar membrane parameters such as the perm-selectivity (or specifically ion transport numbers) and the salt diffusivity. Interestingly, Strathmann et al. [33] shows qualitatively the influence of membrane features, such as the fixed charge density of the first limiting current (in reverse bias mode), as well as the effect of the solution bulk concentration. Particularly, the first limiting current density was found to increase with both salt diffusivity and salt concentration in solution [33]. On the other hand, the limiting current decreases with the fixed charge density of the BPM-layers (assumed equal for the AEL and CEL). Moreover, the calculated limiting currents may reach up to 50 A m^{-2} , in their investigated conditions, thus resulting non-negligible [33]. Furthermore, Wilhelm et al. [70] found an inverse dependence of the limiting current on the BPM-layers thicknesses, thus also geometrical features may play an important role on the limiting current. In particular, they found that the lower the BPM-layers thicknesses, the higher the first limiting current density. Specifically, with thicknesses lower than $100 \text{ }\mu\text{m}$, the limiting current showed an exponential increase [70]. Although some evidence of the co-ion leakage through the BPM-layers is mostly attributed to the cationic leakage through AELs [71], with dilute solutions this contribution is small enough to be neglected [72]. Conversely, with highly concentrated solutions the salt flux contribution increases [70]. When the over-limiting current is reached, it is noted that the ion current associated with salt flux is proportional to the proton and hydroxide ion currents [73]. The proportionality constant was found to be a function of the layer selectivity with respect to the co-ions, which, in turn, was found to be dependent on the solution concentrations and the fixed charge density [73]. Water flow modelling is a problem mostly at high current densities in reverse bias, when there is a risk of BPM-junction drying [26]. The experimentally observed enhancement of water dissociation with temperature has been, at least qualitatively,

mathematically described by the work of Ramirez et al. [32], assuming an Arrhenius relationship for the reaction rate constants.

3 Bipolar Membrane Electrodialysis processes

Bipolar membrane electrodialysis is a technology combining solute and solvent dissociation [74], thus leading to the production of chemicals. In recent decades, bipolar membrane electrodialysis has been studied for many purposes, e.g. for the production of valuable acid and base solutions by using salty streams. Despite many works having carried out experimental investigations, so far only a few efforts have been devoted to process modelling. In the present chapter, the development of a Bipolar Membrane Electrodialysis mathematical model based on a multi-scale approach with distributed parameters is presented. Five models related to four different dimensional scales were fully integrated to form a comprehensive tool. Indeed, the integrated model was developed using the process simulator gPROMS Model builder, and is based on a semi-empirical approach combining high simulating accuracy and low computational burden. Once validated across a wide range of experimental data, a sensitivity analysis was performed to assess the effectiveness of this technology for industrial-scale applications. Interestingly, results suggest that an average Specific Energy Consumption of $0.8 \text{ kWh kg}^{-1} \text{ HCl}$ can be reached. Moreover, under the operating conditions investigated here, higher current density values led to poorer stack performance.

3.1 *Conventional Electrodialysis: General overview and working principle*

ElectroDialysis (ED) or Conventional ElectroDialysis (CED) is an electro-membrane process that dates back to Maigrot and Sabates' conceptualisation of the idea in 1890 [75]. Since then, ED has been employed across different fields; for example, the most important application at industrial scale is the desalination of brackish water [76]. Moreover, electrodialysis has been used for investigating industrial waste treatments [77,78], municipal water [78,79] and the chemical and biochemical industries [80–82]. The success of ED has mainly been due to its versatility and its low environmental impact; indeed, it can be used in many processes and has an almost null utilization of chemical compounds. Conventional electrodialysis (CED) is a unit operation whereby, when a potential difference is applied, salts are removed from saline solutions. As a result, two streams, each with a different concentration of the solute (i.e. one dilute and one concentrated) are produced [83]. The CED unit is a stack including many repetitive units called cell pairs or cells, and the conventional ED cell is made up of Cation- and Anion-Exchange Membranes (CEM and AEM, respectively) with interposed channels (Figure 10), which are typically created by separating the membranes by net spacers.

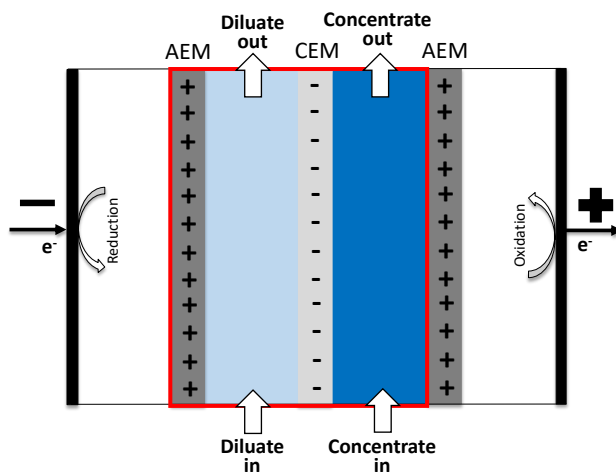


Figure 10. Schematic of a CED unit.

Within this setup, the Ion-Exchange Membranes (IEMs) act as barriers that selectively allow the passage of counter-ions while rejecting co-ions, due to the effect of the so-called “Donnan exclusion” [84]. The CED equipment is commonly made using a plate-and-frame configuration, thus the repetitive units are arranged between two end-plates containing the electrodes. Furthermore, an external DC electric generator establishes an electron flux through the electric circuit. Particularly, the end-plates are in contact with the Electrode Rinse Solution (ERS), thus allowing electron charge transfer from the electrodes to the ionic species in solution by redox reactions. Therefore, the applied electric field drives the ionic current through the stack; in this way, cations migrate towards the cathode whilst anions migrate towards the anode. The result is the production of two streams, one being dilute and one being concentrated.

3.2 Bipolar Membrane Electrodialysis

Bipolar membrane electrodialysis is an efficient method for the production acid and base solutions [74]. It is distinguished by its eco-friendly qualities, which have led to it receiving increasing attention from both academia and industry [85]. A BMED device is characterized by the presence of bipolar membranes that allow the water dissociation reaction, which separates proton and hydroxide ions, and thus produces acid and base solutions. A scheme of the BMED process with three-chamber units is depicted in Figure 11.

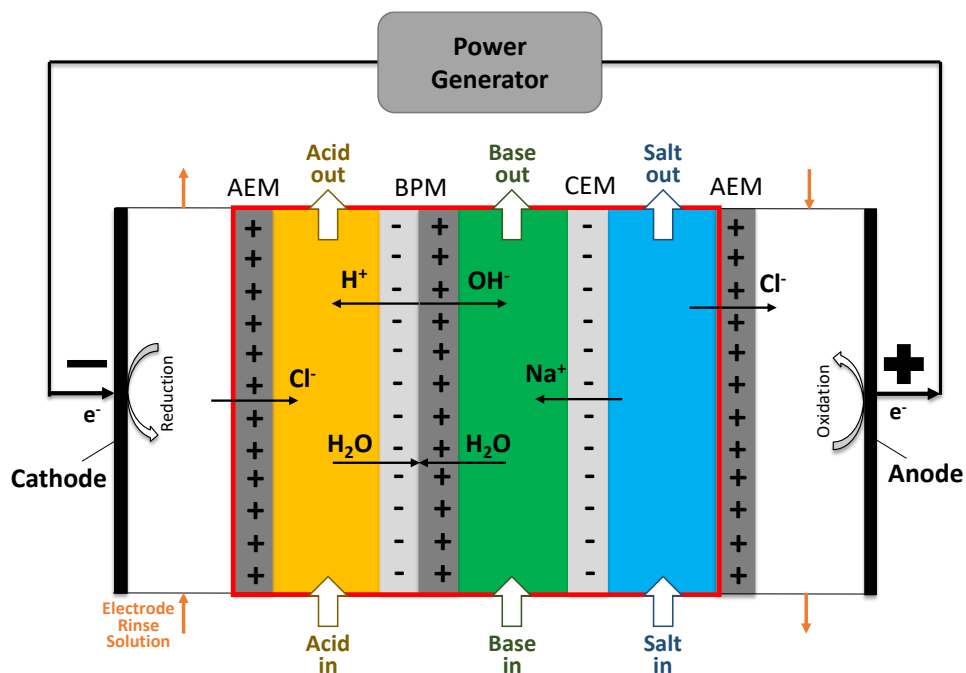


Figure 11. Schematic of a Bipolar Membrane Electrodesalination (BMED) unit.

In principle, fresh water enters the acid and base channels while salt water enters the salt channel (inlet streams Figure 11). In the interlayer of the bipolar membrane, the water dissociation occurs, thus producing proton ions on one side and hydroxide ions on the other side of the bipolar membrane (Figure 11). The salt ions in the salt channel are forced to move towards opposite directions depending on their charge and the applied electric field. Therefore, the production of the acid and base molecules is achieved.

BMED can be applied to many processes, such as the production of several organic and inorganic acids, as well as base compounds. Common BMED modules can operate with very high current densities within the range 250-1000 A/m² [86]. However, depending on the BPM characteristics, BMED stacks may even reach 2000 A/m² [33]. Currents as high as this make BMED applications well-suited to meeting the needs of industrial plants. For this reason, BMED may be used for synthesis processes, e.g. in the food industry [87], chemical and biochemical productions [80] and wastewater treatment [88].

In the last few decades, several studies have focused on the development and characterization of BMED processes. Particularly, several cell configurations have been proposed for a wide range of applications.

3.2.1 Configurations of BMED units

A BMED module is usually composed of several repetitive units stacked together. Many different configurations of the repetitive units have been investigated so far, and they can be grouped based on the number of channels. The number of channels also identifies the number of membranes. However, the same number of channels/membranes can be used with different combinations of membrane types. Particularly, besides the bipolar membrane, there may be cation-, anion- or both ion-exchange membranes in different configurations. For example, 2-channel configurations may be of two types: BPM-AEM and BPM-CEM. The typical applications for these types of configurations are organic and inorganic acid and base production, as well as treatments of acid neutralisation for controlling pH levels. 2-channel configurations allow better performance in terms of energy consumption [89] due to their lower internal resistance. On the contrary, they offer worse product yields compared with the 3- or 4-channel arrangements. This has been shown by the work of Kravtsov et al. [89], which compared the demineralization yield obtained with BPM-AEM-CEM and BPM-AEM configurations. The latter results in lower yields because of the presence of salt-cations in the streams, whereas the presence of the CEM would allow higher product quality. Consequently, the BPM-AEM configuration may be justified only when a high product purity is not required [90]. Furthermore, the 2-channels configurations showed lower current utilization [91] (i.e. the efficiency with which the applied current is turned into the desired transport of ions). Despite the use of a 3-compartment cell leads to better current utilization, it is lower than 100%. This is due to both the diffusion of sodium and chloride ions through the BPM and the protons and hydroxyl ions leakage through the monopolar membranes (AEM and CEM) [92]. In this regard, the current density should be higher than the “first” BPM limiting current density in order to have water dissociation. Moreover, the feed concentration tends to limit the acid and base leakage. In particular, the higher the salt feed concentration, the lower the co-ion leakage carried by proton and hydroxide ions [92]. Moreover, it was observed that, when the concentration of proton and hydroxide ions increase, their leakage through the IEMs increase [93]. This fact leads to the deterioration of the BMED performance.

In addition, for deacidification processes, when compared to the conventional ED, the use of 2-channel BMED avoids the consumption of the basic solution, thus reducing the economic costs [94]. On the other hand, despite the higher costs, four channel membrane configurations are suitable to achieve higher purities of the product(s) [95]. The most common configuration is the three channels-membranes

constituted by BPM-CEM-AEM, as it represents a trade-off between economic costs and product yields.

3.3 Modelling of the Bipolar membrane electrolysis: state of the art

Although BMED has been widely investigated by experimental works, further studies are required in order to develop effective simulation tools that are able to predict the functioning, to optimise the systems, and eventually to drive the scale-up to the industrial level [96]. Table 2 gives an overview of different BMED modelling approaches, highlighting some of their relevant characteristics.

Table 2. List of the main characteristics of BMED models presented in literature.

| Ref | Domain | | Mass balances | Mass transport | | Non-ideal effects | | |
|-------|--------|-------------|---------------|----------------|-----|-------------------|---------|----------------|
| | lumped | distributed | | N-P | NET | Diffusion | | Shunt currents |
| | | | | | | water | solutes | |
| [97] | ✓ | ✗ | ✓ | ✗ | ✗ | ✗ | ✓ | ✗ |
| [72] | ✓ | ✗ | ✓ | ✗ | ✗ | ✓ | ✓ | ✗ |
| [86] | ✓ | ✗ | ✗ | ✓ | ✗ | ✗ | ✓ | ✗ |
| [98] | ✓ | ✗ | ✗ | ✗ | ✗ | ✗ | ✗ | ✗ |
| [99] | ✓ | ✗ | ✗ | ✓ | ✗ | ✗ | ✓ | ✗ |
| [100] | ✓ | ✗ | ✗ | ✗ | ✗ | ✗ | ✗ | ✗ |
| [101] | ✓ | ✗ | ✓ | ✗ | ✗ | ✗ | ✓ | ✗ |
| [102] | ✓ | ✗ | ✓ | ✓ | ✗ | ✗ | ✓ | ✗ |
| [103] | ✓ | ✗ | ✓ | ✗ | ✓ | ✓ | ✓ | ✗ |

The models presented so far in the literature are simplified lumped tools with at least three empirical parameters [104], with an average of six to eight constants [97]. Mass balances are commonly included to predict the outlet concentrations from the unit [72,105]. However, to the best of the author’s knowledge, there are no models taking into account the local mass balances in the stack along the flow direction (models with distributed parameters) [106].

Regarding the trans-membrane flux calculations, the Nernst-Planck (N-P) approach is generally used [86,98,102], but in some cases the membrane fluxes are

described by the non-equilibrium thermodynamic (NET) approach [103]. The concentrations at the membrane side of the solution-membrane interface are evaluated by applying the Donnan equilibrium equations [99,102]. The interface concentration at the solution side is different from the bulk concentration because of the effects of the boundary-layer (concentration polarization). Although generally not considered for the sake of simplicity, the boundary layer may have a considerable impact, especially in the salt compartment [99]. In other cases, this phenomenon is related to the diffusion-limited current at the monopolar membranes in the salt channel [103] (not to be confused with the first bipolar limiting current, which is discussed in chapter 2). Indeed, the diffusion-limited current is obtained when the electrolyte concentrations at the interface become zero [107]. Interestingly, some studies have demonstrated the electro-convection phenomenon at the monopolar membranes, which enhances the mass transfer at over-limiting electric currents [108,109].

Modelling tools for BMED systems are often limited to the computation of migrative flux, while the ion diffusion is taken into account in only a few cases [97,101,103]. However, the diffusive flux is important for a more complete prediction of the proton leakage through the AEMs [72,101], as well as, in general, for predicting the leakage of all co-ions. Moreover, the water flux, i.e. the osmotic and electro-osmotic contributions, has been modelled only on a few occasions [72,103].

Regarding the voltage-current behaviour, the electromotive-force is calculated by using the Nernst equation [98]. In this sense, the electromotive-force is always considered to be the open circuit voltage of the stack, thus ignoring the effect of the so-called parasitic currents. Parasitic currents (also known as shunt currents) are a source of irreversibility, which dramatically affect the BMED performance [110]. This phenomenon arises in a BMED module because the channels of the same type are arranged hydraulically in a parallel configuration. This leads to the existence of salt-bridges which act as secondary pathways that are eventually parasitic, hence the name [110]. Parasitic currents are conveyed through the manifolds, i.e. the distributors and collectors, especially with highly conductive solutions as in the case of acids and bases. Although parasitic currents have been characterized for conventional electrodialysis and reverse electrodialysis [110–112], their quantitative effects for BMED processes has been poorly studied so far. The effect of shunt currents was found to be greater when the internal resistance increases [113]. Therefore, the use of low resistive membranes, as well as of thin spacers, may be adopted to minimize these effects [114].

Although the BMED models presented in literature do not account for parasitic currents, their predictions agree fairly well with experimental data. This is due to the fact that the model validation has been performed by using modules with low numbers of triplets, within the range of 1-10. Typically, a low number of triplets leads to low or even negligible effects of the shunt currents [110]. However, parasitic currents and their effects can be significant in stacks with more triplets. Therefore, the simulation of bigger modules should take into account parasitic currents in order to predict the reduction of the stack performance [111]. Particularly, the I-V curves may be dramatically affected by increasing the number of triplets, and an effective tool should be able to predict the behaviour of a BMED unit by varying at least the main design stack features. Although some models are valid despite neglecting the effects of parasitic currents, some of the models are only valid at high current density, even though certain applications may require lower currents [86].

Another process parameter that can affect the BMED performance is the operating temperature. In this regard, Vera et al. [98] included the effect of temperature with corrective coefficients that were determined empirically. Finally, BMED performance should incorporate the calculation of the pumping power consumption in order to evaluate the energy required for the process. For this purpose, a set of hydraulic equations could be beneficial to estimate both pressure differences throughout the stack as well as the flow rate distribution channel by channel. All the aspects discussed so far are not insignificant and they should all be taken into account in order to build a comprehensive tool with high prediction capabilities. The mathematical models already developed in literature are not inclusive to such an extent, as they focus only on specific points rather than all of the points together. This fact has led to the development of models which are not general but are strictly valid under certain design and operating conditions, or which are able to predict the system performance qualitatively but not quantitatively.

This work aimed to develop a simulation tool of BMED modules able to predict the process functioning in every aspect. The developed mathematical model follows a multi-scale approach and was implemented within the equation-oriented gPROMS® platform. This comprehensive tool was experimentally validated with experimental data collected in the continuous steady-state mode. The validation was performed across a wide range of operating conditions relevant to typical BMED operations. This model gives insights into BMED functioning, and it may be used for simulating even bigger modules that would be of interest in industry.

3.4 *Industrial applications of the BMED process*

BMED is a very versatile technology. In recent decades, BMED has been studied for acid and base production across many fields of industry. For instance, BMED has been employed for producing high value organic acids. In this regard, citric acid has an important commercial role, especially in the food and pharmaceutical industries, and it is one of the most valuable products that can be produced by the BMED process [87,115]. The reported SEC values indicate that BMED is able to produce citric acid with energy consumption in the range of 3-8 kWh kg⁻¹ which represents ≈15% of the overall BMED costs [87]. Unlike other methods, BMED has the advantage of the concurrent production of an alkaline solution (e.g. sodium hydroxide), which can be sold or re-circulated into other processes [116]. Conversion rates higher than 97% were achieved with an applied current density of 400 A m⁻² and with a starting concentration of sodium citrate of 3.3% [115]. The BMED process is also applicable to other industries, such as cosmetics, agriculture, detergents or medicines, for the production, for example, of formic acid [117]. Interestingly, highly concentrated formic acid may be obtained with high current efficiencies (higher than 80%), despite the greater effects of acid diffusion. Current densities as high as 500 A m⁻² are thought to be a good compromise, allowing us to have a current density high enough to limit the used membrane area [117] (thus reducing the capital cost, which is significantly affected by the high cost of BPMs [118]), whilst also being able to limit proton leakage (thus increasing the product concentration). The production of formic acid was reported to be 2.6 kWh kg⁻¹ at a concentration of 7 mol l⁻¹ [117].

Another important application of BMED is the conversion and recovery of hypersaline industrial wastewaters [119–121]. In this context, many studies have been devoted to promoting applications for the desalination industry. In fact, the use of seawater leads to the production of large amounts of brines (typically retentates of reverse osmosis processes) at high concentrations. The NaCl content of the brines is recovered in the form of hydrochloric acid and sodium hydroxide solutions. HCl solutions may be smartly recirculated to the pre-treatment steps, as part of the functioning of the desalination plant [120]. Moreover, acid and base solutions may be re-used for the cleaning steps of the membrane processes. At the same time, the brine is desalinated, at least partially, thus being recirculated to the desalination plant or even recovered, in order to achieve (near) zero liquid discharge approaches. Within the concept of the circular economy, Zero Liquid Discharge (ZLD) is a wastewater management strategy [122,123] aiming to minimize the industrial waste streams. Particularly, the increased interest in BMED has been due to its low use of chemical reagents, and to the fact that it has almost no by-products. For example, in

this field BMED can be employed for waste brines valorisation, as stated above, as well as in the recovery of NaCl streams [94] through conversion into HCl and NaOH streams even at high concentrations [95]. Additionally, from the point of view of the electricity requirements, BMED may be cleverly integrated with photovoltaic solar power. This may be carried out with the use of proper control systems [115].

Many works have investigated the valorisation of brine solutions originating from different industrial processes via BMED. The average current density used is $\approx 500 \text{ A m}^{-2}$ [120]. Typical current efficiencies range from a minimum of $\approx 10\%$ for feeds coming from evaporative cooling processes [92], up to $\approx 90\%$ for feeds originating from industrial water production [124]. The Specific Energy Consumption depends on the operating conditions, with an average of 11 kWh kg^{-1} of HCl or 10 kWh kg^{-1} of NaOH produced [120].

Other branches of industry, e.g. textile, deal with the disposal of brines [81]. Another important field of application for BMED is the recovery of high value resources, such as lithium and boron, from aqueous solutions [125–127]. As a matter of fact, lithium is widely used for the production of Li-ion batteries, while boron is a fundamental component used in the industry of glass and ceramics, as well as of semiconductors [125]. It was found that the separation efficiency (i.e. the ratio between the concentration difference obtained during the process over the initial concentration of the component) of lithium and boron were higher than 90%, thus proving the applicability of BMED for such a purpose [125]. This performance may even be improved by tuning the applied voltage or by operating with higher feed flow rates [126]. Choosing an optimal initial pH of the solutions can improve the performance. Particularly, using a higher initial pH was found to increase the boron separation efficiency [127]. The specific consumption for lithium and boron was 18 kWh m^{-3} on average, with initial concentrations of 0.34 g l^{-1} and 1.0 g l^{-1} of lithium and boron respectively [125]. BMED may be smartly employed in those processes that need pH-control, e.g. whey acid neutralization [89,128–131]. For all of BMED's potential applications, it seems to offer an effective alternative that supports sustainable development.

3.5 *Description of the multi-scale model of BMED*

This work focused on the development of a BMED model for the most common three-chamber configuration of the repetitive unit, i.e. BPM-CEM-AEM membranes with acid, salt and base solutions. This choice should not be thought of as a limitation. Indeed, the same model structure and equations may be used with small adjustments

to simulate a wider range of BMED configurations. Therefore, this model has a general validity.

This tool may be placed among the advanced, semi-empirical models with a multi-scale architecture. It has been integrated with correlations coming from Computational Fluid Dynamic (CFD) simulations performed in the finite-volume code Ansys® CFX®. Four different scales or dimensional levels including a total of five different models have been developed with distributed parameters. The lowest level is characterized by both the single channel and the single bipolar membrane models. Whilst the former allows the calculation of physical properties of the electrolyte solutions, Sherwood numbers and distributed pressure losses along the channel, the latter is able to predict the behaviour of the bipolar membrane in terms of ion and water fluxes and the evaluation of the first limiting current density. The middle level is represented by the single repetitive unit, i.e. the triplet. This scale allows the computation of the mass balances taking the whole triplet as the boundary. In addition, the triplet model provides the relevant electrical quantities such as the internal resistance and the electrical potential of the repetitive unit. The highest scale simulate the BMED module including all the triplets, and has been developed by two sub-models: the first solves the equivalent electric circuit of the whole unit (i.e. including both the stack and the external electric circuit), and the second calculates the flow distribution triplet by triplet and the pressure losses through the equivalent stack hydraulic circuit. Figure 12 depicts the structure of the multi-scale model.

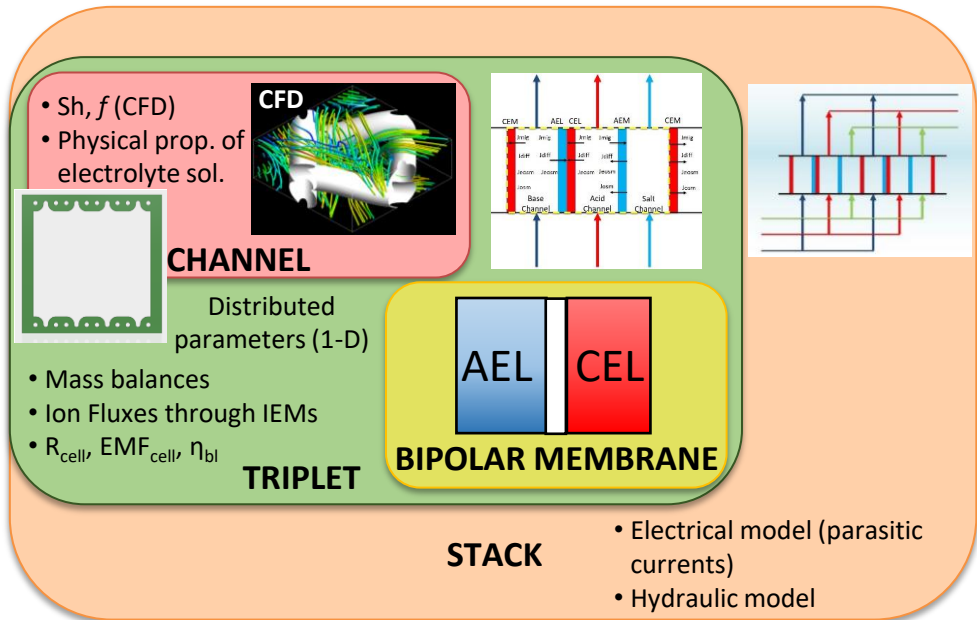


Figure 12. Scheme of the multi-scale model.

From the lowest scale to the stack level (included), all the models simulate the steady-state operation. The highest scale includes material balances at the stack level. The overall, combined solutions of all the models allows us to study the effect of both process variables and design parameters on all the main phenomena involved in the BMED process, as well as on its main figures of merit. Each level of the multi-scale model characterizes the effect of detrimental phenomena, thus giving insights about the BMED functioning and possible improvements. For instance, the channel and triplet models allow the estimation of the concentration polarization. The stack model quantifies the incidence of the parasitic currents, which is one of the most important problems of a BMED unit, because they lead to a significant reduction of the process efficiency. The stack and the external circuit levels estimate the pressure losses and, thus, the power required to pump the solutions through the stack and the external hydraulic circuit, respectively. This highest scale enables the evaluation of the best-known BMED figures of merit cited in the literature: the conversion ratio for computing the salt conversion (in terms of species concentration, e.g. NaCl) in acid and/or base; the current efficiency, i.e. the percentage of electrical current used for producing acid and base molecules; and the specific energy consumption, which represents the energy spent by the device per unit volume (generally expressed in kWh/m³) of acid or base (or sometimes of both). All the models are integrated in the gPROMS Model Builder[®] platform, which is an equation-oriented software with no

requirements to elaborate any solving algorithm. The built-in solvers provide the results of each simulation. In the following sections, all the scales and the equations of the relevant models are presented.

3.5.1 Lowest scale: Channel model

The channel level is a one-dimensional model. Here, the channel length is divided into 30 numerical intervals, as this was identified as a good trade-off between the accuracy of the solution and the computational burden by preliminary simulations. This model allows the calculation of the physical properties of the electrolyte solutions flowing in all the channels of the stack. This level includes correlations coming from CFD simulations designed to predict a) the Sherwood number for the evaluation of the polarization coefficients, b) the frictional factor coefficients for assessing the distributed pressure losses and c) the pressure drops at the inlet/outlet regions of the channels connected to the manifolds. For these purposes, advanced three-dimensional simulations were performed to predict flow and mass transport for a fully developed regime, i.e. simulating channel zones out of the boundaries. All the details of the CFD simulations settings can be found in previous works of the research group [106].

Darcy friction factor and Sherwood numbers were calculated with the following correlations:

$$\frac{f \text{Re}}{96} = a_1 \text{Re}^3 + a_2 \text{Re}^2 + a_3 \text{Re} + a_4 \quad (12)$$

$$\text{Sh} = (b_1 \cdot \text{Re} + b_2) \left(\frac{\text{Sc}}{\text{Sc}_{ref}} \right)^{0.5} \quad (13)$$

in which f is the friction factor, Re is the Reynolds number, Sh is the Sherwood number, Sc and Sc_{ref} are the actual and the reference Schmidt numbers [106], respectively. The following regression coefficients were used according to previous simulation results for a woven spacer with pitch-to-height ratio of 2 and flow attack angle of 45° ($\text{Re} < 30$): $a_1 = -2.1 \cdot 10^{-5}$, $a_2 = 0.0024$, $a_3 = 0.001$, $a_4 = 14.831$, $b_1 = 2.81$, and $b_2 = 14.5$ [132].

CFD simulations were performed for larger computational domains to calculate pressure drops at the spacer-filled channel zones near the distributors and the collectors holes. In order to limit the computational burden, the net spacer was simulated as a continuous porous medium, whose pressure drop features were set using the previous unit cell simulation results. Moreover, one single hole and the associated region were simulated, assuming periodic conditions at the lateral boundaries (see Figure 13).

Notably, a full computational domain including the inlet and outlet manifolds and the whole channel was also built. Corresponding CFD simulations were preliminarily carried out and the relevant results were compared with those pertaining to the periodic domain. Only very slight differences (maximum discrepancy lower than 4%) were found, thus indicating that adopting a periodic domain is a reliable approach. From this simple modelling approach, the following kind of correlation for the local loss coefficient k_{spacer} was obtained

$$k_{spacer} \text{Re} = c_1 \text{Re} + c_2 \quad (14)$$

where the coefficients c_1 and c_2 depend on the geometry. For example, for a spacer with a shape such as that reported in Figure 13, with manifolds diameter $d_{man} = 8$ mm and 7 inlet/outlet holes in 25 cm of width, the values of the coefficients were: $c_1 \approx 2,400$ and $c_2 \approx 166,000$ ($\text{Re} < 30$). Note that at the low Reynolds numbers there is only a small discrepancy from an in-out symmetric behaviour, i.e. the local loss coefficients k_{spacer} (and thus c_1 and c_2) are the same for inlet and outlet regions.

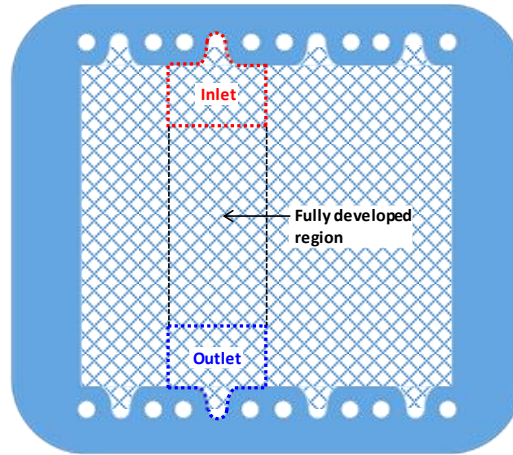


Figure 13. Net spacer provided with gasket. The computational domains used in the CFD simulations of the inlet/outlet regions are highlighted.

Correlations reported in Eqs. (12) and (14) are used in the stack hydraulic sub-model, while that reported in Eq. (13) is used in the triplet sub-model.

Electrolyte solutions are characterized by a multi-ionic system with four ions, i.e. H^+ , OH^- , Na^+ and Cl^- . Therefore, they require appropriate correlations and models to properly predict the physical properties. Solution conductivity (σ_{sol}), viscosity (μ_{sol}) and ion diffusivities ($D_{i,sol}$) are evaluated by correlations obtained by interpolation of data derived from OLI studio surveys. The correlation for the generic property of an electrolyte (acid, base or salt) solution (ζ_{sol}) shall take the form

$$\zeta_{sol} = k_{\zeta,sol,1} C_{i,sol} + k_{\zeta,sol,2} C_{j,sol} + k_{\zeta,sol,3} \quad (15)$$

where C_i is the molar concentration of the ion i , and C_j is the molar concentration of the ion j , expressed in mol m^{-3} and $k_{\zeta,sol,1}$, $k_{\zeta,sol,2}$ and $k_{\zeta,sol,3}$ are the regression coefficients (see Table A.1). All the regression coefficients are computed at 25 °C.

Mass density is computed by using Laliberté's model [133], activity coefficients by Pitzer's virial equations for multi-component systems [134,135].

3.5.2 Lowest scale: Bipolar Membrane model

The bipolar membrane model is devoted to the estimation of the ion fluxes through the bipolar membrane layers. In particular, through the CEL, the migrative flux is calculated for H^+ , Na^+ and Cl^- ions, while the diffusive flux is assessed only for the latter two. On the other hand, through the AEL, migrative flux is attributed to OH^- , Na^+ and Cl^- while the diffusive flux is calculated only for the latter two. The calculation of the migrative fluxes involves the salt limiting current density. It is the maximum salt current before the interlayer becomes depleted of salt ions and water dissociation begins. By following the Strathmann's approach [33], the limiting current is assessed by computing a mass balance in the interlayer of the bipolar membrane:

$$V_{tr} \frac{dC_{Na,tr}}{dt} = A (J_{mig,Na,AEL} + J_{mig,Na,CEL} + J_{diff,Na,AEL} + J_{diff,Na,CEL}) \quad (16)$$

where V_{tr} is the BPM transition region (interlayer) volume (m^3), $C_{Na,tr}$ is the sodium ion concentration in the interlayer (mol m^{-3}), A is the membrane area (m^2), $J_{mig,Na,AEL}$ and $J_{mig,Na,CEL}$ are the migrative fluxes of sodium ions in the AEL and CEL respectively, $J_{diff,Na,AEL}$ and $J_{diff,Na,CEL}$ are the anionic and cationic diffusive fluxes respectively. In fact, following the Strathmann assumption, the bipolar membrane is modelled as symmetrical. Migrative and diffusive fluxes are calculated as follows,

$$J_{mig,Na,AEL} = \frac{t_{Na,AEL} i_{lim}}{z_{Na} F} \quad (17)$$

$$J_{mig,Na,CEL} = -\frac{t_{Na,CEL} i_{lim}}{z_{Na} F} \quad (18)$$

$$J_{diff,Na,BPL} = D_{NaCl} \frac{C_{Na,BPL,ch^-} - C_{Na,BPL,tr}}{d_{BPL}} \quad (19)$$

in which i_{lim} is the limiting current density ($A\ m^{-2}$), $t_{Na,AEL}$ and $t_{Na,CEL}$ are the sodium ion transport numbers in the two layers of the BPM, z_{Na} is the sodium ion valence, F is the Faraday constant, D_{NaCl} is the salt diffusion coefficient ($m^2\ s^{-1}$) (fixed equal to $2 \times 10^{-11}\ m^2/s$), $C_{Na,BPL,ch}$ and $C_{Na,BPL,tr}$ are the sodium ion concentration ($mol\ m^{-3}$) in the BPM layers, at the channel and at the transition region side respectively.

Following the Strathmann approach [33], it is assumed that the ion transport numbers related to the limiting current density are 99% for the counter-ion and 1% for the co-ion. Therefore, the sodium and chloride ion transport numbers are related to the i_{lim} as,

$$t_{Na,AEL} = 0.01 \cdot abs\left(\frac{i_{lim}}{i}\right) \quad (20)$$

$$t_{Cl,AEL} = 0.99 \cdot abs\left(\frac{i_{lim}}{i}\right) \quad (21)$$

in which i is the cell current density ($A\ m^{-2}$).

Accordingly, the hydroxide ion transport number $t_{OH,AEL}$ is calculated as

$$t_{OH,AEL} = 1 - t_{Na,AEL} - t_{Cl,AEL} \quad (22)$$

Given that the bipolar membrane is modelled as symmetrical, the following equalities for the CEL are applied

$$t_{Na,CEL} = t_{Cl,AEL} \quad (23)$$

$$t_{Cl,CEL} = t_{Na,AEL} \quad (24)$$

$$t_{H,CEL} = t_{OH,AEL} \quad (25)$$

The migrative fluxes of hydroxide ions through the CEL, as well as of proton ions through the AEL, are neglected, and thus their transport numbers are null.

The following Donnan equilibrium equation at each membrane-solution interface is applied

$$\frac{R_g T}{z_{Na} F} \ln \frac{C_{Na,sol,int}}{C_{Na,BPL,int}} = \frac{R_g T}{z_{Cl} F} \ln \frac{C_{Cl,sol,int}}{C_{Cl,BPL,int}} \quad (26)$$

where $C_{i,sol,int}$ and $C_{i,BPL,int}$ are the ion concentrations at the interface between the solution and membrane, on the solution side and BPM-layer side, respectively. R_g is the gas constant and T is the temperature.

Moreover, the electro-neutrality within the bipolar membrane layer is considered with the general expression:

$$X + \sum C_{co,BPL} = \sum C_{ct,BPL} \quad (27)$$

Where BPL is the generic layer of the BPM (i.e. AEL or CEL), X is the fixed charge group concentration in the IEL, and $C_{co,BPL}$ and $C_{ct,BPL}$ are the co-ion and counter-ion concentrations in the membrane phase.

At the membrane-solution interface on the interlayer side, the following assumptions are used

$$C_{Na,CEL,tr} = X \quad (28)$$

$$C_{Na,AEL,tr} = 0 \quad (29)$$

3.5.3 Middle low scale: Triplet model

At the middle-low level of simulation, all the triplets of the stack are simulated by a stationary, one-dimensional model, with the same spatial discretization degree as that of the channel. Figure 14 shows a scheme of a triplet, where each membrane can be crossed by ion (Ohmic and diffusive) transport and water (osmotic and electro-osmotic) transport. The membrane-solution interfaces 1 (left) and 2 (right) are indicated for each channel.

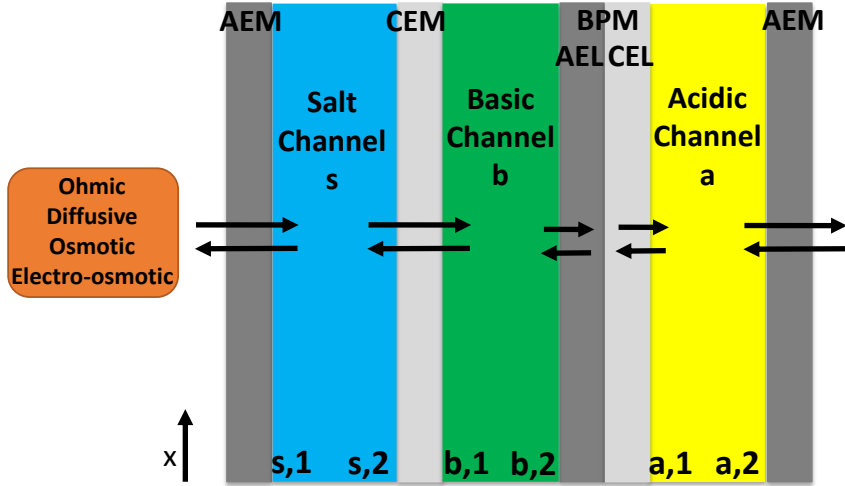


Figure 14. Scheme of the triplet (with an additional CEM). All the possible fluxes of ions and water through the membranes are listed. The membrane-solution interfaces in each channel are indicated as “sol,1” (on the left) and “sol,2” (on the right), “sol” being either salt (s), base (b) or acid (a) solution.

3.5.3.1 Ions and water fluxes

Bipolar membrane fluxes are calculated with the bipolar membrane model previously shown, whilst monopolar membrane (MPM) fluxes are evaluated by adopting the Nernst-Planck-Donnan approach for multi-ion systems [67]. Particularly, the ion transport through the membrane is given by the sum of the diffusive and Ohmic conduction terms and follows the general expression

$$J_{i,MPM} = -\sum_j D_{i,j,MPM} \nabla C_{j,MPM} + \frac{t_{i,MPM} i}{z_i F} \quad (30)$$

in which $J_{i,MPM}$ is the total molar flux of the i -th ion across the generic monopolar membrane MPM (i.e. CEM or AEM), $D_{i,j,MPM}$ is the cross-diffusion coefficient (defined later), $C_{j,MPM}$ is the concentration in the membrane phase of the j -th ion, $j = 1, 2, \dots, n$ (where n is the number of ion species), $t_{i,MPM}$ is the transport number of the i -th ion at the solution-membrane interface in the membrane phase (assuming a linear profile of the concentration within the membrane), i is the current density, z_i is the ion charge and F is the Faraday constant. $J_{i,MPM}$ is assumed to be positive if entering the channel, negative if exiting the channel. It should be noted that the Nernst-Planck approach is strictly valid for diluted electrolytes. A rigorous approach including activity would require the adoption of the Stefan-Maxwell equation which cannot be used without the availability of the cross-phenomenological coefficients taking into account ion-ion interactions. These coefficients could be assessed only by carrying out suitably devised experiments. This is why the Nernst-Planck approach, although less rigorous, is the one commonly used [136].

The overall Ohmic fluxes of the species i across the two membranes bounding each of the three compartments can be calculated as

$$J_{ohm,i,a} = \frac{(t_{i,CEL} - t_{i,AEM})i}{z_i F} \quad (31)$$

$$J_{ohm,i,b} = \frac{(t_{i,CEM} - t_{i,AEL})i}{z_i F} \quad (32)$$

$$J_{ohm,i,s} = \frac{(t_{i,AEM} - t_{i,CEM})i}{z_i F} \quad (33)$$

where $J_{ohm,i,a}$, $J_{ohm,i,b}$, $J_{ohm,i,s}$ are the overall Ohmic fluxes of each acid, base and salt channels respectively, $t_{i,CEL}$, $t_{i,AEL}$, $t_{i,CEM}$, $t_{i,AEM}$ are the transport numbers of the i -th ion in the cation and anion exchange layers of the bipolar membrane and in the cation and anion exchange membranes, respectively. $J_{ohm,i,sol}$ is positive if entering the channels, negative otherwise. The ion transport numbers in the bipolar membranes are calculated within the bipolar membrane model, and the ion transport

numbers in the monopolar membranes are related to the ion diffusion coefficients of all the ions and to the average ion concentration within the membrane by the expression

$$t_{i,MPM} = \frac{z_i^2 D_{i,MPM} \overline{C_{i,MPM}}}{\sum_j z_j^2 D_{j,MPM} \overline{C_{j,MPM}}} \quad (34)$$

in which $D_{i,MPM}$ is the diffusion coefficient of the i -th ion, and $\overline{C_{i,MPM}}$ is the average ion concentration within the monopolar membrane. $D_{i,MPM}$ is a parameter of the model. Preliminary empirical data regarding ion diffusivities for Na^+ and Cl^- through the AEM were estimated by performing experiments with a two-chamber diffusion cell. Given the lack of experimental data, the other AEM ion diffusivities were assumed to be inversely proportional to the hydrated radius of Na^+ , as follows from the Stokes-Einstein relation, and the values of the hydrated radii were taken from [137]. For the CEM, the diffusion coefficients of the ions were kept the same as those used for the AEM, but each value was divided by 3. This factor was calibrated in order to predict the observed experimental pH at the salt channel outlet (i.e. $\text{pH} \approx 2$). $\overline{C_{i,MPM}}$ is calculated from the membrane-solution interface concentrations on both membrane sides, which in turn depend on the Donnan equilibrium between the two phases. The following $n-1$ Donnan equilibrium equations at the membrane-solution interfaces are applied:

$$\frac{R_g T}{z_i F} \ln \frac{C_{i,sol,int}}{C_{i,MPM,int}} = \frac{R_g T}{z_{i+1} F} \ln \frac{C_{i+1,sol,int}}{C_{i+1,MPM,int}} \quad (35)$$

where $C_{i,sol,int}$ and $C_{i,MPM,int}$ are the ion concentrations at the interface on the solution and membrane side, respectively, R_g is the gas constant and T is the temperature.

Likewise with the bipolar membrane interfaces, the electro-neutrality within the monopolar membrane is considered with the general expression:

$$X + \sum C_{co,MPM} = \sum C_{ct,MPM} \quad (36)$$

where X is the fixed charge group concentration in the IEM, $C_{co,MPM}$ and $C_{ct,MPM}$ are the co-ion and counter-ion concentrations at the solution-membrane interface in the membrane phase (assuming a linear profile of the concentration within the membrane).

According to the diffusion-conduction equation, Eq. (30), the diffusive flux of the ion species i through a monopolar membrane MPM is

$$J_{diff,i,MPM} = - \sum_j D_{i,j,MPM} \nabla C_{j,MPM} \quad (37)$$

where the concentration gradients are calculated by solving the Donnan equilibrium expressions, and the cross-diffusion coefficients $D_{i,j,MPM}$ are expressed as follows:

$$D_{i,j,MPM} \equiv D_{i,MPM} \delta_{ij} + \frac{t_{i,MPM}}{z_i} z_j (D_{i,MPM} - D_{j,MPM}) \quad (38)$$

where δ_{ij} is the Kronecker delta.

The total i -th ion flux across the two membranes bounding each channel $J_{tot,i,sol}$ is calculated as the sum of the overall Ohmic contribution (Eqs. (31-33)) and the two diffusive contributions

$$J_{tot,i,sol} = J_{ohm,i,sol} + J_{diff,i,m,1} + J_{diff,i,m,2} \quad (39)$$

in which $J_{diff,i,m,1}$ and $J_{diff,i,m,2}$ are the diffusive fluxes across the left (1) and right (2) generic membranes m (i.e. CEM, AEM or BPM), bounding the channel.

The osmotic fluxes are generated by the osmotic pressure difference across the membrane. In formulae:

$$G_{osm,a} = \frac{\rho_w L_p (\pi_{osm,a,2} - \pi_{osm,s,1})}{3.6 \cdot 10^9} \quad (40)$$

$$G_{osm,b} = \frac{\rho_w L_p (\pi_{osm,b,1} - \pi_{osm,s,2})}{3.6 \cdot 10^9} \quad (41)$$

where $G_{osm,a}$, $G_{osm,b}$ are the osmotic mass fluxes of the acid and base channels, expressed in $\text{kg m}^{-2} \text{s}^{-1}$, ρ_w is the water mass density at 25°C in kg m^{-3} , L_p is the Osmotic permeability (expressed in $\text{ml m}^{-2} \text{h}^{-1} \text{bar}^{-1}$), $\pi_{osm,a,2}$, $\pi_{osm,s,1}$, are osmotic pressures at the left and right side respectively of the AEM and $\pi_{osm,b,1}$, $\pi_{osm,s,2}$ are those of the CEM (all expressed in bar). $G_{osm,sol}$ is negative when entering the channel, positive otherwise.

The electro-osmotic fluxes represent the number of molecules entrained by the solvation shell of each ion passing across the MPMs. These fluxes can be calculated as

$$G_{e.osm,sol} = 10^{-3} M_{H_2O} \sum_i J_{tot,i,sol} n_{h,i} \quad (42)$$

where M_{H_2O} is the molar mass of water in g mol^{-1} and $n_{h,i}$ is the number of water molecules with the solvation shell per each ion (considered equal to 1 for H^+ and OH^- [138], 6 for Na^+ and 8 for Cl^- [139]). $G_{e.osm,sol}$ is positive when entering the channel, negative otherwise.

In the acid and base compartments, the stoichiometric water flux through the BPM due to the water dissociation is

$$G_{split,sol} = -\frac{t_{i,IEL} i}{2F} M_{H_2O} \cdot 10^{-3} \quad (43)$$

where $t_{i,IEL}$ is the transport number of proton ions in the CEL or hydroxide ions in the AEL of the BPM. $G_{split,sol}$ is positive when entering the channel, negative otherwise.

The overall water mass fluxes $G_{w,sol}$ (positive when entering the channel, negative otherwise) for the acid and base channels are evaluated according to the equations

$$G_{w,sol} = G_{e,osm,sol} - G_{osm,sol} + G_{split/recomb,sol} \quad (44)$$

The water mass flux for the salt channels is related to the water fluxes calculated for the acid and base compartments

$$G_{w,s} = -G_{w,a} - G_{w,b} \quad (45)$$

3.5.3.2 Electromotive force and electrical resistance

The electric potential generated across the IEMs in the triplet E can be written as

$$E = EMF + \eta_{BL} \quad (46)$$

where EMF is the triplet electromotive force that would be generated by the membranes in contact with the bulk solutions, and η_{BL} is the contribution to E due to concentration polarization boundary layers.

The electromotive force is calculated by the general Nernst equation [56]

$$EMF = \sum_{IEMS} \left(-\frac{R_g T}{F} \int_{left,IEM}^{right,IEM} \sum_i \frac{t_i}{z_i} d \ln a_{int,i} \right) \quad (47)$$

where $a_{int,i}$ is the activity of the i -th ion at the solution side of the membrane-solution interface (i.e. $right,IEM$ and $left,IEM$ that are the right and the left side of each membrane, as shown in Figure 14), expressed in mol m^{-3} .

η_{BL} accounts for the non-Ohmic variation of E in a triplet due to the effects of concentration polarization phenomena in the boundary layers on all the six solution-membrane interfaces [140]

$$\eta_{BL} = -\frac{R_g T}{F} \sum_{int} \sum_{ions} \frac{t_i}{z_i} \ln \theta_{i,sol,int} \quad (48)$$

in which $\theta_{i,sol,int}$ are the six polarization coefficients, defined as

$$(\theta_{i,sol,int})^{sgn(J_{diff,i,sol,int})} = \frac{C_{i,sol,int}}{C_{i,sol}} \quad (49)$$

where $C_{i,sol}$ and $C_{i,sol,int}$ are the concentrations of the i -th ion in the *sol* channel (i.e. acid, base or salt) in the bulk and at the solution-membrane interface, respectively, and $sgn(J_{diff,i,sol,int})$ is the sign of the diffusive flux of the i -th ion at the interface with the membrane, solution side. By imposing the continuity of the total flux at the interface, it can be calculated as

$$J_{diff,i,sol,int} = J_{diff,i,m} + \frac{(t_{i,m} - t_{i,sol})i}{F} \quad (50)$$

where $t_{i,sol}$ is the ion transport number in the solution

$$t_{i,sol} = \frac{z_i^2 D_{i,sol} C_{i,sol}}{\sum_j z_j^2 D_{j,sol} C_{j,sol}} \quad (51)$$

in which $D_{i,sol}$ is the ion diffusion coefficient of the i -th ion in the solution. From the definition of the Sherwood number, it follows that the polarization coefficient can be calculated as

$$\theta_{i,sol,int} = \left(1 - \frac{J_{diff,i,sol,int} 2 d_{sol}}{Sh_{sol,int} D_{i,sol} C_{i,sol}}\right)^{sgn(J_{diff,i,sol,int})} \quad (52)$$

where d_{sol} is the spacer thickness and $Sh_{sol,int}$ is the Sherwood number in the considered interface, which is evaluated by CFD correlations (Eq.(13)).

The triplet electric resistance R (in Ω) is calculated as follows

$$R = \sum_{sol} R_{sol} + \sum_m R_m \quad (53)$$

where R_{sol} and R_m are the electrical resistance in the feed channels (i.e. acid, base and salt) perpendicular to the membranes and the electrical resistance of the membranes (i.e. CEM, AEM and BPM). R_{sol} are calculated as

$$R_{sol} = f_s \frac{d_{sol}}{b \Delta x \sigma_{sol}} \quad (54)$$

in which f_s is the spacer shadow factor (which can be assumed, for example, equal to the inverse of the volume porosity), b is the channel width, Δx is the length of a discretization interval (e.g. equal to 1/30 of the channel length) and σ_{sol} is the electrical conductivity of the electrolyte solution. In the case of commercial membranes, R_m can be known under specific conditions (composition and concentration of the electrolyte solution) from manufacturers technical sheets. Otherwise it can be experimentally evaluated, with the advantage to have more detailed information on the membrane behaviour under different conditions.

3.5.3.3 Mass balances

For each control volume of each channel, one-dimensional co-current mass balance equations are written for each ion species and the electrolyte solution.

Mass balances for the acid channels are:

$$\frac{\partial Q_a C_{Na^+,a}}{\partial x} = b J_{tot,Na^+,a} \quad (55)$$

$$\frac{\partial Q_a C_{Cl^-,a}}{\partial x} = b J_{tot,Cl^-,a} \quad (56)$$

$$\frac{\partial Q_a C_{H^+,a}}{\partial x} = b (J_{tot,H^+,a} - J_{tot,OH^-,a}) \quad (57)$$

$$C_{OH^-,a} = 10^3 \cdot 10^{\left(-14 - \log \frac{C_{H^+,a}}{10^3}\right)} \quad (58)$$

$$\frac{\partial Q_a \rho_a}{\partial x} = (J_{tot,Na^+,a} M_{Na^+} + J_{tot,Cl^-,a} M_{Cl^-} + (J_{tot,H^+,a} - J_{tot,OH^-,a}) M_{H^+}) b 10^{-3} + G_{w,a} b + J_{tot,OH^-,a} M_{H_2O} b 10^{-3} \quad (59)$$

where Q_a is the acid volume flow rate and ρ_a is the acid mass density.

Similar expressions can be written for the salt channels:

$$\frac{\partial Q_s C_{Na^+,s}}{\partial x} = b J_{tot,Na^+,s} \quad (60)$$

$$\frac{\partial Q_s C_{Cl^-,s}}{\partial x} = b J_{tot,Cl^-,s} \quad (61)$$

$$\frac{\partial Q_s C_{H^+,s}}{\partial x} = b (J_{tot,H^+,s} - J_{tot,OH^-,s}) \quad (62)$$

$$C_{OH^-,s} = 10^3 \cdot 10^{\left(-14 - \log \frac{C_{H^+,s}}{10^3}\right)} \quad (63)$$

$$\frac{\partial Q_s \rho_s}{\partial x} = (J_{tot,Na^+,s} M_{Na^+} + J_{tot,Cl^-,s} M_{Cl^-} + (J_{tot,H^+,s} - J_{tot,OH^-,s}) M_{H^+}) b 10^{-3} + G_{w,s} b + J_{tot,OH^-,s} M_{H_2O} b 10^{-3} \quad (64)$$

Regarding the base compartments, the equations used for evaluating the material balances are given by

$$\frac{\partial Q_b C_{Na^+,b}}{\partial x} = b J_{tot,Na^+,b} \quad (65)$$

$$\frac{\partial Q_b C_{Cl^-,b}}{\partial x} = b J_{tot,Cl^-,b} \quad (66)$$

$$\frac{\partial Q_b C_{OH^-,b}}{\partial x} = b (J_{tot,OH^-,b} - J_{tot,H^+,b}) \quad (67)$$

$$C_{H^+,b} = 10^3 \cdot 10^{\left(-14 - \log \frac{C_{OH^-,b}}{10^3}\right)} \quad (68)$$

$$\frac{\partial Q_b \rho_b}{\partial x} = (J_{tot,Na^+,b} M_{Na^+} + J_{tot,Cl^-,b} M_{Cl^-} + (J_{tot,OH^-,b} - J_{tot,H^+,b}) M_{OH^-}) b 10^{-3} + G_{w,b} b + J_{tot,H^+,b} M_{H_2O} b 10^{-3} \quad (69)$$

In the present simulations, Ohmic, diffusive, osmotic and electro-osmotic fluxes are computed across the monopolar cation and anion exchange membranes. Concerning the bipolar membranes, the water dissociation reaction is assumed to be infinitely fast, for the sake of simplicity.

3.5.4 Middle-high scale: Stack model

The stack is considered as a unit containing several triplets that are hydraulically connected in parallel. The middle-high modelling level is for the simulation of the stack, and it involves two sub-models: the hydraulic model and the electrical model. Making use of CFD correlations for pressure drops, the former resolves three separate hydraulic circuits, i.e. one for each solution, consisting of spacer-filled channels connected by manifolds, thus predicting the pumping power consumption over the stack. The latter simulates the equivalent electrical circuit of the stack, including the ionic shortcut currents *via* manifolds, thus predicting the distribution of the electric current and of the electric potential throughout the stack (and the external circuit). Therefore, important electrical performance parameters can be calculated, such as the power required by the stack or the main figures of merit of a BMED unit, e.g. the Specific Energy Consumption or the Current Efficiency.

3.5.4.1 Hydraulic model

The simple hydraulic circuit considered for each solution is shown in Figure 15. The hydraulic circuit is based on the assumption that the different “slices” of spacer-filled channel with one single hole for inlet and one for outlet (see dashed line in Figure 13) have an identical behaviour and are fluxed by the same flow rate. Therefore, one single node within the manifolds of the hydraulic circuit in Figure 15 represents any and all the manifolds sections downstream or upstream one channel (whose number is equal to that of the inlet/outlet holes, N_{holes})

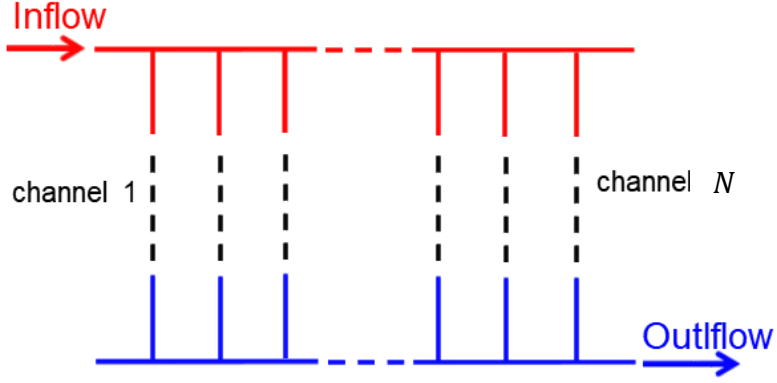


Figure 15. Scheme of the hydraulic circuit for one of the three solutions. Vertical lines represent the channels, where pressure drops occur in the inlet/outlet regions (continuous vertical lines) and in the region with developed flow (dashed lines) Horizontal lines represent the manifolds, i.e. distributor and collector, connecting the channels.

Assuming a negligible mass density variation among the nodes, the continuity equation can be written as follows

$$Q_{c,sol,k} = Q_{c,sol,k-1} + Q_{c,k}(x = L) \quad (70)$$

$$Q_{c,sol,1} = Q_{sol,1}(x = L) \quad (71)$$

$$Q_{d,sol,k} = Q_{d,sol,k+1} + Q_{d,k}(x = 0) \quad (72)$$

$$Q_{d,sol,N} = Q_{sol,N}(x = 0) \quad (73)$$

where the subscripts c and d refer to the collector and the distributor, respectively, and $k = 1, 2, \dots, N$ indicates the generic triplet, N being the total number of triplets in the stack. The validity intervals of Eqs. 70 and 72 are for $k [2;N]$ and $[1;N-1]$, respectively. The total feed flow rate $Q_{d,sol,1}$ is imposed in the simulations, while the total outlet flow rate $Q_{c,sol,N}$ may be higher or lower due to water transport through the membranes, computed at the triplet level.

The pressure drop within the fully developed region (vertical dashed tract in Figure 15), i.e. the part of the spacer-filled channel where the velocity has one single component (rectilinear and parallel streamlines), is calculated by the definition of the (Darcy) friction factor

$$\Delta P_{fd,sol} = f \rho_{sol} \frac{L}{4 d_{sol}} (u_{ch,sol})^2 \quad (74)$$

where f is related to the Reynolds number by the CFD correlation reported in Eq. (12), and $u_{ch,sol}$ is the mean velocity of the solution (i.e. acid, base or salt) in the channel.

Note that, similarly to the channel and triplet models, the subscript k is omitted, as the equation applies indistinctly to all channels. The localized pressure losses in the inlet/outlet region of the spacer-filled channel (vertical continuous tracts in Figure 15) $\Delta P_{l,sol}$ are calculated by the definition of the local loss coefficient

$$\Delta P_{l,sol} = k_{spacer} \frac{\rho}{2} (u_{ch,sol})^2 \quad (75)$$

where k_{spacer} is related to the Reynolds number by the CFD correlation reported in Eq. (14). The pressure drop in the small tracts of manifolds between consecutive channels (horizontal continuous tracts in Figure 15) are calculated with a similar equation, where the flow velocity is that along the manifolds in the pertinent tract, and the loss coefficient is set by rough estimations.

The total stack pressure loss ΔP_{stack} is the sum of two contributions: the first one is obtained by the difference between the inlet to the distributor and the outlet from the collector (Figure 15) pressures by fixing the outlet gauge pressure equal to zero. The second addend is related to further contributions to the pressure drop occurring in the distribution/collection systems among the manifolds, i.e. among the virtual ducts formed by holes in spacers gaskets and membranes.

3.5.4.2 Electrical model

The electrical model is devoted to quantify the currents circulating throughout the stack, including parasitic currents via manifolds. They circulate through the alternative pathways offered by manifolds and the longitudinal direction in the channels, with detrimental effects on the process efficiency, related to an average internal current lower than the external one [111]. The equivalent electric circuit solved by the electrical sub-model of stack is shown in Figure 16.

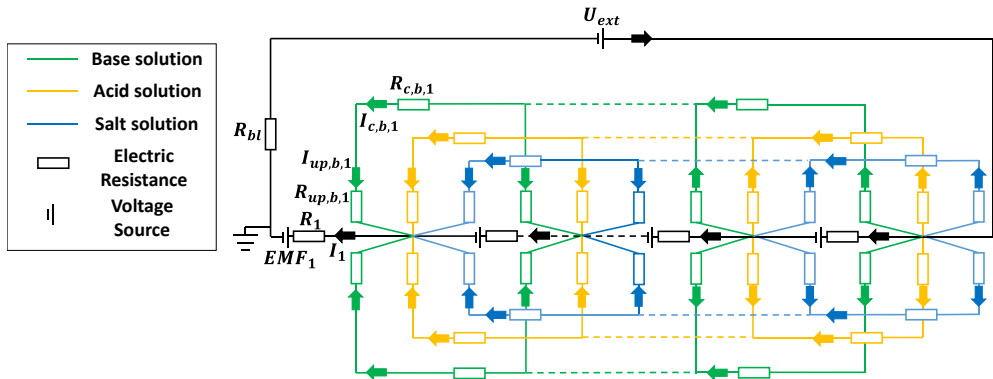


Figure 16. Scheme of the equivalent electric circuit of the BMED stack.

Two longitudinal resistances are considered for each channel, while in the direction perpendicular to the membranes a voltage source and an electric resistance are considered to represent each triplet. A voltage source is also included in the external circuit. Other electrical resistances are in the manifolds between two consecutive channels of the same solution and in the electrode compartments. The equations system is composed of the nodes Kirchhoff's law and the Ohm's law. The following node Kirchhoff's law is applied in all the nodes of the electric circuit:

$$\sum_j I_j = 0 \quad (76)$$

where I_j is the generic electric current inputting to or outputting from each node. Positive cell currents are directed towards the cathode (i.e. the negative pole in a BMED unit), longitudinal currents are assumed to be positive when exiting the channels. Distributor or collector electric currents, as well as the external current are positive from left to right.

Taking into account the sources of voltage in the triplets, Ohm's law is applied as follows:

$$\Delta V_{man,sol,k} = I_{man,sol,k} R_{man,sol,k} \quad (77)$$

$$\Delta V_{x,sol,k} = I_{x,sol,k} R_{x,sol,k} \quad (78)$$

$$I_k = \frac{(-E_{av,k} - \Delta V_k)}{R_{av,k}} \quad (79)$$

$$I_{ext} = \frac{-U}{R_u - R_{bl}} \quad (80)$$

$$U_{ext} = I_{ext} R_u \quad (81)$$

where $\Delta V_{man,sol,k}$, $\Delta V_{x,sol,k}$ and ΔV_k are the k -th voltage difference over each manifold ($man=c$, collector, or d , distributor), the longitudinal ($x=up$ or $down$) and the cell triplet electric resistances, respectively, U is the potential difference over the series of R_u and R_{bl} resistances, U_{ext} is the potential difference over the resistance R_u . $I_{sol,x,k}$ and $I_{sol,man,k}$ are the electric currents flowing in the flow direction and in the manifolds, $E_{av,k}$ is the average voltage generated by the cell triplet, R_u , R_{bl} and $R_{av,k}$ are the external, the blank and the average cell resistance of the k -th cell. $R_{man,sol,k}$ and $R_{x,sol,k}$ are the manifold and the longitudinal resistances along the channel. The average triplet membrane potential $E_{av,k}$ is calculated as

$$E_{av,k} = \frac{1}{L} \int_{x=0}^{x=L} E_k(x) dx \quad (82)$$

The average cell resistance $R_{av,k}$ is given by

$$R_{av,k} = \frac{1}{L} \int_{x=0}^{x=L} R_k(x) dx \quad (83)$$

where local values are computed at the triplet level of simulation. As shown in Figure 17, each longitudinal electric resistance along the flow direction $R_{x,sol,k}$ can be considered as the resistance along half channel length in the active area in series with the parallel of the electrical resistances out of the active area. $R_{x,sol,k}$ and $R_{man,sol,k}$ are given by

$$R_{x,sol,k} = f_s \frac{L_x/2}{d_{sol} b \sigma_{x,sol,k}} + f_s \frac{l_{oma}}{\sigma_{x,sol,k} d_{sol} d_{oma} N_{holes}} \quad (84)$$

$$R_{man,sol,k} = \frac{l_{man}}{N_{holes} \pi \frac{d_{man}^2}{4} \sigma_{man,sol,k}} \quad (85)$$

where f_s is the spacer shadow factor, L_x is half channel length, $\sigma_{x,sol,k}$ is the solution mean conductivity in the upward or downward path along the channel, l_{oma} and d_{oma} are the length and average width of the spacer regions out of the active area (i.e. in correspondence of the spacer holes), d_{man} is the diameter of the manifolds (i.e. of the spacer holes) and $\sigma_{man,sol,k}$ is the conductivity of the solution in the manifolds. l_{man} in Eq. (85) is the sum of the membranes and spacers thicknesses for a single triplet

$$l_{man} = d_{CEM} + d_{AEM} + d_{BPM} + d_a + d_b + d_s \quad (86)$$

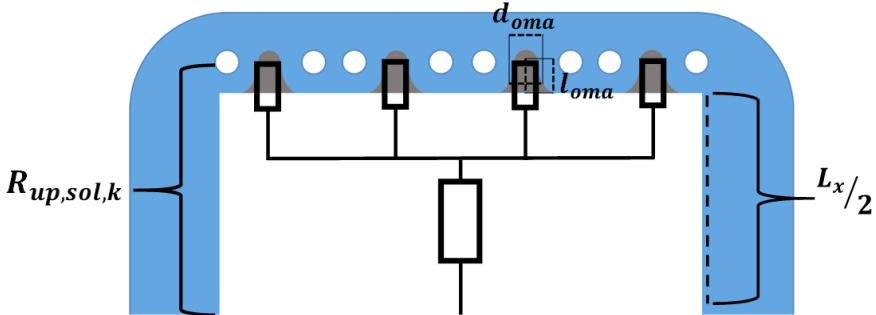


Figure 17. Electric resistances scheme along the flow direction within the channels.

To evaluate $\sigma_{man,sol,k}$, mass balances in the manifolds (i.e. collector and distributor) are computed. The following equations are applied

$$C_{i,man,sol,k} = \frac{C_{i,man,sol,k-1} Q_{man,sol,k-1} + C_{i,sol,k}(x=L) Q_{sol,k}(x=L)}{Q_{man,sol,k}} \quad (87)$$

$$C_{i,man,sol,1} = C_{i,sol,1}(x=L) \quad (88)$$

The validity interval of Eq. 87 is for $k [2;N-1]$.

Volume flow rates $Q_{man,sol,k-1}$ and $Q_{sol,k}$ are already calculated by the hydraulic model.

The outlet concentrations from the stack are equal to the last collector concentrations $C_{i,c,sol,N-1}$.

The gross power density GPD per total membrane area provided to the external load, can be simply calculated as

$$GPD = \frac{I_{ext} U_{ext}}{3 N b L} \quad (89)$$

where $b \cdot L$ is the active area of one single membrane and U_{ext} is the potential difference over the external resistance R_u .

The net power density (NPD) is calculated as

$$NPD = GPD + PPD \quad (90)$$

where PPD is the pumping power density given by,

$$PPD = \frac{\Delta P_{stack,a} Q_{tot,a} + \Delta P_{stack,b} Q_{tot,b} + \Delta P_{stack,s} Q_{tot,s}}{\chi N b L} \quad (91)$$

where χ is the pump efficiency. $Q_{tot,sol}$ are the total inlet flow rates to the stack distributor per each solution.

3.5.5 Evaluation of the process performance

In this paragraph, the main figures of merit used to characterize the performance of BMED processes are defined. The Specific Energy Consumption per unit mass (SEC_m) represents the energy consumed by the process to produce 1 kg of HCl. It is given by [121]

$$SEC_m = \frac{U_{ext} I_{ext}}{3600 M_{HCl} Q_{tot,a} (C_{HCl,c,a,N-1} - C_{HCl,d,a,1})} \quad (92)$$

where SEC_m is expressed in kWh kg_{HCl}⁻¹.

The total or net Specific Energy Consumption by the process to produce 1 kg of HCl ($SEC_{m,net}$) represents the total energy consumed by the process taking into account the power spent on pumping.

$$SEC_{m,net} = \frac{U_{ext} I_{ext} + PPD L b N}{3600 M_{HCl} Q_{tot,a} (C_{HCl,c,a,N-1} - C_{HCl,d,a,1})} \quad (93)$$

where $SEC_{m,net}$ is expressed in kWh kg_{HCl}⁻¹.

The Specific Energy Consumption per unit volume (SEC_v) represents the energy consumed by the process to produce 1 m³ of HCl solution.

$$SEC_v = \frac{U_{ext} I_{ext}}{3.6 \cdot 10^6 \cdot Q_{tot,a}} \quad (94)$$

where SEC_v is expressed in kWh m_{HCl}⁻³.

The current efficiency (η_c) is the amount of HCl moles produced by the process per unit of transported charge. It has been calculated as:

$$\eta_c = \frac{F Q_{tot,a} (c_{HCl,c,a,N-1} - c_{HCl,d,a,1})}{N_{tr} I_{ext}} 100 \quad (95)$$

in which η_c is the current efficiency.

The conversion rate of the hydrochloric acid (τ) is the ratio between the amount of acid produced during the process time over the initial sodium chloride as

$$\tau = \frac{Q_{tot,a} (c_{HCl,c,a,N-1} - c_{HCl,d,a,1})}{Q_{tot,s} c_{NaCl,d,s,1}} \quad (96)$$

3.6 Steady-state model validation

The model predictions have been compared with experimental results obtained using a lab-scale test-rig.

The experimental setup (FT-ED-100, purchased from Fumatech BWT GmbH, Germany) was equipped with commercial ion-exchange membranes: fumasep® FAB as AEM, fumasep® FKB as CEM and fumasep® FBM as BPM. The stack was assembled with a number of triplets (repetitive units) ranging from 10 to 38. The membrane active area was 10 × 10 cm² and PVC/ECTFE woven spacers (thickness = 480 μm) were used to create the channels between adjacent membranes. Spacers had three inlet/outlet holes per channel and the hole diameter was 8.5 mm. Two DSA-type electrodes were used in the end-compartments to convert ionic fluxes into electric fluxes (areal blank resistance of 72 Ω cm²). A cross-flow arrangement was adopted for feeding solutions that were prepared by using demineralized water, NaCl (NaCl 99.7% ChemSolute), HCl (37% Merck) and NaOH (98-100% Honeywell Fluka). The electrode rinse solution was an aqueous solution 0.5 M in FeCl₂/FeCl₃ (99% ChemSolute) and 0.6 M in HCl. Peristaltic pumps (BT601S, Lead Fluid Technology, CO LTD, China) were used for feeding all the solutions with a fluid velocity in the channels in the range 0.2-0.5 cm/s. All the measurements have been carried out at room temperature (~20 °C). Tests were performed in steady-state condition and each test was conducted in once-through (single pass) configuration. A BK Precision 1902

DC Power Supply was used for the BMED experiments, which were operated in galvanostatic mode. All the experiments were replicated at least twice to verify their reliability. Samples for the inlet and outlet solutions were collected to perform both titration and chromatography analysis, in order to compare the ion concentrations in each compartment. Ion chromatography was performed with an Ion Chromatography (IC) Metrohm 882 Compact IC plus. Each sample was prepared with Milli-Q water.

Feed solutions were prepared at different compositions and concentrations. Each peristaltic pump was calibrated prior to use in order to be able to set a specific mean channel flow velocity. Once the pumps started allowing the flow of the electrolyte solutions through the stack, they operated for at least 5 minutes to ensure good membrane conditioning. Subsequently, the electric current was applied by the external power supply. The operation continued until reaching a constant external voltage (measured by the voltmeter), and then samples of the outlet solutions were collected to measure the pH and the ion concentrations of the processed solutions. Figure 18 depicts the experimental set-up utilised here.

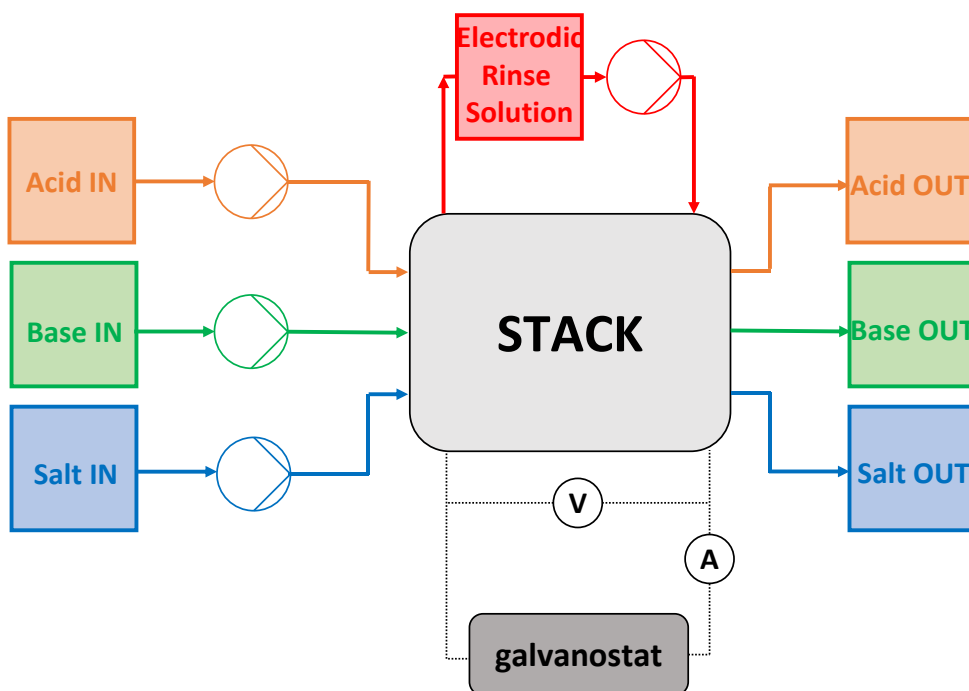


Figure 18. Scheme of the adopted experimental set-up.

3.6.1 Comparison between experimental data and model predictions

This section is devoted to the experimental validation of the CFD simulations and process model in steady-state mode.

3.6.1.1 CFD model validation

CFD predictions of inlet-outlet pressure drops in spacer-filled channels were validated against the experimental data of a previous work [141]. The results reported in Figure 19 show a good agreement (average discrepancy of $\sim 4\%$).

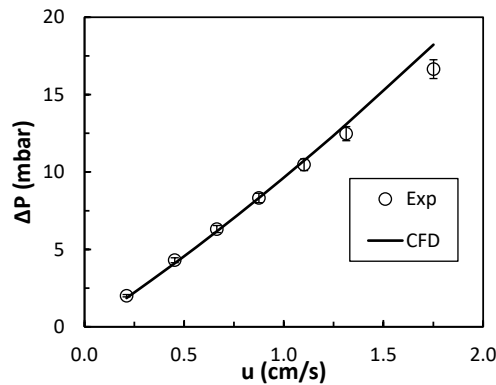


Figure 19. Inlet-outlet pressure losses in a single spacer-filled channel flow cell as a function of the fluid velocity. Experimental data taken are from a previous work [141]. The main spacer features are: woven filaments, thickness of $480\ \mu\text{m}$, angle between filament of 90° , flow attack angle of 45° , pitch to height ratio of 2.42, flow path length of 10 cm (excluding divergent and convergent regions at inlet/outlet), width of 10 cm, and three inlet/outlet holes with diameter of 8.5 mm.

3.6.1.2 Process model validation

The data from the steady-state experiments were compared with model predictions. The empirical voltage-current curves may be grouped into two sets: Firstly, tests were performed with inlet concentrations in the acid and base channels equal to 0.2M of HCl and NaOH respectively, and 0.25 M NaCl in the salt channels. For these tests, the number of triplets was varied from 20 to 38. Secondly, tests were performed by using the same inlet compositions and concentrations, but adding 0.25 M NaCl to the acid and base compartments as salt background. Here, the number of triplets was varied from 10 to 30. Therefore, the predictive capability of the model was tested under different operating conditions.

Figure 20 shows the polarization curves of the BMED process performed without the salt background.

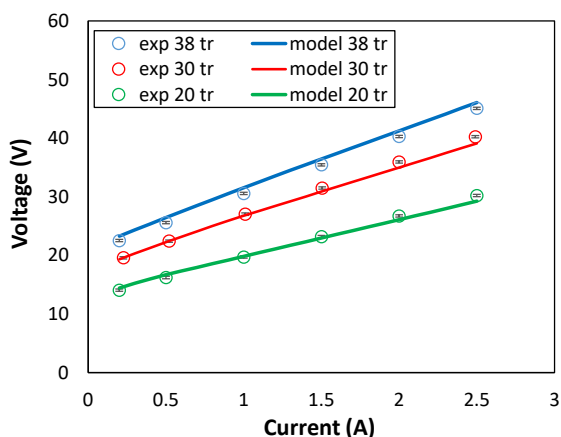


Figure 20. Voltage-current curves by varying the number of triplets for the first set of experiments (i.e. without the presence of salt background), in $10 \times 10 \text{ cm}^2$ stacks with Fumatech membranes (FAB, FKB, FBP) and with spacers provided with 3 inlet/outlet holes (diameter of 8 mm). Mean flow velocity of the electrolyte solutions in each channel equal to 1 cm s^{-1} . Symbols refer to experimental data, continuous lines to the model predictions. Inlet concentrations: 0.2 M HCl and NaOH in the acid and base channels respectively and 0.25 M NaCl in the salt channel. Areal blank resistance: $72 \Omega \text{ cm}^2$.

The experimental data showed high repeatability, as shown by the reported maximum percent error of $\sim 1\%$.

The model predictions were in good agreement with the experimental results for a wide range of external currents, i.e. from 0.2 A to 2.5 A , corresponding to current densities in the interval $20\text{--}250 \text{ A m}^{-2}$. The maximum discrepancy was $\approx 3\%$.

Figure 21 illustrates the polarization curves for the second set of experiments, i.e. with the presence of salt background in the acid and base solutions.

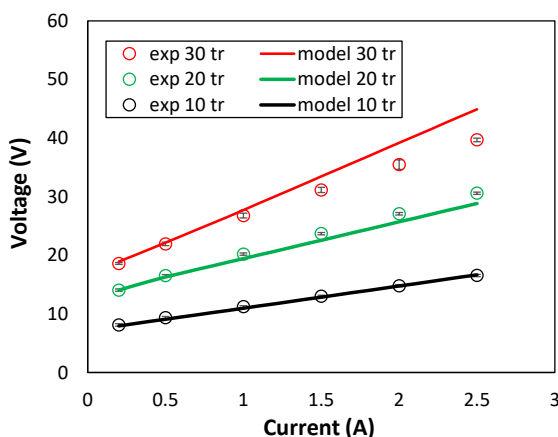


Figure 21. Voltage-current curves by varying the number of triplets for the second set of experiments (i.e. with the presence of salt background), in $10 \times 10 \text{ cm}^2$ stacks with Fumatech membranes (FAB, FKB, FBP) and with spacers provided with 3 inlet/outlet holes (diameter of 8 mm). Mean flow velocity of the electrolyte solutions in each channel equal to 1 cm s^{-1} . Symbols refer to experimental data, continuous lines to the model predictions. Inlet concentrations: 0.2 M HCl and NaOH in the acid and base channels respectively with the presence of 0.25 M NaCl (salt background) and 0.25 M NaCl in the salt channel. Areal blank resistance: $72 \Omega \text{ cm}^2$.

The collected data showed high repeatability since the maximum empirical error was $\approx 2.8\%$.

As noted in Figure 21, even in the presence of salt background the agreement was fairly good, with a maximum error of 6% and 2.2% for the cases with 20 and 10 triplets, respectively. In the case of a 30-triplet stack, there was a maximum discrepancy of 11.6% at 250 A m^{-2} . This error may be indicative of an under-estimation of non-ideal phenomena which make the stack resistance decrease at higher values of electric current.

A comparison between the model outcome and the empirical data was also performed in terms of outlet concentrations. Empirical data were collected by titration of samples of the acid and base outlet solutions, and chromatography analysis of samples of the salt outlet solutions. Titration and chromatography were performed at least twice, finding negligible errors. All the tests were performed by using a stack with 10 triplets, at a constant mean channel flow velocity equal to 0.2 cm s^{-1} , and without the presence of NaCl as salt background in the acid and base channels. The inlet composition and concentrations are reported in Table 3.

Bipolar Membrane Electrodialysis processes

Table 3. Summary of the used inlet concentrations in the stack (i.e. outlet concentrations from the tanks) and applied current densities in $10 \times 10 \text{ cm}^2$ stacks with Fumatech membranes (FAB, FKB, FBP) and with spacers provided with 3 inlet/outlet holes (diameter of 8 mm). Mean flow velocity of the electrolyte solutions in each channel equal to 0.2 cm s^{-1} . Areal blank resistance: $72 \Omega \text{ cm}^2$.

| Test | i_{ext} | $C_{HCl,d,a,1}$ | $C_{NaOH,d,b,1}$ | $C_{NaCl,d,s,1}$ |
|------|-----------------------|-------------------------|-------------------------|-------------------------|
| (-) | (A m^{-2}) | (mol m^{-3}) | (mol m^{-3}) | (mol m^{-3}) |
| 1 | 100 | 0.00 | 0.00 | 992 |
| 2 | 100 | 205 | 192 | 991 |
| 3 | 100 | 0.00 | 0.00 | 1941 |
| 4 | 200 | 0.00 | 0.00 | 1941 |
| 5 | 100 | 0.00 | 0.00 | 936 |

Model outcome and experimental results are compared in Figure 22.

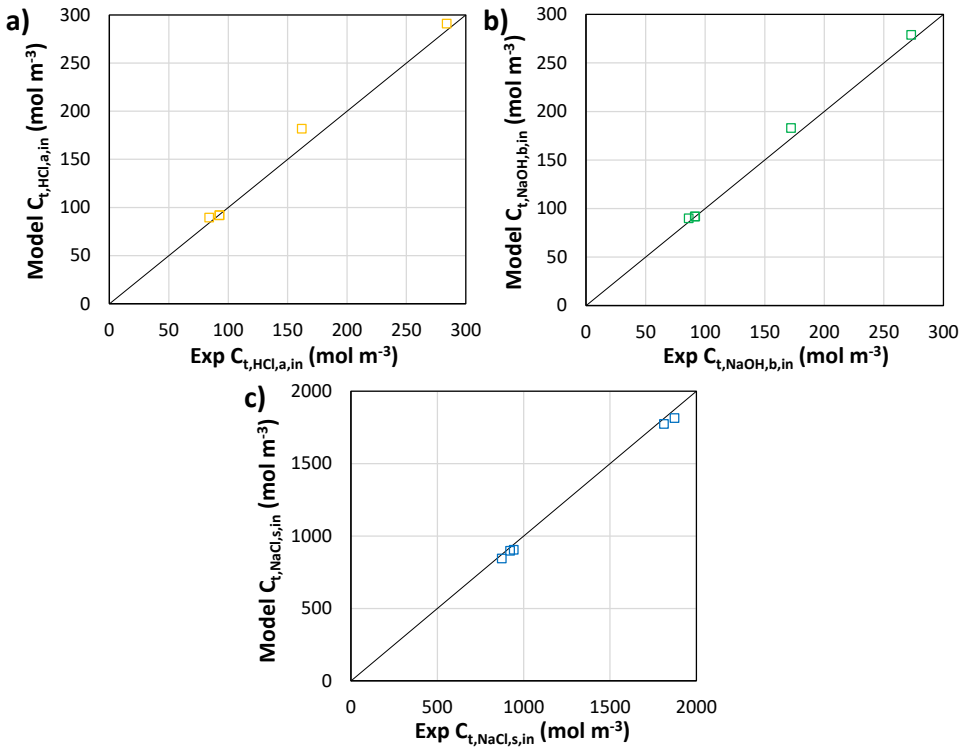


Figure 22. Parity plots for the comparison of model outcome and experimental results for the concentration values at the stack outlet (i.e. downstream tank inlet) of BMED tests with single-pass: a) Outlet HCl concentration in the acid tank, b) Outlet NaOH concentration in the base tank and c) Outlet NaCl concentration in the salt tank.

The ion concentration is well-predicted. Interestingly, the average error in absolute terms is 3.3% distributed as follows (Table 4),

Table 4. Average (over five tests) model discrepancy of the HCl, NaOH and NaCl outlet concentrations in $10 \times 10 \text{ cm}^2$ stacks with Fumatech membranes (FAB, FKB, FBP) and with spacers provided with 3 inlet/outlet holes (diameter of 8 mm). Mean flow velocity of the electrolyte solutions in each channel equal to 0.2 cm s^{-1} . Areal blank resistance: $72 \Omega \text{ cm}^2$.

| | $C_{\text{HCl},c,a,N-1}$ | $C_{\text{NaOH},c,b,N-1}$ | $C_{\text{NaCl},c,s,N-1}$ |
|---------------|--------------------------|---------------------------|---------------------------|
| | (mol m^{-3}) | (mol m^{-3}) | (mol m^{-3}) |
| Average error | 4.3% | 2.6% | 3.0% |

These model-experiment discrepancies fall within the potential range of experimental/operator error.

The wide range of concentrations and electric currents investigated suggest that the model is able to simulate the BMED process with high reliability.

3.7 Simulations of industrial scale BMED units

In this section, the potential of the BMED for use at the industrial scale is demonstrated by a preliminary sensitivity analysis. The simulated process relates to the treatment of industrial brines of sodium chloride. The simulations were performed for stacks with 100 triplets and with the operating and design characteristics reported in Table 5.

Table 5. Inputs of the multi-scale model for the simulations of scaled-up BMED units.

| Geometrical features | | | | | |
|----------------------|--|---------|---------|------|------|
| Spacer thickness | μm | 500 | | | |
| N° spacer holes | - | 3 | | | |
| Spacer hole area | cm^2 | 4 | | | |
| Membrane properties | | | | | |
| | | AEM | CEM | AEL | CEL |
| Thickness | μm | 130 | 130 | 95 | 95 |
| Areal resistance | $\Omega \text{ cm}^2$ | 7 | 6 | 6.5 | 6.5 |
| H+ diffusivity | $\text{m}^2 \text{ s}^{-1}$ | 2.0E-11 | 0.7E-11 | - | - |
| Na+ diffusivity | $\text{m}^2 \text{ s}^{-1}$ | 1.6E-11 | 0.5E-11 | - | - |
| Cl- diffusivity | $\text{m}^2 \text{ s}^{-1}$ | 1.7E-11 | 0.6E-11 | - | - |
| OH- diffusivity | $\text{m}^2 \text{ s}^{-1}$ | 1.9E-11 | 0.6E-11 | - | - |
| Water permeability | $\text{ml bar}^{-1} \text{ h}^{-1} \text{ m}^{-2}$ | 8 | 8 | - | - |
| Fixed charge group | mol m^{-3} | 5000 | 5000 | 5000 | 5000 |

| Initial conditions of the solutions | | |
|-------------------------------------|--------------------------|------|
| $C_{HCl,d,a,1}$ | mol m ⁻³ | 50 |
| $C_{NaCl,d,a,1}$ | mol m ⁻³ | 250 |
| $C_{HCl,d,s,1}$ | mol m ⁻³ | 10 |
| $C_{NaCl,d,s,1}$ | mol m ⁻³ | 1000 |
| $C_{NaOH,d,b,1}$ | mol m ⁻³ | 50 |
| $C_{NaCl,d,b,1}$ | mol m ⁻³ | 250 |
| R_{bl} | Ω cm ² | 72 |

The inlet salt concentration was fixed to 0.25M in order to simulate a typical operation of BMED, in which acid and base solutions are contaminated with salt, due to the non-ideal functioning of the ion exchange membranes.

Three case studies were performed, each differing in terms of the active membrane area, i.e. 0.75×0.75, 0.50×0.50 and 0.25×0.25 m², hereafter named as case A, B and C, respectively. For each case study, two sets of simulations were performed: the first regards the variation of the current density within the interval 100-500 A m⁻² by fixing the mean channel flow velocity at 1 cm s⁻¹; the second regards the variation of the mean channel flow velocity within the interval of 0.5-5 cm s⁻¹ by fixing the current density to 300 A m⁻².

3.7.1 Current density analysis

Figure 23 shows the conversion rate as a function of the applied current density for the three case studies.

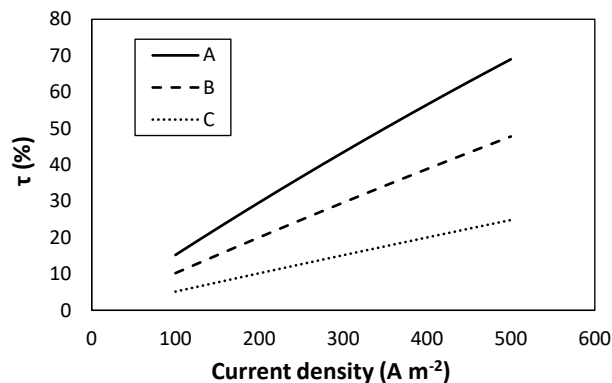


Figure 23. Conversion rate of hydrochloric acid as a function of the current density for the three cases (A, B and C) of active area (75×75 , 50×50 and 25×25), with a fixed mean channel flow velocity of $1\ cm\ s^{-1}$.

The average conversion rates were found to be 42.1, 29.3 and 15.1% for case A, B and C respectively. Theoretically, the conversion rates should follow a linear trend with the spacer length. As an example, by increasing the spacer length from 0.25 m to 0.75 m, the conversion rate values should raise from 15.1% to 45.3% (i.e. the theoretical average τ A). The discrepancy between the actual and theoretical τ A of 7.3% can be ascribed to the non-ideal phenomena (e.g. diffusion, water flux, parasitic currents) which decrease the unit performance. The increase of conversion rates from cases C to A is due to the increase of the membrane fluxes, which is a consequence of the increased membrane area. The result of the raised conversion rate is the increase of the outlet acid and base concentrations. As an example, the outlet concentration of HCl is reported in Figure 24.

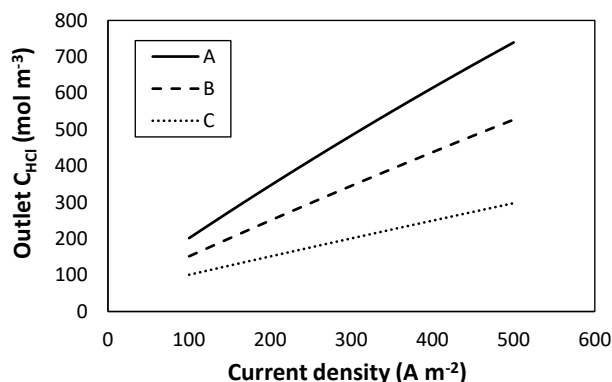


Figure 24. Outlet hydrochloric acid concentration as a function of the current density for the three cases (A, B and C) of active area (75×75 , 50×50 and 25×25), with a fixed mean channel flow velocity of $1\ cm\ s^{-1}$.

The maximum obtained concentration is $\approx 0.7\text{M}$, which corresponds to a conversion rate just below $\approx 70\%$. Clearly, the maximum obtainable HCl concentration is $\approx 1\text{M}$, corresponding to a stoichiometric conversion of NaCl into HCl and NaOH. Therefore, this preliminary analysis shows that the use of feasible BMED designs (in terms of triplet numbers, membrane area) may allow us to obtain high conversion of the salt content into acid and base in continuous once-through mode.

Figure 25 shows the Specific Energy Consumption for the three case studies.

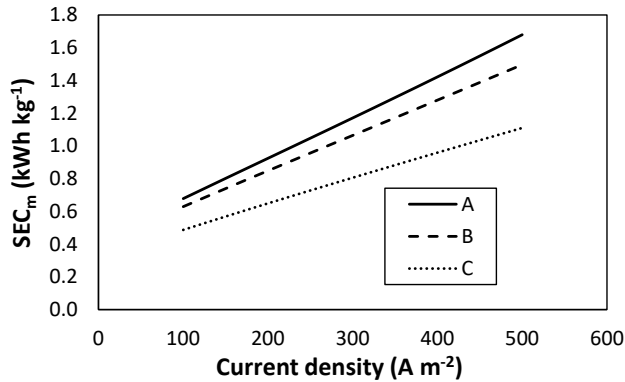


Figure 25. Specific Energy Consumption per kilogram of produced acid as a function of the current density for the three cases (A, B and C) of active area (75×75 , 50×50 and 25×25), with a fixed mean channel flow velocity of 1 cm s^{-1} .

The SEC values range from a minimum of 0.49 kWh kg^{-1} for case C at 100 A m^{-2} , to a maximum of 1.68 kWh kg^{-1} for case A at 500 A m^{-2} . The increase in current density from 100 to 500 A m^{-2} causes an increase in SEC of ~ 2.4 times on average. In absolute terms, Case study C shows better performance. On the other hand, when the membrane area passes from $0.75 \times 0.75 \text{ m}^2$ (case study A) or $0.5 \times 0.5 \text{ m}^2$ (case study B) to $0.25 \times 0.25 \text{ m}^2$ (i.e. 9 and 4 times lower respectively), the average SEC changes from 1.2 or 1.1 to 0.8 kWh kg^{-1} . However, at fixed current densities, the obtained outlet concentration of acid and base is different. Therefore, a more detailed analysis should take into account the conversion rate as well as the obtained concentrations (Figure 26).

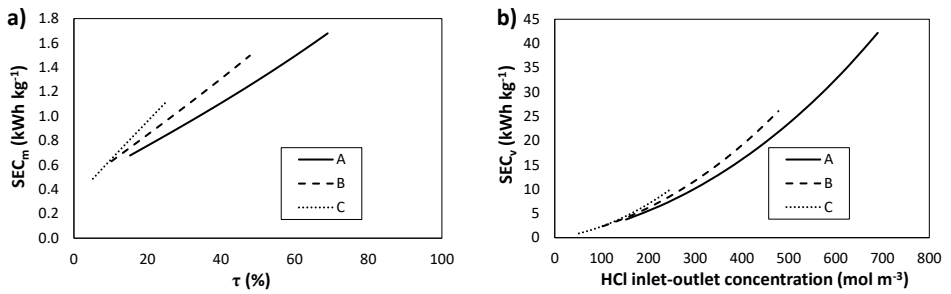


Figure 26. a) Specific Energy Consumption per kilogram of produced acid as a function of the conversion rate and b) Specific Energy Consumption per cubic meter of produced acid solution as a function of the inlet-outlet concentration difference of HCl for the three cases (A, B and C) of active area (75×75, 50×50 and 25×25), with a fixed mean channel flow velocity of 1 cm s⁻¹.

As shown in Figure 26a and b, when the conversion rate or, similarly, the concentration difference is fixed, case study A shows better performance. This fact, at first, seems to contradict the predictions reported in Figure 25, because the higher the membrane active area, the higher the resulting diffusion and water flux phenomena. However, with higher spacer length, there is a lower effect of the parasitic currents via the manifolds, which predominate over the other detrimental effects (the parasitic currents will be discussed in much more detail in Chapter 5). Therefore, the diminished specific consumption for case study A in Figure 26 is the effect of an increased current efficiency (Figure 27) and does not contradict the predictions shown in Figure 25.

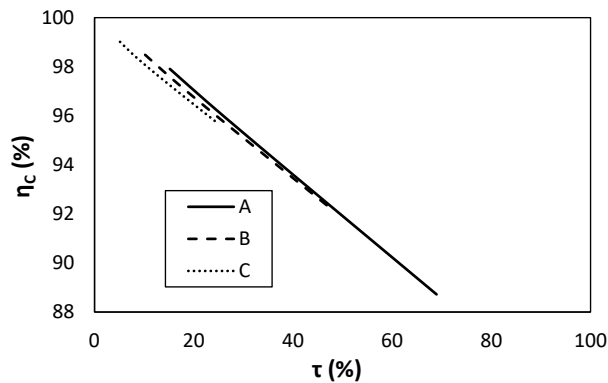


Figure 27. Current efficiency as a function of the conversion rate for the three cases (A, B and C) of active area (75×75, 50×50 and 25×25), with a fixed mean channel flow velocity of 1 cm s⁻¹.

Figure 28 illustrates the computed current efficiency as a function of the applied current density.

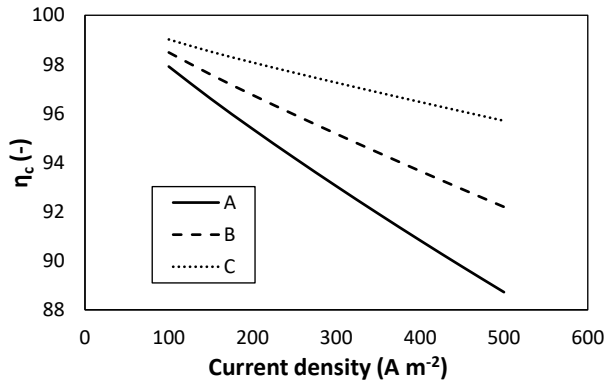


Figure 28. Current efficiency as a function of current density for the three cases (A, B and C) of active area (75×75 , 50×50 and 25×25), with a fixed mean channel flow velocity of 1 cm s^{-1} .

As expected, as the current density increases, the current efficiency decreases. However, the increase in the current density is not matched by a proportional increase in the outlet acid and base concentrations. This is the effect of direct and indirect phenomena. Particularly, at higher current densities, the electro-osmotic flux will be more pronounced. The diffusion phenomenon is not directly related to the current density, as the driving force of diffusion is the concentration gradient of the species. However, it can be enhanced by the resulting increase in the average concentration difference along the channels. Furthermore, the average current efficiencies are 93.1, 95.2 and 97.3% for cases A, B and C respectively. This is due to the more pronounced effect of the diffusion and water flux phenomena when using a stack with higher membrane active area. Moreover, the fact that the reported current efficiencies are very high suggests that most of the carried current is being used in the production of acid and base molecules.

3.7.2 Mean channel flow velocity analysis

Figure 29 shows the conversion rate as a function of the mean flow velocity for the three case studies.

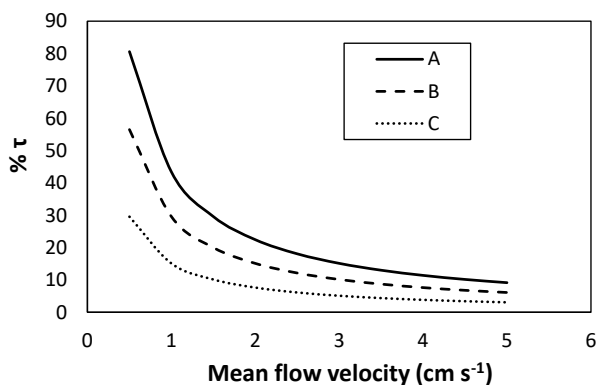


Figure 29. Conversion rate of hydrochloric acid as a function of the mean flow velocity for the three cases (A, B and C) of active area (75×75 , 50×50 and 25×25), with a fixed applied current density of 300 A m^{-2} .

The average conversion rates were found to be ≈ 25.3 , 17.3 and 8.85% for case studies A, B and C respectively. It is interesting to note that, regardless of the specific case study, the conversion rate drastically decreases at low mean flow velocities and tends to flatten at higher velocities. This trend is due to the reduction of the axial concentration change, which was taken into account in the multi-scale model through the numerical discretization of the channel domain.

The graph in Figure 30 reports the Specific Energy Consumption for the three case studies.

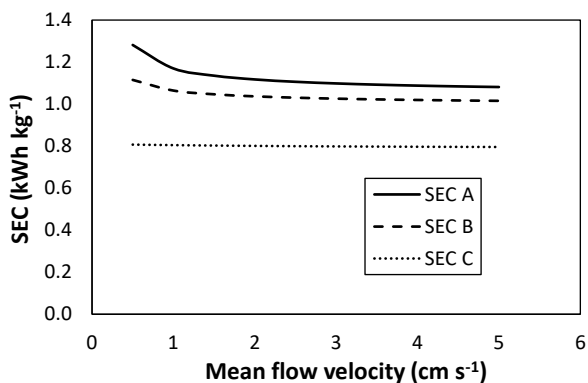


Figure 30. Specific Energy Consumption per kilogram of produced acid as a function of the mean flow velocity for the three cases (i.e. SEC A, SEC B and SEC C), with a fixed applied current density of 300 A m^{-2} .

The SEC values remarkably resemble the ones seen in Figure 25, with averaged values in the order of 1.12 , 1.04 and 0.8 kWh kg^{-1} . Increasing the mean flow velocity

slightly decreases the energy consumption, and this is particularly evident for cases A and B. Overall, no significant variations in the SEC across increasing mean flow velocities were reported, due to the fact that the mean flow velocity does not significantly affect the gross power input into the system. Indeed, the only differences in gross power input can be ascribed to the concentration differences in the electrolytes in the channels from the inlet to the outlet, which are relatively small at increased values of mean flow velocities. For example, Figure 31 shows the outlet concentration of HCl as a function of the mean flow velocity.

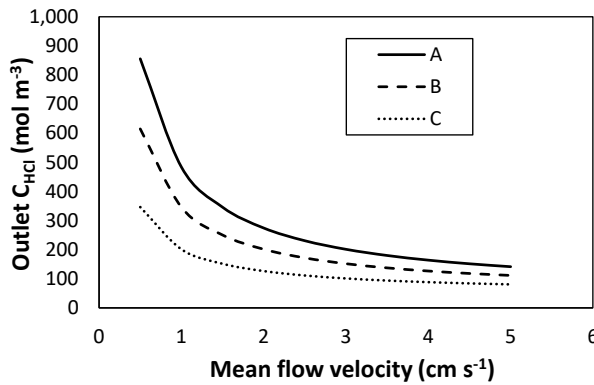


Figure 31. Outlet hydrochloric acid concentration as a function of the mean flow velocity for the three cases (A, B and C) of active area (75×75 , 50×50 and 25×25), with a fixed applied current density of 300 A m^{-2} .

In terms of outlet HCl concentration, the only non-negligible differences were reported at mean flow velocities lower than 1 cm s^{-1} , and for cases A and B.

Figure 32 shows the current efficiencies for the three case studies.

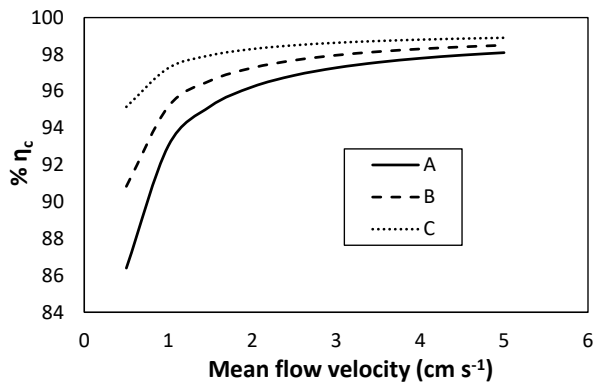


Figure 32. Current efficiency as a function of mean flow velocity for the three cases (A, B and C) of active area (75×75 , 50×50 and 25×25), with a fixed applied current density of 300 A m^{-2} .

Current efficiencies were found to increase with mean flow velocity, and this is due to the reduced effect of the axial polarization, which decreases the diffusion phenomena. Moreover, the current efficiency tends to flatten at higher mean flow velocity, because higher values of these have a lower effect on the outlet concentration (as shown in Figure 28).

The trends in the current efficiencies presented here seem to mirror the trend in the conversion rates (Figure 29). In fact, the current efficiency is calculated by the quantity of produced acid (or base) over the total carried electric charge. As before, for the three case studies, the current efficiency is not such a significant limitation. This is because the average values were higher than 95%, even though from 0.5 to 5 cm s^{-1} , the relative differences (with respect to 0.5 cm s^{-1}) were 13.5, 8.43 and 3.94% for cases A, B and C respectively.

Finally, the comparison between net and gross Specific Energy Consumption is reported in Figure 33.

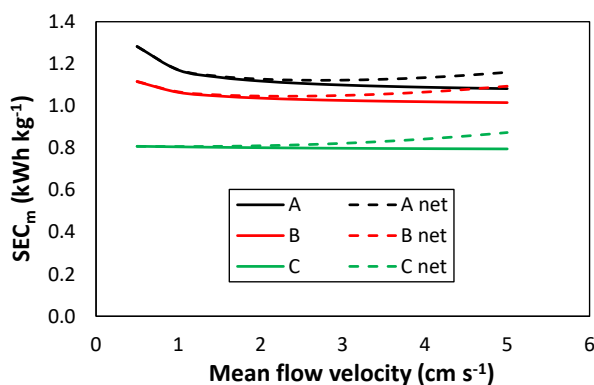


Figure 33. Gross and Net Specific Energy Consumption as a function of the mean channel flow velocity for the three cases (A, B and C) of active area (75×75 , 50×50 and 25×25), with a fixed applied current density of 300 A m^{-2} . Continuous lines: gross SEC_m . Dashed lines: net SEC_m .

As expected, this figure indicates that increases in the mean flow velocity lead to greater differences between the gross and the net SEC_m . Particularly, increasing the mean flow velocity from 0.5 cm s^{-1} to 5 cm s^{-1} was associated with relative increases (with respect to 0.5 cm s^{-1}) in the net SEC_m of 2.0, 8.1 and 9.6% for case studies A, B and C respectively. The increase in the mean flow velocity leads to an increase in the pumping power density (PPD), as a result of the higher localized and distributed pressure losses. This result suggests that lower mean flow velocities may be beneficial to decrease the energy spent on pumping the electrolyte solutions, even though it leads to slightly lower current efficiencies.

In this chapter, the BMED technology was firstly presented with a critical literature review. Following this, for the first time, a fully integrated BMED process model with distributed parameters was developed following a multi-scale simulation strategy. The process model was shown to be robust and reliable by validation against experiments conducted in a steady-state mode. This model was then used to perform a preliminary sensitivity analysis. The analysis suggested that high conversion rates of hydrochloric acid (about 70%) can be reached by increasing the applied current density to 500 A m^{-2} in stacks with $75 \times 75 \text{ cm}^2$ of active membrane area. However, the higher the current densities, the lower the resulting current efficiency. In addition, it was found that typical ranges of mean flow velocities ($1\text{-}5 \text{ cm s}^{-1}$) do not significantly affect the module performance.

4 Bipolar Membrane Reverse Electrodialysis

Bipolar membrane reverse electrodialysis represents an innovative way to produce electric energy by exploiting pH and salinity gradients. Interestingly, the theoretical energy density extractable from the mixing of acidic and alkaline solutions may be very high, reaching 200 kWh m^{-3} when utilizing highly concentrated solutions at ambient temperature and pressure. Therefore, BMRED is an interesting, yet poorly studied technology for the conversion of chemical energy into electricity. BMRED may be applied for the neutralization of waste acids and bases produced by industrial processes. Although it shows promising performance, only few works have been presented in the literature so far, and no models have been developed yet.

This chapter presents a mathematical multi-scale model based on a semi-empirical approach. The model was validated against experimental data and was applied across a variety of operating conditions, showing that it may represent an effective tool for the prediction of the process performance. A sensitivity analysis was performed in two different scenarios, i.e. (i) a reference case and (ii) an improved case with high-performance membrane properties. Results showed that a Gross Power Density of 42 W m^{-2} would be obtainable at a current density of 200 A m^{-2} and with HCl and NaOH solutions at concentration of 1 M.

4.1 Conventional Reverse electrodialysis: general overview and working principle

The production of sustainable energy is one of the main technological challenges of our time. Using renewable energy sources is a possible way to address this issue. Among them, Salinity Gradient Energy (SGE, or blue energy or osmotic energy) can be harvested through properly engineered systems that exploit the Gibbs free energy through the mixing of two solutions at different salt concentrations [142]. Conventional Reverse Electrodialysis (RED) [143] is among the most investigated of the SGE technologies [144].

The RED process is carried out in a stack (Figure 34) equivalent to a conventional electrodialysis (ED) unit, which is composed of several repetitive units called “cell pairs” sandwiched between two end-plates containing the electrode compartments. Each cell pair consists of a Cation-Exchange Membrane (CEM), an Anion-Exchange Membrane (AEM), a concentrate channel and a dilute channel. In RED, the co-ion exclusion (or Donnan exclusion) gives rise to an electric potential over each membrane to equilibrate the difference in chemical potential between the

two solutions [145,146]. The sum of all the membrane potentials is, ideally, the open circuit voltage (OCV) of the stack. When the circuit is closed, redox reactions (typically occurring with a reversible couple) take place [147], thus converting the internal ions current (selective transport from concentrate to dilute) into an external electrons current. In this way, electric energy is supplied to an external load, which is the final user.

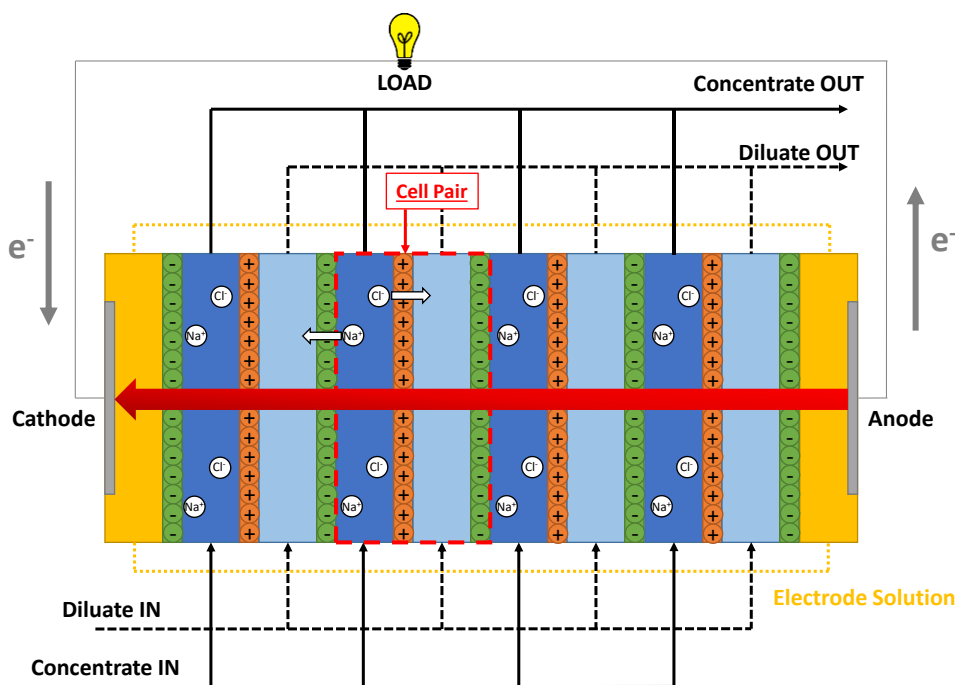


Figure 34. Schematic drawing of a RED stack. The large red arrow from the anode to the cathode indicates the desired direction of the electric current; the other large pink arrows indicate the electrical parasitic pathways (shortcuts) via manifolds in the concentrate hydraulic circuit.

Pattle carried out a pioneering work on RED in 1954, attaining a power density of 0.2 W/m^2 [148]. Since then, significant improvements have been achieved, especially in the last decade. With artificial seawater and river water at ambient temperature, Vermaas et al. [149] reported gross power densities up to 2.2 W/m^2 , while Kim et al. [150] reached slightly higher values (2.4 W/m^2) by developing high-performing IEMs. Higher values can be attained by increasing the driving force in stacks fed in the concentrate by brines [151], which can be drawn from industrial processes (e.g. desalination), hypersaline lakes and saltworks [152–155]. A power output up to 1.35 W m^{-2} was reached by a full-scale RED pilot plant [156]. The highest power density, reported by Daniilidis et al. [157], was of 6.7 W m^{-2} (5 M -

0.01 M NaCl solutions at 60 °C). Net power is a very important performance indicator, given by the produced gross power minus the power spent for pumping the solutions. The maximization of net power density has often been used as an optimization criterion, given the high cost of the membranes [158–161]. Several detrimental phenomena affect the performance of RED processes. The most investigated are (i) co-ion transport and (ii) water transport through the membranes, (iii) uphill transport and effects of divalent ions on membrane resistance and permselectivity, (iv) concentration polarization, and (v) energy spent for pumping the solutions. The first three depend on membrane properties, such as fixed charge density [162], water permeability [163,164] and monovalent-selectivity [165,166], as well as on solution concentration and composition. The fourth and fifth phenomenon strongly depend on the fluid-dynamic conditions [141,149,167–169]. Other aspects concern the spacer shadow effect [167,170,171], and membrane deformation along with its effects [172–174].

Further steps have recently been taken to integrate RED in coupled/hybrid systems (RED/Electrodialysis (ED) [27,28], RED/Reverse Osmosis (RO) [29,30] and RED/Membrane Distillation [31–33]), thus extending the applications of this technology. Closed-loop RED has gained attention since it can be a valuable route to convert low-grade waste heat into electrical power [11,34–37] through the so called RED Heat Engine (RED-HE). It has already been successfully tested at the prototype level by using solutions of thermolytic salts, such as ammonium bicarbonate [38–40], and integrating a “classical” RED unit with a regeneration unit composed of a vapour stripping column and a barometric condenser [22].

In the last decades, alternatives to the conventional RED process have been investigated, involving the neutralization of acid and base solutions. Mei et al., proposed an RED chemical cell fed with acid, base and neutral solutions in a four-compartment unit configuration, to produce energy from acid/base neutralization [175]. They proposed a RED chemical cell fed with acid, base and neutral solutions in a four-compartment unit configuration, to produce energy from acid/base neutralization [175]. With 0.3 M HCl/NaOH solutions and 0.01 M NaCl neutral solution, a maximum gross power density (GPD) of $\sim 0.5 \text{ W m}^{-2}$ was achieved. With respect to that obtained by conventional RED with only neutral solutions, the GPD was significantly enhanced. However, its actual performance is far from the theoretical values. Indeed, the obtained energy density was $\sim 17\%$. The performance reduction is ascribed to the non-ideal acid-base neutralization [175]. The use of this alternative RED process may be possible by using special homopolar membranes with very high selectivity. A more promising alternative, which has been poorly studied, is the Bipolar Membrane Reverse ElectroDialysis (BMRED), which

integrates the use of the bipolar membranes, thus exploiting better the mixing entropy associated to the pH gradient.

4.2 Bipolar Membrane Reverse Electrodialysis

As in the case of BMED, the key role of the BMRED process is associated with the bipolar membrane. BMRED dates back to 1982 when Walther and Skaneateles published their patent [176]. In its first conceptualization, this technology consisted of a single cell provided with an individual bipolar membrane separating two compartments, which hosted the acid and base solutions. The idea behind it was to perform controlled neutralization through the use of the bipolar membrane. This membrane should be able to direct the migration of the proton and hydroxide ions through their respective selective layers (i.e. CEL and AEL). In analogy with the semi-conductors theory, the bipolar membrane during the BMRED process acts as a p-n junction under a forward bias [26]. Subsequently, the idea of a BMRED device was developed in a way similar to BMED devices, using several repetitive units stacked together. Additionally, the only BMRED configuration studied so far is the one comprising cells with three membrane types, i.e. CEM, AEM and BPM, and three channels, i.e. acid, base and salt (Figure 35).

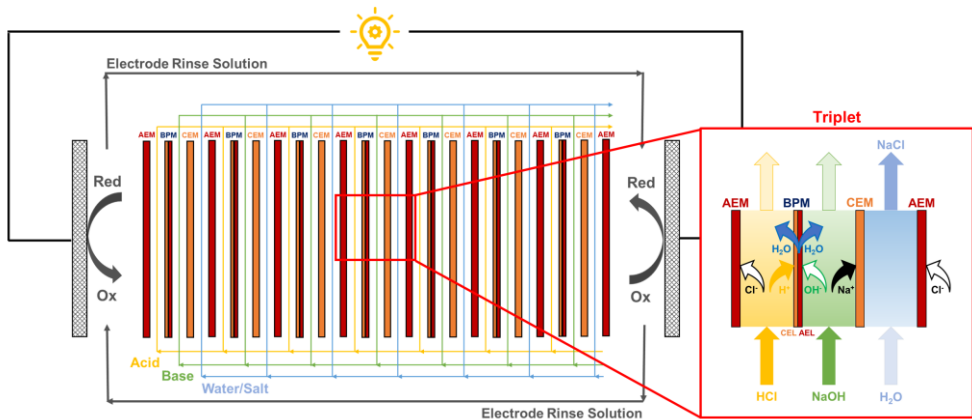


Figure 35. Scheme of an entire Bipolar Membrane Reverse Electrodialysis (BMRED) module (with 7 repeating units, acid: HCl, base: NaOH). The inset on the right shows an enlarged view of the repeating unit (triplet) with an additional anion-exchange membrane (AEM) along with the ions and water main fluxes.

In other terms, BMRED may be seen as the reverse process of BMED. While the latter involves the transformation of electric energy into chemical energy in the form of chemical products, i.e. acid and base water solutions, the former instead involves a process where chemical energy, in the form of a pH gradient, is converted

into electricity for final users. The driving force is the neutralization reaction (i.e. the opposite reaction of water dissociation) which takes place at the interlayer of the bipolar membrane. The neutralization reaction is a very energetic process which causes, on one hand, the production of water molecules from proton and hydroxide ions, and, on the other hand, determines the passage of the respective conjugated base (Cl^- ions) and acid (Na^+ ions) from the acid and base channels to the salt compartment. In this way, the electroneutrality is satisfied. The ion current is then converted into electricity in the external circuit thanks to the redox reactions at the electrode compartments. The neutralization reaction presents, as is well-known, a Gibbs energy at 25 °C and 1 bar equal to -80 kJ mol^{-1} . This is the theoretical energy that would be released if the process had 100% efficiency. This would correspond to an energy density of 22 kWh m^{-3} of acidic (or basic) solution at concentration of 1 M. It is worth noting that this energy density value is an increasing function of the acid and base concentrations [177]. Figure 36 represents the energy density trend that is the effect of only the pH gradient (with equal acid and base concentrations).

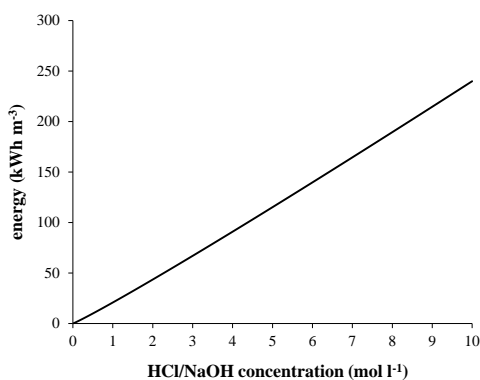


Figure 36. Theoretical energy density (mixing free energy per unit volume of one solution) as a function of the strong acid/base concentration (e.g. HCl and NaOH).

As is clear from Figure 36, at acid and base concentrations equal to 10 M, and at ambient temperature and pressure, the energy density would be higher than 200 kWh m^{-3} . This energy density value would make this technology very competitive for the recovery of energy from pH gradients. To reach this goal, further studies should be performed to develop high-performance IEMs able to limit co-ion leakages under severe operating conditions in terms of acid and base concentration, as well as over long-run operations. For instance, bipolar membranes should have very high selectivity to proton and hydroxide ions in the cationic and anionic exchange layers, respectively, as well as presenting high water permeability. The latter is a very important characteristic as, at high current densities, the amount of water molecules

produced as a result of the acid-base neutralization is very high. Therefore, bipolar membranes should guarantee a high outgoing water flux from the BPM transition region. This property is crucial to avoid any risk of delamination of the bipolar membrane, thus allowing for operations at high current densities [178]. Furthermore, as an example, at 1 M of acid and base, a theoretical electromotive force of 0.83 V is generated over a BPM [178]. However, it is worth noting that the BMRED configuration consists of three membranes and three channels. Therefore, the electromotive force is a function of the concentration at both sides of all the membranes. The generic Nernst equation for a stack of N triplets reads:

$$EMF = N \left[\frac{R_g T}{zF} \left(\ln \frac{a_{H^+}|_{ac}}{a_{H^+}|_{bp}} + \ln \frac{a_{OH^-}|_{bp}}{a_{OH^-}|_{ba}} + \ln \frac{a_{Na^+}|_{ba}}{a_{Na^+}|_{sa}} + \ln \frac{a_{Cl^-}|_{sa}}{a_{Cl^-}|_{ac}} \right) \right] \quad (97)$$

where EMF is the electromotive force of the BMRED stack, a is ion activity, R_g is universal gas constant ($8.314 \text{ J mol}^{-1} \text{ K}^{-1}$), T is temperature, z is the ion valence, F is Faraday's constant (96485 C mol^{-1}) and ac , bp and ba subscripts refer to the acidic solution/BPM-interlayer interface, the interlayer of the bipolar membrane and the alkaline solution/BPM-interlayer, respectively.

Eq. 97 shows the bipolar membrane contribution, i.e. the first two addends, and the monopolar membrane contributions, i.e. the other two addends. By way of example, the histogram in Figure 37 shows the EMF and the bipolar and monopolar membrane contributions computed by Eq. 97 in four different scenarios: high or low acid and base concentrations with the presence or not of NaCl as background salt in the acid and base compartments.

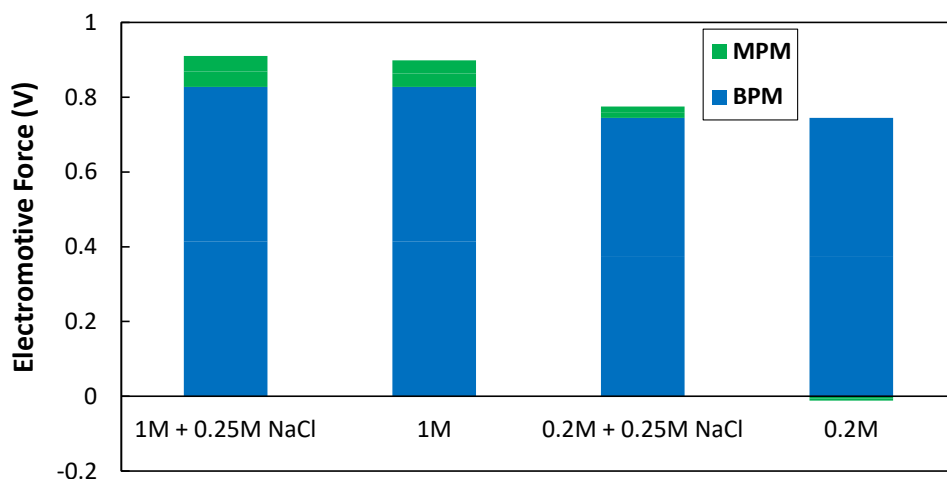


Figure 37. EMF contributions for a BMRED triplet. Blue and green areas refer to BPM and MPMs contributions respectively. Inlet concentrations: 0.2 M or 1 M HCl/NaOH with or without the presence of 0.25 M NaCl of background salt in the acid and base compartments. Salt stream: 0.25 M NaCl.

It is clear that, regardless of the scenario, the BPM contribution to the EMF is always predominant and depends on the acid and base concentrations only, and not on the presence of NaCl as background. On the other hand, the contribution of MPMs is shown to be dependent on both acid/base and salt concentrations in the acid and base compartments. For instance, with HCl and NaOH concentrations equal to 1 M, the presence of background salt increases the EMF by $\sim 1.3\%$. Furthermore, the lower the HCl/NaOH concentration, the higher the effect of background salt. Particularly, with a HCl/NaOH concentration equal to 0.2 M, the background salt raises the EMF by $\sim 5.4\%$, and the contribution of MPMs inverts from negative to positive.

As already stated, the reported EMF or the energy density values are only theoretical. This means that the BMRED technology has to deal with some source of inefficiency that ultimately affects the actual performance, e.g. the internal stack resistance and the non-ideal behaviour of the membranes, which are not 100% selective. Due to the presence of three compartments in a single repetitive unit, one may incorrectly assume that there will be higher internal ohmic losses in BMRED units than in conventional (i.e. two-compartment) RED units. However, unlike with the conventional RED process, the concentrate compartments of a BMRED module are the acid and base channels; these hold the acid and base solutions which, by nature, are highly conductive. Moreover, the dilute compartments are the salt channel and the interlayer of the bipolar membrane. Unlike with the conventional RED process, the salt channels in a BMRED unit typically have conductivities in the order

of $2\text{-}5\text{ S m}^{-1}$ (computed with OLI studio Stream Analyzer ®). These conductivities result to be 1 order of magnitude higher than the conductivity of river water, which is commonly utilized for the dilute compartment of a conventional RED system. Even though the interlayer of the bipolar membrane is highly diluted, its thickness is small enough to give only a relatively small increase in the overall resistance of the bipolar membrane.

On the other hand, highly conductive solutions may give rise to quite a few problems in terms of parasitic currents (i.e. the ionic current by-pass through the manifolds instead of across the membranes [111]). Another potential source of efficiency loss is the concentration polarization phenomenon, which causes the boundary layer voltage drop [168]. This fact leads to the decrease of the cell electromotive force, causing a reduction of the overall efficiency.

Furthermore, among the possible detrimental phenomena there is the power consumption due to the pumping of the solutions. This fact is crucial for RED systems because the higher the pumping power, the lower the available power for the final user. In this respect, BMRED takes advantage of a high energy density, which is (at a concentration of 1M of acid and base) \approx 1 order of magnitude higher than the energy released by mixing salt and fresh water. For this reason, in BMRED, the fraction of energy spent on pumping the electrolytes is lower than the one necessary for conventional RED processes, thus it should have negligible effects on the net power density.

In terms of environmental impact, BMRED is a safe technology. In fact, even considering the possibility of an accidental breakage of the electrolyte solution storage tanks, it does not have serious implications as the acidic and basic solutions would neutralize, thus producing a harmless NaCl solution. Despite BMRED represents an interesting technology for converting pH and salinity gradients into electricity, it has been poorly investigated. For example, to date only up to 1M of HCl and NaOH solutions have been studied [177]. The very few works presented in the literature are summarized below.

4.2.1 *State of the art*

The BMRED literature regards this technology as the discharge phase of the Acid-Base Flow Battery. In this chapter, the discharge aspects of the AB-FB will be analyzed, whereas in Chapter 6 this study will be extended to both the phases and the overall functioning of the battery.

Emrén and Holmström [179] explored the battery using a seven-triplet stack, recording a maximum output voltage of 1.8 V (current density of $\approx 1.4 \text{ A m}^{-2}$) with an estimated perm-selectivity of the BPMs of $\approx 50\%$ during the discharge experiment.

Pretz and Staude [180] studied the range of concentration of 0.1-1 M of acid and base. The current efficiency decreased by one order of magnitude when passing from 0.1 to 1 M due to the non-ideal behaviour of the IEMs. Depending on the type of bipolar membrane used, the maximum energy efficiency of the process was found to be 22%. In terms of voltage-current trend, by using an external resistance equal to the internal one, the stack voltage is theoretically 50% of the open circuit voltage. However, a lower electric potential was observed, and this was attributed to the higher electric resistance (up to 15 times increase) due to water accumulation in the bipolar membrane interlayer at higher electric currents. The water flux may also irreversibly damage the BPMs through delamination.

Zholkovskij et al. [181] investigated a 4-compartment BMRED stack. The measured values of membrane resistance were 5, 2 and $6.8 \Omega \text{ cm}^2$ for AEM, CEM and BPM, respectively. They explored the electric current interval 0.001 - 5 mA, corresponding to current densities up to $\approx 2 \text{ A m}^{-2}$. Moreover, the maximum studied concentrations were $\approx 0.03 \text{ M}$ of acid and base. They reported specific energy of 0.1 Wh kg^{-1} and a maximum GPD (per kilogram of product) of 0.005 W kg^{-1} .

Kim et al. [182] explored the acid/base concentration range of 0.1 - 0.7 M with a single-cell stack. The open circuit voltage (OCV) was 6% lower on average than the theoretical one. This discrepancy was explained by two reasons: i) the effect of the excessive water formation due to the neutralization reaction in the interlayer and ii) the overvoltage of the electrode reactions. Particularly, the greater reductions in electric potential were found to occur at higher concentrations, where the water formation in the interlayer was higher. Maximum values of GPD ranged from 6.6 to 11.6 W m^{-2} .

Van Egmond et al. [177] performed experiments by using a single-triplet stack with active membrane area of 0.01 m^2 and by exploring a wide range of acid and base concentration, i.e. 0 – 1 M of HCl and NaOH. The OCV was found to be 0.83 V at 1 M of acid and base, corresponding to 89% of apparent permselectivity of the membrane stack. Moreover, they performed discharge tests with current densities in the interval 5 - 15 A m^{-2} . The delamination of the bipolar membranes was observed at 20 A m^{-2} . A maximum GPD of 3.7 W m^{-2} and a specific energy density of 2.9 Wh kg^{-1} were achieved.

Xia et al. [178] first investigated BMRED units with a single triplet, and afterwards they used a variable number of repetitive units in the range of 5 to 20

[183]. The single triplet experiments were performed with acid and base concentration in the range of 0 - 1 M [178]. Stack experiments [183] were performed with a fixed acid/base concentration equal to 1M or 0.5M. Single cell experiments showed that the maximum achievable specific power was $\approx 95 \text{ W kg}^{-3}$, which was found at a concentration of 0.75 M [183]. Compared to the other works presented in literature, this value seems to be unrealistic, as it should be $\approx 60 \text{ W m}^{-2}$. However, this value from literature is improbable, thus it could be suggested that previous calculations have been inconsistent. Although the specific power reached at 1 M was lower ($\approx 65 \text{ W kg}^{-3}$), this result was affected by the fact that the experiment at 1 M was limited to a lower current density, thus not achieving the power peak. Furthermore, the OCV values measured by varying the number of repeating units (from 5 to 20) were lower than the values calculated by a linear extrapolation of the OCV for a single triplet [49]. Particularly, the higher the number of triplets, the higher the discrepancy. This was due to the detrimental effects of the shunt currents through the manifolds. However, a maximum GPD of $\sim 16 \text{ W m}^{-2}$ (excluding electrode losses) was found with a stack equipped with 20 triplets, at a current density of 100 A m^{-2} [183]. Moreover, delamination issues did not occur up to $200\text{-}400 \text{ A m}^{-2}$ [183], i.e. values of current density that are one order of magnitude higher than those found in previous works.

The present literature review shows that membrane properties are crucial for the BMRED process performance. Specifically, the bipolar membrane performance should be improved by increasing its stability and selectivity, in order to allow high current densities. In fact, high current densities are today unfeasible due to the limited performance of the available bipolar membranes, although this is expected to change in the near future. Indeed, the rapid increase in attention on BPMs over the last two decades has already led to major improvements in the BPM properties [35].

4.3 *Acid/Base neutralization of waste streams and production of energy*

Large volumes of acidic wastewater are produced in many industrial processes, from electroplating [184], iron and steel production to pickling operations [185], from food processing [186] to drugs production and mining activities. Therefore, acidic wastewater disposal is one of the most important issues for the modern industries, since wastewater must be treated under controlled conditions before the final discharge [187]. A common practice in treating acid streams is the neutralization process with large amount of alkaline reagents (e.g. calcium carbonate, calcium oxide, magnesium hydroxide, sodium hydroxide or carbonate) [188], especially whether the landfilling or the discharge in sea locations are still the primary options. Although widely used by industries the neutralization of acid

streams presents high treatment costs as well as it produces metals rich brines containing heavy metal components. Furthermore, the acid solution is lost during neutralization processes, while it could be recovered and/or reused through a sustainable approach. Many technologies are currently studied for acid recovery [187,189], including electro-dialytic techniques [78,190].

Similar considerations apply for alkaline solutions. High amounts of spent sodium hydroxide solutions are regularly disposed by the several industry sectors. A typical source of caustic soda wastes is the anodizing industry, which uses highly concentrated NaOH solutions at high temperature, particularly for removing aluminium from the extruder matrixes [191]. In fact, the inner surface of the extrusion dies has to be perfectly clean in order to produce high quality extruded products [192]. Textile dyeing industry as well as metal finishing processes are other sources of caustic soda with an average concentration of 12% weight. The outgoing spent caustic soda solutions presents on average a concentration of 4% weight, which is typically lost by neutralization [193]. Sodium hydroxide solutions with a concentration in the range 5-10% weight are commonly used in the oil refining desulfurization process, which produces consumed caustic soda solutions [194]. Finally, spent caustic soda solutions are also produced by ethylene plants [195].

In order to reduce the costs of the wastewater treatment, a very promising option may be to neutralize the acid and base solutions while a concurrent production of electric energy is performed by exploiting the pH gradient. To this purpose, several approaches have been proposed over the years. A solution consisted in harvesting mechanical energy by carrying out the neutralization reaction, with waste acid or base, inside an ion-exchange polymer causing a reversible swelling and shrinking of the polymer phase because of the water transport inwards and outwards [196–198]. Another approach involved the energy storage derived by proton insertion/de-insertion cycle in a so-called neutralization pseudo-capacitor, where energy storage was derived from the partial entropy change related to the difference in the acid concentration of the electrolytic solution [199]. RED technology can be a sustainable and effective way for producing energy from waste solutions [153,200,201]. In this regard, an ammonium bicarbonate-based Reverse Electrodialysis system was proposed to treat waste acid streams and, simultaneously, to produce hydrogen gas [202]. An innovative way in reusing waste acid streams for energy production can be based on harvesting the energy derived from acid-base neutralization through Bipolar Membrane Reverse Electrodialysis.

The optimization of stack design and operating conditions will be crucial for the process competitiveness of the BMRED technology. Therefore, the development of suitable modelling tools is crucial to assess the process performance under different working conditions and its potential achievements with high-performance membranes.

4.4 Modelling of the bipolar membrane reverse electrodialysis: state of the art

Conventional RED processes have been studied by a wide variety of mathematical models, including several simulation approaches from the very simplified lumped to the more complex multi-physics and multi-scale models. The simplified models allow the prediction of the RED behaviour only qualitatively as they are based on numerous simplifying hypotheses. On the other hand, the advanced ones try to simulate with high accuracy the process at a cost of a large computational burden. Some numerical models have been based on the Nernst-Planck theory [162,163] or on the resolution of the Stefan-Maxwell equation [203]. However, the most effective approach for the development of membrane process models is based on a separation of spatial scales and the use of accessible empirical parameters characterizing the membrane properties. These multi-scale semi-empirical models describe the ED/RED process behaviour by solving material mass balances for the repetitive units calculating membrane fluxes and requiring, as only input, membrane characteristics such as their electrical resistance [112,204]. Semi-empirical models are a good compromise in terms of predictive accuracy and computational cost.

Unlike the conventional RED, very few modelling attempts have been presented so far in literature for the BMRED process. In the first model developed by Pretz and Staude [180] the OCV was calculated as proportional to the cells number. Moreover, the evaluation of the gross power and the internal resistance were proposed. The model predictions were not in a good agreement with the experimental data, especially the OCV, for which an important discrepancy was observed by increasing the number of repetitive units, due to the occurrence of parasitic currents. Zholkovskij et al. [181] showed the calculation of the EMF by considering not only the bipolar membrane electrical potential but also the one related to the monopolar membranes. Furthermore, parameters as specific capacity, energy density and power density were assessed. To obtain these system characteristics, the calculation of the external voltage by varying the current portion for a fixed discharge time was proposed. The developed equations were simplified by considering two limiting conditions, i.e. very slow or rapid process. They obtained a complex system of equations which presents quite a few resolution difficulties as well as the need of not easily empirically accessible parameters. Despite the numerical complexity, the

maximum discrepancy with the experimental results was high, in the order of 30%. Therefore, this model aimed at predicting only qualitative trends of the BMRED process. Finally Xia et al. [178] did not develop a predictive model, but they only calculated parameters as the stack voltage, power density and the voltage efficiency by using the experimental OCV, the external current and the internal resistance. The expression used for the theoretical OCV was derived from the ion electrochemical potential equations at the membrane-solution interfaces.

In the present chapter, a novel comprehensive BMRED mathematical multi-scale model was developed for the first time. It is a semi-empirical model able to predict the behaviour of the BMRED process and the main figure of merits of relevant interest. Once experimentally validated, the model was used to perform a sensitivity analysis to give insights about the potential of this innovative technology for the energy harvesting by acid and base neutralization.

4.5 Description of the multi-scale model

This mathematical model was developed in the gPROMS Model Builder® platform and presents a multi-scale structure. The model presents four levels and three dimensional scales, following the same structure used for BMED described in chapter 3. The model similarly integrates correlations coming from Computational Fluid Dynamic simulations for the calculation of Sherwood numbers and friction factors along the channels and pressure drops at the inlet/outlet regions of the channels connected to the manifolds. Except for the bipolar membrane level, where more significant changes were required, the equations adopted at the various levels or dimensional scales are the same or with only small changes with respect to those used for BMED (chapter 3). In this section, the modifications regarding the bipolar membrane level and other model levels, when needed, will be described. Finally, the main performance parameters will be defined, e.g. energy density and efficiency, which are relevant for the BMRED technology.

4.5.1 Lowest scale: Channel model

This model was already shown in section 3.5.1. All the equations and considerations are still valid without any modifications.

4.5.2 Lowest scale: Bipolar Membrane model

The bipolar membrane is modelled as a two-layer membrane, i.e. CEL and AEL, with an interlayer in which no mass accumulation is assumed. All the bipolar

membranes of a stack are simulated and discretized along the flow direction. Likewise the case of monopolar membranes, bipolar membrane fluxes are evaluated by adopting the Nernst-Planck-Donnan approach for multi-ion systems [67]. Ion transport through the bipolar membrane layers are given by:

$$J_{i,BPL} = -J_{diff,i,BPL} + \frac{t_{i,BPL}i}{z_i F} \quad (98)$$

in which $J_{i,BPL}$ is the total molar flux of the i -th ion across the generic bipolar membrane layer (i.e. CEL or AEL), $J_{diff,i,BPL}$ is the diffusion component of the ion flux, $D_{i,j,BPL}$ is the cross-diffusion coefficient (defined later), $C_{j,BPL}$ is the concentration in the membrane phase of the j -th ion, $j = 1, 2, \dots, n$ (where n is the number of ion species, which is 4 in the present study) at each BPM-layer interface, $t_{i,BPL}$ is the transport number of the i -th ion within the layer, i is the current density, z_i is the ion charge and F is the Faraday constant. $J_{i,BPL}$ is positive if entering the channel, negative if exiting the channel.

At the interlayer interface $C_{j,BPL}$ is assumed to be null for the co-ions in their respective BPM-layer. However, for the counter-ions across the CEL, the Na^+ concentration is assumed to be constant and the H^+ concentration follows from the electro-neutrality relation; for the counter-ions across the AEL, the Cl^- concentration is assumed to be constant and OH^- concentration follows the electro-neutrality relation.

However the effective ion transport numbers $t_{i,BPL}$ in each bipolar membrane layer have to satisfy the overall electroneutrality over the BPM. For this reason, the effective ion transport numbers are calculated as the half-sum of the transport numbers $t_{i,BPL}^*$ of the correspondent counter- and co- ions in the two layers. In other words, the symmetry of the bipolar membrane is taken into account for the calculation of the ion transport numbers.

Taken individually, the ion transport numbers $t_{i,BPL}^*$ for each layer are related to the ion diffusion coefficients of all the ions, and to the average ion concentration within the layer by the expression

$$t_{i,BPL}^* = \frac{z_i^2 D_{i,BPL} \overline{C_{i,BPL}}}{\sum_j z_j^2 D_{j,BPL} \overline{C_{j,BPL}}} \quad (99)$$

in which $D_{i,BPL}$ is the diffusion coefficient of the i -th ion, and $\overline{C_{i,BPL}}$ is the average ion concentration within the bipolar membrane layer. $D_{i,BPL}$ is the ion diffusivity in the membrane phase and it is a parameter of the model.

The following $n-1$ Donnan equilibrium equations at each membrane-solution interface are applied

$$\frac{R_g T}{z_i F} \ln \frac{C_{i,sol,int}}{C_{i,BPL,int}} = \frac{R_g T}{z_{i+1} F} \ln \frac{C_{i+1,sol,int}}{C_{i+1,BPL,int}} \quad (100)$$

where $C_{i,sol,int}$ and $C_{i,BPL,int}$ are the ion concentrations at the interface on the solution and membrane side, respectively, R_g is the gas constant and T is the temperature.

The electro-neutrality within each bipolar membrane layer is considered with the general expression:

$$X + \sum C_{co,BPL} = \sum C_{ct,BPL} \quad (101)$$

where X is the fixed charge group concentration in the IEM, $C_{co,BPL}$ and $C_{ct,BPL}$ are the co-ion and counter-ion concentrations in the bipolar membrane layer.

According to the diffusion-conduction equation Eq. (98), the diffusive flux of the ion species i for each layer taken individually through a bipolar membrane layers is

$$J_{diff,i,BPL}^* = - \sum_j D_{i,j,BPL} \nabla C_{j,BPL} \quad (102)$$

where the concentration gradients are calculated by assuming a linear profile between the boundary values of concentration calculated by solving the Donnan equilibrium expressions, and the cross-diffusion coefficients $D_{i,j,BPL}$ are expressed as follows:

$$D_{i,j,BPL} \equiv D_{i,BPL} \delta_{ij} + \frac{t_{i,BPL}^*}{z_i} z_j (D_{i,BPL} - D_{j,BPL}) \quad (103)$$

where δ_{ij} is the Kronecker delta.

The effective diffusive fluxes $J_{diff,i,BPL}$ in each bipolar membrane layer has to satisfy the overall electroneutrality. For this reason, the effective ion diffusive flux is calculated as the half-sum of the ion flux of the correspondent counter- (i.e. Na^+ and H^+ in CEL and Cl^- and OH^- in AEL) and co- (i.e. Na^+ and H^+ in AEL and Cl^- and OH^- in CEL) ions in the two layers. Particularly, the correspondent co-ions in CEL are Cl^- and OH^- for Na^+ and H^+ respectively and vice-versa for AEL. In other words, again a symmetry of the bipolar membrane is taken into account. Particularly, since $J_{diff,i,BPL}^*$ is positive when the ion species enters the channel, the following relation is applied

$$J_{diff,i,CEL} = -J_{diff,i,AEL} \quad (104)$$

The concentration gradient $\nabla C_{j,BPL}$ in Eq. 102 may be calculated by knowing the membrane ion concentration at the interlayer interfaces.

Finally, by following the assumption of no mass accumulation in the interlayer, a further salt flux should be considered to satisfy mass balances through the bipolar membrane system. Particularly, this salt mass flux G_{salt} is due to the migration of sodium and chloride ions through the bipolar membrane layers. It is computed as follows:

$$G_{salt,BPL} = -\frac{(t_{Na,BPL} + t_{Cl,BPL})i}{2F} M_{NaCl} \cdot 10^{-3} \quad (105)$$

4.5.3 Middle-low scale: Triplet model

The equations already presented in section 3.5.3 are valid for the BMRED model without variations.

4.5.4 Middle-high scale: Stack model

In the BMRED process, the produced electricity is conveyed along the external electric circuit toward an external load, which represents the final user. For the BMRED process, the equivalent electric circuit solved by the electrical sub-model of stack is shown in Figure 38.

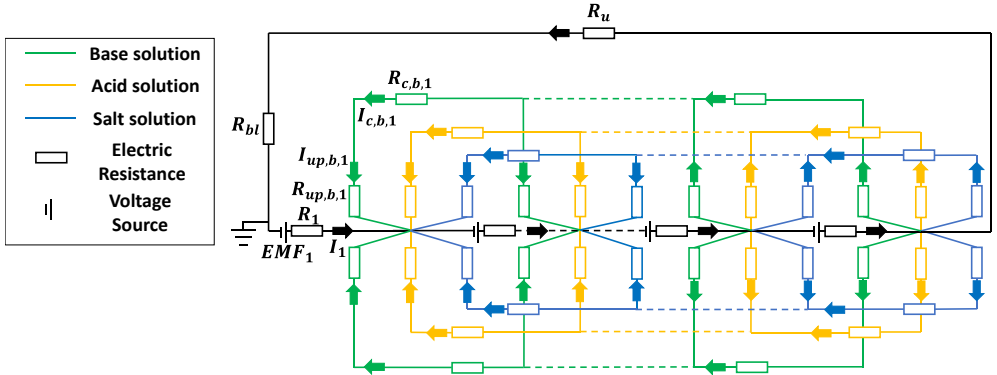


Figure 38. Scheme of the equivalent electric circuit of BMRED stacks.

The equations already presented in section 3.5.4.2 are still valid but with some differences. The cell current I_k for the k -th node and the external current I_{ext} are calculated as:

$$I_k = \frac{(E_{av,k} - \Delta V_k)}{R_{av,k}} \quad (106)$$

$$I_{ext} = \frac{U}{R_u + R_{bl}} \quad (107)$$

The gross power density GPD per triplet provided by the power provided to the external load, can be simply calculated as

$$GPD = \frac{I_{ext} U_{ext}}{N b L} \quad (108)$$

where $b \cdot L$ is the active area of one single membrane.

The net power density (NPD) is calculated as

$$NPD = GPD - PPD \quad (109)$$

where PPD is already calculated in chapter 3.

4.5.5 Figures of merit of BMRED processes

In this section, the main figures of merit of BMRED units are described. In a specular way to BMED, the mass Gross Energy Density (GED_m) represents the energy recovered by the process neutralizing 1 kg of HCl. It is given by

$$GED_m = \frac{U_{ext} I_{ext}}{3600 M_{HCl} Q_{tot,a} (C_{HCl,d,a,1} - C_{HCl,c,a,N-1})} \quad (110)$$

where GED_m is expressed in kWh kg_{HCl}⁻¹.

The current efficiency (η_c) is the amount of the produced external charge per unit of HCl moles neutralized by the process. It is calculated according to

$$\eta_c = \frac{N_{tr} I_{ext}}{F Q_{tot,a} (C_{HCl,d,a,1} - C_{HCl,c,a,N-1})} \quad (111)$$

in which η_c is the current efficiency.

The conversion rate of the hydrochloric acid is the ratio between the amount of produced sodium chloride during the process time over the initial hydrochloric acid as

$$\tau = \frac{Q_{tot,s} (C_{NaCl,c,s,N-1} - C_{NaCl,d,s,1})}{Q_{tot,a} C_{HCl,d,a,1}} \quad (112)$$

where τ is the conversion rate of hydrochloric acid.

Another important performance parameter is the energy density (energy extracted from a unit volume of processed solution). The gross energy density (GED_v), i.e. neglecting the energy loss due to pumping, in a similar manner to BMED, represents the gross energy collected over a complete neutralization of the pH gradient, divided by the used volume of acid solution, as reported in Eq. (113):

$$GED_v = \frac{U_{ext} I_{ext}}{3.6 \cdot 10^6 \cdot Q_{tot,a}} \quad (113)$$

where GED_v is expressed in kWh m_{HCl}^{-3} .

Moreover, the efficiency of the process η was evaluated as:

$$\eta_{BMRED} = \frac{GED_v}{GED_{v,th}} \quad (114)$$

in which $GED_{v,th}$ is the theoretical gross energy density (kWh m^{-3}) and it is calculated as follows

$$GED_{v,th} = \frac{F}{3.6 \cdot 10^6} \int_{10^{-4}}^{C_{t,HCl,out,a}} EMF dC_{t,HCl,out,a} \quad (115)$$

4.6 Steady-state model validation

BMRED experiments were collected by using a commercial lab-scale module (FT-ED-100) from Fumatech BWT GmbH (Germany). The stack was equipped with the following IEMs: fumasep® FAB, fumasep® FKB and fumasep® FBM as AEM, CEM and BPM, respectively. The electrodes were DSA (Dimensionally Stable Anode)-type electrodes, suitable for the redox electrode reactions, with an area of 10×10 cm². IEMs were separated by PVC/ECTFE spacers (made by woven filaments and with a thickness of 500 μ m). Spacers had three inlet/outlet holes and each hole diameter was 8.5 mm. The membranes active area was 10×10 cm². The stack was assembled with different number of repeating units in the interval 5-38. Acid, base and salt solutions were prepared using Hydrochloric Acid (HCl 37% Merck), Sodium Hydroxide (NaOH 98-100% Honeywell Fluka) and Sodium Chloride (NaCl 99.7% ChemSolute), respectively. The electrode rinse solution was an aqueous solution 0.5 M in FeCl₂/FeCl₃ (99% ChemSolute) and 0.6M in HCl. HCl was added to prevent possible iron oxy-hydroxide precipitation [205]. AEM was used as end- membrane. Peristaltic pumps (BT601S, Lead Fluid Technology, CO LTD, China) were used for circulating all the acid, base and salt streams as well as the electrode rinse solution. A BK Precision 8540 DC Electronic Load was used in galvanostatic mode. All the experiments were re-tested a minimum of two times to verify their reliability. Inlet and outlet solution samples were collected for the analysis of both titration and chromatography to compare the ion concentrations in each compartment. Ion chromatography was performed with an Ion Chromatography (IC) Metrohm 882 Compact IC plus. Milli-Q water was used to prepare each sample.

Analogously to the BMED tests (chapter 3), the open-loop configuration was used for every experiment. Various compositions and concentrations were properly chosen. At

the beginning of the experiment, samples of the initial solutions were collected to perform chromatography and titration analysis. Each peristaltic pump was calibrated prior to use in order to be able to set a specific mean channel flow velocity. Once the pumps started flowing the electrolyte solutions through the stack, they operated for at least 5 minutes to ensure good membrane conditioning. Subsequently, the external circuit was closed by setting the load to provide the desired electric current. The operation continued until reaching a constant external voltage (measured by the voltmeter), and then samples of the outlet solutions were collected to determine pH and ion concentrations of the outlet solutions. The used experimental set-up is depicted in Figure 18.

4.6.1 Comparison between experimental data and model predictions

The experiments were performed in a steady-state regime, and with three different acid and base concentrations, i.e. 0.2, 0.6 and 1 M, as well as with or without the presence of 0.25 M NaCl of salt background in the acid and base compartments. The NaCl concentration at the inlet of the salt channels was kept constant at 0.25 M for all the experiments. The tests were performed by varying the number of triplets from 5 to 38 for the set of experiments without the presence of salt background, and from 5 to 30 for the set of experiments with the presence of salt background.

Figure 39 shows the polarization curves for the 0.2 M experiments without the presence of background salt, and for stacks with different numbers of triplets, along with the model predictions.

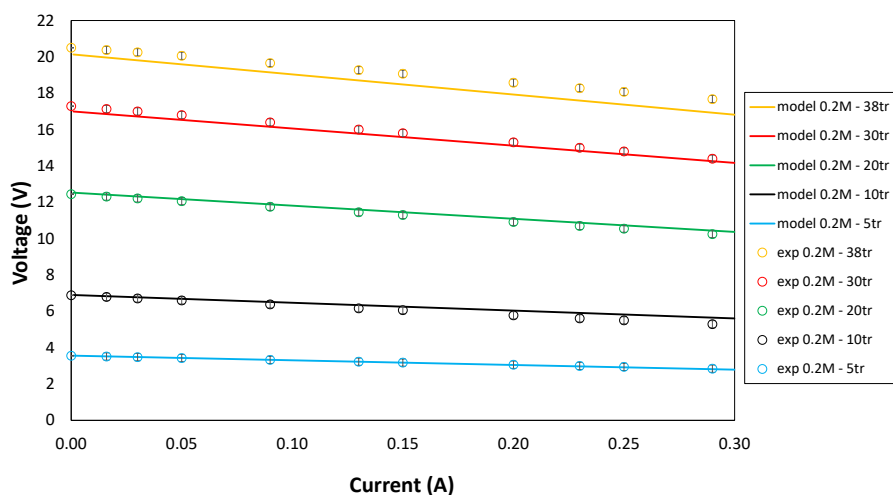


Figure 39. Voltage-current curves by varying the number of triplets, in $10 \times 10 \text{ cm}^2$ stacks with Fumatech membranes (FAB, FKB, FBP) and with spacers provided with 3 inlet/outlet holes (diameter of 8 mm). Mean flow velocity of the electrolyte solutions in each channel equal to 1 cm s^{-1} . Symbols refer to experimental data, continuous lines to the model predictions. Inlet concentrations: 0.2M HCl and NaOH in the acid and base channels respectively and 0.25M NaCl in the salt channel. Areal blank resistance: $72 \Omega \text{ cm}^2$.

The experiments in Figure 39 showed high repeatability since the average empirical error was $\approx 2.5\%$. The maximum empirical error was obtained in the tests using 5 triplets, and it was 5.7%. The model predictions were in good agreement with the experimental data, regardless of the number of triplets. The overall average discrepancy was $\approx 1.9\%$, with a minimum of 0.35% for the experiments conducted at 5 triplets, whereas the maximum discrepancy was obtained for the 10-triplet stack, which is characterized by an average discrepancy of 3.3%. Interestingly, even at high numbers of triplets the model predicts the experimental results with high accuracy as the maximum absolute discrepancy was found to be 4.2% for the case of 38 triplets at a current density of 29 A m^{-2} . The maximum current density was limited at 29 A m^{-2} , to avoid the delamination of the BPMs.

Figure 40 illustrates the polarization curves for the 0.6 M cases without the presence of background salt.

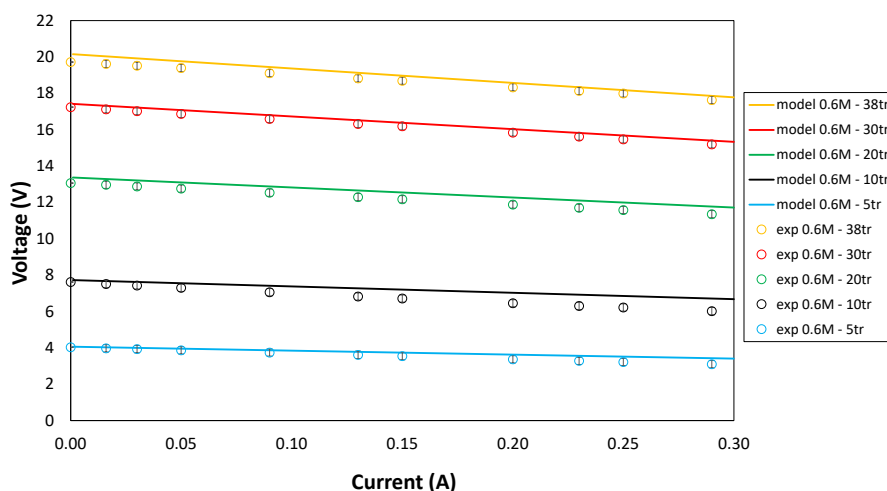


Figure 40. Voltage-current curves by varying the number of triplets, in $10 \times 10 \text{ cm}^2$ stacks with Fumatech membranes (FAB, FKB, FBP) and with spacers provided with 3 inlet/outlet holes (diameter of 8 mm). Mean flow velocity of the electrolyte solutions in each channel equal to 1 cm s^{-1} . Symbols refer to experimental data, continuous lines to the model predictions. Inlet concentrations: 0.6M HCl and NaOH in the acid and base channels respectively and 0.25M NaCl in the salt channel. Areal blank resistance: $72 \Omega \text{ cm}^2$.

The results reported in Figure 40 show high repeatability since the average empirical error was $\approx 2.3\%$. The maximum empirical error found was for the 5 triplets experiment curve, with an average of 5.2%. Overall, the discrepancy was $\approx 3.6\%$, with a relative minimum error of 1.2% for the experimental curve at 30 triplets, and a maximum model discrepancy of 6.7% on average. At the highest number of triplets that was investigated, the model predicts the empirical data with high accuracy, as the average model discrepancy was 1.6%.

Figure 41 reports the polarization curves for the 1 M cases without the presence of background salt.

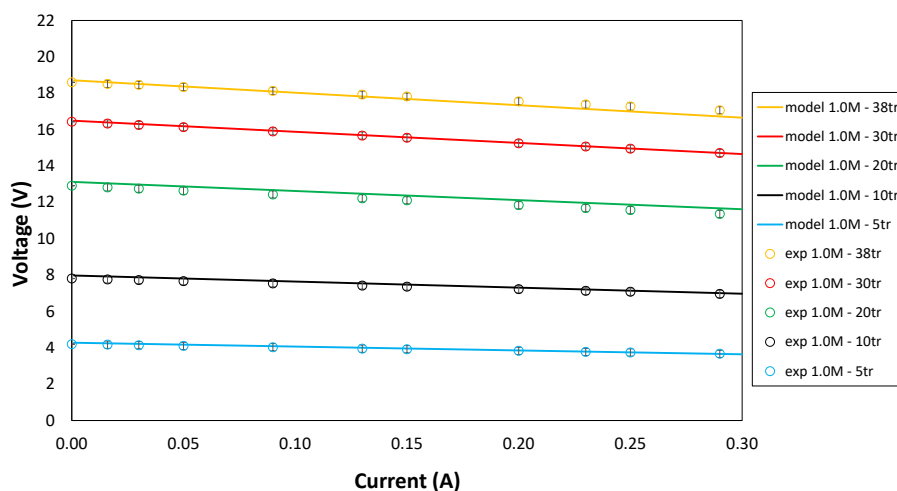


Figure 41. Voltage-current curves by varying the number of triplets, in $10 \times 10 \text{ cm}^2$ stacks with Fumatech membranes (FAB, FKB, FBP) and with spacers provided with 3 inlet/outlet holes (diameter of 8 mm). Mean flow velocity of the electrolyte solutions in each channel equal to 1 cm s^{-1} . Symbols refer to experimental data, continuous lines to the model predictions. Inlet concentrations: 1 M HCl and NaOH in the acid and base channels respectively and 0.25M NaCl in the salt channel. Areal blank resistance: $72 \Omega \text{ cm}^2$.

The empirical data illustrated in Figure 41 has high reliability as the empirical error was $\approx 2.2\%$ on average. As in the two previous graphs, the maximum empirical error found was recorded in the tests with 5 triplets, and the average error was 4.7%. Even employing 1M of acid and base, the model simulations were in fairly good agreement regardless of the number of cells. The overall average discrepancy was $\approx 1.2\%$, with a minimum of 0.17% for the case with 30 triplets. The maximum discrepancy was obtained for the experiments conducted at 20 triplets, where the average error was 2.2%. The experiments conducted at 1 M had the best fit with the model predictions. For the stack equipped with 38 triplets, the maximum model error was $\approx 0.9\%$.

The next results concern the set of experiments conducted with the presence of background salt in the acid and base compartments.

Figure 42 shows the polarization curves for the 0.2 M cases with the presence of background salt.

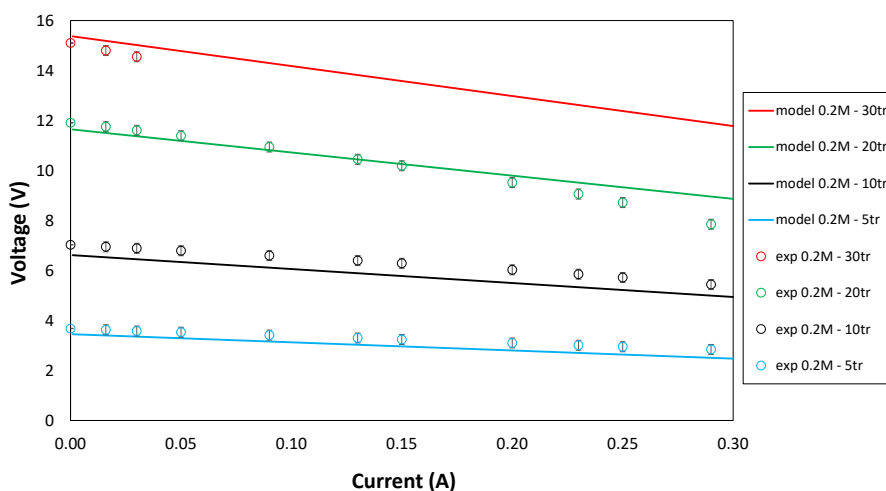


Figure 42. Voltage-current curves by varying the number of triplets, in $10 \times 10 \text{ cm}^2$ stacks with Fumatech membranes (FAB, FKB, FBP) and with spacers provided with 3 inlet/outlet holes (diameter of 8 mm). Mean flow velocity of the electrolyte solutions in each channel equal to 1 cm s^{-1} . Symbols refer to experimental data, continuous lines to the model predictions. Inlet concentrations: 0.2M HCl and NaOH in the acid and base channels respectively with the presence of salt background and 0.25M NaCl in the salt channel. Areal blank resistance: $72 \Omega \text{ cm}^2$.

The experimental data present high repeatability since the reported average deviation with the test-retest process was $\approx 3\%$. The maximum empirical deviation was recorded with the 5-triplet experiments, where the average error of the curve was 5.6%. The model simulations were in good agreement even when varying the number of triplets. Particularly, the overall average variation was $\approx 5.8\%$. The discrepancy ranged from a minimum of 3.2% for the experiments conducted at 30 triplets, to a maximum deviation recorded for the experiments performed at 5 triplets, where an average relative error of $\approx 8.6\%$ was found. The experiments performed at 30 triplets were stopped at a current density of 3 A m^{-2} , because the stack voltages fell at higher current densities. This was attributed to the accumulation of salt inside the BPM interlayer which, in turn, negatively influenced the stack voltage.

Figure 43 illustrates the polarization results obtained in the case of 0.6 M tests with the presence of background salt.

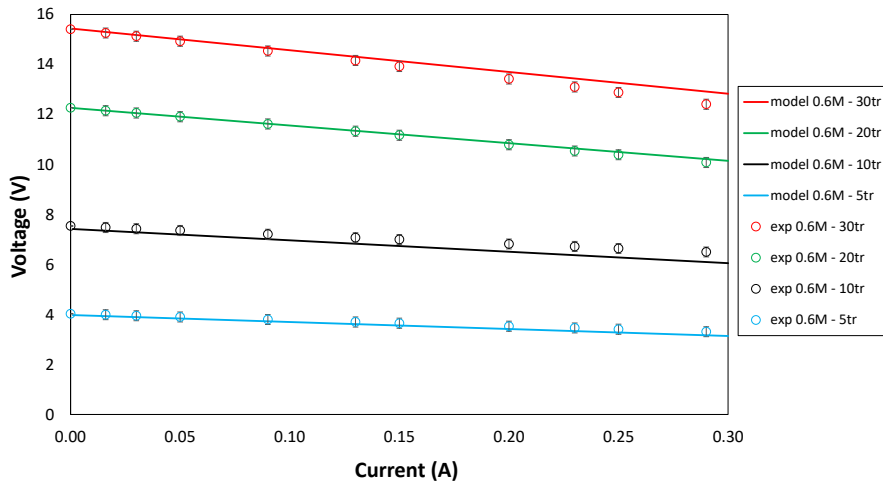


Figure 43. Voltage-current curves by varying the number of triplets, in $10 \times 10 \text{ cm}^2$ stacks with Fumatech membranes (FAB, FKB, FBP) and with spacers provided with 3 inlet/outlet holes (diameter of 8 mm). Mean flow velocity of the electrolyte solutions in each channel equal to 1 cm s^{-1} . Symbols refer to experimental data, continuous lines to the model predictions. Inlet concentrations: 0.6M HCl and NaOH in the acid and base channels respectively with the presence of salt background and 0.25M NaCl in the salt channel. Areal blank resistance: $72 \Omega \text{ cm}^2$.

Figure 43 showed high repeatability as the average empirical error was $\approx 2.6\%$. The maximum experimental deviation was found to be $\approx 5\%$ for the 5-triplet tests. The model results are in a fairly good agreement with the experimental behaviour when varying the number of triplets in the stack, as there was a discrepancy of 2.1% on average. A minimum discrepancy of 0.5% was recorded for the experiments conducted at 20 triplets, and the maximum discrepancy was obtained for the cases conducted at 10 triplets, with an average discrepancy of $\approx 3.7\%$. Moreover, the experiments showed high model accuracy both at low and high number of triplets. Interestingly, for a stack provided with 30 triplets, the average relative error was 1.6%, thus confirming the applicability of this model across a wide range of sizes.

Figure 44 shows the polarization curves obtained for the experiments conducted at 1 M with the presence of background salt, and across stacks with varying numbers of triplets.

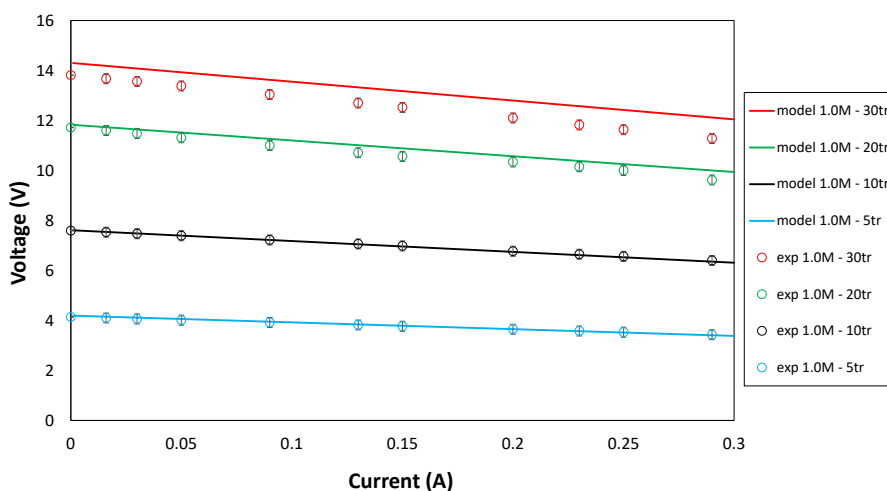


Figure 44. Voltage-current curves by varying the number of triplets, in $10 \times 10 \text{ cm}^2$ stacks with Fumatech membranes (FAB, FKB, FBP) and with spacers provided with 3 inlet/outlet holes (diameter of 8 mm). Mean flow velocity of the electrolyte solutions in each channel equal to 1 cm s^{-1} . Symbols refer to experimental data, continuous lines to the model predictions. Inlet concentrations: 1 M HCl and NaOH in the acid and base channels respectively with the presence of salt background and 0.25M NaCl in the salt channel. Areal blank resistance: $72 \Omega \text{ cm}^2$.

The experimental data reported in Figure 44 show high reliability since the test-retest process reported an average empirical error of $\approx 2.7\%$. Again, the maximum empirical error was recorded for the 5-triplet tests, with the average error standing at 4.8%. The average model discrepancy was found to be 2.1%; a minimum of 0.3% was recorded for the experiments conducted at 10 triplets, and the maximum discrepancy was obtained for the cases at 30 triplets, which are characterized by an average discrepancy of 5.2%.

Overall, the above results show the validity of the developed model for the prediction of the polarization curves of BMRED systems at different number of repetitive units, across a wide range of acid and base concentrations (i.e. 0.2-1M), and with or without the effect of the background salt in the acid and base compartments.

The comparison between model predictions and experimental data was also made in terms of the outlet ion-concentrations. The tests were performed by using a variable number of triplets within the range of 10-38, at a fixed mean channel flow velocity of 1 cm s^{-1} , and without the presence of NaCl as salt background in the acid and base channels. A fixed current density equal to 29 A m^{-2} was used for all the experiments.

The inlet composition and concentrations are reported in Table 6. Titration and chromatography were repeated at least one time, finding negligible errors.

Table 6. Summary with the used inlet concentrations in 10×10 cm² stacks with Fumatech membranes (FAB, FKB, FBP) and with spacers provided with 3 inlet/outlet holes (diameter of 8 mm). Mean flow velocity of the electrolyte solutions in each channel equal to 1 cm s⁻¹.

| Test | $C_{t,HCl,a,out}$ | $C_{t,NaOH,b,out}$ | $C_{t,NaCl,s,out}$ |
|------|------------------------|------------------------|------------------------|
| (-) | (mol m ⁻³) | (mol m ⁻³) | (mol m ⁻³) |
| 1 | 200 | 198 | 260 |
| 2 | 627 | 577 | 273 |
| 3 | 1032 | 998 | 284 |
| 4 | 212 | 193 | 268 |
| 5 | 622 | 671 | 276 |
| 6 | 1045 | 1165 | 287 |
| 7 | 199 | 183 | 245 |
| 8 | 600 | 555 | 257 |
| 9 | 1000 | 952 | 263 |

Model outcome and experimental results are compared in Figure 45.

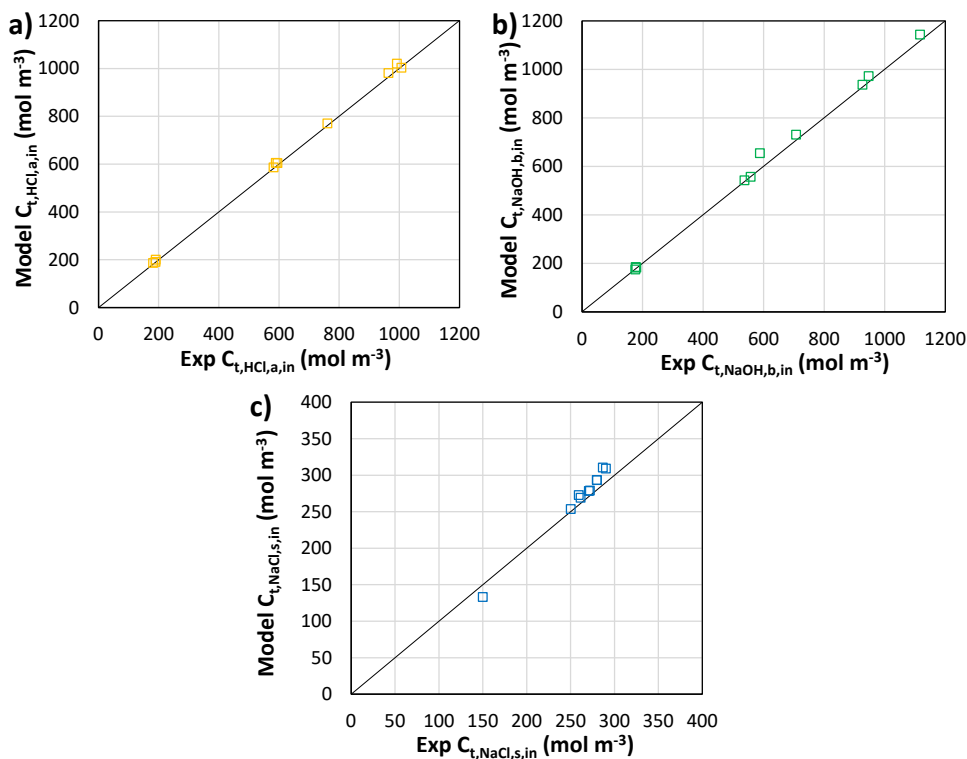


Figure 45. Parity plots for the comparison of model outcome and experimental results for the concentration values at the stack outlet (i.e. downstream tank inlet) of BMRED tests with single-pass: a) Outlet HCl concentration in the acid tank, b) Outlet NaOH concentration in the base tank and c) Outlet NaCl concentration in the salt tank.

Figure 45 suggests that, apart from a few isolated cases, the ion concentrations were well-predicted at the outlet of the acid, base and salt compartments. The average error in absolute terms was 3.2%, and was distributed as follows (Table 7),

Table 7. Average model discrepancy of the HCl, NaOH and NaCl outlet concentrations for each compartment for the BMRED process.

| | HCl - Acid | NaOH - Base | NaCl - Salt |
|---------------|------------|-------------|-------------|
| Average error | 2.0% | 2.6% | 5.0% |

These model-experiments deviations fall within the potential range of experimental/operator errors.

4.6.2 Energy density and prospective Cost analysis

An estimation of the experimental gross energy density GED_v (kWh m^{-3}) achievable from a complete neutralisation of the acid and base solutions was performed. The BMRED model was used to simulate a multi-stage process with complete neutralisation and make a further comparison with the experimental result for validation purposes. Particularly, the experimental GED_v was evaluated from once-through steady-state experiments at different inlet concentrations, mimicking some sequential stages (Figure 46). It was calculated as reported in Eq. 116.

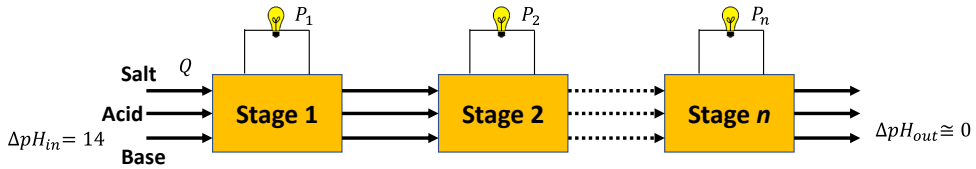


Figure 46. Schematic representation of the multi-stage process analysed for the estimation of the Gross Energy Density.

$$GED_v = \frac{N_s \bar{P}}{Q \times 3.6 \times 10^6} \quad (116)$$

where N_s is the number of sequential stages, Q is the total acid flow rate (in $\text{m}^3 \text{s}^{-1}$) and \bar{P} is the average gross power calculated as follows:

$$\bar{P} = \frac{\int_{C_{HCl,in}}^{C_{HCl,fin}} P dC_{HCl}}{C_{HCl,in} - C_{HCl,fin}} \quad (117)$$

where P is the gross power, $C_{HCl,in}$ and $C_{HCl,fin}$ are the initial (inlet of stage 1) and final (outlet from stage N_s) hydrochloric acid concentration achieved in the whole neutralization process, respectively.

In particular, P was experimentally measured at different inlet concentrations, and thus at different inlet-outlet average concentrations (estimated by titration). The trend of the produced power as a function of the average concentration was experimentally obtained, either with or without the presence of background salt in the acid and base channels, and can be expressed with the following equation:

$$P = p_1 C_{HCl}^2 + p_2 C_{HCl} + p_3 \quad (118)$$

where p_1 , p_2 and p_3 are the regression coefficients listed in Table 8.

The number of stages N_s is given by

$$N_s = \frac{C_{HCl,in} - C_{HCl,fin}}{\Delta C_{in-out}} \quad (119)$$

where ΔC_{in-out} is the inlet-outlet mean concentration difference observed in a single passage during the experiments, reported in Table 8.

Table 8. List of the *P* regression coefficients and inlet-outlet mean concentration differences.

| Case | <i>i</i> (A m ⁻²) | $\Delta C_{inl-out}$ | | p₁ | p₂ | p₃ |
|------|-------------------------------|----------------------|--------------|----------------------|----------------------|----------------------|
| A | 29 | 0.02 M | With salt | -1.01 | 1.76 | 1.11 |
| B | 29 | 0.017 M | Without salt | 0 | 0.50 | 1.51 |
| C | 100 | 0.022 M | Without salt | -3.00 | 6.25 | 1.96 |

The experiments considered for the calculation of the GED_v regard a 10 cm long stack provided with 10 triplets, fed at a fluid velocity of 1 cm s⁻¹ with 1 M acid and base initial concentration and with 0.25 M NaCl solution in the salt compartments. Three different cases were analysed: 29 A m⁻² either with (case A) or without (case B) 0.25 M NaCl as background salt concentration in the acid and base channels and 100 A m⁻² without NaCl as salt background (case C).

The comparison between the experimental results obtained under these conditions and the relative model outcome are summarized in Table 9.

Table 9. Comparison between experimental data and model outcome for GED and BMRED efficiency for the three cases A, B and C.

| Case | GED (kWh m ⁻³) | | η_{BMRED} | |
|------|----------------------------|-------|----------------|-------|
| | exp | model | exp | model |
| 1 | 5.79 | 6.09 | 24% | 25% |
| 2 | 4.60 | 3.95 | 19% | 16% |
| 3 | 10.3 | 8.74 | 43% | 36% |

Interestingly, the model prediction of GED is in good agreement with the estimation made from empirical data either with or without the presence of salt in the acid and base streams and by varying the current density. The maximum discrepancy is of 15%. This difference may be reduced with a more rigorous experimental evaluation, for example by considering the actual concentration difference by varying the average concentration for each stage and with a more reliable gross

power function by varying the acid/base concentration from 1 M to the complete discharge.

At a current density equal to 29 A m^{-2} the efficiencies were in line with the model prediction. The presence of the background salt decreases the efficiency. This phenomenon is observed both experimentally and by the model simulations. This is mainly due to the reduction of the membrane selectivity, as predicted by the model. It is worth noting that the electrical efficiency, calculated as the power delivered to the external load divided by the total (internal and external) dissipated power [110] was higher than 50% (which, instead, would occur at the maximum GPD) at 29 A m^{-2} due to the relatively closeness to the open circuit condition. On the other hand, at 100 A m^{-2} the working point was relatively close to the maximum power density, thus resulting in a lower electrical efficiency, about 50%. It is clear that these experiments were performed with a test-rig unit which is not optimized to be used in the industry. Improvements in the components (mainly membranes) and the optimization of stack design and operating conditions can lead to better performance and must converge towards the best compromise between GPD and GED, which is eventually governed by economic aspects (maximum profit). By way of example, proper geometrical choices may cut down the parasitic currents, or high-performance membranes may reduce the internal losses associated to co-ion leakages and to the electrical resistance. Note that the above estimations do not take into account pressure losses.

A perspective cost analysis was performed in order to evaluate the profitability of the energy recovery by BMRED. The present experimental results at 100 A m^{-2} were used for the economic calculations. The used parameters and the results of the cost analysis are reported in Table 10. It can be observed that the Levelized Cost Of Electricity (LCOE) [154] is 0.09 € kWh^{-1} in the scenario considered here. Thanks to the low cost of membranes considered for a future-based perspective (one order of magnitude lower than the current cost), especially for the BPMs, the process economics is satisfactory. Note that, however, this cost analysis was performed with the present experimental results, which are far from being optimal. Several improvements could enhance significantly the BMRED performance and thus the process profit, such as high-performance membranes, optimized stacks and operating conditions. Moreover, the use of more concentrated solutions could boost the recovered energy. For example, an increase of 50% in the GPD (from 13.7 to 20.6 W m^{-2}), which can be expected in suitably designed stacks, would result in a LCOE of 0.06 € kWh^{-1} . Furthermore, another important source of income may be a partial saving in the costs of treatment of solutions already neutralized by BMRED (instead of the complete treatment of acid and alkaline solutions). Therefore, practical

Bipolar Membrane Reverse Electrodialysis

applications of the BMRED technology could be prospected in the future, provided that the current bottleneck given by the membrane cost is overcome.

Table 10. Perspective economic analysis of the BMRED process.

| Items | Value | Notes |
|--------------------------------------|--|---|
| BMRED system | | |
| Fluid velocity | 1 cm s ⁻¹ | |
| Membrane area | 0.1 × 0.1 m ² | |
| Channel thickness | 500 μm | |
| Number of triplets per stage | 10 | |
| Number of stages | 45 | |
| GED (average GPD) | 10.3 kWh m ⁻³ (13.7 W m ⁻²) | |
| Working hours | 8000 h y ⁻¹ | It corresponds to a capacity factor of ~90% [154] |
| Membrane life-time | 3 y | |
| Investment and operating cost | | |
| AEM/CEM cost | EUR 4 m ⁻² | [154] |
| BPM cost | EUR 20 m ⁻² | 5 × AEM/CEM cost |
| Total membrane cost | EUR 126 | |
| Cost of stacks (including membranes) | EUR 189 | 1.5 × total membrane cost [146] |
| Cost of peripherals | EUR 95 | 0.5 × stacks cost [146] |
| Capital cost | EUR 284 | Stacks + peripheral costs [146] |
| Maintenance | EUR 28.4 y ⁻¹ | 0.1 × capital cost [146] |
| Economic parameters | | |
| Discount rate | 5% | [154] |
| Outcome | | |
| LCOE | EUR 0.09 kWh ⁻¹ | |

4.7 Performance analysis of BMRED in different scenarios

In this section, the BMRED potential was investigated. In particular, the process with the neutralization of hydrochloric acid and sodium hydroxide solutions was studied. The simulations were performed with stacks provided with 50 triplets. Two

different scenarios were investigated: i) a reference case with input parameters shown in Table 11 and ii) an improved case with better membrane performance.

Table 11. Inputs of the multi-scale model for the simulations of BMRED units.

| Geometrical features | | | | | |
|-------------------------------------|--|---------|---------|---------|---------|
| Spacer length | cm | 50 | | | |
| Spacer width | cm | 50 | | | |
| Spacer thickness | μm | 500 | | | |
| Number of triplets | - | 50 | | | |
| N° spacer holes | - | 3 | | | |
| Spacer hole area | cm^2 | 4 | | | |
| Membrane properties | | | | | |
| | | AEM | CEM | AEL | CEL |
| Thickness | μm | 75 | 75 | 60 | 60 |
| H+ diffusivity | $\text{m}^2 \text{s}^{-1}$ | 2.0E-11 | 0.7E-11 | 2.0E-11 | 0.7E-11 |
| Na+ diffusivity | $\text{m}^2 \text{s}^{-1}$ | 1.6E-11 | 0.5E-11 | 1.6E-11 | 0.5E-11 |
| Cl- diffusivity | $\text{m}^2 \text{s}^{-1}$ | 1.7E-11 | 0.6E-11 | 1.7E-11 | 0.6E-11 |
| OH- diffusivity | $\text{m}^2 \text{s}^{-1}$ | 1.9E-11 | 0.6E-11 | 1.9E-11 | 0.6E-11 |
| Water permeability | $\text{ml bar}^{-1} \text{h}^{-1} \text{m}^{-2}$ | 8 | 8 | - | - |
| Fixed charge group | mol m^{-3} | 5000 | 5000 | 5000 | 5000 |
| Initial conditions of the solutions | | | | | |
| $C_{t,NaCl,a,out}$ | mol m^{-3} | 250 | | | |
| $C_{t,HCl,s,out}$ | mol m^{-3} | 10 | | | |
| $C_{t,NaCl,b,out}$ | mol m^{-3} | 250 | | | |
| R_{bl} | $\Omega \text{ cm}^2$ | 72 | | | |

The improved scenario differs in the membrane properties shown in Table 12.

Table 12. List of the membrane properties for the improved membrane properties scenario.

| Improved membrane properties | |
|------------------------------|----------------------------|
| Electrical resistance | Current value (Table 11)/4 |
| Ion diffusivities | Current value (Table 11)/2 |
| Water permeability | Current value (Table 11)/2 |

Current density, mean channel flow velocity, inlet acid/base and salt concentrations were allowed to vary within a wide range of values.

4.7.1 Sensitivity on current density

Current density analysis was performed with the mean flow velocity fixed at 1 cm s^{-1} , the inlet HCl and NaOH concentrations equal to 1 M (with the presence of salt background), and the NaCl inlet concentration to 0.25 M . The current density was varied within the range of $50\text{-}200 \text{ A m}^{-2}$.

Figure 47 shows the Gross Power Density as a function of the external current density for the two scenarios.

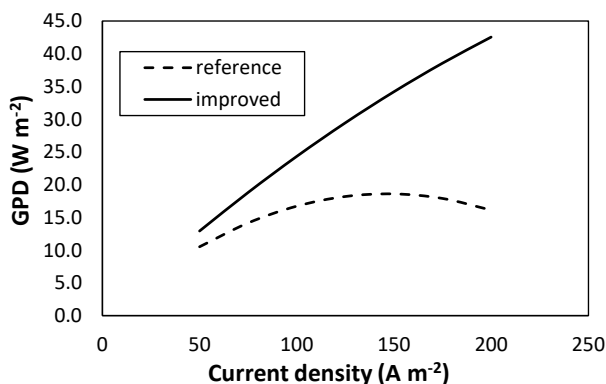


Figure 47. Gross Power Density as a function of the current density for the reference and improved scenarios with a fixed mean flow velocity of 1 cm s^{-1} , an inlet acid/base concentration of 1 M and an inlet salt concentration of 0.25 M .

The GPD increases in the improved scenario due to the lower internal resistance. The GPD values range from a minimum of 10.5 W m^{-2} for the reference case, to a maximum of 42.6 W m^{-2} for the improved case. It is interesting to note that the reference case reaches the power peak at $\approx 140 \text{ A m}^{-2}$, while in the improved case the power peak falls at a higher current density (i.e. out of the investigated range of currents). Therefore, the improved case may reach even higher power values, provided that BPMs are able to tolerate very high current densities without delamination issues. At the peak point of the reference case, the GPD is $\approx 60\%$ lower than the one reached at the same current density by the improved case.

The operating current density affects also the Gross Energy Density per unit mass, which is reported in Figure 48 for the two studied scenarios.

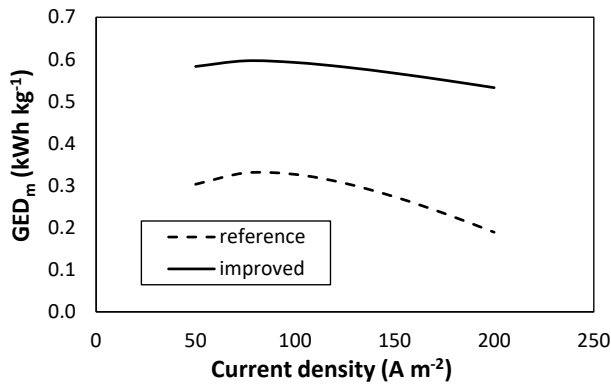


Figure 48. Gross Energy Density per unit mass as a function of the current density for the reference and improved scenarios with a fixed mean flow velocity of 1 cm s^{-1} , an inlet acid/base concentration of 1 M and an inlet salt concentration of 0.25 M .

Both the improved and reference scenarios show a maximum GED_m value around 75 and 80 A m^{-2} , respectively. Large differences were found in the GED_m values between the two scenarios of membrane properties over the whole range of simulated current densities. Particularly, the average GED_m difference resulted to be 0.29 kWh kg^{-1} . The improved GED_m was found to be ≈ 2.1 times higher than the reference GED_m .

Figure 49 shows the conversion rate as a function of the current density for the two scenarios.

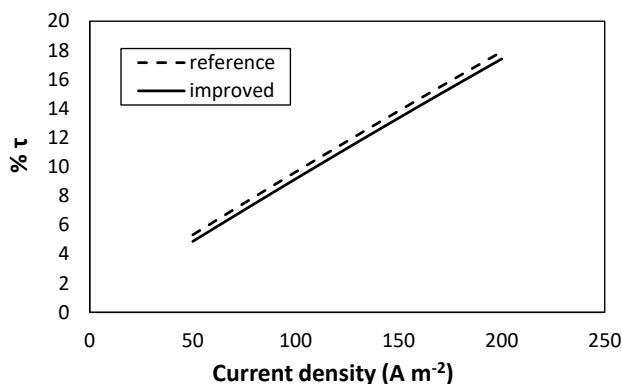


Figure 49. Conversion rate as a function of the current density for the reference and improved scenarios (i.e. τ reference, τ improved) with a fixed mean flow velocity of 1 cm s^{-1} , an inlet acid/base concentration of 1 M and an inlet salt concentration of 0.25 M .

There were no appreciable differences in conversion rates across the investigated range of current densities. For both scenarios, τ ranges from $\sim 4.9\%$ to $\sim 18\%$. The small decrease of conversion rate in the improved case (4.7% in relative terms) is due to the lower diffusive fluxes. Moreover, it is worth noting that the outlet solutions have high acid and base content. Therefore, in the once-through mode, and with the investigated operating conditions, the energy recovered from the pH gradient is still low.

Finally, Figure 50 illustrates the current efficiency as a function of the current density for the two scenarios with different membrane features.

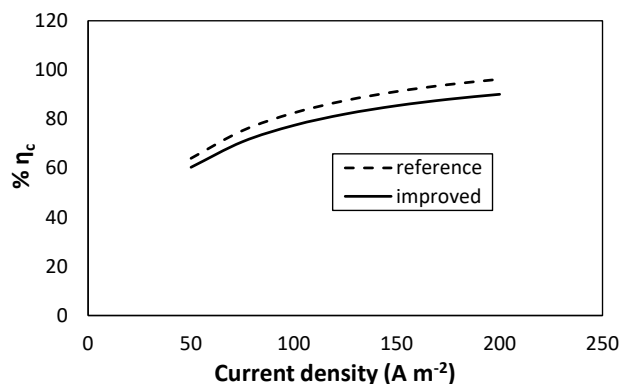


Figure 50. Current efficiency as a function of the current density for the reference and improved scenarios (with a fixed mean flow velocity of 1 cm s^{-1} , an inlet acid/base concentration of 1 M and an inlet salt concentration of 0.25 M).

The current efficiency is higher in the reference scenario and increases as the current density increases. From 50 to 200 A m^{-2} , the current efficiency increases by $\approx 50\%$ for both scenarios. In the improved case, the reduction of the current efficiency is due to the increase in the average cell current which, in turn, leads to a faster reduction of the pH gradient.

4.7.2 Sensitivity on mean channel flow velocity

The effect of the mean flow velocity was analysed by fixing the current density at 100 A m^{-2} , the inlet HCl and NaOH concentrations equal to 1 M in the acid and base channels, respectively, and the NaCl inlet concentration in the salt channel to 0.25 M. Mean flow velocity was varied within the interval $0.5\text{-}5 \text{ cm s}^{-1}$.

Figure 51 reports the Gross and Net power densities when varying the mean channel flow velocity for the reference and the improved scenarios.

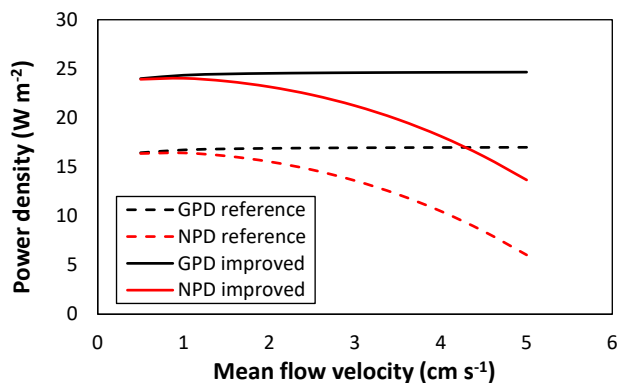


Figure 51. GPD (black lines) and NPD (red lines) as a function of the mean flow velocity for the reference and improved scenarios with a fixed current density of 100 A m^{-2} , an inlet acid/base concentration of 1M and an inlet salt concentration of 0.25 M.

No important differences in GPD were shown when varying the mean flow velocity for both the reference and improved scenarios. The average GPD were 16.9 and 24.5 W m^{-2} for the reference and improved scenarios, respectively. The small increase in GPD at higher velocities is due to the higher average electromotive force. Instead, significant differences can be observed for the NPD. Particularly, by increasing the mean flow velocity from 0.5 to 5 cm s^{-1} , NPD decreased by $\approx 63\%$ and $\approx 43\%$ for the reference and improved cases, respectively. The different relative effect of the mean flow velocity on the NPD in the two scenarios is caused by the fact that the Pumping Power Density (function of the mean flow velocity) was practically the same.

No appreciable effects of the fluid velocity on the GED_m were observed. The average values were 0.38 and 0.60 kWh kg^{-1} for the reference and the improved scenarios respectively.

Figure 52 shows the conversion rate as a function of the mean channel flow velocity for the reference and improved scenarios.

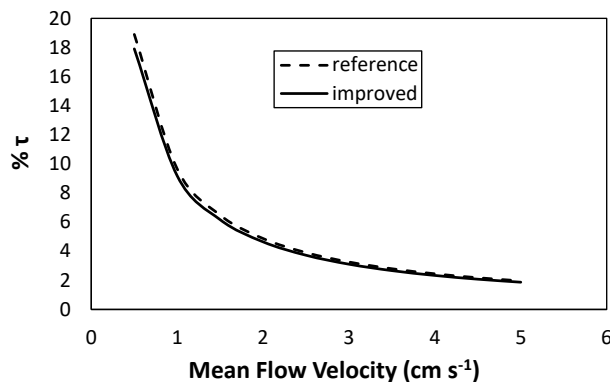


Figure 52. Conversion rate as a function of the mean flow velocity for the reference and improved scenarios with a fixed current density of 100 A m^{-2} , an inlet acid/base concentration of 1 M and an inlet salt concentration of 0.25 M .

The higher the mean flow velocity, the lower the conversion rate, as expected. Particularly, from 0.5 cm s^{-1} to 5 cm s^{-1} , the conversion rate was found to be ≈ 1 order of magnitude lower as result of the higher outlet acid (and base) concentrations. Moreover, only a slight difference was found between the two scenarios (i.e. an average relative difference of 4.7%), which is caused by the higher ion diffusion in the reference case.

The current efficiencies were found to be practically constant when varying the mean flow velocity. Specifically, the current efficiencies were 82 and 77% for the reference and improved cases respectively.

4.7.3 Sensitivity on inlet acid/base concentrations

The effect of the inlet acid/base concentration was assessed by fixing the current density at 100 A m^{-2} , the mean channel flow velocity at 1 cm s^{-1} , and the NaCl inlet concentration at 0.25 M . The inlet acid/base concentrations were varied within the range $0.2\text{--}1 \text{ M}$.

Figure 53 shows the GPD by varying the acid/base inlet concentrations for the reference and improved scenarios.

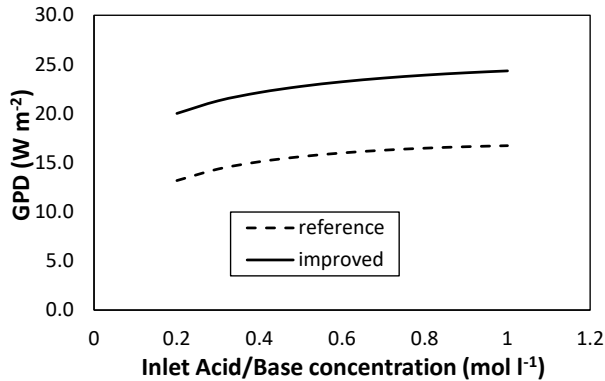


Figure 53. GPD as a function of the inlet acid/base concentration for the reference and improved scenarios with a fixed current density of 100 A m^{-2} , a mean flow velocity of 1 cm s^{-1} and an inlet salt concentration of 0.25 M .

The GPD shows an increasing trend towards a maximum, ranging from 13.2 to 16.7 W m^{-2} and from 20.0 to 24.3 W m^{-2} for the reference and improved scenarios, respectively. The increasing values can be explained simply by the higher electromotive force when raising the acid/base concentration. When applying Eq. 47, the electromotive force in fact increases as the acid/base concentration increases, moving from 35.5 V to 42.1 V . The average relative difference of 46.5% in the GPD between the reference and the improved scenario is a direct consequence of the reduced membrane electrical resistances.

Figure 54 illustrates the results obtained for the Gross Energy Density per unit mass by varying the inlet acid/base concentration for the reference and improved scenarios.

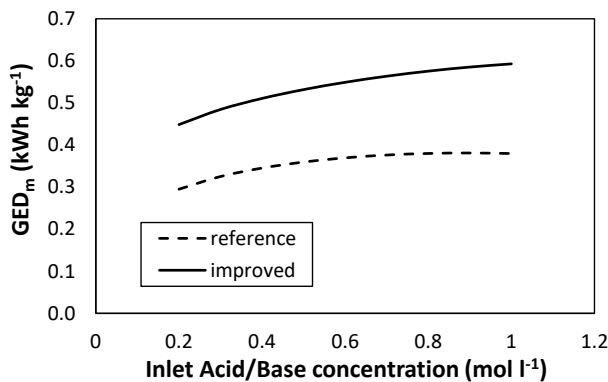


Figure 54. GED_m as a function of the inlet acid/base concentration for the reference and improved scenarios with a fixed current density of 100 A m^{-2} , a mean flow velocity of 1 cm s^{-1} and an inlet salt concentration of 0.25 M .

Figure 54 shows that the GED_m curves exhibit increasing values that tend to flatten in the upper range of acid/base concentrations. Overall, from 0.2 M to 1 M of acid/base, the GED_m varies by 28.8 and 32.2% for the reference and the improved cases respectively.

Figure 55 shows the conversion rate curve as a function of the inlet acid/base concentration for the investigated scenarios.

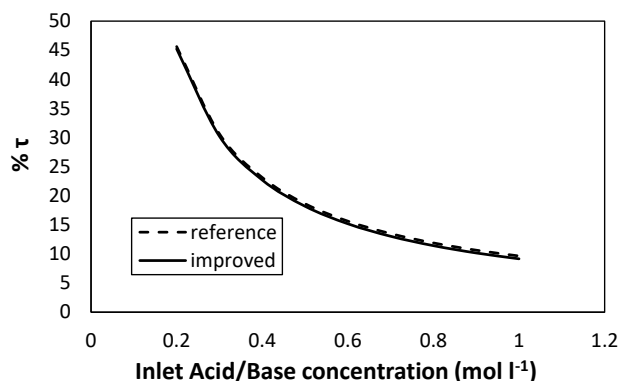


Figure 55. Conversion rate as a function of the inlet acid/base concentration for the reference and improved scenarios with a fixed current density of 100 A m^{-2} , a mean flow velocity of 1 cm s^{-1} and an inlet salt concentration of 0.25 M .

Conversion rate values differ by less than 3% on average in the two different scenarios. The pronounced decreasing trend is a consequence of the inverse relationship between conversion rate and inlet acid concentration. The ion diffusion could soften this behaviour; however, the negligible differences between the two scenarios indicate negligible effects of ion diffusion.

Figure 56 illustrates the current efficiency values as a function of the inlet acid/base concentration for the two scenarios.

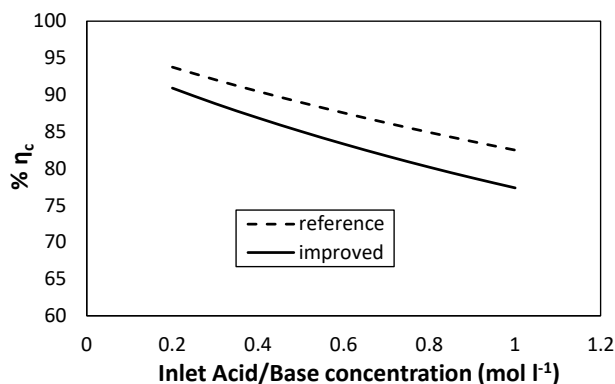


Figure 56. Current efficiency as a function of the inlet acid/base concentration for the reference and improved scenarios with a fixed current density at 100 A m^{-2} , a fixed mean flow velocity of 1 cm s^{-1} and an inlet salt concentration of 0.25 M .

By increasing the acid/base concentration within the investigated range, the current efficiency decreases, losing 11.3 and 15.3 percentage points for the reference and improved cases respectively. The reduction of the current efficiency explains the decreasing rate of increase of energy density per unit mass of transported acid shown in Figure 54.

4.7.4 Sensitivity on inlet salt concentration

The effect of the inlet salt concentration was performed by fixing the current density at 100 A m^{-2} , the mean channel flow velocity at 1 cm s^{-1} , and the HCl and NaOH inlet concentrations at 1 M . The inlet salt concentration was varied within the range $0.1\text{-}1 \text{ M}$.

No important variations were recorded when varying the salt inlet concentrations for the main figures of merit, thus only averaged values are reported in Table 13 for both membrane properties scenarios.

Table 13. Main results of the sensitivity on inlet salt concentrations, with a fixed current density at 100 A m^{-2} , a fixed mean flow velocity of 1 cm s^{-1} and inlet acid and base concentration of 1 M .

| | Reference scenario | Improved scenario |
|---|--------------------|-------------------|
| GPD (W m^{-2}) | 16.4 | 24.0 |
| GED _m (kWh kg^{-1}) | 0.38 | 0.59 |

Bipolar Membrane Reverse Electrodialysis

| | | |
|------------|------|------|
| % τ | 9.0 | 8.6 |
| % η_c | 82.8 | 77.6 |

Compared to the reference case, the improved case reported lower values for the conversion rate and current efficiency, contrary to expectations. In fact, in the improved case, there is an increase in the average cell current, which causes a decrease in the acid and base outlet concentrations. This fact can be attributed to the non-linear trend of the parasitic currents as a function of the internal resistance. However, further simulations will be performed to assess the impact of the internal resistance on stack performance.

4.8 Example of an industrial BMRED scheme for energy recovery from waste streams

In this section, a possible scheme for industrial application of energy recovery via BMRED from waste streams is designed. The neutralization of waste acid and base solutions from the pickling and the manufacturing industries was considered. HCl and NaOH waste solutions were simulated with the presence of background salt. It is well known that exhausted solutions from pickling operations range from 20 to 150 g l⁻¹ [185]. Spent caustic soda solutions may present a concentration of around 4% weight [193]. Usually, these waste products are neutralized and disposed of at high costs [187]. An innovative use of these waste products comes from the production of electrical energy with BMRED. The present simulations assessed the energetic yield of a multi-stage process. Energy density and process efficiency were evaluated following the approach formulated in section 4.6.2, with the stack features shown for the improved scenario in the previous section (Table 11 and Table 12). Particularly, the acid, base and salt solution composition and concentrations are reported in Table 14.

Table 14. Initial composition and concentrations – example of industrial BMRED scheme

| Inlet composition and concentrations | | |
|--------------------------------------|---------------------|------|
| $C_{t,HCl,a,out}$ | mol m ⁻³ | 2700 |
| $C_{t,NaCl,a,out}$ | mol m ⁻³ | 250 |
| $C_{t,HCl,s,out}$ | mol m ⁻³ | 10 |
| $C_{t,NaCl,s,out}$ | mol m ⁻³ | 250 |

| | | |
|--------------------|---------------------|-------------|
| $C_{t,NaOH,b,out}$ | mol m ⁻³ | 300 or 1000 |
| $C_{t,NaCl,b,out}$ | mol m ⁻³ | 250 |

Acid and base concentrations were chosen according to the above mentioned literature data. Since the acid and base concentrations are different, a possible process scheme could be a multi-stage system with the acid solution processed sequentially and the base and salt solutions processed singularly (Figure 57). In this way, the outlet concentration of both the acidic solution (from the last stage) and the alkaline solution (from each stage) was close to zero, thus obtaining a high degree of neutralization for both solutions.

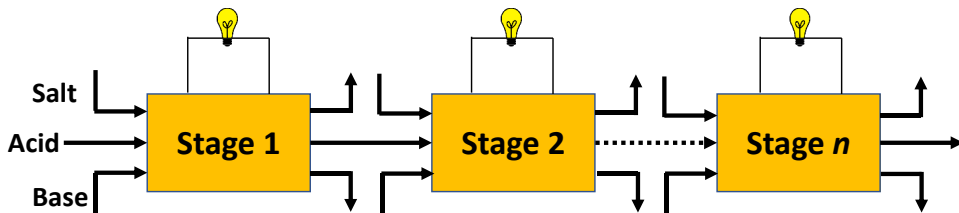


Figure 57. Scheme of the multi-stage BMRED process.

Simulation results showed that 15 BMRED stages were needed for the complete neutralization of the acid solution. The gross energy density was found to be 53.5 and 48.3 kWh m⁻³ of acidic solution in the two cases of 1 M and 0.3 M of inlet concentration of NaOH, respectively. Interestingly, even using a spent sodium hydroxide solution of less than 1.2% weight (i.e. ~0.3M), the energy efficiency was 82%, while by using 1 M of inlet NaOH concentration it reached 91%. Under equal current density, the use of a more concentrated base solution (i.e. 1 M NaOH) causes an increase in the average power per stage. This fact leads to a higher GED_v resulting in a higher energy efficiency.

These interesting preliminary results suggest that neutralizing waste acid/base streams in BMRED units to produce electric power may be a very promising option that should be further investigated to eventually lead its technology development.

5 Ionic shortcut currents in electro-membrane processes

In the last decades, electro-membrane processes have received increasing attention for their versatility of use from the ED production of drinking water to the BMED production of valuable acid and base solutions. Recently, many efforts have been devoted to improving the performance of electro-membrane units by developing new ion-exchange membranes and by reducing the detrimental phenomena affecting the process. Among these sources of “irreversibility”, the shortcut currents (or parasitic currents) flowing through alternative pathways may affect the process efficiency. Although such phenomena occur in several electrochemical processes (e.g. fuel cells, bipolar plate cells and vanadium redox flow batteries), they have received a poor attention in BMRED and BMED units. In this chapter, a mathematical model was developed and experimentally validated under a wide range of conditions. The present model was used then to characterize the shortcut currents impact in conventional RED and ED as well as in BMRED and BMED. Modules performance were assessed under different designs and operating conditions. Results showed that shortcut currents can play a crucial role in stacks with a large number of repetitive units when the electrical resistance of the parasitic pathways is relatively low, e.g. configurations with highly concentrated solutions, high resistance membranes, short channels or large manifolds. This model may aid the future design of industrial-scale units which intrinsically includes several repetitive units (i.e. triplets for BMRED/BMED or cell pairs for RED/ED). This should lead to a significant increase of these large scale stacks performance.

5.1 Literature review and working principle

Recently, many efforts have been devoted to improving the performance of electro-membrane units, by developing new ion-exchange membranes and by reducing the detrimental phenomena affecting the process. By way of example, electro-membrane processes are affected by sources of “irreversibility” as the co-ion transport or the concentration polarization. Among these detrimental phenomena, ionic shortcut currents have received a poor attention in both conventional and bipolar electro dialysis and reverse electro dialysis processes, i.e. ED and BMED, and RED and BMRED respectively.

These ionic currents originate since the repetitive units of a RED/BMRED/ED/BMED module are arranged electrically in series but hydraulically in a parallel fashion. Therefore, channels of the same solution subjected to a voltage difference act as “salt bridges” offering alternative “parasitic” pathways

(Figure 34), through the manifolds especially in the low-resistance concentrate circuits. As a result, a partial transport of the ionic current occurs along the channels and through the manifolds, rather than across the IEMs in the direction perpendicular to them.

The effects of shortcut currents in RED/BMRED/ED/BMED units can be explained with the help of the schematic drawings reported in Figure 58 and Figure 59, respectively. In RED/BMRED, for any given external electric current, which is the useful one delivered to the external load, the occurrence of the shortcut currents in a parallel branch via manifolds leads to an increase of the electric current flowing through the stack in the direction perpendicular to the membranes (Figure 58). This effect occurs also under open circuit conditions, i.e. a completely parasitic internal current flows within the stack with a null external current. From the increase of the internal current it follows that, for any external current, Ohmic and non-Ohmic (salinity and pH gradients consumption and concentration polarization) voltage drops increase. Therefore, the stack voltage and the power delivered to the external load are lower.

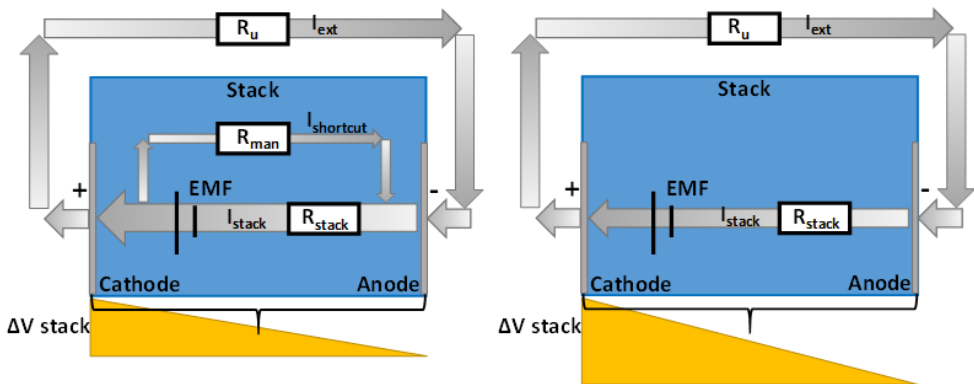


Figure 58. Simplified diagrams of the electric currents flowing inside the stack in a RED/BMRED process. a) with parasitic currents, b) without parasitic currents.

Similar statements can be argued for ED/BMED. For any useful internal current, depending on the desired product, the shunt current in the parallel branch inside the stack requires a higher external current (lower current efficiency) (Figure 59). Since the stack voltage is fixed by the desired generation of salinity or pH gradient and the useful current, a higher power consumption is required.

Of course, much more complex circuits represent real stacks, including several channels and parasitic pathways, the transport of electric current by two ionic species and the presence of non-perfectly permselective membranes. Overall, the presence

of shortcut currents has eventually detrimental effects on the performance of the process, reducing its efficiency.

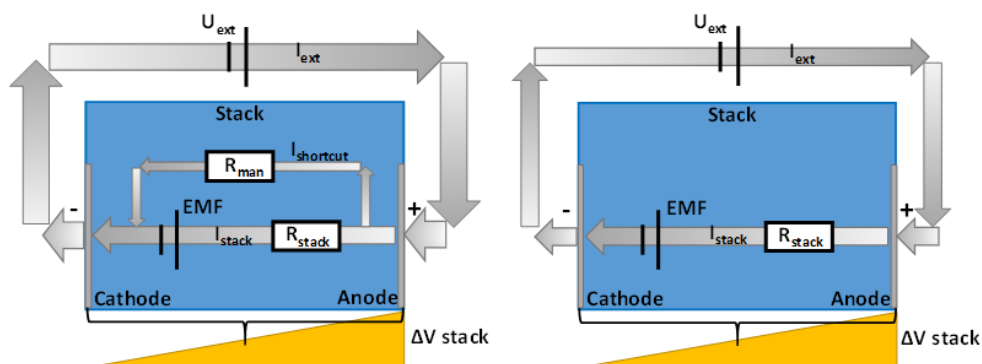


Figure 59. Simplified diagrams of the electric currents flowing inside the stack in an ED/BMED process. a) with parasitic currents, b) without parasitic currents.

There are several experimental evidences of shunt currents and their effects. In RED/BMRED as well as ED/BMED, leakage currents lessen the apparent stack resistance [206]. The parasitic pathways may be thought ideally as parallel electric paths (Figure 58a and Figure 59a), hence they reduce the equivalent stack resistance. In RED, the effect of leakage currents may be observed at open circuit by carrying out measurements of stack potential (OCV). In particular, the OCV is lower than the theoretical one especially in stacks with many cell pairs, i.e. it does not increase proportionally with the cell pairs number [110]. Leakage currents entail the “self-discharge” of the energy stored in the salinity gradient even if the external electric circuit is open, thus lowering the apparent average perm-selectivity [157]. The OCV reduction with respect to the expected value by increasing the number of repetitive units was observed also for the BMRED process. Particularly, Pretz and Staude [180] found that the OCV increased with the number of triplets until reaching a plateau. With a device provided with 20 cells, the OCV resulted to be less than 50% of the theoretical value. They interpreted this phenomenon as the effect of a capacitor-like behaviour of the bipolar membranes. Only recently, the non-proportionality of the stack voltage with the cell triplet number in BMRED units has been explained with the presence of the shunt currents. Xia et al. [183] found a 6% reduction of the OCV with respect to the theoretical one by passing from 1 to 20 repeating cell units in a BMRED system. Likewise RED processes under OCV condition, parasitic currents allow the running of neutralization reactions in BMRED processes thus self-discharging the pH gradient [183]. Particularly, they found that the incidence of self-discharge increases with the number of cell units. The presence of the shunt currents affect the processes also when the external circuit is closed [157] (i.e. when the

electric current flows on the external load), thus reducing the produced power [110]. Another possible electric bypass may be given by the connection of the electrode compartments using a reversible redox couple [207]. However, the tubing length is usually sufficient to give an electrical resistance so high as to make this shunt current negligible. Moreover, shortcut currents may cause an excessive overheating (ED/BMED), with consequent fall of the current efficiency [208], and even irreversible damage. This effect may be more pronounced with lower manifolds electrical resistances [114].

The amount of shunt currents depends on the relative importance of the electrical resistance of the bypasses. In conventional RED/ED processes, whereas leakage currents are hardly detectable at low salt concentration [209], they lead to the variation of the stack potential distribution at higher salt concentrations [210]. Similarly, in BMRED/BMED processes the highly conductive acid and base solutions result in low manifolds resistances, thus influencing dramatically the stack performance [114]. The length of the ionic bypass and their cross sectional area play an important role likewise the conductivity of the electrolyte solutions [210]. In addition, the number of repetitive units is crucial. Particularly, the higher the number of repetitive units, the higher the effect of the shunt currents either in conventional RED/ED [110] and BMRED/BMED [183] due to the larger amount of parasitic pathways and to the larger voltage available. It is interesting to note that, for BMED stacks even using modules provided with 5 repetitive units only, it is possible to detect the effect of parasitic currents [114]. The percentage of the current loss due to parasitic currents increases considerably with the number of repeating units, particularly in BMRED/BMED processes where the electrolyte solutions present low electrical resistances. Moreover, the effect of the shortcut currents changes with the cell position along the stack. Particularly, the effect of the parasitic currents is more pronounced moving towards the middle of the stack, where the cell current results to be the maximum in BMRED [183] (or inversely the minimum in BMED). Furthermore, the ionic current along the manifolds is assumed to be symmetrical along the stack [114]. The isolation of blocks of repetitive units may prevent the leak of currents through the manifolds [211]. The distribution of the solutions into the channels may be performed by rotative valves, hence reducing the parasitic pathways [212]. Moreover, the use of thin plastic film around the inlet/outlet holes of the membranes allows for the electrical insulation of the membrane active area close to the distributors and collectors, thus reducing shunt currents and their impact [208].

Typical ED/RED applications where stacks have low-resistance paths through the concentrate circuit and, thus, may be affected by significant shunt currents, are: ED of seawater, e.g. for salt production [56,206,210,211,213], ED metathesis [208],

RED with seawater [110,207], or concentrated brines [151,154,155,157,161], including closed-loop systems [214,215], and ED/RED with bipolar membranes [216].

Moreover, it is worth noting that the importance of such parasitic phenomenon has been widely studied in other technologies, including fuel cells [217,218], bipolar plate cells [219], and the vanadium redox flow batteries [220].

5.2 *Modelling of the shortcut currents: state of the art*

Despite their detrimental effects on the process efficiency, shunt currents have been explicitly modelled only in very few works. With reference to ED systems, Mandersloot and Hicks [206] gave a simplified equation of the fraction of the electrical leakage, highlighting the role of the ratio between the manifolds and the cell pair electric resistances. Similarly, Doležel and Keslerová [210] provided an expression of the leakage current putting the emphasis on the role of the ratio between the solutions and the membrane conductivities. Tanaka [56] developed a model following a purely Ohmic approach, based on the equivalent electric circuit formulated by Wilson [221]. Peng and Sun [114] elaborated a simplified ohmic model of the equivalent electric circuit for BMED processes and it was solved on Multisim®. They do not provide any equation of the model.

Regarding RED/BMRED systems, Rubinstein et al. [216] developed a mathematical model to simulate a simplified electric circuit scheme. In particular, the model predicted the “saturation” effect of the leakage currents on the OCV as the number of cell pairs increased in stacks with bipolar membranes.

A similar mathematical model was formulated by Veerman et al. [110], who included also the branch of the resistances of the electrode compartments and of the external load in the equivalent electric scheme. However, this model followed still a simplified approach, simulating the drain branches of the concentrate solution only. The model predictions showed that leakage currents lead to a reduction of the stack potential and to a loss of electric power over the external load, thereby decreasing the process efficiency. Simulation results were useful to describe the shortcut currents phenomena and to quantify their impact on the process performance. However, the model was not “fully predictive”, being limited to the simulation of systems experimentally tested for the calibration.

In the work of Tedesco et al. [151], the shortcut currents were modelled within a comprehensive multi-scale process simulator with higher predictive capabilities, where salt and water fluxes, along with mass balances, were simulated at the cell pair scale, while the electrical behaviour of the stack was simulated by an equivalent

circuit of the entire unit. The two levels of modelling interact each other, providing a powerful simulation tool, which does not require any calibration, but only easily measurable membrane properties (electrical resistance, perm-selectivity, water and salt permeability). However, no experimental validation of the parasitic currents model was provided, and any discussion about the specific influence of the leakage currents on the performance of RED stacks was reported.

Despite several multi-scale semi-empirical models have demonstrated their effectiveness in the simulation of both the ED [204,222] and RED [106,214,223] processes, they often do not include at all the shunt currents, by assuming an identical behaviour of all cell pairs. Therefore, the simulation results (i) are affected by some approximation when they are used to predict the operation of industrial-size units with hundreds of cell pairs fed by highly concentrated solutions, (ii) or refer to special stacks suitably tailored to minimize the shunt currents.

The aim of this chapter is to investigate in depth on the parasitic currents phenomena in RED/BMRED and ED/BMED applications, through the development of a suitable electrical model experimentally validated. The model was developed in gPROMS model builder and it was already presented in a simplified form in chapter 3. In this chapter it will be fully described. This model was also integrated in pre-existent semi-empirical simulators for RED and ED processes. This model requires only input parameters concerning the membrane properties, which are easily accessible by experiments, thus overcoming the typical limits of calibrated Ohmic models, and allowing for the prediction of the operation and performance of RED/BMRED and ED/BMED units with different design features and operating conditions. Once validated under several experimental conditions, the simulation results were discussed with particular focus on the distribution of parasitic currents and on their influence on the processes performance. A sensitivity analysis was performed to identify the critical conditions where shunt currents play a crucial role, thus providing important suggestions for the design of improved industrial stacks with higher efficiency.

5.3 *Ionic shortcut currents model description*

This model represents a mathematical tool able to simulate the equivalent electric circuit of RED/BMRED and ED/BMED modules. It calculates the electric currents flowing in each branch and the voltage difference between the nodes of the stacks equivalent electrical circuits, thus allowing the prediction of the shunt currents and their impact on the stack performance. By way of example, in Figure 60 the scheme applicable for the conventional RED process is shown.

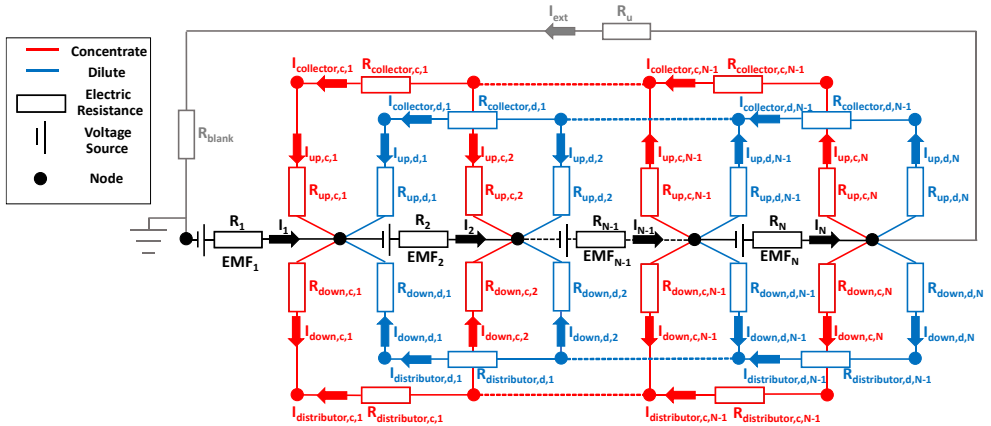


Figure 60. Scheme of the equivalent electric circuit of a conventional RED stack.

The scheme in Figure 60 may be easily modified to be used for electro dialysis processes by substituting the load resistance R_u with a voltage or current generator. A similar electrical scheme may be adopted to simulate BMED and BMRED processes. For example, Figure 61 can be used for a BMRED process.

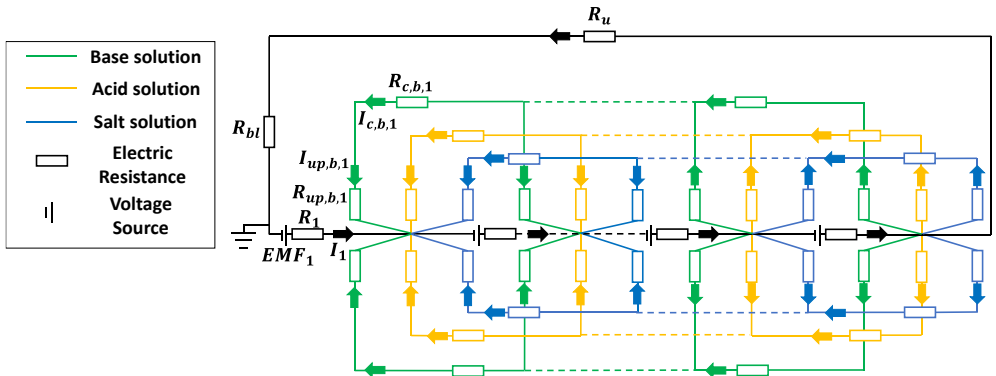


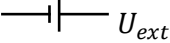
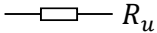
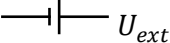
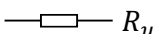
Figure 61. Scheme of the equivalent electric circuit of a BMRED stack.

Again, the scheme in Figure 61 may be easily modified to be used for BMED processes by substituting the load resistance R_u with a voltage or current generator.

The differences among the simulated conventional ED and RED as well as BMED and BMRED were summarized in Table 15.

Table 15. Summary of the main differences of the equivalent electrical circuits of the investigated processes.

| Process | channels per cell | External circuit element |
|---------|-------------------|--------------------------|
|---------|-------------------|--------------------------|

| | | |
|-------|------------------------|--|
| ED | dilute and concentrate |  U_{ext} |
| RED | dilute and concentrate |  R_u |
| BMED | acid, base and salt |  U_{ext} |
| BMRED | acid, base and salt |  R_u |

This tool presents a general validity and it may be used for simulating repetitive units with more than 2 compartments (e.g. for BMED processes with 3 or 4 compartments per unit cell).

Two longitudinal resistances are calculated for each channel, while a voltage source along with its relevant resistance are calculated per each cell unit. The other electrical resistances of the equivalent circuit include those in the manifolds (interposed between two channels of the same solution), in the electrode compartments and in the external load (in RED and BMRED processes). A positive longitudinal current means that the electric current is outgoing the channel while a negative one is ingoing into the channel.

At each node of the electrical scheme, the Kirchoff's node law is applied. In particular, at each node with ingoing and outgoing cell currents, it is:

$$I_{k-1} = I_k + \sum_{sol} I_{up,sol,k-1} + I_{down,sol,k-1} \quad (120)$$

in which the subscript *sol* refers to the generic solution (i.e. either the concentrate or the diluate for a conventional RED process) I_k and I_{k-1} are the electric currents flowing in the k -th and $(k-1)$ -th cell, respectively, $I_{up,sol,k-1}$, $I_{down,sol,k-1}$ are the electric currents flowing along the main flow direction in the channels for the generic solution in the $(k-1)$ -th cell. Eq. 120 is valid within the range [2;N] (where N is the number of cell pairs).

The external circuit current I_{ext} is correlated with the stack currents by the equation:

$$I_{ext} = -I_N + \sum_{sol} I_{up,sol,N} + I_{down,sol,N} \quad (121)$$

The first Kirchoff law applied at each of the [2;N-1] manifolds node for the generic solution (i.e. diluate or concentrate) is written as follows

$$I_{man,sol,k-1} + I_{x,sol,k} = I_{man,sol,k} \quad (122)$$

where the subscript *man* refers either to the collector or the distributor, the subscript *x* refers either to *up* or *down*. In the first and the *N*-th channel, the electrical current is simply

$$I_{x,sol,1} = I_{man,sol,1} \quad (123)$$

$$-I_{x,sol,N} = I_{man,sol,N-1} \quad (124)$$

The first Ohm law is applied over each resistance of the equivalent circuit. In particular, the voltage drop over each of the [1;N-1] manifold resistances for the generic solution (e.g. diluate or concentrate for a conventional RED process) is computed as

$$V_{man,sol,k} - V_{man,sol,k+1} = I_{man,sol,k} \cdot R_{man,sol,k} \quad (125)$$

where $V_{man,sol,k}$ and $V_{man,sol,k+1}$ are the voltages at the *k*-th and (*k*+1)-th nodes of the manifolds respectively (i.e. distributor or collector) and $R_{man,sol,k}$ is the electrical resistance of the *k*-th manifold. For the generic solution (i.e. diluate or concentrate) $R_{man,sol,k}$ is calculated as

$$R_{man,sol,k} = \frac{l_{man}}{N_{holes} \pi \frac{d_{man}^2}{4} \sigma_{man,sol,k}} \quad (126)$$

where N_{holes} is the number of inlet/outlet spacer holes, d_{man} is the manifold diameter, $\sigma_{man,sol,k}$ is the electrical conductivity of the solution flowing in the *k*-th manifold (i.e. distributor or collector), and l_{man} is given by the sum of the thicknesses of the cell pair elements:

$$l_{man} = \sum_{IEM} d_{IEM} + \sum_{sol} d_{sol} \quad (127)$$

where the subscript *IEM* refers to the generic ion-exchange membrane.

To calculate $\sigma_{man,sol,k}$ the salt concentration along the manifolds is necessary. It is calculated by mass balances in the manifolds developed in the semi-empirical models of which the parasitic current model is a part.

The voltage drop over each resistance along the flow direction in the channel is given by

$$V_k - V_{man,sol,k} = I_{x,sol,k} \cdot R_{x,sol,k} \quad (128)$$

where V_k and $V_{man,sol,k}$ are the voltages at the *k*-th node of the cell and the manifold (i.e. distributor or collector) respectively, $I_{x,sol,k}$ is the electric current along the channel in the flow direction and $R_{x,sol,k}$ is the electrical resistance along the channel of the *k*-th cell. Eq. 128 is applied for *k* in the range [1;N]. $R_{x,sol,k}$ ($R_{up,sol,k}$ and

$R_{down,sol,k}$ in Figure 60 and Figure 61) are calculated as a series of a resistance in the membrane active area and a parallel of N_{holes} -resistances out of the membrane active area. It is given by the relation

$$R_{x,sol,k} = f_s \cdot \frac{L_x/2}{d_{sol} \cdot b \cdot \sigma_{x,sol,k}} + f_s \cdot \frac{l_{oma}}{\sigma_{x,sol,k} \cdot d_{sol} \cdot d_{oma} \cdot N_{holes}} \quad (129)$$

where f_s is the spacer shadow factor, L_x is the average distance between the inlet and the outlet spacer holes, and l_{oma} and d_{oma} are the length and average width of the spacer region out of the active area (Figure 62), $\sigma_{x,sol,k}$ is the conductivity of the solution calculated as a function of the average salt concentration between the middle of the channel and the outlet (for $x=up$) or the inlet (for $x=down$).

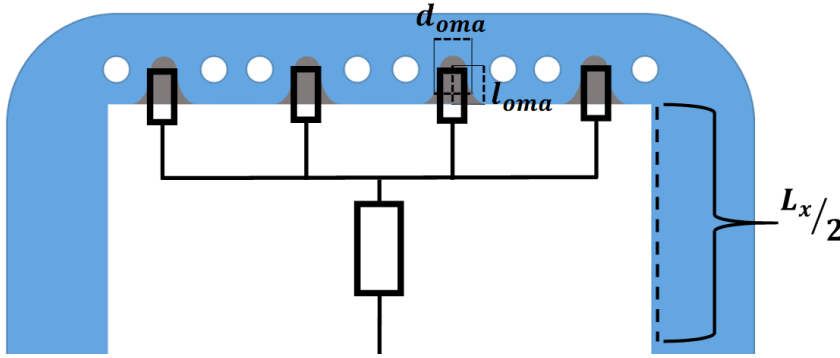


Figure 62. Schematic representation of the electrical resistances along the longitudinal direction in the spacer-filled channel. Grey regions are out of the membrane active area.

The (useful) electric current flowing in a cell pair in the direction perpendicular to the membranes is calculated as

$$I_k = \frac{(V_{k-1} - V_k \pm EMF_{av,k})}{R_{av,k}} \quad (130)$$

$$I_1 = \frac{(-V_1 \pm EMF_{av,1})}{R_{av,1}} \quad (131)$$

in which $EMF_{av,k}$ is the average electromotive force along the channel and $R_{av,k}$ is the average resistance of the repetitive unit. The sign for EMF in Eqs. 130-131 is negative for RED/BMRED processes and positive for ED/BMED processes. Likewise the solution conductivities, $EMF_{av,k}$ and $R_{av,k}$ are calculated by equations developed in the semi-empirical models of which the parasitic model is part. Eq. 130 is valid for k within the interval $[2; N]$.

The electric current flowing through the external circuit I_{ext} , (i.e. sent to the final user), is calculated as follows,

$$I_{ext} = \frac{\pm V_N}{R_u \pm R_{bl}} \quad (132)$$

in which V_N is the voltage of the N-th cell, R_u is the external load resistance and R_{bl} is the blank resistance, accounting for the resistance of the electrode compartments and of the end-membrane, and for the overvoltage due to the electrochemical reactions at the electrodes. The signs in Eq. 132 are both positive for RED/BMRED processes while both negatives for ED/BMED processes.

The potential difference over the external load U_{ext} is computed as

$$U_{ext} = I_{ext} \cdot R_u \quad (133)$$

5.3.1 Performance parameters of the shortcut currents

Suitable parameters were defined in order to assess the impact of the shortcut currents.

The relative loss of *GPD* with respect to an ideal case without parasitic currents was calculated for RED/BMRED Eq. 134 and ED/BMED Eq. 135.

$$\psi_p = \left(1 - \frac{GPD}{GPD_{no\ par}}\right) \cdot 100 \quad \text{RED/BMRED} \quad (134)$$

$$\psi_p = \left(1 - \frac{GPD_{no\ par}}{GPD}\right) \cdot 100 \quad \text{ED/BMED} \quad (135)$$

in which $GPD_{no\ par}$ is the gross power density calculated by simulations of the reference case neglecting parasitic currents, carried out by a simplified model where the stack is simply modelled without the shunt currents branches in the equivalent electric circuit (i.e. the stack is modelled as a series of identical cell resistances and EMFs, together with the blank resistance and the external resistance).

The % parasitic loss of current (I_{loss}) is the relative difference between the average cell current and the external current. It is given by

$$I_{loss} = \frac{\frac{\sum_1^N I_k}{N} - I_{ext}}{\frac{\sum_1^N I_k}{N}} \quad \text{RED/BMRED} \quad (136)$$

$$I_{loss} = \frac{I_{ext} - \frac{\sum_1^N I_k}{N}}{\frac{\sum_1^N I_k}{N}} \quad \text{ED/BMED} \quad (137)$$

where Eq. 136 is used for RED/BMRED and Eq. 137 for ED/BMED processes.

For ED/BMED processes % $SEC_{m,loss}$ is evaluated as

$$\% SEC_{m,loss} = \frac{SEC_m - SEC_{m,no\ par}}{SEC_m} \times 100 \quad (138)$$

in which $SEC_{m,no\ par}$ is the SEC_m calculated by simulations without the presence of parasitic currents.

For RED/BMRED processes % $GED_{m,loss}$ is evaluated as

$$\% GED_{m,loss} = \frac{GED_{m,no\ par} - GED_m}{GED_{m,no\ par}} \times 100 \quad (139)$$

in which $GED_{m,no\ par}$ is the GED_m calculated by simulations without the presence of parasitic currents.

The % current efficiency loss ($\eta_{c,loss}$) is given by

$$\eta_{c,loss} = \eta_{c,no\ par} - \eta_c \quad (140)$$

where $\eta_{c,no\ par}$ is the current efficiency calculated by simulations neglecting the parasitic currents.

Finally, the cell current efficiency is assessed by Eqs. 141-142

$$\eta_k = \frac{I_{ext}}{I_k} \times 100 \quad \text{RED/BMRED} \quad (141)$$

$$\eta_k = \frac{I_k}{I_{ext}} \times 100 \quad \text{ED/BMED} \quad (142)$$

where Eq. 141 is used for RED/BMRED and Eq. 142 for ED/BMED processes.

5.4 Ionic shortcut model validation

Model validation was performed with two different test-rig units adopted for conventional RED and BMRED tests.

Conventional RED experimental data were collected using a lab-scale stack (provided by REDstack BV, The Netherlands) with a co-flow configuration. The cell pairs number ranged from 5 to 50 in the experimental campaign. The stack was equipped with Fujifilm Type 10 membranes (Table 16, FujiFilm Manufacturing Europe B.V.), with an active area of 100 cm² (10 cm length, 10 cm width), along with 330 μm polyamide woven spacers (Deukum GmbH, Germany), made up of 4 inlet/outlet holes with a diameter of 6 mm each (see Figure 62) with a volume porosity of 0.8. The electrodes were of Dimensionally Stable Anodes (DSA)-type.

Table 16. Fujifilm type 10 membranes characteristics from [58].

| | CEM | AEM |
|---|------------|------------|
| Reinforcement | polyolefin | polyolefin |
| Thickness dry (μm) | 125 | 135 |
| Resistance ($\Omega \text{ cm}^2$) | 1.7 | 2.0 |
| Perm-selectivity (%) | 95 | 99 |
| Water permeation ($\text{ml bar}^{-1} \text{ m}^{-2} \text{ h}^{-1}$) | 6.5 | 6.5 |
| Burst strength (kg cm^{-2}) | 2.8 | 2.8 |
| pH stability (-) | 1-13 | 1-13 |
| Temperature stability ($^{\circ}\text{C}$) | 60 | 60 |

The NaCl concentration in the concentrate was fixed at 5 M (typical of concentrated brines), while that in the diluate was either 0.017 M or 0.05 M. A concentrated brine was used in the concentrate compartments in order to magnify the shortcut currents and their effects. The electrode rinse solution was a reversible redox couple with 0.1 M concentration of $\text{K}_3\text{Fe}(\text{CN})_6/\text{K}_4\text{Fe}(\text{CN})_6$ and 2.5 M concentration of NaCl as supporting electrolyte. From experiments with different number of cell pairs, the value of the areal blank resistance (electrode compartments with an additional CEM) was evaluated to be within the range $\sim 60\text{-}72 \Omega \text{ cm}^2$.

BMRED tests were performed using a lab-scale module (provided by Fumatech BWT GmbH, Germany). Acid and base solutions were fed to the stack with a co-current flow distribution, whilst salt solution was fed in cross-flow with respect to them. The triplet number ranged from 5 to 38. The stack was equipped with commercial IEMs provided by Fumatech BWT GmbH, Germany (Table 17), with an active area of 100 cm^2 (10 cm length, 10 cm width), along with $500 \mu\text{m}$ polyamide woven spacers (Fumatech BWT GmbH, Germany), made up of 3 inlet/outlet holes with a diameter of 8.5 mm each with a volume porosity of 0.8. The electrodes were of Dimensionally Stable Anodes (DSA)-type.

Table 17. Fumatech membranes characteristics from [224].

| Name | Type | Thickness (μm) | IEC (meq g^{-1}) | Selectivity (%) | Areal resistance ($\Omega \text{ cm}^2$) |
|------|-------|-----------------------------|-----------------------------|-----------------|--|
| FAB | Anion | 100-130 | 1.0-1.1 | 94-97 | 4-7 |

Ionic shortcut currents in electro-membrane processes

| | | | | | |
|-----|---------|---------|---------|-------|-------|
| FKB | Cation | 100-130 | 1.2-1.3 | 98-99 | 4-6 |
| FBM | Bipolar | 180-200 | *n.p. | *n.p. | *n.p. |

*n.p. means not provided

Acid, base and salt solutions were prepared using Hydrochloric Acid (HCl 37% Merck), Sodium Hydroxide (NaOH 98-100% Honeywell Fluka) and Sodium Chloride (NaCl 99.7% ChemSolute), respectively. Acid and base streams were fed to the stack with equal initial concentration (i.e., 0.2 M, 0.6 M or 1 M aqueous solutions), the salt stream was an aqueous solution 0.25 M in NaCl in every test. Aqueous solutions 0.5 M in FeCl₂/FeCl₃ (99% ChemSolute) were used as electrode rinse solutions (ERSs). HCl was added to the ERS to maintain the solution pH lower than 2.3 to prevent possible iron oxy-hydroxide precipitation [205]. From experiments with different number of triplets, the value of the areal blank resistance (electrode compartments with an additional AEM) was evaluated to be $\sim 72 \Omega \text{ cm}^2$.

The electrical conductivity of the solution was measured by a WTW 3310 conductometer.

Peristaltic pumps (Lead Fluid Technology Co., Ltd.) were used to circulate all the streams, including the electrode rinse solution, through the RED/BMRED stack. The electrolyte solutions were fed in once-through mode with a flow rate suitably chosen to guarantee a channel mean flow velocity of 1 cm s^{-1} in all tests. Conversely, the electrode solution was continuously recirculated to the reservoir. Current-voltage characteristics were recorded by using a 150 W DC Electronic Load (BK Precision 8540) operating in potentiostatic mode. A scheme of the test-rig set-up is reported in Figure 18.

The experiments were performed at ambient temperature ($\sim 20 \text{ }^\circ\text{C}$). All experiments were carried out at least twice. Average values along with corresponding error bars are reported in the graphs.

5.4.1 Ionic shortcut RED model validation results

Figure 63 shows the Open Circuit Voltage (OCV) (i.e. the voltage difference over the stack when no current flows in the external circuit) as a function of the cell pairs number, comparing experimental data and model predictions.

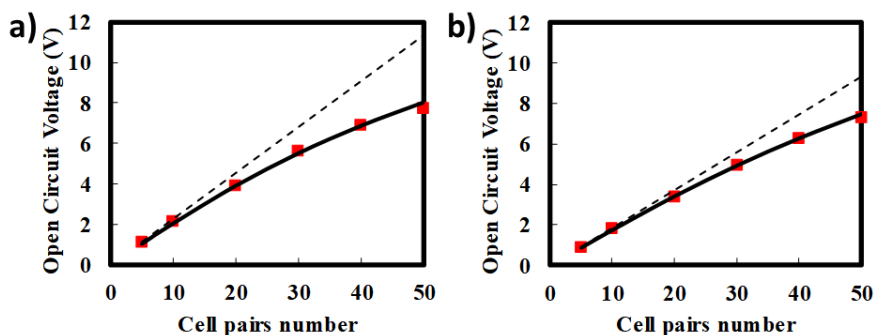


Figure 63. Open Circuit Voltage (OCV) as a function of the cell pairs number in $10 \times 10 \text{ cm}^2$ stacks with Fujifilm Type 10 membranes and with spacers provided with 4 inlet/outlet holes (diameter of 6 mm). Mean flow velocity of the electrolyte solutions in each channel equal to 1 cm s^{-1} . Symbols refer to experimental data, continuous lines to the model predictions, and broken lines to the ideal (i.e. no shunt currents) OCV. Inlet solution concentrations (NaCl): a) $0.017 \text{ M} - 5 \text{ M}$; b) $0.05 \text{ M} - 5 \text{ M}$. Areal blank resistance: a) $72 \Omega \text{ cm}^2$, b) $60 \Omega \text{ cm}^2$.

As it can be seen, both the experiments and the model predictions exhibit a deviation of the OCV from the ideal linear trend (no shunt currents) as the cell pairs number increases. A very good agreement between experiments and model was found at any concentration. Such deviation can be attributed to the effect of shunt currents. As a matter of fact, the higher the cell pairs number, the higher the number of the ion bypass pathways (see Figure 60). This fact leads to the existence of a cell current even under open circuit condition, associated to an ion current through the manifolds (as they collect the ion current coming from the channels) and to a reduction of the OCV, as mentioned above. In other words, the occurrence of parasitic currents causes a higher consumption of the salinity gradient. Particularly, in the case of a higher concentration in the diluate (Figure 63b), the lower driving force results in a lower OCV reduction compared to the 0.017 M case (Figure 63a). Interestingly, the relative effect of parasitic current is lower, due to the lower resistance of the desired current path (perpendicular to the membranes). The maximum deviation at 50 cell pairs is 23.4% and 12.4% in the case of 0.017 M and 0.05 M , respectively (Figure 63).

Data under closed circuit conditions are reported in Figure 64, which shows the Gross Power Density (GPD) delivered by the stack when the applied voltage is equal to $\text{OCV}/2$ as a function of the cell pairs number.

$\text{OCV}/2$ was chosen as it simulates the stack operation with the ideal (when no shunt currents) maximum power. Actually, the maximum power is obtained at lower values of the stack voltage, due to the ionic shortcut currents and to other reasons

(e.g. the variation of the conditions along the channels). However, we found by both experiments and simulations that the discrepancy between the maximum power and the power delivered at OCV/2 was only of a few percent. Therefore, the OCV/2 condition was used to represent with very good approximation the maximum power condition.

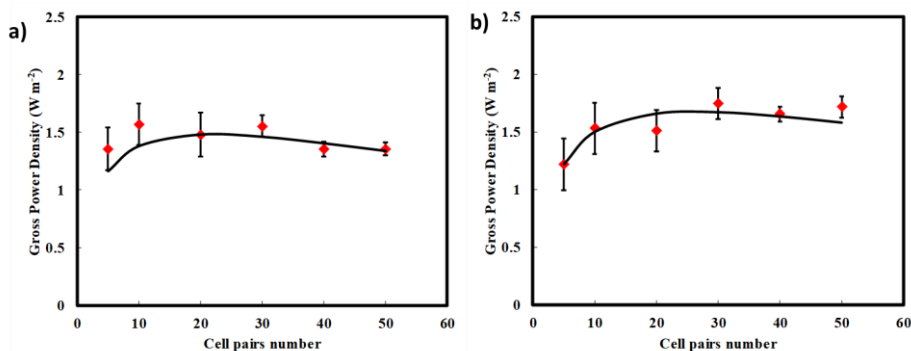


Figure 64. Gross Power Density (GPD) produced with an applied voltage equal to OCV/2 as a function of the cell pairs number in $10 \times 10 \text{ cm}^2$ stacks with Fujifilm Type 10 membranes and with spacers provided with 4 inlet/outlet holes (diameter of 6 mm). Mean flow velocity of the electrolyte solutions in each channel equal to 1 cm s^{-1} . Symbols refer to experimental data, continuous lines to the model predictions. Inlet concentrations (NaCl): a) $0.017 \text{ M} - 5 \text{ M}$; b) $0.05 \text{ M} - 5 \text{ M}$. Areal blank resistance: a) $72 \Omega \text{ cm}^2$, b) $60 \Omega \text{ cm}^2$.

Overall, the model predictions are in good agreement with the experimental data. A variation is found at the lowest cell pairs number (where the effect of parasitic current is expected to be very low) for case a), probably due to an overestimation of the resistance in the electrode compartments (blank resistance). As a matter of fact, the error bars tend to reduce in stacks with a larger number of cell pairs (N), i.e. where the effect of the blank resistance is lower. This suggests that the lower repeatability of the experimental results found at low values of N is likely caused by some variation in the electrode compartments or, more specifically, in the electrode rinse solution. For example, it can be altered by salt diffusion from the 5 M concentrated brine compartment.

An increase in GPD is observed as the number of cell pair increases, due to the decreasing relative impact of the blank resistance. This would lead to an asymptotic trend. Conversely, a maximum is exhibited by the GPD, because it is also affected by the parasitic currents, which count more at large N . The maximum occurs in stacks with ~ 21 and ~ 27 cell pairs fed by $0.017 \text{ M} - 5 \text{ M}$ and $0.05 \text{ M} - 5 \text{ M}$ solutions, respectively. Beyond the maximum point, the impact of the shortcut currents prevails, and the GPD decreases. The loss of power ψ_p (eq. 134) is $\sim 20\%$ and $\sim 16\%$

for the two feeding conditions, respectively, in stacks with 50 cell pairs, i.e. about one fifth and one sixth of the producible power density are lost due to shortcut currents.

Moreover, Table 18 shows the diluate and concentrate average (among the channels) conductivities at the outlet, by varying the external voltage difference in the stack with 50 cell pairs (largest effect of shunt currents) and for the case 0.017 M - 5 M.

Table 18. Comparison between model outcomes and experimental results of the diluate and concentrate outlet conductivities for a $10 \times 10 \text{ cm}^2$ stack with Fujifilm Type 10 membranes and with spacers provided with 4 inlet/outlet holes (diameter of 6 mm), equipped with 50 cell pairs, fed by 0.05 M – 5 M inlet concentrations. Mean flow velocity of the electrolyte solutions in each channel equal to 1 cm s^{-1} . Areal blank resistance: $60 \Omega \text{ cm}^2$.

| External voltage | Diluate outlet conductivity (mS cm^{-1}) | | Concentrate outlet conductivity (mS cm^{-1}) | |
|------------------|---|-------|---|-------|
| | Experimental | Model | Experimental | Model |
| OCV | 6.82 | 7.25 | 241 | 244 |
| OCV/2 | 7.39 | 8.47 | 241 | 244 |
| 0 V | 8.06 | 9.73 | 241 | 244 |

A fair agreement between experimental measurements and simulation results is found for the data reported in Table 18 (maximum discrepancy of 17%).

Parasitic currents and their effects on the process performance can be significant also in RED units fed by “standard” solutions of seawater and river water, depending on the constructive features of the stack. For example, non-negligible shunt currents may occur in stacks with high-resistance membranes. As a further validation step, results from the present model were also compared with data by Veerman et al. [110], which include both predictions of their own model and experimental results for stacks fed by artificial seawater and river water. The investigated stacks were i) with Ralex anion and cation exchange membranes, designated as R1.0 and ii) with Fumasep anion and cation exchange membranes denoted F0.2. In particular, Figure 65a1 and Figure 65b1 reports the OCV and Figure 65a2 and Figure 65b2 the Max Gross Power as functions of the cell pairs number for two stack configurations, respectively (different spacers and membranes, see figure caption).

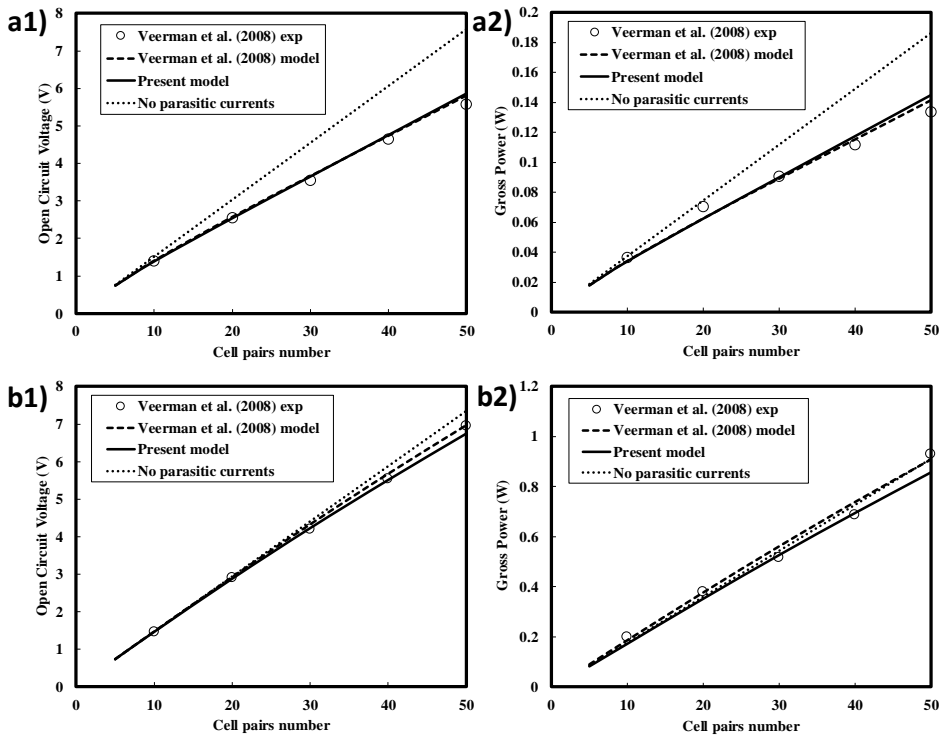


Figure 65. Comparison between the present model predictions and data by Veerman et al. [110] as functions of the cell pairs number in stacks with 1 inlet/outlet hole (diameter of a1, a2) 10 mm and b1, b2) 8 mm). Dotted line refers to the ideal (i.e. no shunt currents). Mean flow velocity of the electrolyte solution in each channel equal to 1 cm s^{-1} . a1) Open Circuit Voltage and a2) Maximum Gross Power for stacks provided with Ralex membranes (0.65 mm thick) and spacers 1 mm thick [Stack named R1.0]; b1) Open Circuit Voltage and b2) Maximum Gross Power for stacks provided with Fumasep membranes (0.2 mm thick) and spacers 0.082 mm thick [Stack named F0.2]. Inlet concentrations (NaCl): 1 g l^{-1} – 30 g l^{-1} (0.017 M–0.513 M). Areal blank resistance: a1, a2) $262 \Omega \text{ cm}^2$, b1, b2) $12 \Omega \text{ cm}^2$.

The developed model provides outcomes which are in very good agreement with the data by Veerman et al. [110], thus obtaining a further validation. The ratio between the average manifold resistance of the concentrate solution, especially for a stack of 50 cell pairs (4.39Ω for R1.0 stack and 1.17Ω for F0.2 stack) and the average cell resistance (1.52Ω for R1.0 stack and 0.246Ω for F0.2 stack) plays a key role in the currents distribution within the stack. In particular, a higher average manifolds resistance (especially of the concentrate solution) and/or a lower average cell resistance lead to lower shunt currents and a consequent higher cell current (i.e. the useful one). In fact, within the simulated conditions, the loss of power decreased from $\sim 22\%$ for the R1.0 stack to $\sim 6\%$ for the F0.2 stack.

5.4.2 Ionic shortcut BMRED model validation results

Figure 66 reports the comparison between model and experimental data for the Open Circuit Voltage and Gross Power Density at 29 A m^{-2} by varying the triplets number. Particularly, Figure 66 shows the results for inlet acid/base concentration of 0.2M without the presence of background salt and 0.25M NaCl in the salt compartment.

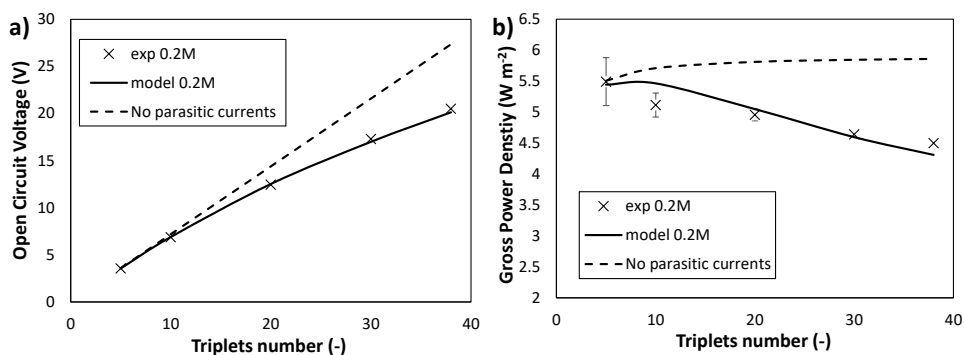


Figure 66. Comparison between the predictions of the model and the experimental data as functions of the triplets number. Dotted line refers to the ideal (i.e. no shunt currents). Mean flow velocity of the electrolyte solution in each channel equal to 1 cm s^{-1} . a) Open Circuit Voltage and b) Gross Power Density producible with external current density fixed at 29 A m^{-2} . Inlet solution concentrations: acid and base 0.2M of HCl and NaOH and salt: 0.25M of NaCl .

Error bars for the OCV are not visible in the figure since the average error (equal to 16 mV) is negligible compared to the voltage values. As may be seen in Figure 66a, both the model and the experimental data are in excellent agreement in showing a significant deviation from the linearity, which is representative of the theoretical values. Already at the relatively low acid and base concentration (i.e. 0.2M), it is possible to observe an important effect of the parasitic currents. This is due to the high solution conductivities of the acid and base solutions already at low concentrations. Specifically, the OCV deviation from the theoretical value results to be $\approx 26\%$ at 38 triplets. Figure 66b, illustrates the Gross Power Density obtainable from a closed circuit condition by fixing the external current density to 29 A m^{-2} . The experimental GPDs values exhibit a very high reproducibility since the reported maximum empirical error with the test-retest process is 7% . By varying the number of triplets, the experimental and the simulated GPD result in good agreement. Also in this case, a significant deviation from the theoretical GPD profile of $\approx 25\%$ at 38 triplets can be observed.

Figure 67 shows the comparison between model and experimental data for the Open Circuit Voltage and Gross Power Density at 29 A m^{-2} by varying the triplets number. Error bars for the OCV are so small that the average error can be considered to be negligible. Particularly, Figure 67 shows the results for inlet acid/base concentration of 0.6M without the presence of background salt and 0.25M NaCl in the salt compartment.

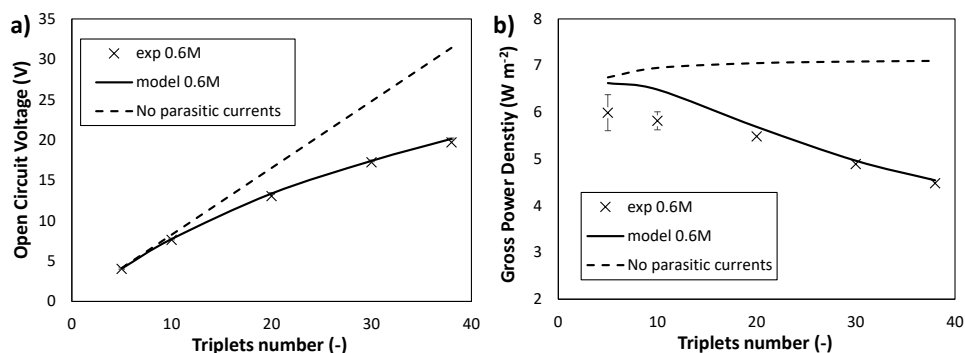


Figure 67. Comparison between the predictions of the model and the experimental data as functions of the triplets number. Dotted line refers to the ideal (i.e. no shunt currents). Mean flow velocity of the electrolyte solution in each channel equal to 1 cm s^{-1} . a) Open Circuit Voltage and b) Gross Power Density producible with external current density fixed at 29 A m^{-2} . Inlet solution concentrations: acid and base 0.6M of HCl and NaOH and salt: 0.25M of NaCl.

Open Circuit Voltage (Figure 67a) results were also well predicted in the case of inlet acid and base concentration equal to 0.6M regardless the number of triplets. Interestingly, the deviation due to the presence of parasitic currents is higher in this case, as it was found to be $\approx 37\%$ at 38 triplets. Therefore, the increased acid and base concentrations result in a more pronounced effect of the shortcut currents as expected. This is due to (i) the reduced electrical resistances of the electrolyte solutions and (ii) the higher electromotive force, which in turn enhance this detrimental effect. The collected GPD data (Figure 67b) showed high repeatability with a maximum error of 6.4% . Compared with the empirical value, the GPD is also well predicted by the model. The maximum model error is found to be 11.4% at 10 triplets. The GPD at 38 triplets is 36% lower than the theoretical value.

Figure 68 shows the comparison between model and experimental data for the Open Circuit Voltage and Gross Power Density at 29 A m^{-2} by varying the triplets number. Particularly, Figure 68 shows the results for inlet acid/base concentration of 1M without the presence of background salt and 0.25M NaCl in the salt compartment.

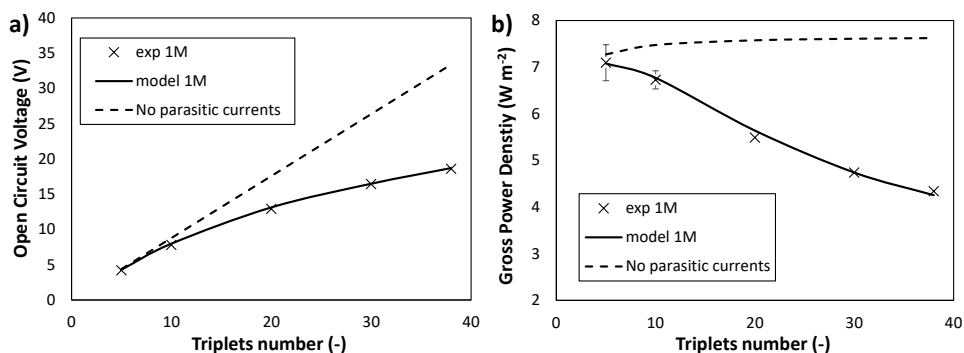


Figure 68. Comparison between the predictions of the model and the experimental data as functions of the triplets number. Dotted line refers to the ideal (i.e. no shunt currents). Mean flow velocity of the electrolyte solution in each channel equal to 1 cm s^{-1} . a) Open Circuit Voltage and b) Gross Power Density producible with external current density fixed at 29 A m^{-2} . Inlet solution concentrations: acid and base 1M of HCl and NaOH and salt: 0.25M of NaCl.

Again error bars for the collected OCV (Figure 68a) were hidden because they are negligible. The predicted OCV is in excellent agreement with the experimental data. Results obtained at 1M of acid and base confirmed the increasing trend of the effect of the parasitic currents by increasing the acid and base concentrations. In fact, at 38 triplets the deviation from the theoretical line is over 44%. The experimental error for GPD (Figure 68b) was found to be 5.4%. GPD results were also well predicted and at 38 triplets the discrepancy from the theoretical curve was a little less than 44%, thus, a huge percentage of the produced power is dissipated in the parasitic resistances.

5.4.3 Ionic shortcut model capabilities

As discussed in section 5.2, the simplified model for parasitic currents by Veerman et al. [110] was based on the simulation of the stack electrical behaviour only. It is a “purely Ohmic” model calibrated on experimental data, which used constant electrical resistances and cell pair potentials. The obvious advantages of such a model were (i) ease of implementation and (ii) speed of computing. However, the predictive capability of Veerman et al. model is limited by the availability of experimental data for the calibration. The present multi-scale model, instead, following the approach by Tedesco et al. [151], is based on a process simulator assessing fluxes and mass balances at the cell pair scale fully coupled with the electrical behaviour of the stack. The higher complexity of this model and the larger computational effort that it requires for the simulations, are justified by the higher predictive capabilities.

This can be shown by a comparison between the two models in the simulation of generic conditions not tested experimentally. For comparison purposes, the simulations were performed also by implementing the model by Veerman et al. [110]. The input parameters used for the simulations performed with the Veerman model (in terms of electrical resistances and EMF) were calculated with the inlet conditions. Note that these simplifying assumptions, which are needed to follow the Veerman approach, affect the driving force, the channel resistances, and the resistances of the parasitic pathways. For example, Figure 69a1 and Figure 69a2 report the OCV and Figure 69b1 and Figure 69b2 the Gross Power Density as functions of the cell pairs number for stacks 10 cm long and 50 cm long, respectively.

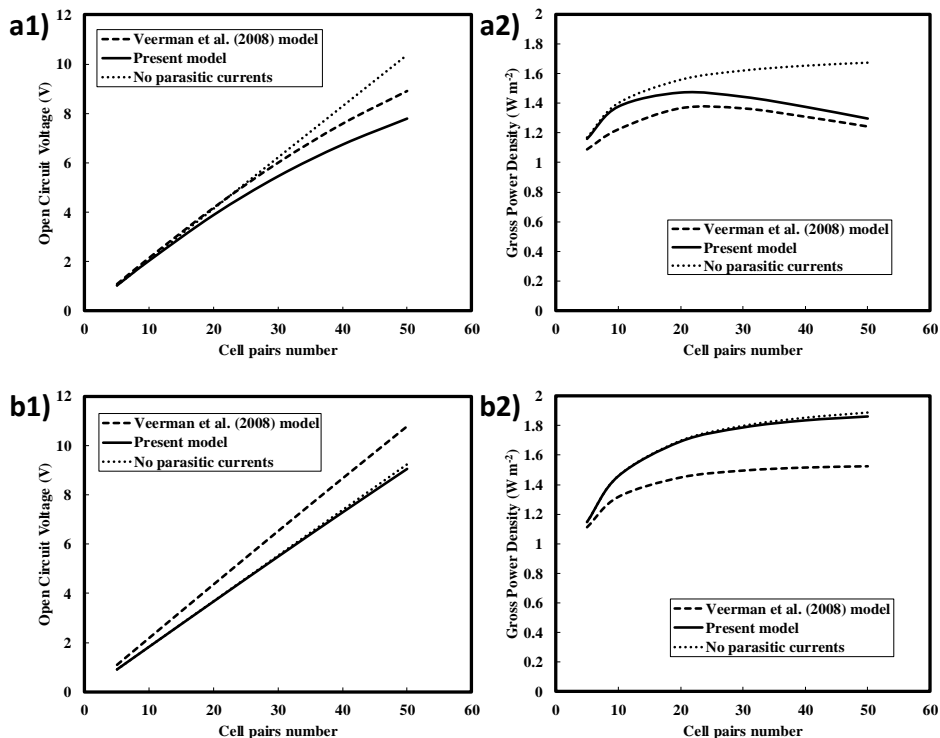


Figure 69. Comparison between the predictions of the present model and those of the model by Veerman et al. [110] as functions of the cell pairs number. Dotted line refers to the ideal (i.e. no short currents). Mean flow velocity of the electrolyte solution in each channel equal to 1 cm s^{-1} . a1) Open Circuit Voltage and a2) Gross Power Density producible with an applied voltage equal to $OCV/2$ in 10 cm long and 50 cm wide stacks; b1) Open Circuit Voltage and b2) Gross Power Density producible with an applied voltage equal to $OCV/2$ in $50 \times 50 \text{ cm}^2$ stacks. Spacers provided with 12 inlet/outlet holes (diameter of 1 cm). Fujifilm Type 10 membranes. Inlet solution concentrations (NaCl): $0.017 \text{ M} - 5 \text{ M}$. Areal blank resistance: $72 \Omega \text{ cm}^2$.

There is a non-negligible discrepancy between the two models outcomes for short-channel stacks (10 cm length), especially in terms of OCV (Figure 69a1). Note that the small discrepancy found in the GPD (Figure 69a2) is only the complex result of the compensative effects of the Ohmic model assumptions. Therefore, larger differences can be found under other design and operating conditions. As a matter of fact, Figure 69b1 and Figure 69b2 show significant discrepancies between the two models in the simulation of stacks with long channels (50 cm), where the average conditions along the channels are very different from the inlet conditions. In particular, the simplifications (use of the inlet concentrations) needed in the model by Veerman et al. [110] led to an overestimation of the OCV and an underestimation of the GPD.

These results highlight the limits of an Ohmic model, and, at the same time, show that a multi-scale process simulator is a more effective, powerful and flexible tool for the simulation of RED units, including the effects of shortcut currents.

Finally, it can be drawn that stacks with shorter channels are affected at a larger extent from shortcut currents, due to the lower resistance of the parasitic pathways. In particular, under the conditions simulated in Figure 69, a channel length of 50 cm leads to negligible shunt currents (Figure 69b) in stacks with 5-50 cell pairs.

5.5 *Simulation analysis of the ionic shortcut currents*

In this paragraph, the effect of the parasitic currents is assessed for RED/BMRED and ED/BMED processes for different design features and operating conditions.

5.5.1 *Conventional RED analysis*

The developed model was used to investigate the distribution of the electric current in the lab-scale stack with 50 cell pairs used for the experiments (see section 5.4). The maximum number of cell pairs used in the experiments was chosen in the present simulations in order to have the largest parasitic currents. Figure 70 shows the distribution of the cell current (I_k) within the equivalent circuit of the stack (see Figure 60) under different values of applied external voltage, i.e. OCV, OCV/2 (~maximum power) and 0 voltage (short-circuit).

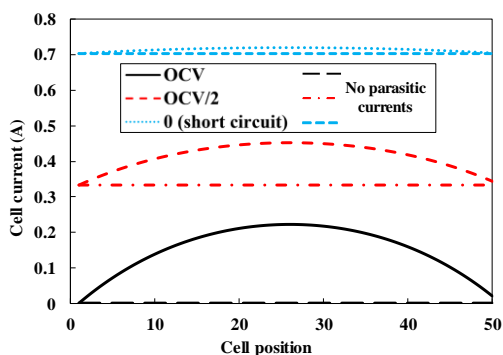


Figure 70. Predicted profiles of cell current (I_k) at different values of the external voltage for 10×10 cm^2 stacks equipped with 50 cell pairs, with Fujifilm Type 10 membranes and with spacers provided with 4 inlet/outlet holes (diameter of 6 mm), fed by 0.017 M - 5 M solutions. Mean flow velocity of the electrolyte solution in each channel equal to 1 cm s^{-1} . Areal blank resistance: $72 \Omega \text{ cm}^2$.

The average cell current is 0.15 A, 0.41 A and 0.71 A and the external current (i.e. supplied to the external load) is 0 A, 0.33 A and 0.70 A in OCV, OCV/2 and 0 (short-circuit), respectively. The largest effects of the shortcut currents on the cell currents occur under open circuit conditions, as can be also observed from the higher curvature of the cell current profiles within the stack. This means that the relative weight of the current leakage with respect to the cell current is maximum under open circuit conditions and decreases as the external current increases, with significant variations. As a consequence, the departure of the cell current profile from the ideal flat trend (i.e. without the parasitic currents), which would occur in absence of shunt currents, is larger at higher values of the external voltage. The reason behind this behaviour can be explained as follows. Considering the simplified electrical circuit reported in Figure 58a, one can easily infer that as the stack voltage increases, the cell current decreases, while the manifolds current increases. It should be noted that in the actual system simulated (Figure 60) the electromotive forces and the resistances are not fixed, but depend on the stack voltage itself, which affects the solutions concentrations. However, despite these complications, simulation results showed that parasitic currents were higher as the stack voltage increases, both in absolute terms and in relative terms with respect to the cell currents. Note that the amount of shortcut currents and their effects on the process performance depend strongly on the electrical resistance of the manifolds and of the channels compared to the cell resistance, as discussed in the next sub-section.

Moreover, in Figure 70 the highest percentage deviation of the cell current compared to the average is $\sim 100\%$, $\sim 20\%$ and $\sim 2\%$. Note that the small asymmetry in the equivalent circuit of Figure 60 is reflected on the current distribution. For

example, the cell current of the 1st cell pair differs from that of the last one (i.e. the 50th).

In order to explain the shape of the cell current profiles, Figure 71 reports the distribution of the electric current along the lower longitudinal branches of the concentrate and the diluate channels $i_{down,c,k}$ and $i_{down,d,k}$ (see Figure 60) for the same conditions of applied voltage considered in Figure 70. The distribution in the upper branches is qualitatively and quantitatively identical and is not reported.

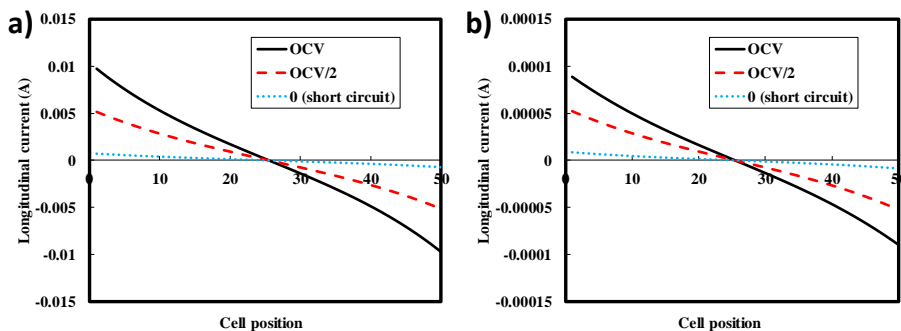


Figure 71. Predicted profiles of the longitudinal current flowing along the lower branch of the a) concentrate channels $i_{down,c,k}$ and b) diluate channels $i_{down,d,k}$ at different values of the external voltage for $10 \times 10 \text{ cm}^2$ stacks equipped with 50 cell pairs, with Fujifilm Type 10 membranes and with spacers provided with 4 inlet/outlet holes (diameter of 6 mm), fed by 0.017 M - 5 M solutions. Mean flow velocity of the electrolyte solution in each channel equal to 1 cm s^{-1} . Areal blank resistance: $72 \Omega \text{ cm}^2$.

As shown in Figure 71a, the maximum longitudinal leakage currents are $\sim 0.01 \text{ A}$, $\sim 0.005 \text{ A}$ and $\sim 0.0007 \text{ A}$ in OCV, OCV/2 and 0 (short-circuit), respectively. They exhibit these largest values at the extreme channels, i.e. close to electrode compartments, while they vanish close to the central channels. A positive longitudinal current means that the electric current is outgoing the channel while a negative one is ingoing into the channel. With reference to the equivalent circuit reported in Figure 60, this behaviour can be qualitatively intuited. Note that lower values of the longitudinal leakage currents are found as the stack voltage decreases (i.e. as the external current increases). Moreover, the driving force for the passage of the electric current along a channel branch is the voltage difference between the middle node of the channel and the distributor/collector node. Therefore, this voltage difference varies cell by cell and, in particular, it decreases towards the central part of the stack. The current profiles among the diluate channels (Figure 71b) are qualitatively but non quantitatively the same of the concentrate channels. In particular, the current distribution in the diluate channels is two orders of magnitude

lower than in the concentrate channels. As a matter of fact, the electric resistances of the diluate solution is high enough to make very low its contribution to diluate ducts shunt currents. On the other hand, a high electrical resistance in the diluate channel can make the cell pairs resistance higher than that in the concentrate manifolds, thus increasing the relevant parasitic currents.

Longitudinal currents in the channels are collected/distributed in/by the manifolds. Electric current profiles along the lower concentrate and diluate manifolds (distributors), which are $I_{distributor,c,k}$ and $I_{distributor,d,k}$, respectively, are reported in Figure 72.

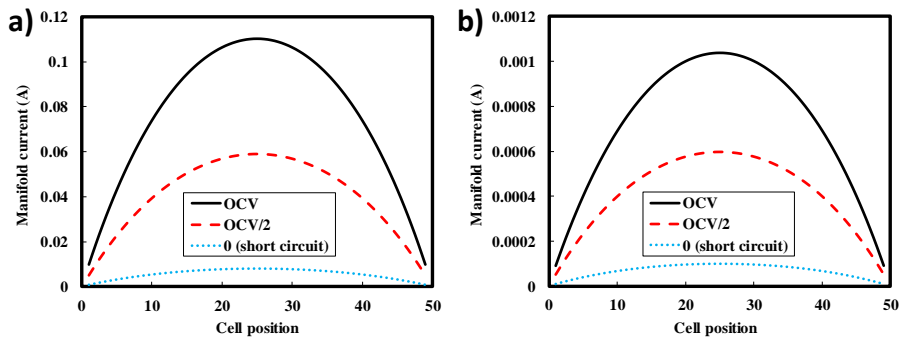


Figure 72. Predicted profiles of current along the lower (distributor) a) concentrate manifolds $I_{distributor,c,k}$ and b) diluate manifolds $I_{distributor,d,k}$ at different values of the external voltage for $10 \times 10 \text{ cm}^2$ stacks equipped with 50 cell pairs, with Fujifilm Type 10 membranes and with spacers provided with 4 inlet/outlet holes (diameter of 6 mm), fed by $0.017 \text{ M} - 5 \text{ M}$ solute. Mean flow velocity of the electrolyte solution in each channel equal to 1 cm s^{-1} . Areal blank resistance: $72 \Omega \text{ cm}^2$.

The parasitic current via manifolds exhibits a trend qualitatively similar to the profile of the cell current (Figure 70), with a maximum located approximately at the central part of the stack. As a difference, however, the average value of the parasitic current decreases as the external voltage decreases, while the opposite occurs for the average cell current (Figure 70). This shows the lower relative weight of the shunt currents at lower values of the external voltage. The negligible amount of shunt currents along the diluate parasitic pathways is shown by the low values of the electric currents via the diluate manifolds (Figure 72b): as it can be seen on the Y-axes of Figure 72, the effect of parasitic currents in the diluate pathway is 100 times lower than that pertaining to concentrate circuit.

In order to assess the effects of parasitic currents in RED stacks with different manifolds size, a sensitivity analysis was performed by varying the manifolds diameter from 2 mm to 14 mm. In this simulations set, the number of cell pairs was increased up to 500 and the active area to $50 \times 50 \text{ cm}^2$, in order to mimic the features

of a possible industrial scale stack. All the other constructive features, e.g. an inlet/outlet holes per each 4 cm (thus with a total of 12) and all the operating conditions were assumed equal to those of the experimental tests. Simulation results for the OCV are reported in Figure 73.

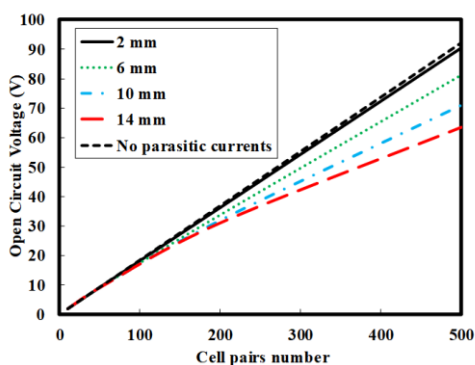


Figure 73. Predicted Open Circuit Voltage (OCV) as a function of the cell pairs number in 50×50 cm^2 stacks with Fujifilm Type 10 membranes and with spacers provided with 12 inlet/outlet holes (diameter ranging from 2 mm to 14 mm). The dashed black line refers to the OCV predicted by the model neglecting the shunt currents. Inlet concentrations (NaCl): 0.017 M - 5 M. Mean flow velocity of the electrolyte solution in each channel equal to 1 cm s^{-1} . Areal blank resistance: $72 \Omega \text{ cm}^2$.

As the inlet/outlet holes diameter increases, the OCV decreases significantly. Moreover, this effect is larger in stacks with a higher number of cell pairs. With 500 cell pairs, a manifolds diameter of 6 mm gave rise to a reduction in OCV of $\sim 10\%$ with respect the ideal case where parasitic currents are not simulated (i.e. simplified model without the presence of shunt currents); a manifolds diameter of 14 mm led to a loss of $\sim 30\%$. By decreasing the manifolds diameter, it is possible to diminish strongly the shunt currents phenomena thanks to the higher electrical resistance of the parasitic pathways. In particular, shunt currents and their effects were almost negligible when the manifolds diameter was reduced to only 2 mm, with a maximum loss of OCV of 1.9% at 500 cell pairs with respect to the ideal case without shortcut currents. Note that the above estimations do not take into account pressure losses.

The effects of the leakage currents are of higher practical interest in terms of delivered power under closed circuit conditions. Therefore, Figure 74 reports the Gross Power Density and the corresponding loss ψ_p associated to parasitic currents when the applied voltage is equal to $\text{OCV}/2$.

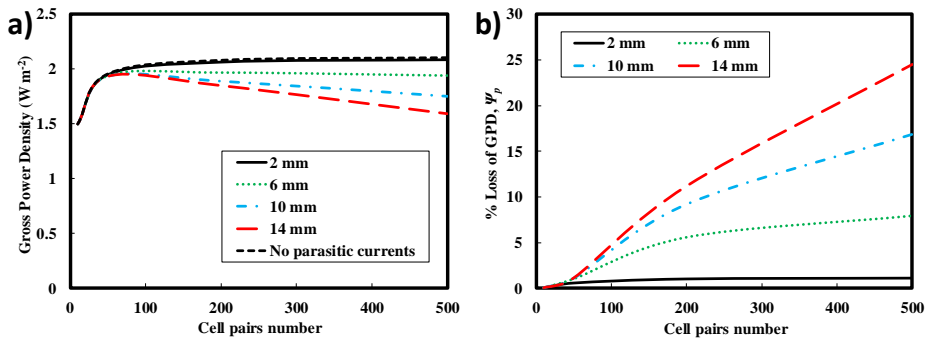


Figure 74. Predicted a) Gross Power Density (GPD) producible with an applied voltage equal to OCV/2 and b) corresponding % loss due to parasitic currents (ψ_p) as functions of the cell pairs number in $50 \times 50 \text{ cm}^2$ stacks with Fujifilm Type 10 membranes and with spacers provided with 4 inlet/outlet holes (diameter from 2 mm to 14 mm). The dashed line refers to the predictions of the model neglecting the shunt currents. Inlet concentrations (NaCl): 0.017 M - 5 M. Mean flow velocity of the electrolyte solution in each channel equal to 1 cm s^{-1} . Areal blank resistance: $72 \Omega \text{ cm}^2$.

As shown in Figure 74a, leakage currents lead to the presence of a maximum in the Gross Power Density as a function of the cell pairs number. This occurs approximately between 90 cell pairs and 60 cell pairs for stacks with 6 mm and 14 mm of manifolds diameter, respectively. The corresponding (i.e. at these maximum GPD) power loss due to parasitic currents is below 5%, as shown in Figure 74b. By further increasing the cell pairs number, the increment of parasitic currents causes a reduction in GPD and a consequent larger loss of efficiency. The process performance depends significantly on the manifolds diameter, which affects the electrical resistance against the parasitic currents. The loss of power is between 8% and 25% in stacks with 500 cell pairs with 6 mm and 14 mm of manifolds diameter, respectively. A different behaviour characterizes stacks with very low manifolds diameter (2 mm), which exhibit an asymptotic behaviour in GPD up to the maximum cell pairs number considered here (i.e. 500) with a maximum loss of only $\sim 1.3\%$.

Finally, in order to compare the effect of salt concentration on the parasitic currents, two different feeds were compared, namely river water-seawater (0.017M-0.513M) and river water-brine (0.017M-5M), under OCV/2 functioning. In particular, this comparison was made in terms of cell current efficiency (Figure 75), which was defined in Eq.141.

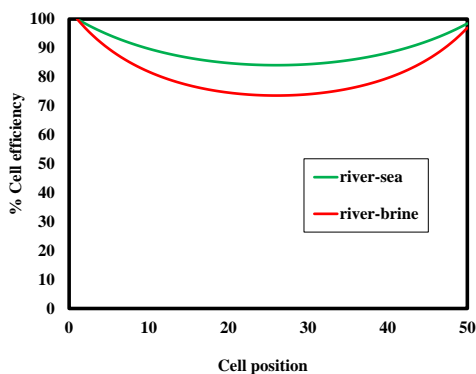


Figure 75. Cell current efficiency as a function of the cell position for different feeds, in $10 \times 10 \text{ cm}^2$ stacks equipped with 50 cell pairs, with Fujifilm Type 10 membranes and with spacers provided with 4 inlet/outlet holes (diameter of 6 mm). Mean flow velocity of the electrolyte solution in each channel equal to 1 cm s^{-1} . Areal blank resistance: $72 \Omega \text{ cm}^2$.

As expected, the reduction of solute concentration in the concentrate compartment resulted in a decrease of the effect of the parasitic currents, as caused by the higher ohmic resistances of the electrolyte solution. Specifically, the minimum cell efficiencies were found to be 84.1% and 73.6% in the case of river water-seawater and river water-brine respectively. Moreover, the average values were 88.9% and 80.9% for river water-seawater and river water-brine respectively. As a result, at lower salt concentrations the effect of parasitic currents had a small impact on the performance of a conventional RED unit, as it accounted for about 11% of the cell current efficiency.

5.5.2 Conventional ED analysis

In this section, the present model was applied to ED processes of seawater to predict the effect of the shortcut currents for large stacks. Stacks with a large number of cell pairs especially when fed by concentrated solutions may suffer from significant parasitic currents [110] that lead to lower current efficiency. In fact, as schematically depicted in Figure 59 (section 5.1) for any useful internal current, depending on the desired desalted/concentrated product, the shunt current in the parallel branch inside the stack requires a higher external current. Since the stack voltage is fixed by the desired generation of salinity gradient and the useful current, a higher power consumption is required. Unless otherwise noted, simulations were performed with stack features identical to those used for the RED analysis (see 5.5.1). The simulations were performed with feed at seawater concentration. Particularly, an average seawater concentration of 30 g l^{-1} (i.e. 0.513 M NaCl) was used.

Figure 76 shows the parasitic current loss as a function of the cell pairs number.

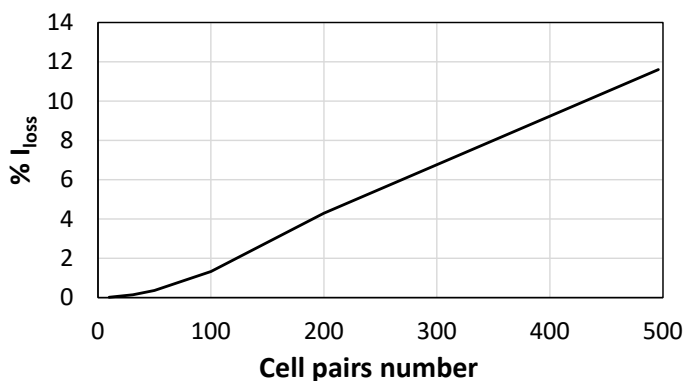


Figure 76. % current loss due to parasitic currents as functions of the cell pairs number in $44 \times 44 \text{ cm}^2$. Inlet concentrations (NaCl): 0.513 M.

Likewise the conventional RED process, cell pair number is crucial for the conventional ED process. In fact, the higher the cell pairs number, the higher the corresponding I_{loss} . As shown in Figure 76, stacks provided with 496 cell pairs (i.e. the simulated maximum number of cell pairs) show a parasitic current loss of $\approx 12\%$. Despite of the low concentration of the feed (i.e. 0.513M), the parasitic current loss is not negligible. A possible solution of this detrimental effect lies in the adoption of modular cell-pair blocks with small parasitic circuits. Particularly, each block can be regarded hydraulically as a single stack. Each block has a small number of cell pairs so that the parasitic currents within each block can be neglected. Additionally, the only ion shortcut may exist along the manifolds connecting the blocks (Figure 77). Therefore, a stack of 496 cell pairs was compared to a stack provided with 16 blocks including 31 cell pairs each. More precisely, it is supposed that each block is fed by a single distributor for each solution (i.e. concentrate or diluate) and that the outlet solution coming from each block is drawn by a single collector. The parasitic current effect was neglected inside a single block of 31 cell pairs, since they count $\approx 0.14\%$ of parasitic loss at 100 A m^{-2} as reported in Figure 76. Therefore, each set of 31 cell pairs mimics a single isolated block. However, the presence of a main manifold that feeds and collects the 16 blocks, results in an additional parasitic pathway. This stack configuration presents the equivalent electric circuit shown in Figure 77.

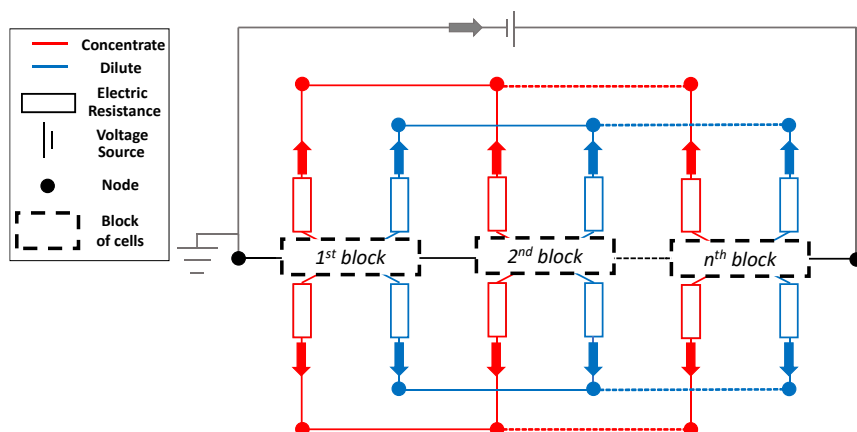


Figure 77. Equivalent electric circuit for a stack provided with n -blocks of 31 cell pairs.

Clearly, all the electrical resistances depend on the geometrical features of the distributors and collectors that feed to or withdraw from the blocks. Therefore, in order to simulate these manifolds, the electrical resistances were chosen to be equal and were varied in the range 100-1000 Ω each. These electrical resistances are hereinafter referred to as R^* .

Figure 78 shows the comparison between the conventional and the block-type configurations for the diluate outlet concentration (Figure 78a) and the parasitic loss of current (Figure 78b) as a function of the external current.

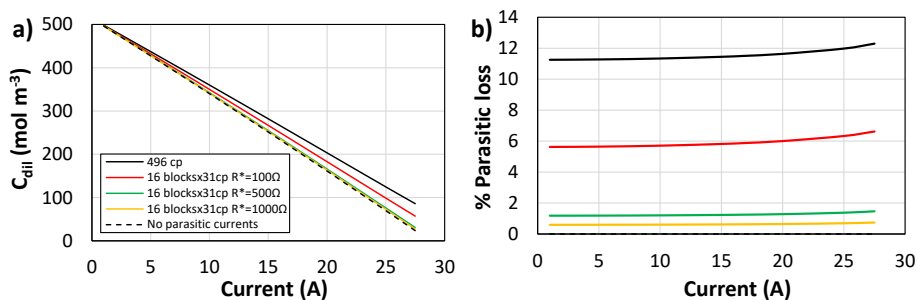


Figure 78. Diluate outlet concentration a) and parasitic loss of current b) as functions of the external current density for an ED stack of 496 cell pairs with $44 \times 44 \text{ cm}^2$ of membrane active area. Manifolds area $440 \times 5 \text{ mm}^2$. Inlet concentrations: 0.513M.

The manifolds area was chosen to be rectangular with area $440 \times 5 \text{ mm}^2$. As reported in Figure 78b, without any measures to tackle the shortcut currents an average of 11.6% decrease of the cell current is expected for a stack of 496 cell pairs. Particularly, the higher the external current, the higher the detrimental effect. Moreover, parasitic currents result in a higher outlet concentration of the diluate

solution. In particular, at the maximum simulated current (i.e. 27.5A) the dilute concentration was found to be ≈ 3.7 times higher due to the presence of the shortcut currents. A simple strategy characterized by the use of isolated blocks with main manifolds (for the fed and collected solutions) represents a solution to this phenomenon. The results reported in Figure 78 refer to R^* equal to 100, 500 and 1000 Ω . Interestingly, by applying a R^* higher than 500 Ω the parasitic current loss was found to be less than 2%.

In the stack provided with 496 cell pairs with the configuration similar to Figure 60 (i.e. no presence of blocks) the electromotive forces and the resistances are clearly a function of the external voltage. This fact results in a variable solutions concentrations depending on the stack voltage. Simulations suggest that the higher the stack voltage, the higher the leakage currents effect. Moreover, attention should be paid to those operating conditions in which solutions concentrations (especially the dilute solution) approach the limiting value. At that point, in fact, the overall stack resistance increases fast, thus enhancing the effect of parasitic currents.

Figure 79 shows the cell current and main manifold current for 496 cell pairs stacks.

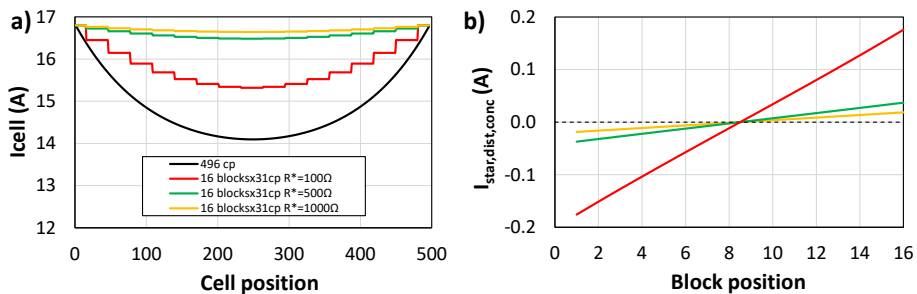


Figure 79. Cell current a) and parasitic current via the main manifold b) for an ED stack of 496 cell pairs with $44 \times 44 \text{ cm}^2$ of membrane active area. Manifolds area $440 \times 5 \text{ mm}^2$. Inlet concentrations: 0.513M.

As can be seen, the stack configuration with multiple blocks arranged electrically in series, the cell current profiles present more homogenous profiles regardless of the R^* values. This is the effect of the lower presence of parasitic currents. Interestingly even using R^* equal to 100 Ω , the minimum cell current (in the central block) is 15.3 A, which is $\approx 9\%$ higher than the minimum current obtained for a single stack composed of 496 cell pairs. The affordability of the adoption of this stack configuration is also highlighted by the low manifold currents depicted in Figure 79b. With R^* values of 500 Ω or more, the maximum manifold current is (in absolute terms) 0.037 A.

Figure 80 shows the diluate outlet concentration and the percentage of parasitic loss for a smaller stack (i.e. $10 \times 10 \text{ cm}^2$) in order to evaluate the impact of different membrane active area.

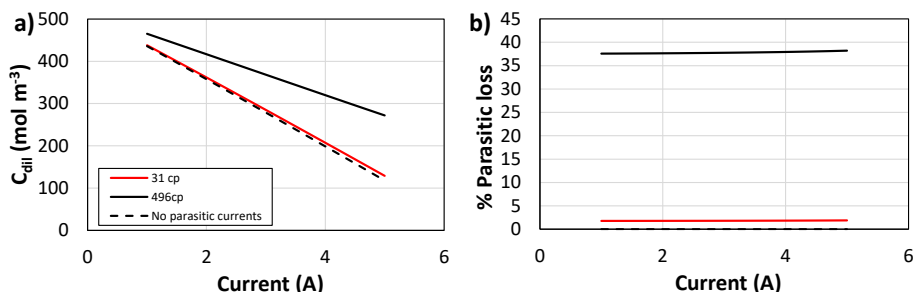


Figure 80. Diluate outlet concentration a) and parasitic loss b) for ED stacks with $10 \times 10 \text{ cm}^2$ of membrane active area. Manifolds area $100 \times 5 \text{ mm}^2$. Inlet concentrations: 0.513 M . Red line: 31 cell pairs. Black line: 496 cell pairs. Dashed line: No presence of parasitic currents.

The smaller size of the membrane active area results to a larger impact of the parasitic currents. Particularly, by operate with a stack of 496cp and 31cp, the percentage of parasitic loss is 37.8% and 1.8% on average, both with a slight increase with the applied external current. Therefore, compared to a stack of $44 \times 44 \text{ cm}^2$, by using a membrane area $10 \times 10 \text{ cm}^2$, the parasitic loss is more than 3 times for 496cp and more of 1 order of magnitude for 31cp on average. This fact is due to the combination of two factors: on the one hand, the increased stack resistance promotes the by-pass of the current through the manifolds and on the other hand, the lower lateral resistances as a consequence of a lower average distance between the inlet and the outlet spacer holes (see Eq. 129). These synergistic factors give rise to worse stack performance.

5.5.3 BMRED analysis

In this paragraph, the impact of the shunt currents will be evaluated for the BMRED process. This analysis was performed to assess the effect of triplet number (up to 500 triplets) as well as current density (up to 300 A m^{-2}) on the parasitic currents. The simulations were performed with stack features identical to the ones used in section 4.7 for the reference case. Figure 81 shows the Gross Energy Density per unit mass and the % of $\text{GED}_{m,loss}$ due to the shunt currents as functions of the number of triplets.

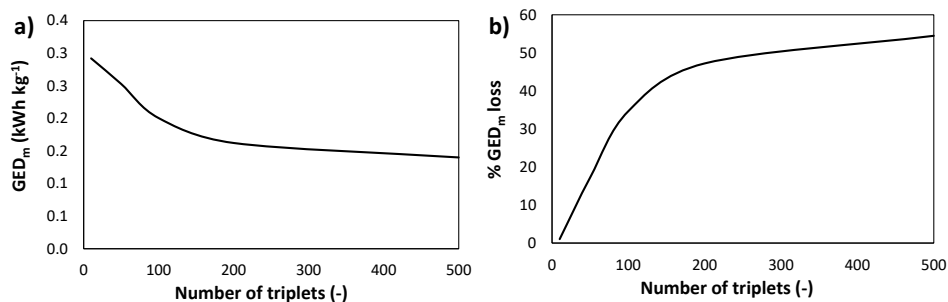


Figure 81. a) Gross Energy Density per kilogram of consumed acid and b) % GED_m loss due to parasitic currents as functions of the triplets number. Mean channel flow velocity: 1 cm s^{-1} . Fixed external current density: 150 A m^{-2} . Inlet concentrations: 1 M HCl and NaOH in the acid and base channels respectively with the presence of 0.25 M NaCl as salt background, and 0.25 M NaCl in the salt channel.

By fixing the current over the external load at 150 A m^{-2} , the Gross Energy Density was found to be within the range $0.14\text{-}0.29 \text{ kWh kg}^{-1}$ as illustrated in Figure 81a. By increasing the number of triplets from 10 to 500, more than half of the produced energy is wasted in the parasitic branches of the equivalent electric circuit. It is worth noting that, in the investigated and design conditions, only modules with less than 30 triplets would allow % GED_m loss lower than 10%. Therefore, the present stack may be used in a framework of blocks made up of a small number of triplets, similarly to conventional ED modules, discussed in section 5.5.2.

Figure 82 shows the current efficiencies (η_c) and the % of η_c loss due to parasitic currents across varying numbers of triplets.

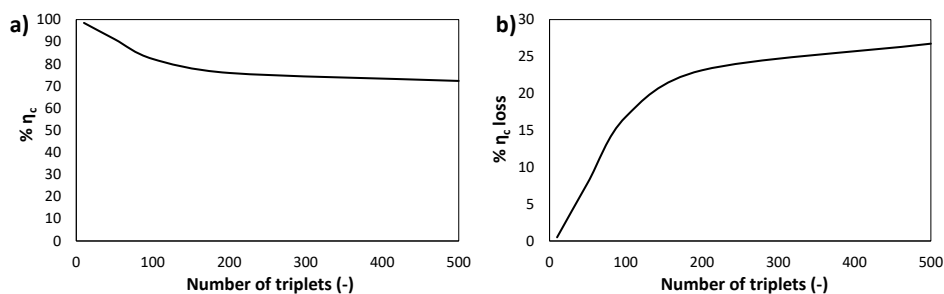


Figure 82. a) Current efficiency and b) % η_c loss due to parasitic currents as functions of the triplets number. Mean channel flow velocity: 1 cm s^{-1} . Fixed external current density: 150 A m^{-2} . Inlet concentrations: 1 M HCl and NaOH in the acid and base channels respectively with the presence of 0.25 M NaCl as salt background, and 0.25 M NaCl in the salt channel.

In terms of current efficiency, Figure 82 shows qualitatively the same outcome as was obtained for GED_m . This is due to the direct proportionality between GED

and η_c . Particularly, the reduction of current efficiency due to parasitic currents was evaluated to be 26.7% at 500 triplets. It is notable that increasing the number of triplets over 100 cells resulted in a flattened profile of the current efficiency curve (Figure 82a). It seems, again, that the shortcut currents have a large effect at low numbers of triplets. When fixing the number of repeating units at 500, the effect of the parasitic currents can be seen by comparing the power density curves for systems with and without shunt currents.

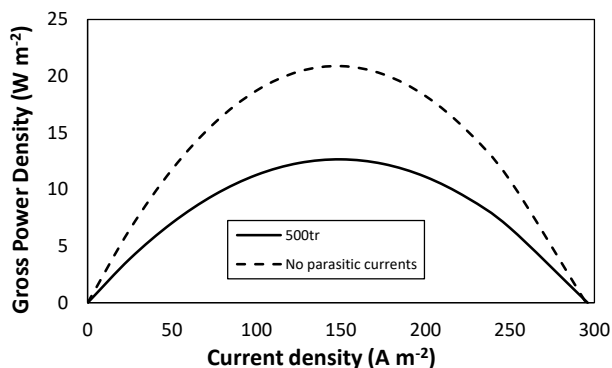


Figure 83. Gross power density curves for a 500 triplets stack with and without the presence of shunt currents. Mean channel flow velocity: 1 cm s^{-1} . Inlet concentrations: 1 M HCl and NaOH in the acid and base channels respectively with the presence of 0.25 M NaCl as salt background, and 0.25 M NaCl in the salt channel.

The impact of parasitic currents on the produced GPD is shown in Figure 83. Significantly, at the peak of the curve, the GPD was 12.7 W m^{-2} , thus meaning it was 39% lower compared to the scenario without parasitic currents.

Figure 84 shows the outlet HCl concentration in the acid tank and the parasitic loss due to leakage currents across varying external current densities for a stack of 500 triplets.

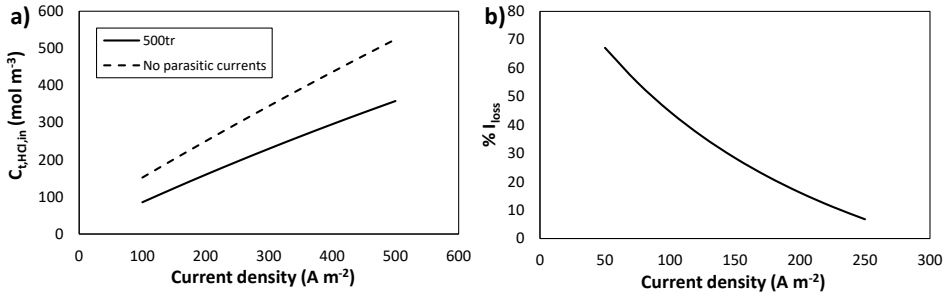


Figure 84. a) outlet HCl concentration in the acid tank and b) % parasitic loss as functions of the triplets number. Mean channel flow velocity: 1 cm s^{-1} . Fixed triplets number: 500 triplets. Inlet concentrations: 1M HCl and NaOH in the acid and base channels respectively with the presence of 0.25M NaCl as salt background, and 0.25M NaCl in the salt channel.

From Figure 84, the detrimental effect of the shunt currents on the electrolyte solutions is evident. The parasitic currents cause part of the energetic content stored in the form of HCl molecules to be wasted (and similarly for the NaOH molecules), thus diminishing the pH gradient that represents the driving force of the BMRED process. Most of the parasitic loss (Figure 84b) occurred at lower current densities. By applying a current density equal to 50 A m^{-2} , most of the current is wasted, as the parasitic current loss (I_{loss}) was found to be higher than 67%. In fact, approaching the Open Circuit Voltage condition (i.e. at 0 A of external current), all the internal electric current is due to the self-discharge of the pH gradient as described in Chapter 4.

Figure 85 shows the cell current and the triplet efficiency as a function of the triplet position for a stack of 500 triplets at different current densities.

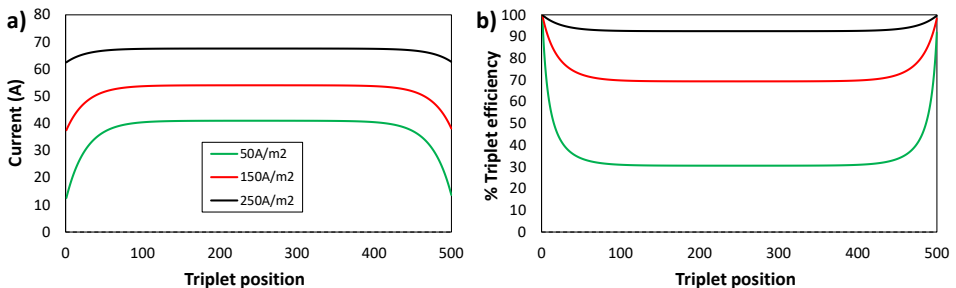


Figure 85. a) Cell current and b) triplet efficiency as functions of the triplet position for different applied current densities (i.e. 50, 150 and 250 A m^{-2}). Mean channel flow velocity: 1 cm s^{-1} . Fixed triplets number: 500 triplets. Inlet concentrations: 1M HCl and NaOH in the acid and base channels respectively with the presence of 0.25M NaCl as salt background, and 0.25M NaCl in the salt channel.

When the applied current density was 50 A m^{-2} , the average cell current was 38.1 A , meaning it was 3.1 times higher than the external current (i.e. 12.5 A). When the current density was fixed at 250 A m^{-2} (i.e. close to the short-circuit condition), the average cell current was 67 A , thus meaning it was only 7% higher than the external one. This behaviour was confirmed by the Triplet efficiency values. In fact, while it was $\approx 93\%$ at 250 A m^{-2} , it reduced to 34.2% on average at 50 A m^{-2} .

5.5.4 BMED analysis

This section is devoted to the evaluation of the effect of shunt currents on BMED processes. Particularly, the effect of the triplets number and the applied external current is assessed. This analysis was performed to show the impact of this detrimental phenomenon on large stacks of industrial interest. The presence of parasitic by-passes through the manifolds result in a lower internal current (as illustrated in Figure 59), and, consequently, in lower production of acid and base concentrations when compared to the scenario without their presence. Shunt currents have an impact on the Specific Energy Consumption and, clearly, on the current efficiency (η_c). Even though the effect of the parasitic currents is qualitatively similar to the one described for conventional ED processes, the same cannot be said for its quantitative influence. The simulations were performed by considering the same stack features as the one described in section 3.7.

Figure 86 show the Specific Energy Consumption (SEC_m) and the % of SEC_m loss due to parasitic currents across varying numbers of triplets.

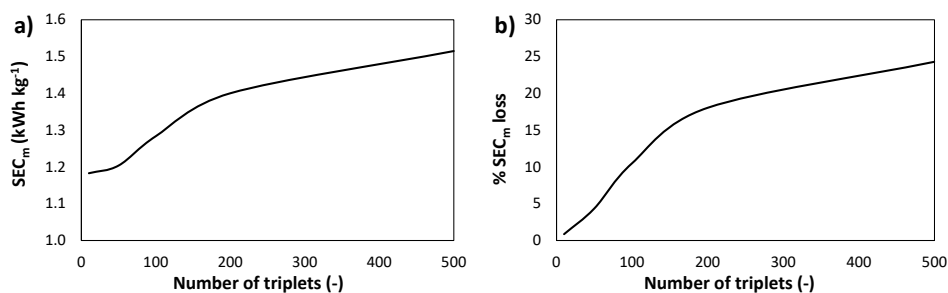


Figure 86. a) Specific Energy Consumption per kilogram of produced acid and b) % SEC loss due to parasitic currents as functions of the triplets number. Mean channel flow velocity: 1 cm s^{-1} . Fixed external current density: 300 A m^{-2} . Inlet concentrations: 0.05 M HCl and NaOH in the acid and base channels respectively with the presence of 0.25 M NaCl as salt background, and 1 M NaCl in the salt channel.

As reported in Figure 86a, the higher the number of triplets, the higher the specific consumption. Particularly, a minimum of 1.18 kWh kg⁻¹ of HCl was recorded at the lowest number of triplets and there was only an increase in the SEC_m of 0.85% due to the shunt currents. However, by increasing the number of triplets to 500, the increase of SEC_m was ≈24%. This results in higher energetic costs required to produce the acidic and alkaline solutions. It is worth noting that, the outlet acid concentration were 0.23M at 500 triplets and 0.36M at 10 triplets, thus exacerbating the performance decrease at higher number of repeating units. Additionally, a lower slope of the curves was obtained at lower number of triplets. This can be attributed to the reduced effect of the blank resistance, which mitigated the effect of the parasitic currents in the first part of the curves. Furthermore, most of the SEC_m increase occurred from 50 to 200 triplets. To obtain negligible parasitic currents, modules of no more than 50 triplets should be used for obtaining %SEC_m loss lower than 9% (Figure 86b).

Figure 87 shows the current efficiencies (η_c) and the % of η_c loss due to parasitic currents across varying numbers of triplets.

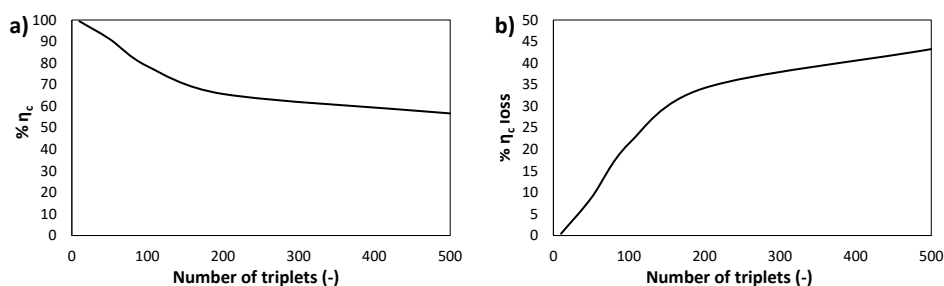


Figure 87. a) Current efficiency and b) % η_c loss due to parasitic currents as functions of the triplets number. Mean channel flow velocity: 1 cm s⁻¹. Fixed external current density: 300 A m⁻². Inlet concentrations: 0.05M HCl and NaOH in the acid and base channels respectively with the presence of 0.25M NaCl as salt background, and 1M NaCl in the salt channel.

The qualitative trend of the current efficiency (η_c) reflects the SEC_m trend (Figure 86), and this is due to the inverse relationship between SEM_m and η_c . As illustrated in Figure 87a, current efficiency decreases as a function of the triplet number. In the simulated stack for the investigated operating conditions, very high current efficiencies (i.e. >90%) were recorded for modules of lower than 50 triplets. When the number of repeating cells was increased, a fall in the current efficiency was observed, leading to a minimum of 57% for a stack provided with 500 triplets. Figure 87b shows the loss of current efficiency due to parasitic currents. Moreover, as reported for the specific consumption, a sharp increase in the efficiency loss was obtained in the range of 50-200 triplets, and this then flattened towards higher

numbers of cells. In this triplet number interval, the loss of efficiency due to shunt currents ranged from 9-43%.

Figure 88 shows the outlet HCl concentration in the acid tank and the parasitic loss due to parasitic currents across varying external current densities for a stack of 500 triplets.

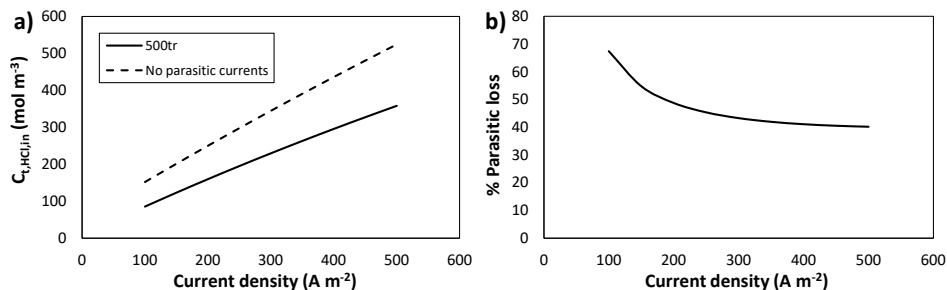


Figure 88. a) outlet HCl concentration in the acid tank and b) % parasitic loss as functions of the triplets number. Mean channel flow velocity: 1 cm s^{-1} . Fixed triplets number: 500 triplets.

In terms of the acidic and basic solutions that were produced, the presence of parasitic currents dramatically affected the stack performance. When increasing the current density, the two curves in Figure 88a diverged. This could suggest that increasing the applied current leads to worse performance. However, when 100 A m^{-2} was applied, the outlet acid concentration was 44% lower than the scenario without the presence of parasitic currents, whereas applying 500 A m^{-2} led to a relative difference of 32%. Therefore, a lower parasitic effect can be obtained by increasing the current density. This fact is confirmed by Figure 88b, in which the parasitic loss is reported. Particularly, the parasitic loss passes from $\approx 67\%$ at 100 A m^{-2} to $\approx 40\%$ at 500 A m^{-2} . It is worth noting that these huge parasitic losses were reached by using a stack mounting 500 triplets, which represents the worst case investigated.

Finally, Figure 89 shows the cell current and the triplet efficiency as a function of the triplet position for a stack of 500 triplets at different current densities.

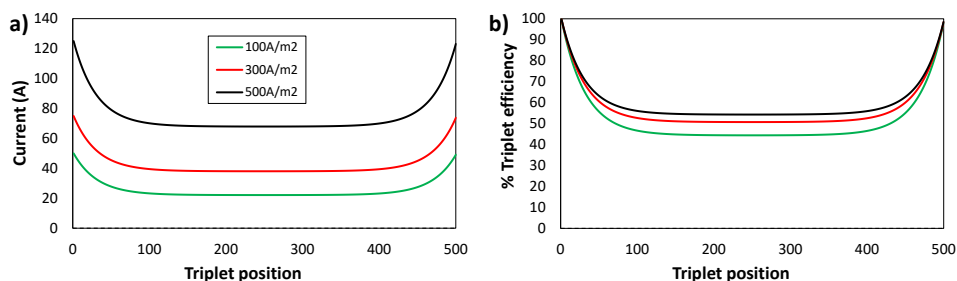


Figure 89. a) Cell current and b) triplet efficiency as functions of the triplet position for different applied current densities (i.e. 100, 300 and 500 A m⁻²). Mean channel flow velocity: 1 cm s⁻¹. Fixed triplets number: 500 triplets.

By looking at Figure 89a, it can be seen that, by increasing the external current, a more pronounced current profile is obtained. This may lead us to wrongly conclude that increasing the applied current causes worse performance. However, compared to the external current, the relative decrease of the triplet currents obtained at 500 A m⁻² was $\approx 40\%$ on average, while at 100 A m⁻² the relative decrease was greater at $\approx 49\%$. This means that the triplet efficiency at 500 A m⁻² was better, as illustrated in Figure 89b.

6 Acid/Base Flow Battery

Electrical energy storage can enhance the efficiency in the use of fluctuating renewable sources, e.g. solar and wind energy. The Acid/Base Flow Battery is an innovative and sustainable process to store electrical energy in the form of pH and salinity gradients via electro-dialytic reversible techniques. Two electro-membrane processes are involved: Bipolar Membrane Electrodialysis during the charge phase and its opposite, Bipolar Membrane Reverse Electrodialysis, during the discharge phase. This chapter aims at predicting the performance of this energy storage device via the development of a dynamic mathematical model based on a multi-scale approach with distributed parameters. The steady-state multi-scale model was fully described in the previous chapters 3 and 4. The dynamic model was preliminary validated under both BMED and BMRED conditions by a comparison with experimental data and a good agreement was found. A sensitivity analysis was performed to identify the most detrimental phenomena. Results indicate that Round Trip Efficiency may be dramatically affected by parasitic currents in the manifolds. Therefore, they may represent the main limit to the present technology performance in scaled-up stacks to converting more power. Suitable geometries and operating conditions should be adopted to tackle this issue (e.g. isolated blocks), thus enhancing the battery Round Trip Efficiency. Compared to closed-loop operation, the Yo-Yo configuration allows better results in term of charge/discharge energy density. Finally, the AB-FB was simulated across upscaled scenarios to demonstrate the technology at kW-MW scale.

6.1 General Overview

In last decades, the demand of renewable energy is rapidly increasing [225]. Moreover, there is a growing interest in finding energy storage technologies for efficient and robust supply chains [226]. The compensation of the mismatch between energy demand and generation from systems harvesting fluctuating sources, such as sun and wind, is crucial for boosting a larger penetration of renewable energies [227]. In this regard, suitable storage systems should be flexible enough in managing the energy surplus, enabling a usage from kWh scale to MWh scale. Furthermore, they should satisfy some criteria, such as safety, sustainability, durability, economic competitiveness and site-independence. The large variety of electrical energy storage technologies can be classified on the basis of the form of the stored energy [228]. Among the electrochemical systems [229,230], flow batteries store the energy in the electrolyte flowing through the device [231,232]. Vanadium Redox Flow Batteries are the mostly studied so far, both by modelling [233,234] and experiments

[235,236], including the development of different membranes [237]. Flow batteries are considered among the most suitable energy storage technologies since they could potentially satisfy all the above mentioned criteria. However, they still suffer from high costs and environmental issues [238–241]. In this context the Concentration Gradient Flow Battery (CGFB) is an innovative electro-dialytic battery that uses harmless NaCl solutions at different salinity as storage vehicles processed in units provided with monopolar ion-exchange membranes [242]. The salinity gradients are generated during the charge phase by Electrodialysis (ED), and are converted by a controlled mixing (selective transport through the membranes) during the discharge phase by Reverse Electrodialysis (RED) to return electrical energy [243]. ED is a well-known desalination technique used for water desalination [244], municipal [245] and industrial [246] wastewater treatment, and other purposes in chemical, biochemical, food and pharmaceutical processes, including industrial applications. RED is the opposite process, where the salinity gradient between two solutions, is used to harvest electricity [247]. Prototypal installations in real life environments have been carried out so far [248]. The ED-RED coupling within the CGFB is currently installed as pilot scale device at The Green Village (Delft, The Netherlands), coupled to a photovoltaic system with an expected power-to-energy ratio of 0.1 (i.e. 1 kW vs 10 kWh) [249]. The theoretical energy density of the electrolyte solutions is in the order of 1 kWh m^{-3} , much lower than that of Vanadium Redox Flow Battery (up to $\sim 35 \text{ kWh m}^{-3}$ [239]). The energy density can be enhanced by adding a bipolar membrane (BPM), thus allowing for the storage of energy in the form of acid, base and saline solutions (i.e. pH and salinity gradients).

6.2 *The Acid/Base Flow Battery: working principle*

Acid/Base Flow Battery (AB-FB) could represent an innovative, safe and sustainable way to store energy with high performance [250]. The AB-FB is an electro-dialytic battery based on the reversible water dissociation. In particular, the Bipolar Membrane Electrodialysis (BMED) process uses electrical energy to produce acidic and alkaline solutions that are then exploited in the reverse process, i.e. the Bipolar Membrane Reverse Electrodialysis (BMRED) to generate electricity.

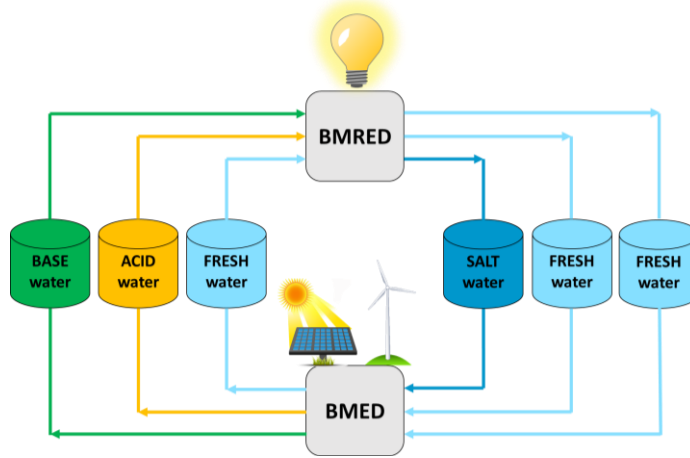


Figure 90. Acid/Base Flow Battery scheme.

The BMED and BMRED stack are the reaction units of the AB-FB. During the charge phase (BMED), water dissociation occurs inside the BPM, whilst during the discharge phase (BMRED) the neutralization reaction takes place, as schematically shown in Figure 91.

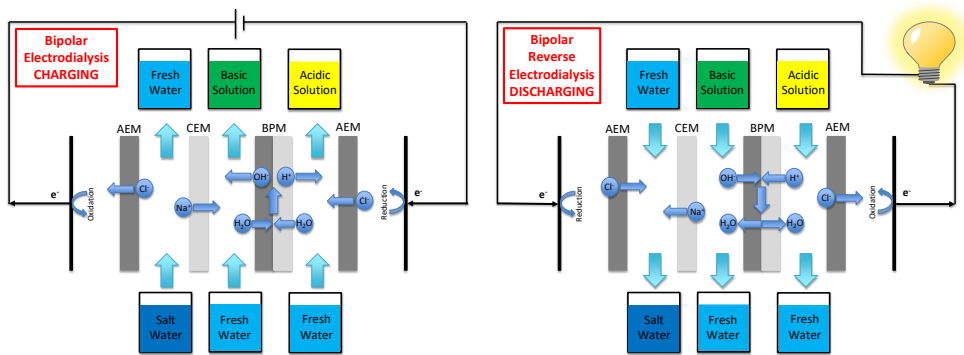


Figure 91. Charging a) and discharging b) operation of the Acid/Base Flow Battery.

Theoretically, an energy density of about 11 kWh m^{-3} can be stored in 1 M acidic and alkaline solutions, although a measured energy density of 2.9 kWh m^{-3} was reported by van Egmond et al. [250]. However, this value is comparable with those obtained with Pumped Hydroelectric Systems ($0.5\text{--}2 \text{ kWh m}^{-3}$) and Compressed Air Energy Storage systems ($2\text{--}6 \text{ kWh m}^{-3}$) that are, on the other hand, strongly site-dependent technologies [228]. Compared to Li-ion or Lead-Acid batteries, the AB-FB suffers of a lower energy density ($200\text{--}620 \text{ kWh m}^{-3}$ for Li-ion battery and $30\text{--}90 \text{ kWh m}^{-3}$ for Lead-Acid battery), but it is designed to work with discharge times of

hours delivering powers in the order of MWs, whilst the former ones have discharge times of minutes and delivered powers in the kW - MW range [251]. The potential Levelized Cost of Storage (LCOS) of AB-FBs (0.44 € kWh⁻¹) would be lower than that estimated for Li-ion batteries (0.61 € kWh⁻¹) but higher than that calculated for Lead-Acid batteries (0.29 € kWh⁻¹) [252].

By testing commercial membranes [253] or custom membranes [254], pioneering studies highlighted the need of high-selective membranes to implement real applications of the AB-FB concept. After several years in which this interesting technology has been almost ignored, more recently some researchers have carried out some studies. Kim et al. [255] reported stable efficiencies over nine cycles, but the operation cyclability was then seriously compromised. This behaviour was attributed to the protons leakage from the acid chamber to the salt and electrode chambers (single-cell experiments). Nine stable cycles were performed in a single-cell unit also by van Egmond et al. [250] who measured a power density of 3.7 W m⁻² per membrane and a round-trip efficiency up to 13.5%, with an energy density up to 2.9 Wh kg⁻¹, as mentioned above. The coulombic efficiencies were moderate (13%–27%), mainly due to unwanted protons and hydroxyl ions transport, which caused an energy loss of ~50%. Moreover, a high internal resistance caused low voltage efficiencies (~50%). Interestingly, during the discharge phase the current density was limited at 15 A m⁻² by delamination (or ballooning) issues, due to a recombination rate of protons and hydroxyl ions higher than the diffusion of the produced water. In order to enhance the power density and the process efficiency, suitable tailor-made membranes are needed.

A similar general conclusion can be drawn from the experimental results by Xia et al. [256] (one-cell unit, 20 cycles). Moreover, the AB-FB performance could be theoretically enhanced by using higher acid/base concentrations (1 M was the “standard” maximum used so far), thus requiring further improved transport properties of the membranes. Another important aspect concerns the need to process larger volumes of the electrolyte solutions in order to convert higher amounts of energy, thus requiring the use of batteries with a higher number of triplets (repetitive units). In such stacks, additional phenomena affecting the process performance arise, namely shunt currents via manifolds [257]. Therefore, some measures have to be taken in the design of scaled-up units, e.g. the implementation of serial flow layouts with isolated blocks.

In order to promote the techno-economic competitiveness of the AB-FB, validated modelling tools can be very useful to assess the process performance and to drive the design and optimization. However, to the authors' knowledge, no studies have been devoted so far to the modelling of AB-FBs. On the other hand, the

phenomenology taking place in an electro-dialytic battery with BPMs is very complex, as it includes fluxes of different kind for several ion species and for water, electrochemical equilibria, Ohmic and non-Ohmic voltage drops, and hydrodynamics. Moreover, the behaviour of an AB-FB is intrinsically transient. In order to simulate such complex systems, multi-scale models can be suitable. Previous works showed the effectiveness of multi-scale tools in providing reliable and accurate predictions, both for ED [258] and RED [112] processes, requiring only empirical data on the membrane properties.

In this Chapter, the multi-scale models developed in Chapters 3 and 4 for BMED and BMRED, respectively, were integrated to elaborate a unique process model able to describe the main phenomena involved in AB-FB systems, thus providing a tool useful to guide the battery design. A wide sensitivity analysis was performed to characterize the battery under several working scenarios. The main figure of merits of the battery will be reported and the impact of the main detrimental phenomena on the battery performance will be assessed.

6.3 *Mathematical modelling of the Acid/Base Flow Battery*

Many irreversibility sources are responsible for the reduction of the process efficiency of the AB-FB. Some of them are associated to the non-ideal transport properties of the ion exchange membranes, others are correlated to geometric features of the stack and operating conditions. With particular reference to the second group, the main issues for internal losses in BMED/BMRED units may be identified in Ohmic and non-Ohmic voltage drops, pressure drops, and concentration polarization phenomena, thus affecting the efficiency of an AB-FB as well. In addition, ionic shortcut currents via manifolds, already discussed in Chapter 5, may arise in stacks with a large number of repetitive cells where the electrical resistance of the parasitic pathways is comparable with the cell resistance in the (desired) direction perpendicular to the membranes.

Note that the various phenomena involved in the internal losses are of different nature and scale but related each other, thus single separate models can only provide partial predictions. On the other hand, an integrated mathematical multi-scale model is the most effective tool to simulate all these phenomena and their interactions at the same time. With specific reference to the shunt currents, as illustrated in Chapter 5, suitable models simulating the electrical behaviour of the stack are needed in order to have reliable predictions. Therefore, a comprehensive AB-FB process simulator based on the multi-scale models described in Chapters 3 and 4 was developed.

The AB-FB tool presents the same multi-scale structure elaborated for the BMED and BMRED models but it also includes a higher scale related to the external hydraulic circuit. This level takes into account the presence of the external hydraulic circuit (and eventually of auxiliary units) as well as the tanks for the storage of the electrolyte solutions, and it will be presented in the next section. Therefore, the AB-FB multi-scale model includes four dimensional scales and five levels, each of them simulated by its specific sub-model(s), and it requires some inputs, as schematically shown in Figure 92. The unidirectional black arrows indicate towards what model-scale the input parameters are sent to. The bidirectional blue arrows indicate how the model levels communicate with each other.

Remember that the process simulated, i.e. the AB-FB, is an electrical energy storage system, thus its operation is transient. The electrolyte solutions can be simply recirculated continuously to the tanks or can be fed to the stack with multiple-passage operations. Moreover, the battery has to work for a number of charge/discharge cycles. The present process model can simulate all these features.

This simulation tool was implemented in the gPROMS® process simulator environment. Unlike the more used sequential modular approach, this software presents an advanced equation-oriented structure. The solution of the mathematical problem is obtained by built-in solvers. gPROMS enables the choice of important numerical constraints especially in the iteration process of the nonlinear solvers, e.g. the maximum residual of each equation. A set of parameters was chosen as a compromise between numerical accuracy and computational time. As a result, under steady-state condition, mass balances residuals were always found to be lower than 10^{-11} . This results in a mass balance residual of less than 0.1% for a round-trip cycle.

The model output consists of the distribution of the variables along with the prediction of the performance parameters of the AB-FB system. Therefore, the developed model provides essential information for the unit design (e.g. manifold size, channel size) and for the choice of operating conditions (e.g. current density, flow rates) able to minimize all the detrimental phenomena.

As shown in Figure 92, the model is completed by Computational Fluid Dynamics (CFD) simulations of spacer-filled channels. CFD results are used in the form of correlations as input data for the triplet sub-model (mass transport) and the stack sub-model (hydraulic friction).

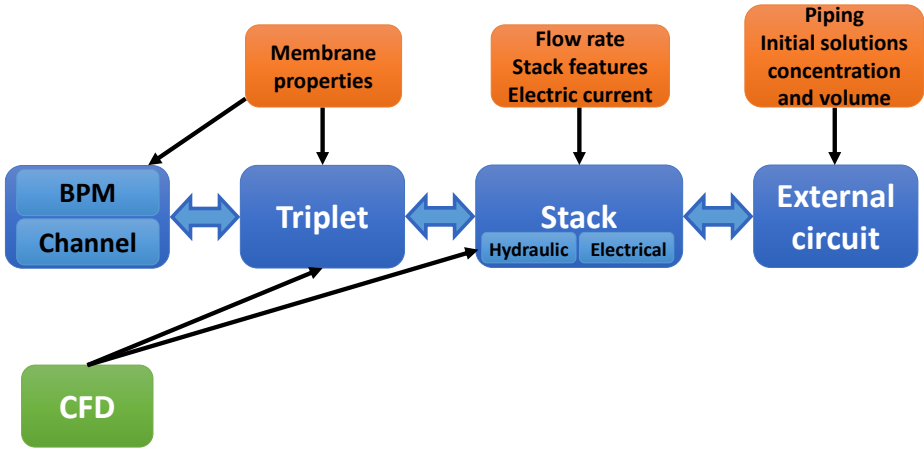


Figure 92. Multi-scale model scheme. The dark blue boxes indicate the four dimensional scales of the model, which interact each other and are integrated in a single tool. Light blue boxes indicate sub-models. Orange boxes report the main input parameters. Correlations for flow and mass transfer characteristics coming from Computational Fluid Dynamics (CFD) simulations are used as input for the triplet simulation and the stack hydraulic sub-model.

6.3.1 Highest scale: External hydraulic circuit and tanks model

The highest scale of the model aims at simulating mass balances and pressure drops in the external hydraulic circuits of the three solutions. It is a 0-dimensional model that can simulate the dynamic behaviour of closed-loop operations with recirculation of the solutions in the tanks. Moreover, hydraulic losses in accessory devices (e.g. valves and pumps) can be included in the calculation of the total pumping power. Dynamic mass balances within the acid and salt storage tanks can be written as follows:

$$\frac{d(\rho_{t,sol}V_{t,sol})}{dt} = Q_{t,in,sol} \rho_{t,in,sol} - Q_{t,out,sol} \rho_{t,out,k} \quad (143)$$

$$\frac{d(C_{t,HCl,out,sol}V_{t,sol})}{dt} = Q_{t,in,sol} C_{t,HCl,in,sol} - Q_{t,out,sol} C_{t,HCl,out,sol} \quad (144)$$

$$\frac{d(C_{t,NaCl,out,sol}V_{t,sol})}{dt} = Q_{t,in,sol} C_{t,NaCl,in,sol} - Q_{t,out,sol} C_{t,NaCl,out,sol} \quad (145)$$

where $V_{t,sol}$ is the solution volume in m^3 , ρ_t^k is the mass density of the solution within the tank, $Q_{t,in}^k$, $Q_{t,out}^k$ are the inlet and outlet volume flow rates, respectively, $C_{t,HCl,in}^k$, $C_{t,HCl,out}^k$, $C_{t,NaCl,in}^k$, $C_{t,NaCl,out}^k$ are the inlet and outlet hydrochloric acid and the inlet and outlet sodium chloride concentrations (all expressed in $mol\ m^{-3}$).

For the base storage tank, the following equations can be written:

$$\frac{d(\rho_{t,b}V_{t,b})}{dt} = Q_{t,in,b} \rho_{t,in,b} - Q_{t,out,b} \rho_{t,out,b} \quad (146)$$

$$\frac{d(C_{t,NaOH,b}V_{t,b})}{dt} = Q_{t,in,b} C_{t,NaOH,in,b} - Q_{t,out,b} C_{t,NaOH,out,b} \quad (147)$$

$$\frac{d(C_{t,NaCl,b}V_{t,b})}{dt} = Q_{t,in,b} C_{t,NaCl,in,b} - Q_{t,out,b} C_{t,NaCl,out,b} \quad (148)$$

Of course, inlet quantities for the tank correspond to outlet quantities for the stack, and *vice versa*. Therefore, $Q_{t,out,sol}$, which is imposed, corresponds to $Q_{d,sol,1}$ for a single stack. In all the simulations, a perfect mixing of the solution in the tank was assumed. Other operations could be with single pass or with multiple passages, where a complete or partial phase (charge or discharge) occurs for the solutions flowing through the stack, which are not recirculated to the feed tank. These operating conditions can be treated as steady or sequences of steady states, adapting the previous equation for mass balances with simpler expressions.

In the hydraulic circuit of any solution, distributed pressure drops in each pipeline tract and distributed pressure drops in each singularity are given by

$$\Delta P_{dist,sol} = 8 f_{ext} \frac{L_{ext} \rho Q_{t,out,sol}^2}{\pi^2 d_{ext}^5} \quad (149)$$

$$\Delta P_{loc,sol} = 8 k_{ext} \frac{\rho Q_{t,out,sol}^2}{\pi^2 d_{ext}^4} \quad (150)$$

in which f_{ext} , L_{ext} and d_{ext} are the friction factor, the length, and the diameter of the generic tract, and k_{ext} is the local loss coefficient of the generic singularity (tank entry or exit, valves or fittings). When the flow is laminar f_{ext} is simply calculated as

$$f_{ext} = \frac{64}{Re_{ext}} \quad (151)$$

otherwise f_{ext} is calculated following the well known Blasius equation:

$$f_{ext} = 0.316 Re_{ext}^{-0.25} \quad (152)$$

The total pressure drop $\Delta P_{tot,sol}$ in each of the three hydraulic circuits is obtained by the sum of the stack and the external parts:

$$\Delta P_{tot,sol} = \Delta P_{stack} + \Delta P_{dist,sol} + \Delta P_{loc,sol} \quad (153)$$

6.3.2 Performance parameters of the Acid/Base flow battery

The AB-FB performance was expressed either in terms of quantities related to each single phase, i.e. charge (BMED) and discharge (BMRED) already formulated

in chapters 3 and 4 (e.g. GPD), and in terms of parameters relevant to full cycles of charge and discharge. Among the latter, the Voltage Efficiency (VE) is the ratio between the average external voltage during discharge and charge. The VE represents an estimation of the internal resistance impact on the stack voltage. It is given by

$$VE = \frac{t_c \int_0^{t_d} U_{ext} dt}{t_d \int_0^{t_c} U_{ext} dt} \quad (154)$$

where t_d and t_c are the discharge and charge process times.

The Coulombic Efficiency (CE) is the ratio between the amount of electric charge transported during the discharge and during charge. It is calculated by

$$CE = \frac{\int_0^{t_d} I_{ext} dt}{\int_0^{t_c} I_{ext} dt} \quad (155)$$

Finally, the Round Trip Efficiency (RTE), which is among the main figures of merit to assess the performance of energy storage technologies, is calculated as the ratio between the (gross) energy delivered to the external load during the discharge phase and that provided by the power supply during the charge phase:

$$RTE = \frac{\int_0^{t_d} I_{ext} U_{ext} dt}{\int_0^{t_c} I_{ext} U_{ext} dt} \quad (156)$$

Finally, in order to assess the impact of parasitic currents on the battery efficiency, the relative loss of RTE with respect to the ideal case without parasitic currents was calculated

$$RTE_{loss} = \left(1 - \frac{RTE}{RTE_{no\ par}} \right) \quad (157)$$

in which $RTE_{no\ par}$ is the RTE computed by simulating the corresponding reference case neglecting shunt currents, carried out by a simplified model where the stack is without the parasitic branches in the equivalent electric circuit (thus it reduces to a series of identical cell resistances and electromotive forces, together with the blank resistance and the external resistance).

6.3.3 Battery configurations

The model was used for the simulation of various flow layouts, including multiple-stage configurations. Hydraulic layouts can be grouped into two main classes, namely open-loop and closed-loop (i.e. batch recirculation of solutions) configurations. Both the two groups could have a variety of possible layouts with multiple stages arranged in series, in parallel, or with hybrid schemes. Finally, a

battery operated with the so-called “Yo-Yo” process mode (multiple passages of the solutions through the stack without recirculation) can be devised. This configuration has hybrid features between open-loop and batch operations, conferring the advantage of avoiding a dissipating mixing, while maintaining compact stack sizes.

6.3.3.1 Closed-loop operation

The principle of the operations with hydraulic closed loop configuration is schematically illustrated in Figure 93.

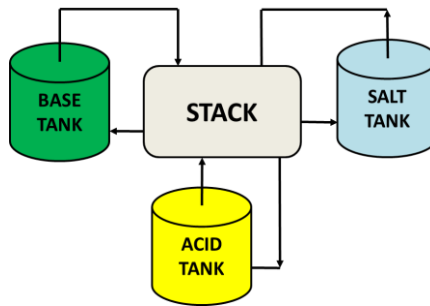


Figure 93. Closed-loop operation.

In principle, the solutions are recirculated in the source tanks until the target concentration for the charge/discharge phase is reached. Following this, the opposite phase commences.

6.3.3.2 Open-loop operation

A general scheme of the open-loop operation is shown in Figure 94.

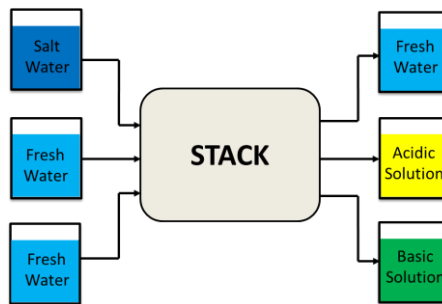


Figure 94. Open-loop operation

The open-loop process consists of the passage of the electrolyte solutions from the inlet tanks to the outlet ones, without recirculation. This can occur in configurations, with either single or multiple passages, until the target concentration

of the charge/discharge phase is reached. From the thermodynamic point of view, open-loop operations are expected to be more efficient than closed-loop operations, because they avoid the dissipating mixing that would occur with the recirculation of the solutions in the tanks.

The model was then used to predict the performance of open-loop multiple-passage configurations, where the solutions pass through a single stack several times until the concentration target of the charge/discharge phase (“Yo-Yo” operation, Figure 95) is reached. Both charge and discharge are simulated as a sequence of steady-state flow stages.

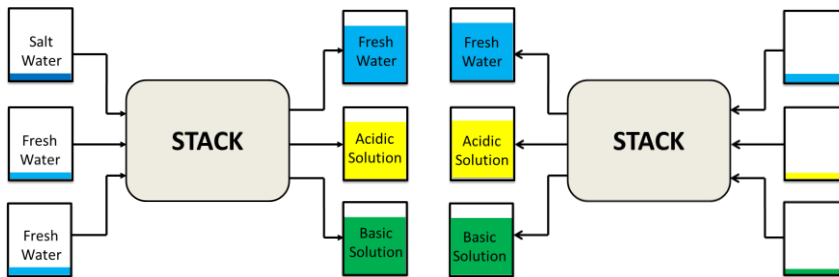


Figure 95. Scheme of the yo-yo operation, based on the open-loop multiple passages process mode.

6.4 AB-FB dynamic model validation

Steady-state model validation for BMED and BMRED have already been shown in Chapter 3 and 4, respectively. In this section, the dynamic model validation is shown for the two battery phases (i.e. charge and discharge). Specifically, the model validation was performed with two process configurations: closed-loop and yo-yo. The experimental set-up was the same as the one used for the BMED and BMRED tests, described in Chapter 3 and 4, respectively. All the error bars of experimental results have been omitted since the maximum deviations were negligible.

The model required a calibration in order to well-predict the behaviour of the battery across long periods of time. The model was calibrated with a tuning parameter of the membrane resistances and by varying the ion diffusivities in the membranes, in order to minimize the discrepancy between the experimental results and the model predictions in terms of external voltage and acid and base concentrations in the time evolution (closed-loop) or in the multiple passages (yo-yo). The ion diffusivities obtained from the model calibration are reported in Table 19.

Table 19. Membrane diffusivities used for AB-FB dynamic model calibration.

| | | AEM | CEM | AEL | CEL |
|-----------------------------|-----------------------------|---------|---------|---------|---------|
| Thickness | μm | 130 | 130 | 95 | 95 |
| Areal resistance | $\Omega \text{ cm}^2$ | 7 | 6 | 6.5 | 6.5 |
| H ⁺ diffusivity | $\text{m}^2 \text{ s}^{-1}$ | 4.0E-10 | 4.9E-11 | 2.0E-11 | 0.7E-11 |
| Na ⁺ diffusivity | $\text{m}^2 \text{ s}^{-1}$ | 4.8E-11 | 1.5E-11 | 1.6E-11 | 0.5E-11 |
| Cl ⁻ diffusivity | $\text{m}^2 \text{ s}^{-1}$ | 8.5E-11 | 3.0E-11 | 1.7E-11 | 0.6E-11 |
| OH ⁻ diffusivity | $\text{m}^2 \text{ s}^{-1}$ | 9.5E-11 | 1.4E-10 | 1.9E-11 | 0.6E-11 |

The tuning parameter for the membrane resistances was multiplied by the reference values of the resistances (as reported on the manufacturer technical sheet). This allowed to take into account the composition and concentration variations of the electrolyte solutions during both the battery phases, by changing the effective membrane resistance values. The effective resistance of any membrane is defined as

$$R_{eff,LEM} = \beta_r \cdot R_{LEM} \quad (158)$$

in which, the calibration parameter β_r is defined as Eq. 159 for BMRED and Eq. 160 for BMED:

$$\beta_r = 1 + 10^{-3} \cdot e^{\frac{60000}{C_{H^+,a}^2(0)}} \cdot \frac{0.34}{\pi} \cdot \tan^{-1}(C_{Na^+,a}(0) - 11) + 0.83 \quad (159)$$

BMRED

$$\beta_r = 3.7 - 0.32 \cdot C_{Na^+,s}^{0.3}(0) \quad \text{BMED} \quad (160)$$

6.4.1 Closed-loop model validation

The present model was calibrated and validated to simulate both the charge and the discharge phases dynamically. Two sets of charge tests were investigated in the closed-loop layout. The first set of data regards a fixed charge current density at 100 A m⁻², and inlet compositions of distillate water in the acid and base tanks and 1 M of NaCl concentration in the salt tank. The following external voltage curves were obtained (Figure 96).

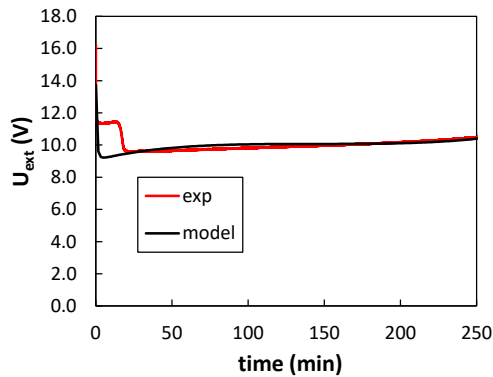


Figure 96. Comparison between experimental results and model predictions of the external voltage as a function of time in the charge phase. Process configuration: closed-loop. Fixed current density: 100 A m^{-2} . Inlet conditions: distillate in the acid and base tanks, 1 M NaCl in the salt tank. Mean flow velocity: 0.2 cm s^{-1} . Blank resistance: 72 ohm cm^2 .

The model predictions of stack voltage are in good agreement with the experimental results during the charge phase. Over the 250 minutes of the charging process, the external voltage was $\approx 10 \text{ V}$ for both the empirical data and the model predictions. The external voltage is almost constant because the only variation can be attributed to the electromotive force. These results indicate that, disregarding the first tract of approximately 40 minutes in which a step was observed experimentally in the shape of the curve, the maximum discrepancy was found to be $\approx 1\%$. The shape of the first tract obtained empirically was attributed to the fact that the salt reservoir was not perfectly mixed.

Figure 97 shows the HCl and NaOH concentration in the acid and base tank, respectively, over time for the same test.

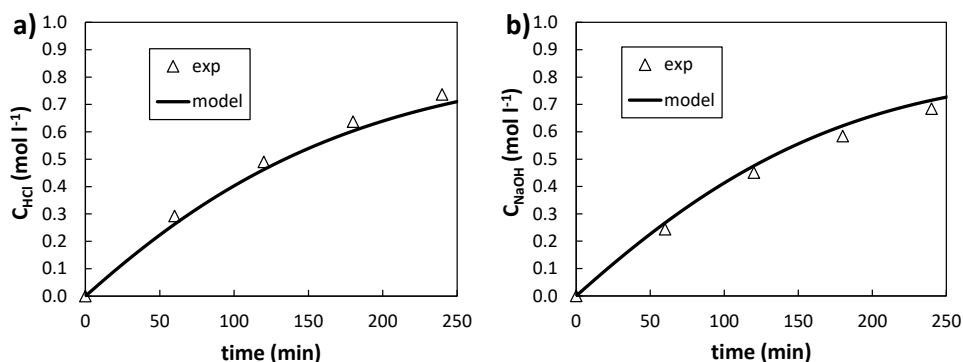


Figure 97. Comparison between experimental results and model predictions of a) HCl concentration in the acid tank and b) NaOH concentration in the base tank as a function of time in the charge phase. Process configuration: closed-loop. Fixed current density: 100 A m^{-2} . Inlet conditions: distillate in the acid and base tanks, 1 M NaCl in the salt tank. Mean flow velocity: 0.2 cm s^{-1} . Blank resistance: 72 ohm cm^2 .

The simulated curves follow the experimental data very closely. The maximum discrepancy was 10.1% and 6.4% for the acid and the base concentration, respectively, occurring around minute 60 and 180, respectively. Overall, the average discrepancy was found to be 6.6% and 4.7% for the acid and base tanks, respectively.

A second set of tests in the charge phase was performed with a fixed charge current density of 200 A m^{-2} , and inlet compositions of distillate water in the acid and base tanks and 2 M of NaCl concentration in the salt tank. Figure 98 shows the comparison between the experimental data and the model outcome for the external voltage during the charging period.

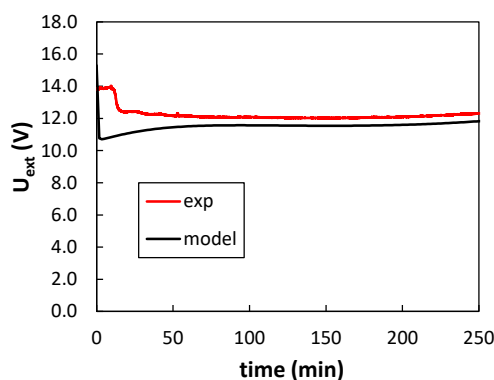


Figure 98. Comparison between experimental results and model predictions of the external voltage as a function of time in the charge phase. Process configuration: closed-loop. Fixed current density:

200 A m^{-2} . Inlet conditions: distillate in the acid and base tanks, 2 M NaCl in the salt tank. Mean flow velocity: 0.2 cm s^{-1} . Blank resistance: 72 ohm cm^2 .

The process time was limited to 250 minutes and the simulated external voltage curve shows a relatively constant difference from 50 minutes after the start onward. This average voltage difference was $\approx 0.5 \text{ V}$, thus resulting in a relative difference of $\sim 4.4\%$ on average. Similarly to the previous experiment, a voltage step was observed experimentally in the first part of the curve, which was attributed to the imperfect mixing of the salt reservoir. Therefore, neglecting the first tract in the calculation, the model predicts an external voltage of $\sim 11.6 \text{ V}$, which is in acceptable agreement with the empirical result of $\sim 12.1 \text{ V}$.

Figure 99 shows the comparison between experimental data and model results of the HCl and NaOH concentration profiles as functions of time.

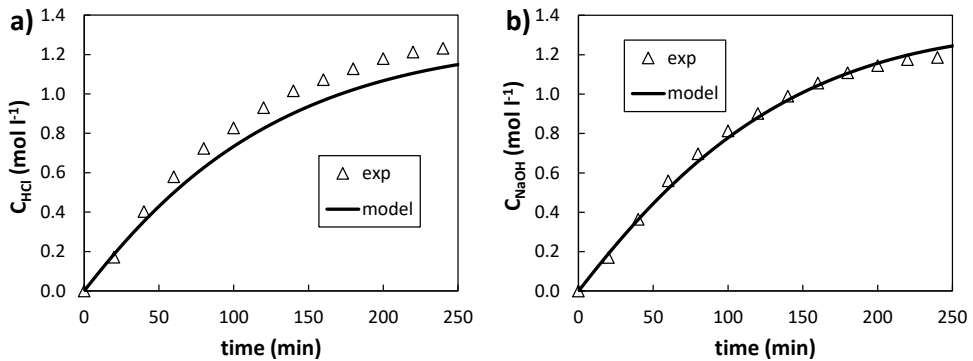


Figure 99. Comparison between experimental results and model predictions of a) HCl concentration in the acid tank and b) NaOH concentration in the base tank as a function of time in the charge phase. Process configuration: closed-loop. Fixed current density: 200 A m^{-2} . Inlet conditions: distillate in the acid and base tanks, 1 M NaCl in the salt tank. Mean flow velocity: 0.2 cm s^{-1} . Blank resistance: 72 ohm cm^2 .

The predicted curve for the NaOH concentration fits the experimental points well, since the average discrepancy during the charge time was 3.5%. The HCl concentration exhibits higher discrepancies, the maximum being 13.9% (around minute 60). It is worth noting that the average HCl concentration model deviation was 10.3% overall. Although the curve seems to diverge more in the second half, the relative difference between the experimental points and the model predictions was $\approx 9\%$, thus causing a small impact on the quality of the mathematical prediction.

Concerning the discharge phase, two sets of tests in the closed-loop layout were studied. Both the sets of data were generated at fixed current density equal to 29 A m^{-2} , but they differed in the inlet HCl and NaOH concentrations. The first set of data was obtained at inlet compositions of 0.8 M of HCl and NaOH in the acid and base tanks, respectively, and 0.1 M of NaCl concentration in the salt tank. Figure 100 shows the comparison between experimental and model results for the stack voltage as a function of time.

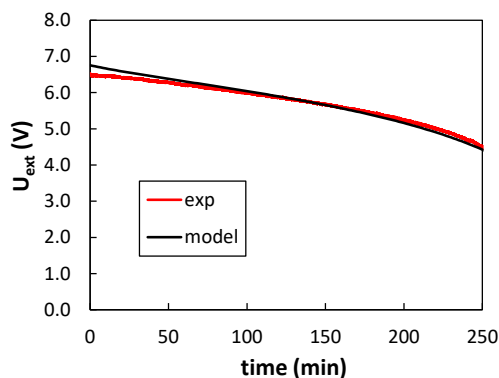


Figure 100. Comparison between experimental results and model predictions of the external voltage as a function of time in the discharge phase. Process configuration: closed-loop. Fixed current density: 29 A m^{-2} . Inlet conditions: 0.8 M HCl and NaOH in the acid and base tanks respectively, 0.1 M NaCl in the salt tank. Mean flow velocity: 0.2 cm s^{-1} . Blank resistance: 72 ohm cm^2 .

In the discharge period considered here, the two curves show a relative difference of 1.3% on average. The maximum errors were reported in the first 50 minutes of the discharge where a maximum deviation of 3.6% and an average of 2.5% were recorded. Therefore, the model error was less than 5% in any time. Within the simulated time window, the external voltage fell within the interval of 6.8-4.4 V.

Figure 101 shows the comparison between the experimental data and the model results of the HCl and NaOH concentration profiles as functions of time.

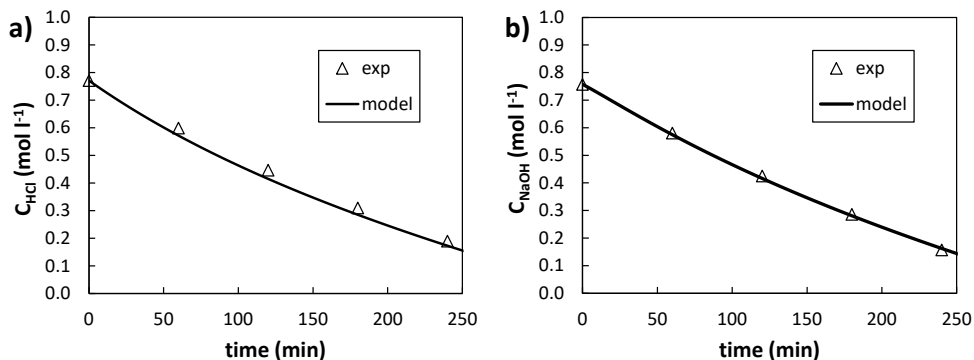


Figure 101. Comparison between experimental results and model predictions of a) HCl concentration in the acid tank and b) NaOH concentration in the base tank as a function of time in the discharge phase. Process configuration: closed-loop. Fixed current density: 29 A m^{-2} . Inlet conditions: 0.8 M HCl and NaOH in the acid and base tanks respectively, 0.1 M NaCl in the salt tank. Mean flow velocity: 0.2 cm s^{-1} . Blank resistance: 72 ohm cm^2 .

The model predictions for the profile of NaOH concentration over time were in very good agreement with the experimental results, as the average error was around 2% and the maximum deviation obtained at minute 240 was 3.5%. Comparisons of the HCl concentration curves resulted in slightly higher discrepancies. Particularly, in that case, the average discrepancy was 7% on average with higher deviations over time. However, the maximum discrepancy was 8.5%.

The final set of experiments conducted with closed-loop configuration in the discharge phase differs from the previous one only in terms of inlet composition. In this case, the composition was 1 M HCl and NaOH in the acid and base tanks respectively and 0.1 M of NaCl concentration in the salt tank. Figure 102 shows the comparison between the experimental data and the model outcome for the external voltage as a function of time.

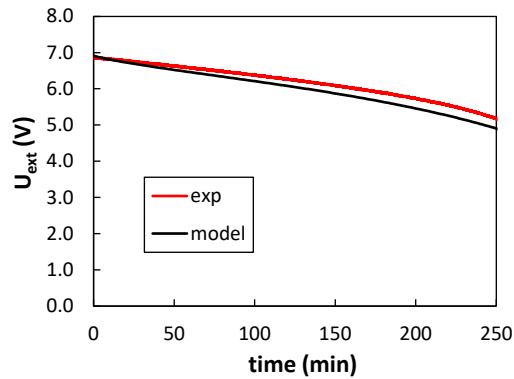


Figure 102. Comparison between experimental results and model predictions of the external voltage as a function of time in the discharge phase. Process configuration: closed-loop. Fixed current density: 29 A m^{-2} . Inlet conditions: 1 M HCl and NaOH in the acid and base tanks respectively, 0.1 M NaCl in the salt tank. Mean flow velocity: 0.2 cm s^{-1} . Blank resistance: 72 ohm cm^2 .

The external voltage was predicted with an average discrepancy of 3.1%. Particularly, the discrepancy increased over time up to 5% at minute 250. Therefore, there is an opposite trend of the relative differences compared to the previous experiment (see Figure 100), where higher model deviations were recorded in the first tract of the curve. As before, the model error was less than 5% at all times, thus confirming the validity of the model simulations. Within the simulated time window, the external voltage fell within the interval of 6.9-4.9 V.

Figure 103 shows the comparison between the experimental data and the model results of the HCl and NaOH concentration profiles as functions of time.

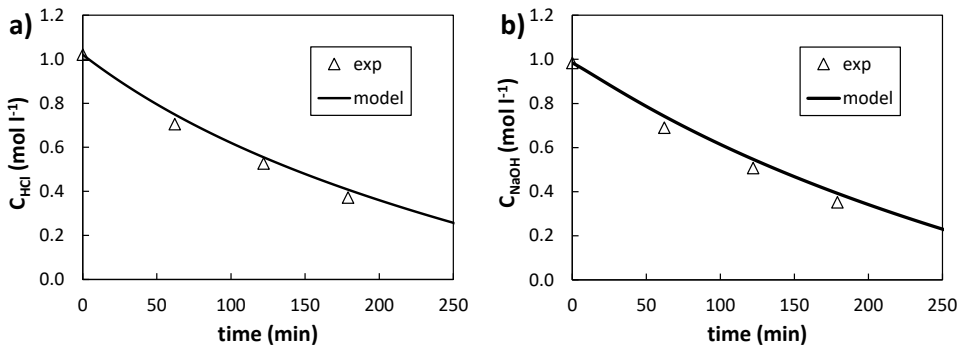


Figure 103. Comparison between experimental results and model predictions of a) HCl concentration in the acid tank and b) NaOH concentration in the base tank as a function of time in the discharge phase. Process configuration: closed-loop. Fixed current density: 29 A m^{-2} . Inlet conditions:

1 M HCl and NaOH in the acid and base tanks respectively, 0.1 M NaCl in the salt tank. Mean flow velocity: 0.2 cm s^{-1} . Blank resistance: 72 ohm cm^2 .

In this experiment, the average model discrepancy of the HCl and NaOH concentrations were 5.3% and 6.7%, respectively. The highest discrepancies were around 9.2% and 10.9% for the acid and base solutions, respectively, both exhibited at minute 180. These highest errors correspond, in absolute terms, to 0.034 M and 0.038 M for the acid and base solutions, respectively.

6.4.2 Yo-Yo model validation

In this section, the model validation for the Yo-Yo configuration in both the charge and discharge battery phases is presented. Concerning the charge phase, two sets of experiments were investigated. The first set of data was generated using a fixed charge current density of 100 A m^{-2} , and inlet compositions of 0.1 M HCl and NaOH in the acid and base tanks and 1 M NaCl concentration in the salt tank. The following external voltage curves were obtained (Figure 104).

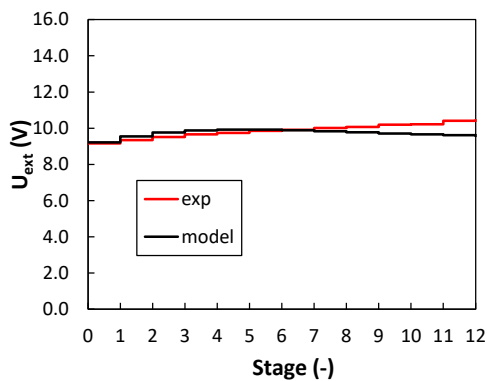


Figure 104. Comparison between experimental results and model predictions of the external voltage as a function of time in the charge phase. Process configuration: Yo-Yo. Fixed current density: 100 A m^{-2} . Inlet conditions: 0.1 M HCl and NaOH in the acid and base tanks, 1 M NaCl in the salt tank. Mean flow velocity: 0.2 cm s^{-1} . Blank resistance: 72 ohm cm^2 .

In this test, there were 12 stages in the charging process, which may also be seen as an interval of time. Each stage corresponds to the emptying time of the inlet external reservoirs, lasting ~ 20 minutes. The average voltage difference between the experimental data and model outcome was found to be $\sim 0.3 \text{ V}$, thus resulting in a relative difference of $\sim 3.2\%$ on average. Moreover, greater discrepancies were recorded at the last stages. For instance, in the second half of the graph, the average deviation was 4.9% with a maximum of 8.1% at stage 12. Overall, the voltages predicted by the model

vary within the range of 9.2-9.9 V. The small variation of the external voltage during time can be attributed to small changes in the electromotive force.

Figure 105 shows the comparison between the experimental data and the model results of the HCl and NaOH concentration profiles as functions of the stage number.

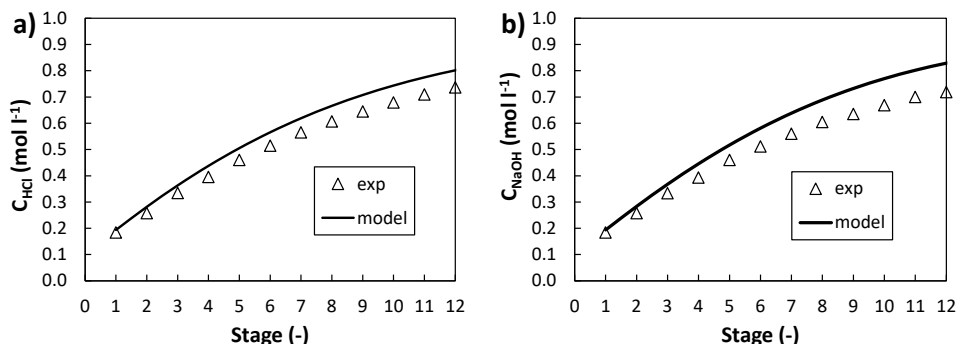


Figure 105. Comparison between experimental results and model predictions of a) HCl concentration in the acid tank and b) NaOH concentration in the base tank as a function of the stage number in the charge phase. Process configuration: Yo-Yo. Fixed current density: 100 A m^{-2} . Inlet conditions: 0.1 M HCl and NaOH in the acid and base tanks respectively, 1 M NaCl in the salt tank. Mean flow velocity: 0.2 cm s^{-1} . Blank resistance: 72 ohm cm^2 .

This test reports an average model discrepancy for the HCl and NaOH concentrations of 8.5% and 11.9%, respectively. Moreover, particularly after the passage 4, both the concentration profiles maintain an almost constant relative discrepancy with maximum deviations of 10.7% and 15.4% for the acid and base solutions, respectively. This may be due to uncertainties about the membrane properties, e.g. the ion diffusivities. However, even the highest discrepancies found are acceptable and make the model reliable.

The second set of data executed in the charge phase was performed with a fixed charge current density of 200 A m^{-2} and inlet compositions of 0.1 M HCl and NaOH in the acid and base tanks, and 1 M NaCl concentration in the salt tank. Figure 106 illustrates the comparison between the empirical and model external voltages as a function of the sequential stage number.

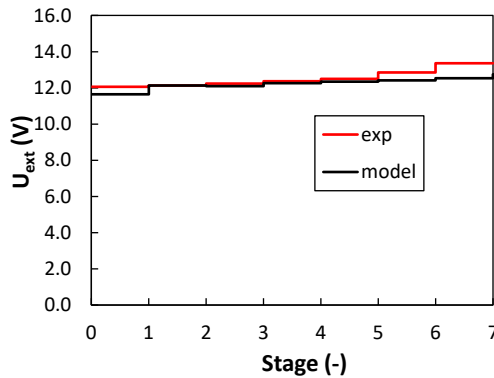


Figure 106. Comparison between experimental results and model predictions of the external voltage as a function of time in the charge phase. Process configuration: Yo-Yo. Fixed current density: 200 A m^{-2} . Inlet conditions: 0.1 M HCl and NaOH in the acid and base tanks, 1 M NaCl in the salt tank. Mean flow velocity: 0.2 cm s^{-1} . Blank resistance: 72 ohm cm^2 .

This test was performed at 200 A m^{-2} , thus at equal inlet NaCl concentration in the salt tank (with respect to the preview experiment), the number of stages necessary to perform the process is lower. This is the reason why the number of stages is here limited to 7 instead of 12. Again, each stage corresponds to the emptying time of the inlet external reservoirs, i.e. ≈ 20 minutes each since both the volume tanks and the flow rates were kept constant among the Yo-Yo experiments. The average discrepancy between the empirical data and model simulations was $\sim 0.3 \text{ V}$, analogously to the test performed at 100 A m^{-2} . Therefore, a relative difference of $\sim 2.3\%$ on average was found. The highest discrepancy was $\sim 6.2\%$, found at the seventh stage.

Figure 107 shows the comparison between experimental data and model results of the HCl and NaOH concentration profiles as functions of the stage number.

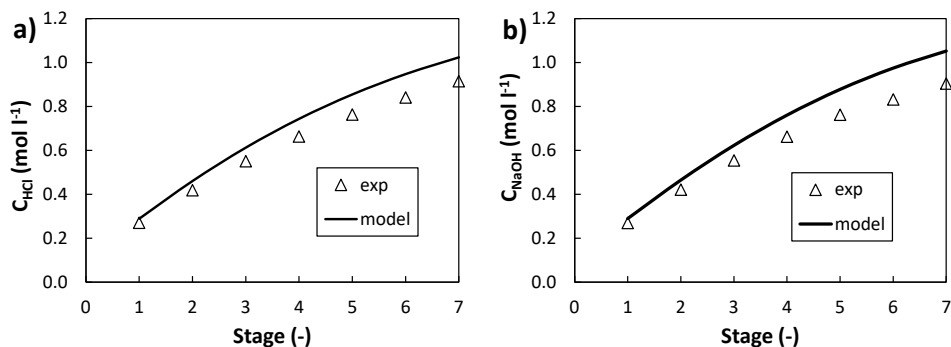


Figure 107. Comparison between experimental results and model predictions of a) HCl concentration in the acid tank and b) NaOH concentration in the base tank as a function of the stage number in the charge phase. Process configuration: Yo-Yo. Fixed current density: 200 A m^{-2} . Inlet conditions: 0.1 M HCl and NaOH in the acid and base tanks respectively, 1 M NaCl in the salt tank. Mean flow velocity: 0.2 cm s^{-1} . Blank resistance: 72 ohm cm^2 .

The average discrepancy for HCl and NaOH concentrations was 9.5% and 11.6%, respectively, which is comparable to that obtained in the previous experiment. Again, after the first four stages, both the concentration profiles present a somehow constant relative discrepancy, with maximum deviations of 12.6% and 17.1% for the acid and base solutions, respectively. More accurate estimations of the ion diffusivities are required to a further reduction of the model error.

In regard to the discharge phase, two sets of tests were performed in the Yo-Yo configuration. A fixed current density equal to 29 A m^{-2} was used, but the two tests differ for the inlet HCl and NaOH concentrations. The first set of data was performed at inlet compositions of 0.8 M of HCl and NaOH in the acid and base tanks, respectively, and 0.1 M of NaCl concentration in the salt tank. Figure 108 shows the comparison between the empirical and simulated voltage values as functions of the stage number.

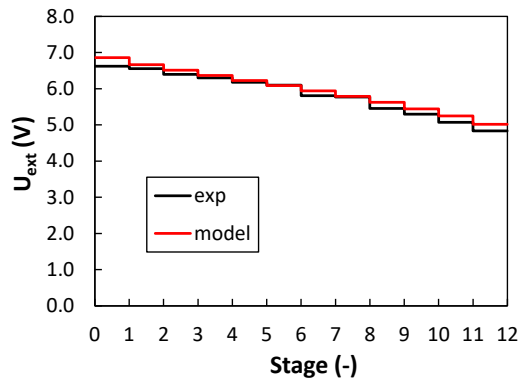


Figure 108. Comparison between experimental results and model predictions of the external voltage as a function of time in the discharge phase. Process configuration: Yo-Yo. Fixed current density: 29 A m^{-2} . Inlet conditions: 0.8 M HCl and NaOH in the acid and base tanks, 0.1 M NaCl in the salt tank. Mean flow velocity: 0.2 cm s^{-1} . Blank resistance: 72 ohm cm^2 .

The investigated number of stages was 12. The average voltage difference between the empirical data and model simulations was found to be $\approx 0.12 \text{ V}$. This corresponds to a relative difference of $\approx 2.2\%$ on average. The maximum discrepancy was found equal to 3.9% at stage 12.

Figure 109 shows the comparison between experimental data and model results of the HCl and NaOH concentration profiles as functions of the stage number.

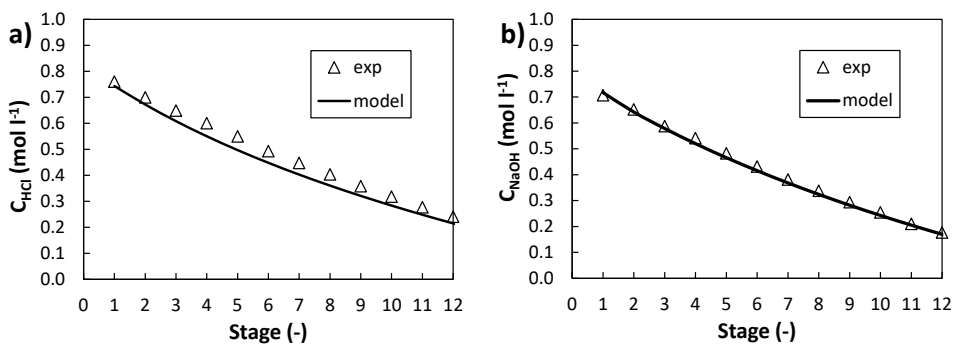


Figure 109. Comparison between experimental results and model predictions of a) HCl concentration in the acid tank and b) NaOH concentration in the base tank as a function of the stage number in the discharge phase. Process configuration: Yo-Yo. Fixed current density: 29 A m^{-2} . Inlet conditions: 0.8 M HCl and NaOH in the acid and base tanks respectively, 0.1 M NaCl in the salt tank. Mean flow velocity: 0.2 cm s^{-1} . Blank resistance: 72 ohm cm^2 .

Overall the two model curves fit well the experimental points. The average model discrepancy of HCl and NaOH concentrations was 7.8% and 3.0%, respectively. The maximum discrepancies were 10.7% and 4.8% for the acid and base solutions, respectively.

The second set of data for the discharge phase was obtained with a fixed discharge current density at 29 A m^{-2} and inlet compositions of 1 M HCl and NaOH in the acid and base tanks, and 0.1 M NaCl concentration in the salt tank. Figure 110 illustrates the comparison between the empirical and model external voltages as function of the sequential stage number.

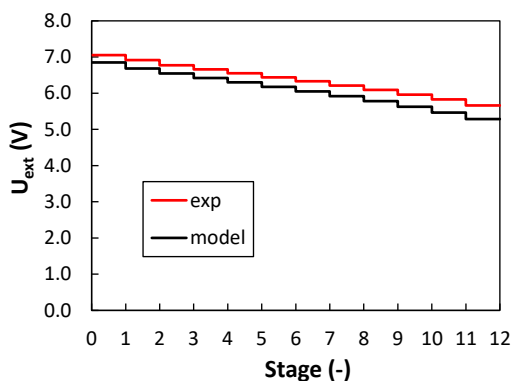


Figure 110. Comparison between experimental results and model predictions of the external voltage as a function of time in the discharge phase. Process configuration: Yo-Yo. Fixed current density: 29 A m^{-2} . Inlet conditions: 1 M HCl and NaOH in the acid and base tanks, 0.1 M NaCl in the salt tank. Mean flow velocity: 0.2 cm s^{-1} . Blank resistance: 72 ohm cm^2 .

The experiment conducted at 1 M of inlet acid and base concentrations resulted in similar model errors compared to the experiment conducted at 0.8 M of inlet acid and base concentrations. Particularly, the average discrepancy was 4.6%, while the maximum one was 6.7%. Overall, the external voltage was well predicted by the model.

Finally, Figure 111 reports the comparison between empirical data and model predictions of the HCl and NaOH concentration profiles as functions of the stage number.

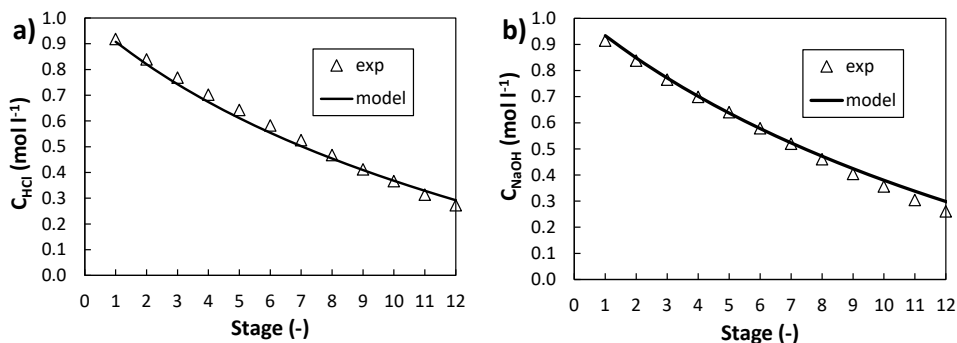


Figure 111. Comparison between experimental results and model predictions of a) HCl concentration in the acid tank and b) NaOH concentration in the base tank as a function of the stage number in the discharge phase. Process configuration: Yo-Yo. Fixed current density: 29 A m^{-2} . Inlet conditions: 1 M HCl and NaOH in the acid and base tanks respectively, 0.1 M NaCl in the salt tank. Mean flow velocity: 0.2 cm s^{-1} . Blank resistance: 72 ohm cm^2 .

The average concentration difference between the model curve and the experimental points was found to be less than 0.02 M for both the acid and base solutions. Moreover, the higher the number of sequential stage, the higher the relative discrepancy. The average model deviations were 3.1% and 3.4% for the acid and base solutions, respectively. The maximum discrepancies were 7.0% and 14.3% for the acid and base solutions, respectively, both obtained at the final stage.

6.5 Sensitivity analysis of the AB-FB

The developed multi-scale model was used to perform a sensitivity analysis to assess the impact of the main detrimental phenomena in the battery on the process efficiency. Four important aspects were identified to be possible detrimental phenomena of the flow battery: (i) energy spent for pumping, (ii) concentration polarization in the boundary layers, (iii) ionic shortcut currents via manifolds and (iv) the performance variation in subsequent battery cycles. Each aspect will be separately addressed in the following sub-sections.

Unless otherwise stated all the simulations reported in this section were performed fixing the geometrical features, the membrane properties and the initial volume and concentration of the solutions in the charge phase at the values reported in Table 20. Moreover, the bipolar membrane was simulated as ideal, by considering unitary ion transport numbers H^+ and OH^- in CEL and AEL respectively.

Table 20. Inputs of the multi-scale model for the sensitivity analysis.

| Geometrical features | | | | |
|--|-----------------------------|---------|---------|-----|
| Spacer length | cm | 25 | | |
| Spacer width | cm | 25 | | |
| Spacer thickness | μm | 475 | | |
| N° spacer holes | - | 7 | | |
| Membrane properties | | | | |
| | | AEM | CEM | BPM |
| Thickness | μm | 130 | 130 | 190 |
| Areal resistance | $\Omega \text{ cm}^2$ | 7 | 6 | 13 |
| H ⁺ diffusivity | $\text{m}^2 \text{ s}^{-1}$ | 2.0E-11 | 0.7E-11 | - |
| Na ⁺ diffusivity | $\text{m}^2 \text{ s}^{-1}$ | 1.6E-11 | 0.5E-11 | - |
| Cl ⁻ diffusivity | $\text{m}^2 \text{ s}^{-1}$ | 1.7E-11 | 0.6E-11 | - |
| OH ⁻ diffusivity | $\text{m}^2 \text{ s}^{-1}$ | 1.9E-11 | 0.6E-11 | - |
| Fixed charge group | mol m^{-3} | 5000 | 5000 | - |
| Initial conditions of the solutions in BMED (charge) | | | | |
| $C_{t,HCl,a,out}$ | mol m^{-3} | 50 | | |
| $C_{t,NaCl,a,out}$ | mol m^{-3} | 250 | | |
| $C_{t,HCl,s,out}$ | mol m^{-3} | 10 | | |
| $C_{t,NaCl,s,out}$ | mol m^{-3} | 500 | | |
| $C_{t,NaOH,b,out}$ | mol m^{-3} | 50 | | |
| $C_{t,NaCl,b,out}$ | mol m^{-3} | 250 | | |
| $\frac{V_{t,a}}{N}$ | 1 | 0.75 | | |
| $\frac{V_{t,s}}{N}$ | 1 | 4.5 | | |
| $\frac{V_{t,b}}{N}$ | 1 | 0.75 | | |
| R_{bl} | $\Omega \text{ cm}^2$ | 72 | | |

The flow velocity, the number of triplets, the external current, and the manifolds diameter were varied.

In most cases, a round trip analysis for a single or multiple cycles of charge/discharge were simulated. The battery is considered charged (100% state of charge, SOC) once the hydrochloric acid concentration in the acid tank reaches 1 M. At that point, the model switches the operating mode from charge to discharge. The latter ends when the hydrochloric acid concentration in the acid tank becomes again 0.05 M (0% SOC).

6.5.1 Energy spent on pumping

Concerning the energy spent for pumping, Figure 112a reports the GPD and NPD values averaged over the charge phase as a function of the mean flow velocity within the channels.

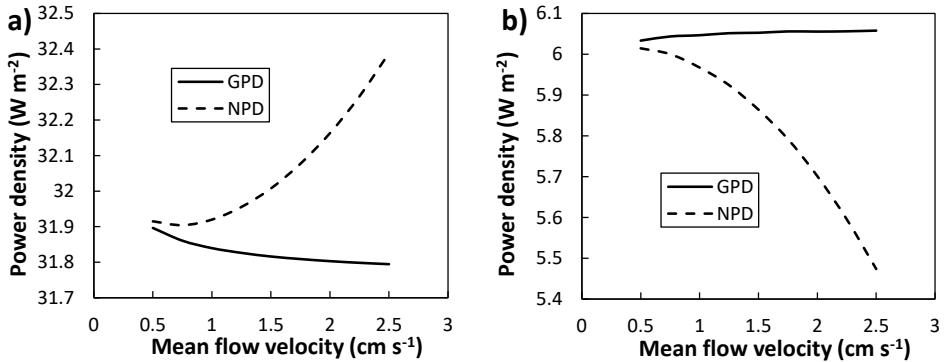


Figure 112. Average gross power density (GPD) and net power density (NPD) for charge a) and discharge b) as functions of the mean flow velocity in the channels for stacks equipped with 40 cell triplets, spacer with inlet/outlet holes diameter of 6 mm. Charge external current of 100 A m^{-2} and discharge external current of 30 A m^{-2} . The distance between the two curves represents the pumping power density (PPD).

It can be observed that while the GPD trend is slightly decreasing with the mean flow velocity, the NPD exhibits an increasing trend. On the contrary, during discharge (Figure 112b), by increasing the velocity, GPD tends to a plateau value around 6.1 W m^{-2} . Instead, the higher the mean flow velocity, the lower the NPD. In both steps (i.e. charge and discharge), the increase of the mean flow velocity causes mainly a flattening of the ion concentration profiles along the channels. This leads triplet potential values averaged over the whole length to be lower during charge and higher during discharge. As a consequence, GPD decreases during charge and increases during discharge (although slightly). Other possible effects of the fluid velocity on the GPD are related to polarization phenomena, as will be discussed in the next section. On the other hand, the NPD exhibits an opposite yet more marked trend. In fact, the rise of the pumping power density with the mean flow velocity prevails on the variation of the GPD leading to an increase of the NPD during charge and a reduction during discharge. Nevertheless, the PPD, given by the difference between GPD and NPD, appears to be relatively small (some % of GPD), thus suggesting that the energy lost for pumping does not represent a major issue for the present system. However, real systems may require larger pumping powers, due to

geometrical irregularities in the stack, effects of tightening, clogging issues, and other “non-ideal” features which can not be included in the simulations.

6.5.2 Concentration polarization effects

Concerning the polarization phenomenon, the variation of the triplet electromotive force η_{BL} was assessed. As shown by the example reported in Figure 113, the highest values of η_{BL} , both in absolute and in relative terms, occur during the charge phase and are higher at lower distances from the channel inlet.

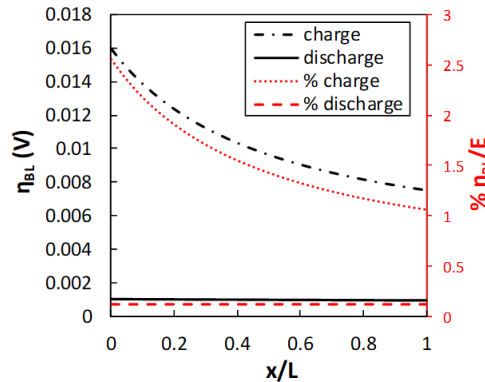


Figure 113. Variation of triplet electromotive force due to concentration polarization in the boundary layers for the 1st triplet at the initial point of charge (SOC=0%) or discharge (SOC=100%), as a function of the non-dimensional coordinate along the channel. Stack equipped with 40 cell triplets, spacer with inlet/outlet hole diameter of 6 mm. Charge external current of 100 A m^{-2} and discharge external current of 30 A m^{-2} .

At the initial point of charge, the acid and base bulk concentrations in the feed solutions are the lowest, thus the voltage variation due to concentration polarization is the highest. In particular, the lower the mean concentration of the feedwater solutions, the lower the polarization factors [259]. On the other hand, at the early point of discharge, the opposite happens and the lowest values of boundary layer voltage drop are obtained. Overall, concentration polarization accounts for less than 3% of the triplet electromotive force (EMF) during charge and around 0.2 % during discharge, thus resulting in a small contribution to the reduction of the process efficiency. As a consequence, the polarization phenomena are not an issue for the AB-FB in the investigated operating conditions. However, larger effects are expected at higher current densities, which should be used in the operation of improved devices.

6.5.3 Ionic shortcut currents effect

In order to analyse the distribution of the electric current within the stack, due to the ionic shortcut currents via manifolds, Figure 114 shows, for the charge step, the distribution triplet by triplet of the ratio between the manifolds current (i.e. collectors and distributors shunt for each compartment cell) and the cell current at four different external currents: 30, 100, 150 and 200 A m⁻².

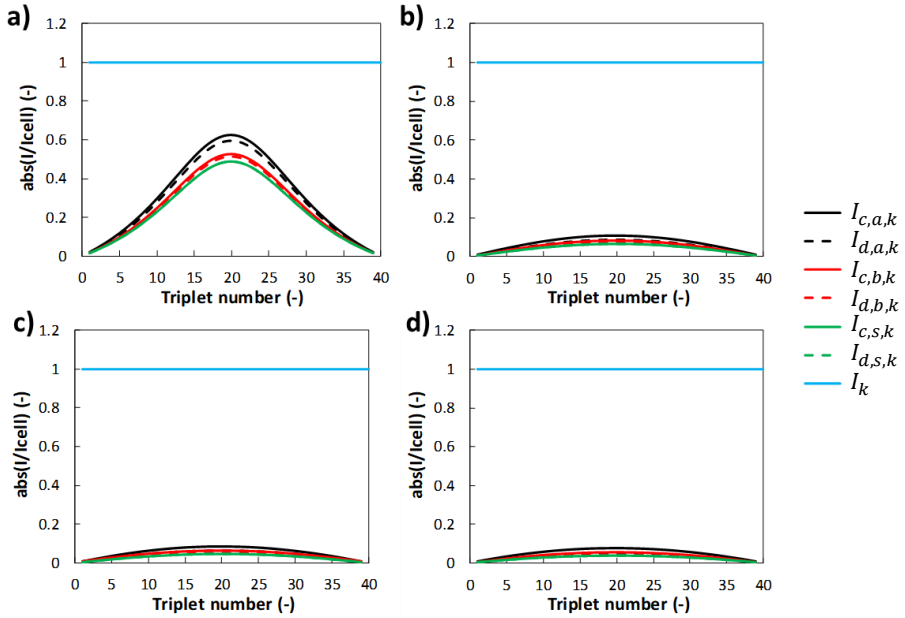


Figure 114. Ratio between the manifolds currents and cell currents as a function of the cell-triplet position within the stack for an external current density of 30 A m⁻² a), 100 A m⁻² b), 150 A m⁻² c) and 200 A m⁻² d) during charge. I_k is the cell-triplet current, $I_{d,a,k}$, $I_{d,b,k}$, $I_{d,s,k}$ are the acid, base and salt electric currents along the distributors, $I_{c,a,k}$, $I_{c,b,k}$, $I_{c,s,k}$ are the acid, base and salt electric currents along the collectors. 40 cell triplets, spacer with inlet/outlet hole diameter 6 mm.

Figure 114 shows how the effect of the leakage currents through the manifolds can be significant. By setting an external current equal to 30 A m⁻² (a), the maximum shunt currents in the manifolds of the three solution are ~50% of the cell triplet current. By increasing the external current, the ratio of the local current leakage through the manifolds to the cell triplet current decreases (b and c), and at 200 A m⁻², it accounts for ~6%.

Similar outcomes were obtained for the discharge (Figure 115): the higher the external current, the lower the importance of the parasitic currents relative to the cell one. When no external current flows through the external circuit (open circuit

condition), this phenomenon is present with the largest effects and would cause a “self-discharge” of the battery by consuming uselessly the pH gradient stored in the acid and base solutions.

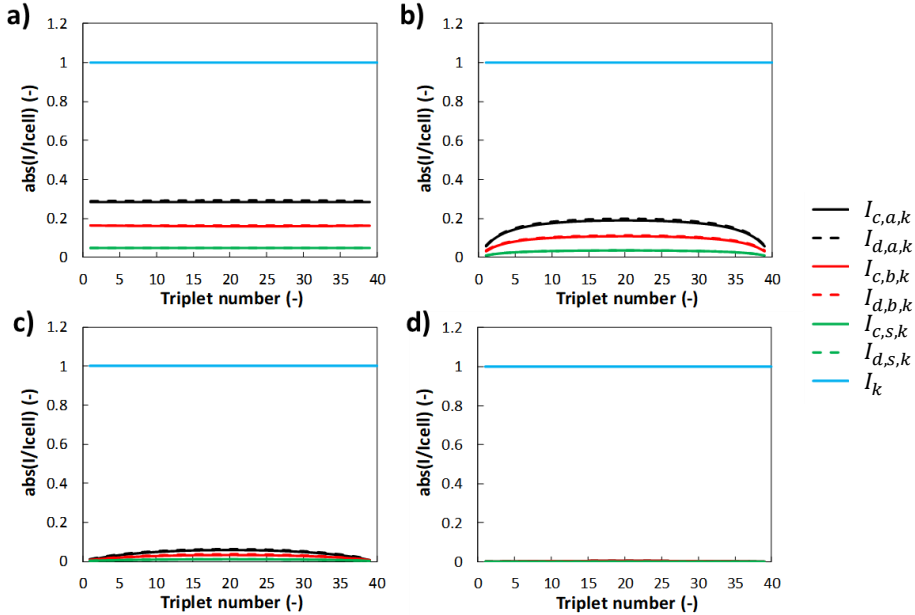


Figure 115. Ratio between the manifolds and cell currents as a function of the cell-triplet position within the stack for open circuit conditions a), an external current density of 30 A m^{-2} b), maximum power c) and short-circuit d) during discharge. I_k is the cell-triplet current, $I_{d,a,k}$, $I_{d,b,k}$, $I_{d,s,k}$ are the acid, base and salt electric currents along the distributors, $I_{c,a,k}$, $I_{c,b,k}$, $I_{c,s,k}$ are the acid, base and salt electric currents along the collectors. 40 cell triplets, spacer with inlet/outlet hole diameter 6 mm.

These results suggest that higher external currents can be beneficial in order to increase the battery efficiency. Therefore, a specific simulations set was performed in order to investigate this aspect. The simulation results are reported in Figure 116. At current densities higher than $\sim 150 \text{ A m}^{-2}$ in both phases, the loss of RTE due to shunt currents is less than 10%. However, the current density may be significantly limited by other phenomena and / or constraints, e.g. by delamination issues occurring in real BPMs. Considering a “safe” current density in the discharge phase equal to 30 A m^{-2} , with a current density in the charge phase within the range $100\text{--}200 \text{ A m}^{-2}$, the RTE lost due to parasitic currents spans between $\sim 25\%$ and $\sim 35\%$.

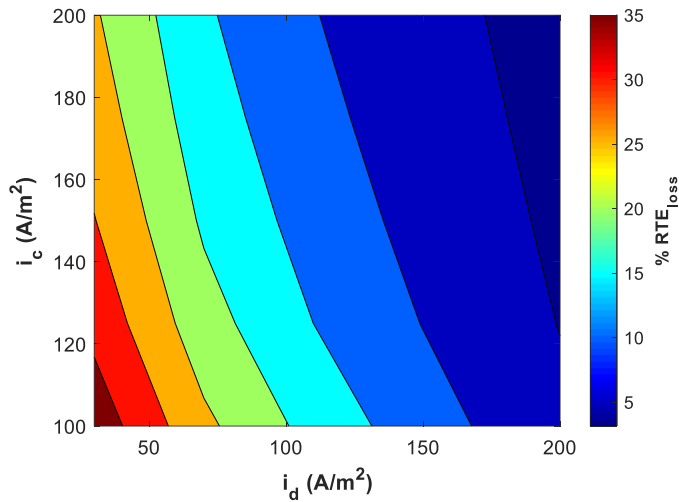


Figure 116. Contour map of percentage of RTE loss due to the parasitic currents via manifolds as function of the discharge and charge external current densities. 40 cell triplets, spacer with inlet/outlet hole diameter of 6 mm.

Parasitic currents are significantly affected also by geometrical features. Among them, the manifolds diameter has important effects on the electrical resistance of the parasitic pathways, thus affecting the RTE, as shown in Figure 117a. In particular, the RTE increases from $\sim 17\%$ to $\sim 40\%$ by reducing the manifolds diameter from 6 mm to 2 mm. On the other hand, small manifolds may accentuate other detrimental phenomena, e.g. pressure drops, flow maldistribution and differential pressures between the channels with consequent solution leakages, or practical problems in stack assembling.

Another important stack feature is the number of triplets, as shown in Figure 117b. The RTE exhibits an increasing trend at low values of the repetitive units number, reaching a maximum value of $\sim 46\%$ when the battery is assembled with 5 triplets. This behaviour is due to the relative effect of the voltage drop due to the blank resistance. Then, a reduction of the RTE can be observed in stacks with a higher number of triplets, where the effects of shunt currents prevail, thus dissipating a larger portion of energy in both the cycle phases.

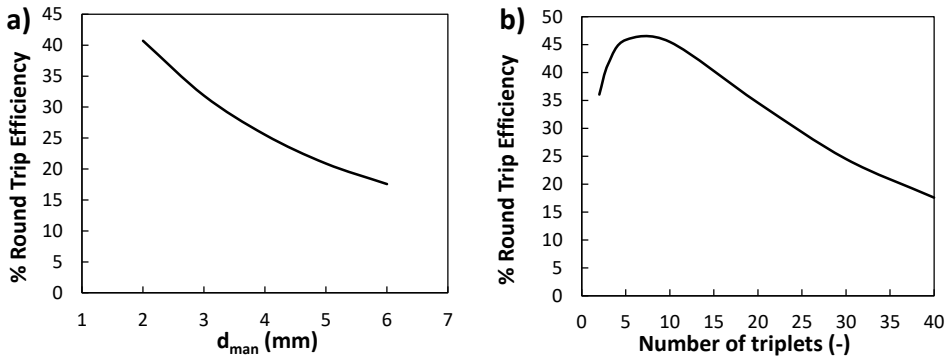


Figure 117. Round trip efficiency as a function of the manifolds diameter for a stack mounting 40 cell triplets a), and of the number of triplets for a manifolds diameter of 6 mm b). Charge external current of 100 A m^{-2} and discharge external current of 30 A m^{-2} .

6.5.4 Multiple battery-cycles effect

So far, the performance of the AB-FB was assessed by performing a single cycle. In this section, multiple cycles were simulated estimating the performance variation over the cycles. This information is important, particularly in view of long terms uses of the battery. Figure 118 shows the effect of multiple battery cycles on the AB-FB performance.

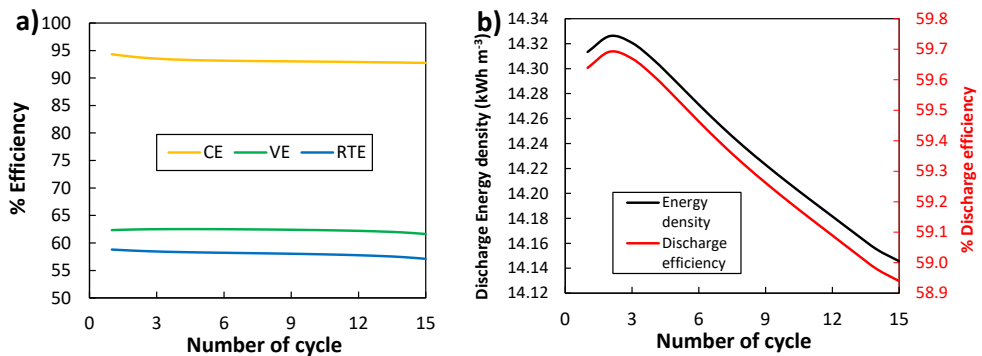


Figure 118. a) Voltage, Coulombic and Round Trip efficiencies and b) discharge energy density and discharge efficiency over a sequence of 15 cycles for a stack with 40 cell triplets. Charge external current of 100 A m^{-2} and discharge external current of 30 A m^{-2} .

The AB-FB functioning was simulated for 15 subsequent cycles. As depicted in Figure 118a, both the coulombic and voltage efficiencies do not present significant variations. The Coulombic efficiency diminishes from the first to the final cycle of only 1.6%, while the voltage efficiency decreases by 0.7%. This results in the

reduction of the RTE from 62.3% (first cycle) to 61.6% (final cycle). Therefore, no significant variations were found even after 15 charge-discharge battery cycles. Moreover, this is observed also in the discharge energy density (Figure 118b), which presents a maximum around the third cycle, and then decreases from $\sim 14.3 \text{ kWh m}^{-3}$ to 14.1 kWh m^{-3} of acid. These values correspond to a less than a percentage point of discharge efficiency variation.

6.6 Comparison of acid/base flow battery operational modes

In this section, the effect of different process configurations will be assessed. First, closed-loop and Yo-Yo configurations will be compared. Then, simulations of various series and parallel stacks configurations will be presented.

6.6.1 Closed-loop vs Yo-Yo operations:

These simulations aim at estimating the different performance occurring in closed-loop and Yo-Yo battery operations. The two configurations were described in section 6.3.3. The adopted model inputs were chosen according to the BAoBaB prototype which will be tested in Pantelleria (Table 21).

Table 21. Inputs of the multi-scale model for the Closed-loop vs Yo-Yo operations comparison.

| Geometrical features | | | | | |
|--|-----------------------------|---------|---------|---------|---------|
| Spacer length | cm | 44 | | | |
| Spacer width | cm | 47.4 | | | |
| Spacer thickness | μm | 475 | | | |
| Area spacer hole | mm^2 | 400 | | | |
| N° triplets | - | 7 | | | |
| N° spacer holes | - | 1 | | | |
| Membrane properties | | | | | |
| | | AEM | CEM | AEL | CEL |
| Thickness | μm | 75 | 75 | 60 | 60 |
| Areal resistance | $\Omega \text{ cm}^2$ | 4 | 3.5 | 2.5 | 2.5 |
| H ⁺ diffusivity | $\text{m}^2 \text{ s}^{-1}$ | 2.0E-11 | 0.7E-11 | 2.0E-11 | 0.7E-11 |
| Na ⁺ diffusivity | $\text{m}^2 \text{ s}^{-1}$ | 1.6E-11 | 0.5E-11 | 1.6E-11 | 0.5E-11 |
| Cl ⁻ diffusivity | $\text{m}^2 \text{ s}^{-1}$ | 1.7E-11 | 0.6E-11 | 1.7E-11 | 0.6E-11 |
| OH ⁻ diffusivity | $\text{m}^2 \text{ s}^{-1}$ | 1.9E-11 | 0.6E-11 | 1.9E-11 | 0.6E-11 |
| Fixed charge group | mol m^{-3} | 5000 | 5000 | 5000 | 5000 |
| Initial conditions of the solutions in BMED (charge) | | | | | |
| $C_{t,HCl,a,out}$ | mol m^{-3} | 50 | | | |

| | | |
|--------------------|---------------------|-----|
| $C_{t,NaCl,a,out}$ | mol m ⁻³ | 250 |
| $C_{t,HCl,s,out}$ | mol m ⁻³ | 10 |
| $C_{t,NaCl,s,out}$ | mol m ⁻³ | 500 |
| $C_{t,NaOH,b,out}$ | mol m ⁻³ | 50 |
| $C_{t,NaCl,b,out}$ | mol m ⁻³ | 250 |
| $V_{t,a}$ | 1 | 10 |
| $V_{t,b}$ | 1 | 10 |
| R_{bl} | Ω cm ² | 79 |

This study may be divided into two sets of simulations: i) by varying the external current density from 70 A m⁻² to 200 A m⁻² during charge and from 30 A m⁻² to 190 A m⁻² during discharge, with a fixed mean channel flow velocity of 0.5 cm s⁻¹ and ii) by varying the mean channel flow velocity from 0.2 cm s⁻¹ to 5 cm s⁻¹, with a fixed external current density to 100 A m⁻² during charge and 30 A m⁻² during discharge. Of course, the process time depends on the volume and concentration of the solutions in the tanks. Particularly, in the case of Yo-Yo operations, when the first of the inlet tanks reaches a volume close to 0 (< 0.01 liters), the flow direction was reversed to start the subsequent stage. The target fixed for the charge phase was 1 M HCl in the outlet acid tank or one of the solutions volumes in the inlet tanks < 0.01 liters, while that for the discharge phase was 0.05 M HCl in the outlet acid tank or one of the solutions volumes in the inlet tanks < 0.01 liters. Salt tank volumes were different in the two cases: 60 liters in the closed-loop operations and 10 liters in the Yo-Yo operations.

Both analysis were evaluated in terms of charge and discharge energy density (i.e. the charge or discharge energy per unit volume of acid) and % Energy lost during charge or gained during discharge. The energy density was calculated simply as the integral of the power consumed (charge phase) or produced (discharge phase) during the process time per unit volume of acid, to reach the target concentration of HCl in a closed-loop mode or with a sequence of once-through stages in a yo-yo mode. The energy lost or gained was calculated as the relative energy difference between the two configurations as

$$\% \text{ Energy lost} = \left(1 - \frac{\text{YoYo Energy}}{\text{CL Energy}} \right) \times 100 \quad (\text{charge phase}) \quad (161)$$

$$\% \text{ Energy gain} = \left(1 - \frac{\text{CL Energy}}{\text{YoYo Energy}} \right) \times 100 \quad (\text{discharge phase}) \quad (162)$$

where *YoYo Energy* and *CL Energy* are the energy (kWh) consumed (charge) or produced (discharge) in the Yo-Yo and Closed-Loop configurations, respectively.

Figure 119 shows the charge energy and the % Energy lost as functions of the applied current density.

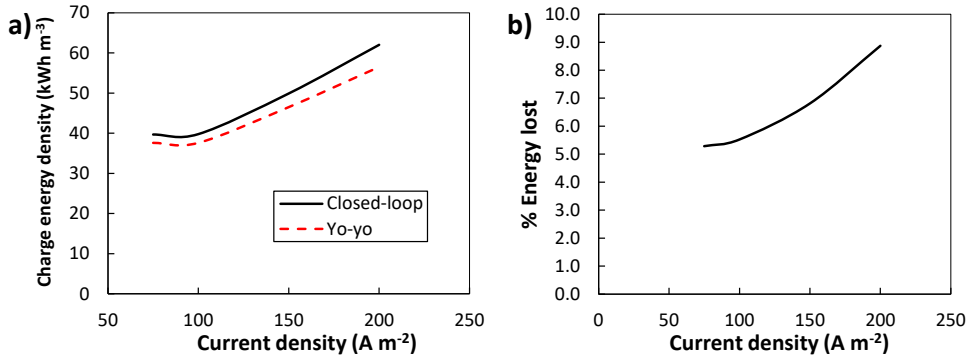


Figure 119. Charge energy density and the % Energy lost as functions of the current density. Mean flow velocity: 0.5 cm s^{-1} .

Compared to the Yo-Yo operations, closed-loop operations require higher values of charge energy density (Figure 119a). An average of 6.6% of relative difference was predicted between the two configurations (Figure 119b). Both the curves reported in Figure 119a present a minimum around 100 A m^{-2} . The difference in charge energy density presents an increasing trend due to the increasing divergence of the two charge energy density curves. This may be noted also by the % Energy lost, which varies within the interval 5.3%-8.9% with a positive slope. Therefore, the best operating condition resulted to be at lower current densities, particularly in correspondence to the minimum of the charge energy density curve and with the Yo-Yo functioning, as this process layout allows a lower consumption of the electric energy.

Figure 120 shows the discharge energy density and the % Energy gain as functions of the applied current density.

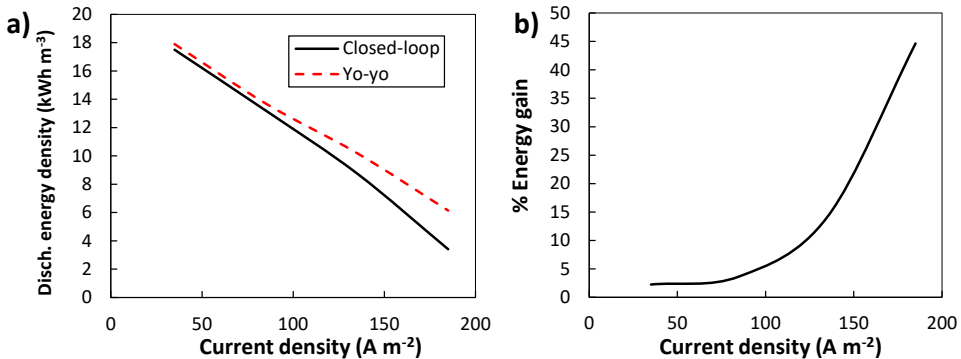


Figure 120. Discharge energy density and the % Energy gain as functions of the current density. Mean flow velocity: 0.5 cm s^{-1} .

The discharge energy density produced by the Yo-Yo operation is higher with respect to the one obtained in closed-loop functioning. Particularly, the higher the current density, the higher the difference of discharge energy density. Results showed that the average produced energy density was 10.7 kWh m^{-3} and 12.0 kWh m^{-3} for the closed-loop and Yo-Yo operations, respectively. The difference between the two configurations was confirmed by the % Energy gain, which increases as the current density increases. By fixing a current density equal to 190 A m^{-2} (i.e. the maximum current investigated), the % Energy gain is $\sim 45\%$. Therefore, almost half of the produced power in Yo-Yo configuration would be lost by the closed-loop functioning. This suggests that, in the presence of closed-loop operations, lower current densities may be useful to avoid excessive energy losses.

Figure 121 shows the charge energy density and the % Energy lost as functions of the mean channel flow velocity.

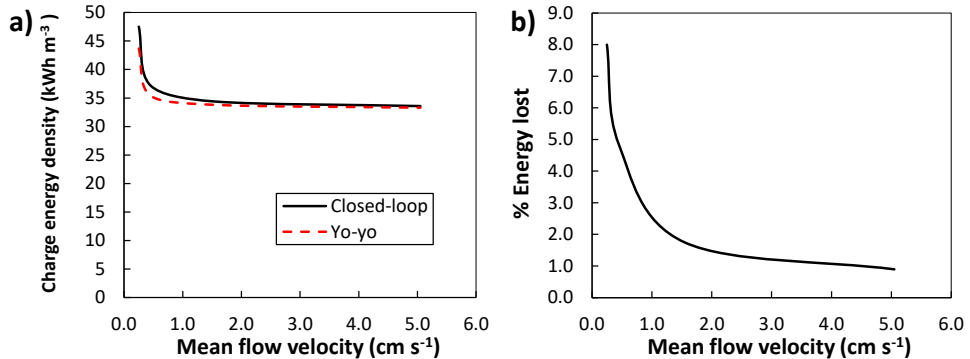


Figure 121. Charge energy density and the % Energy lost as functions of the mean flow velocity. External current density: 100 A m^{-2} .

With the mean flow velocity analysis, similar comparisons can be made between the two configurations. Particularly, by varying the velocity from 0.2 cm s^{-1} to 5 cm s^{-1} , the Yo-Yo configuration required a lower energy consumption for the charge compared to the closed-loop operation (Figure 121a). The % Energy lost due to the use of the closed-loop configuration is depicted in Figure 121b, which exhibits an average percentage lost of 3.9%. It is worth noting that the % Energy lost curve presents a rapid reduction by increasing the mean flow velocity. Therefore, higher velocity values are suggested to limit the energy loss. However, these graphs show the gross energy density required by the process, disregarding the energy spent for pumping. An optimal mean flow velocity should be evaluated to obtain a good compromise among the operating conditions, thus minimizing the energy losses.

Finally, Figure 122 shows the discharge energy density and the % Energy gain as functions of the mean channel flow velocity.

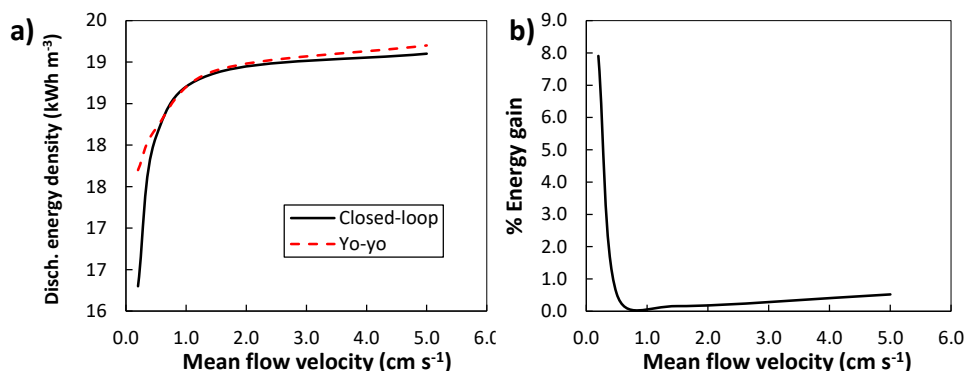


Figure 122. Discharge energy density and the % Energy gain as functions of the mean flow velocity. External current density: 30 A m^{-2} .

No appreciable differences in discharge energy density were shown with mean flow velocities higher than 1 cm s^{-1} (% Energy gain was $\sim 0.5\%$ in the interval $1 \text{ cm s}^{-1} - 5 \text{ cm s}^{-1}$). Only when very low velocities were used, the relative energy difference increased.

6.6.2 Simulations of multi-stage cases

The sensitivity analysis was performed using the input parameters shown in Table 22.

In particular, different multi-stage operations were simulated by varying the number of battery stacks from 4 up to 17 (i.e. batteries hydraulically connected in series, fed with single pass through all 4 to 17 stacks, or “stages”). In all simulations, we assumed a battery state of charge (SOC) of 0% at 0.05 M and 100% at 1.00 M HCl, thus fixing the concentration targets at the outlet of the last stage for both charge and discharge. The electric current was tuned accordingly to achieve the concentration targets in all the simulated scenarios. For the sake of simplicity, the same electric current was used in all the sequential stages. Steady-state simulations were performed, assuming a single charge-discharge cycle.

Table 22. Overview of main input parameters used in the sensitivity analysis.

| Geometrical parameters of the stack | | |
|-------------------------------------|----|----|
| Spacer length, L | cm | 50 |
| Spacer width, b | cm | 50 |

Acid/Base Flow Battery

| | | | | |
|--|----------------------------|------------------------|-----------------------------|------------|
| | Spacer thickness | μm | 475 | |
| Membrane properties | | | | |
| | units | AEM | CEM | BPM |
| Thickness | μm | 130 | 130 | 190 |
| Areal resistance | $\Omega\text{ cm}^2$ | 4.0 | 3.5 | 5.0 |
| H ⁺ diffusivity ¹ | $\text{m}^2\text{ s}^{-1}$ | 2.0E-11 | 0.7E-11 | - |
| Na ⁺ diffusivity | $\text{m}^2\text{ s}^{-1}$ | 1.6E-11 | 0.5E-11 | - |
| Cl ⁻ diffusivity | $\text{m}^2\text{ s}^{-1}$ | 1.7E-11 | 0.6E-11 | - |
| OH ⁻ diffusivity | $\text{m}^2\text{ s}^{-1}$ | 1.9E-11 | 0.6E-11 | - |
| Fixed charge density | mol m^{-3} | 5000 | 5000 | - |
| Feed conditions in the first stage | | | | |
| Feed composition | units | Charge (0% SOC) | Discharge (100% SOC) | |
| HCl in acid compartment | mol m^{-3} | 50 | 1000 | |
| NaCl in acid compartment | mol m^{-3} | 250 | | |
| HCl in salt solution compartment | mol m^{-3} | 10 | | |
| NaCl in salt solution compartment | mol m^{-3} | 1000 | | |
| NaOH in base compartment | mol m^{-3} | 50 | | |
| NaCl in base compartment | mol m^{-3} | 250 | | |
| Fluid flow velocity | cm s^{-1} | 1.0 | 1.0 | |
| Electrode compartments and triplets | | | | |
| Blank resistance | $\Omega\text{ cm}^2$ | 12 ² | | |
| Number of triplets (repeating units) per stack, <i>N</i> | - | 10 | | |

¹ preliminary measurements were performed with NaCl solutions and a two-chamber diffusion cell; then, ion diffusivities were estimated by assuming that they are inversely proportional to the hydrated radius (Stokes-Einstein equation).

² obtained experimentally.

In the previous chapters, performance parameters were formulated for 1 stack. However, the multi-stage operation is characterized by calculating the *GPD* averaged over all the N_s sequential stages as follows

$$\overline{GPD} = \frac{\sum_{k=1}^{N_s} GPD_k}{N_s} \quad (163)$$

The gross power (*P*) of a pilot plant of generic size (i.e., of a given N_p number of stacks hydraulically in parallel) is equal to

$$P = N_p \sum_{k=1}^{N_s} P_k \quad (164)$$

Moreover, the main figure of merits characterizing the charge-discharge cycle of the AB-FB were already described previously. However, here a more convenient definition of Coulombic Efficiency (CE), Voltage Efficiency (VE) and Round Trip Efficiency (RTE) were applied:

$$CE = \frac{I_{ext,d}}{I_{ext,c}} \quad (165)$$

$$VE = \frac{\overline{U_{ext,d}}}{\overline{U_{ext,c}}} \quad (166)$$

$$RTE = \frac{I_{ext,d} \times \overline{U_{ext,d}}}{I_{ext,c} \times \overline{U_{ext,c}}} = CE \times VE \quad (167)$$

in which, $\overline{U_{ext,d}}$ and $\overline{U_{ext,c}}$ are the average values of external voltage in discharge and charge, respectively, and $I_{ext,d}$ and $I_{ext,c}$ are the corresponding external currents (equal for all stages).

The main simulation results are reported in Figure 123, as well as the applied values of current density, highlighting the effect of the number of sequential stages on the process performance.

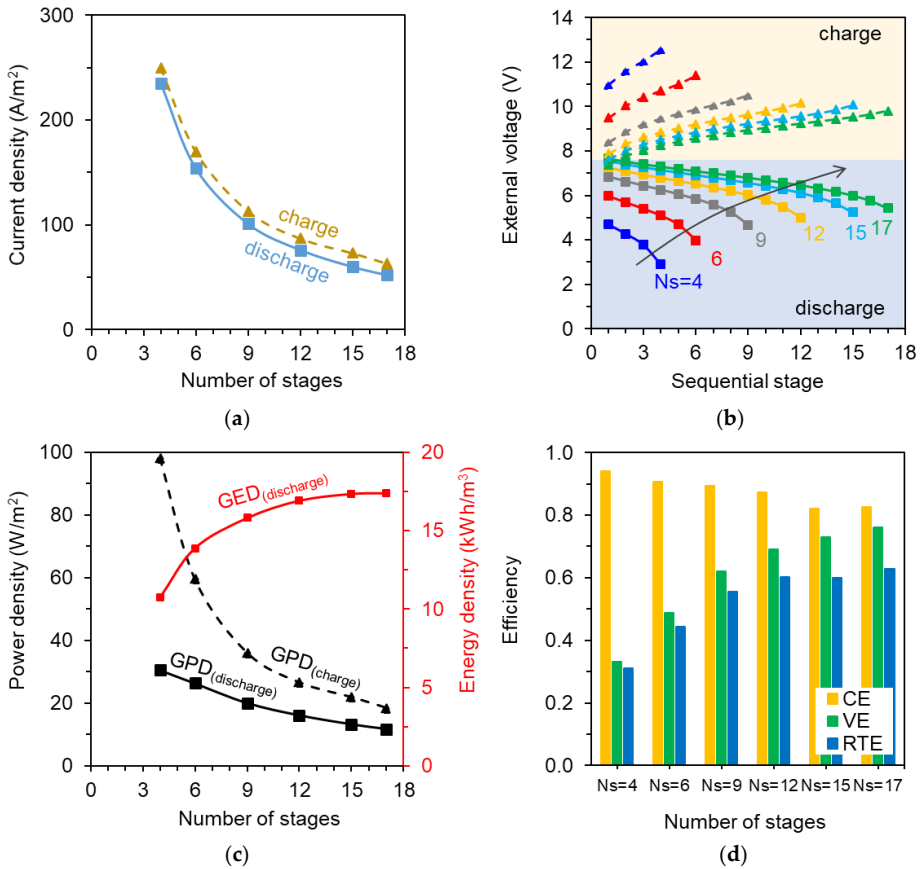


Figure 123. Model predictions of the effect of number of stages on acid-base flow battery. a) Charge and discharge current density fixed equal for all stages; b) Profiles of charge/discharge external voltage at each sequential AB-FB stage; c) Average charge/discharge gross power density (GPD) and (discharge) gross energy density (GED); d) Coulombic efficiency (CE), voltage efficiency (VE), and round-trip efficiency (RTE). Each stage is simulated as an AB-FB stack with a membrane active area of $0.5 \times 0.5 \text{ m}^2$.

In particular, Figure 123a shows the current density (i.e., current divided by the membrane active area) that was required to achieve the same (inlet-outlet) concentration difference for the acid solution, as a function of the number of AB-FB stages. As expected, the required current density decreases as the number of sequential stages N_s increases, due to the accompanying increase in total membrane area (at fixed feed flow rate). However, the total electric current is not constant. As N_s increases, the total electric current increases from $\sim 250 \text{ A}$ to $\sim 270 \text{ A}$ in charge, and decreases from $\sim 235 \text{ A}$ to $\sim 221 \text{ A}$ in discharge, thus indicating a decreasing

current efficiency in both phases. This is simply caused by the increasing total membrane area, and consequently, increasing total mass transported by undesired fluxes of co-ions and water.

The predicted values of voltage over all stacks are reported in Figure 123b. During the discharge phase, the external voltage decreases along the stages due to the decreasing driving force (i.e., pH and concentration difference). Likewise, the voltage increases along the stages during charge, as a result of the increasing concentration difference. As the number of stages increases (Figure 123b), the voltage profiles along the stages tend towards the open circuit conditions (both for discharge and charge), as a result of the decreasing current density in the stacks (Figure 123a). The average gross power density (\overline{GPD}) of the stacks series (Figure 123c) exhibits a decreasing trend with the number of stages (N_s), similarly to the electric current. During the charge phase both the electric current and the average voltage decreases with N_s , thus causing a more pronounced reduction of \overline{GPD} than during the discharge phase. The predicted \overline{GPD} values are in the range of 18.5-98.2 W m^{-2} for charge, and 11.7-30.6 W m^{-2} for discharge.

The discharge gross energy density (GED_v) is reported also in Figure 123c. The gross energy density is equal to 10.4 $\text{kWh m}^{-3}_{\text{acid}}$ for the 4-stage system (discharge energy efficiency η_d of ~45%), and it increases with the number of stages due to the increasing cumulative power, reaching a plateau at $GED_v = 17.4 \text{ kWh m}^{-3}_{\text{acid}}$ for the 17-stage system ($\eta_d \approx 72\%$). This indicates that the overall power ($\sum_{k=1}^{N_s} P_{k,d}$) increased at decreasing rate as a function of N_s , eventually reaching a maximum value. This is because the simulations at higher numbers of stages were based on lower current density values, thus distant from peak power conditions in discharge. The discharge electrical efficiency, defined as the power delivered to the external load divided by the total dissipated power (i.e. the sum of the internal and external power) was comprised between 47% ($N_s = 4$) and 79% ($N_s = 17$). Moreover, the less than proportional increase of the overall power with the number of stages justifies the reduction of \overline{GPD} . Figure 123d shows the efficiency of the process, in terms of Coulombic efficiency (CE), voltage efficiency (VE), and round-trip efficiency (RTE). The CE decreases from 94% to 82% as N_s increases. Such high values of Coulombic efficiency mean that the battery is characterized by high current efficiencies in both phases (charge/discharge). In particular, since parasitic currents in the manifolds are negligible in this case (due to small manifolds size and low number of triplets), the current efficiency is affected only by undesired fluxes (of co-ions and water) through the membranes. The voltage efficiency (VE) increases with the number of stages (from 33% up to 76%), as a result of the more homogeneous voltage distribution among sequential stages both during charge and discharge (Figure 123b). As overall

result, the round-trip efficiency (*RTE*) trend is essentially determined by the increase of the *VE*, with *RTE* values in the range of 31%-63% by increasing the number of stages.

Figure 124 shows the predicted power output (Eq.164) as a function of the total membrane area (increased by increasing the number of parallel stages) for the cases of $N_s = 4$ and $N_s = 17$ sequential stages.

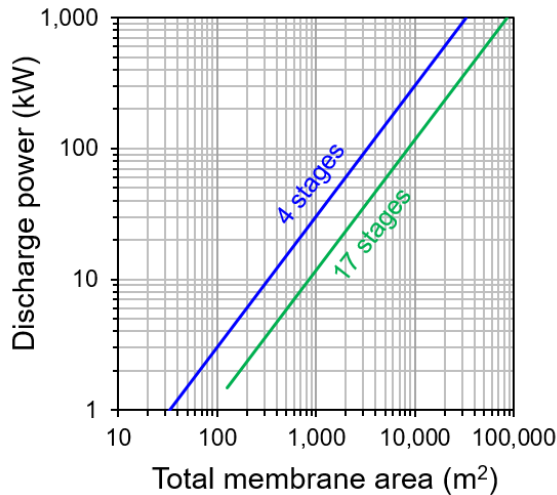


Figure 124. Discharge power as a function of the total membrane area for 4-stage ($N_s = 4$) and 17-stage ($N_s = 17$) AB-FB system. Each stage is simulated an AB-FB stack with a membrane active area of $0.5 \times 0.5 \text{ m}^2$.

With the current performance of commercial (monopolar/bipolar) membranes, a discharge power of 1 kW could be achieved using a 4-stage AB-FB system with a total membrane area of about 30 m^2 (i.e. each stage equipped with 10 triplets and a membrane active area of $0.5 \times 0.5 \text{ m}^2$). For a 1 MW power system, the required membrane area increased up to $30,000 \text{ m}^2$ (i.e., $\sim 10,000$ parallel triplets for each stage of the four serial stages). For the case of 17 stacks in series, the membrane area providing the same discharge power is increased by 2.6 times ($6,730$ parallel triplets for 1 MW). Given the energy density of the system (Figure 123c), the corresponding flow rates to supply 1 MW power are $93 \text{ m}^3 \text{ h}^{-1}$ and $58 \text{ m}^3 \text{ h}^{-1}$ (for each solution) for the 4-stage and 17-stage AB-FB systems, respectively. These modelling results highlight that, to reach AB-FB applications on the kW-MW scale, further optimization studies should focus on plant design to reduce the membrane area and volume of solutions.

7 Acid/Base Flow Battery optimization

The sensitivity analysis performed in chapter 6 showed that contrasting effects on the performance of AB-FB systems arise when varying operating conditions as well as design features. In this chapter, an optimization study of the AB-FB was performed for the first time. A two-objective optimization was conducted by maximizing the net Round Trip Efficiency and the Net Power Density in the discharge phase. The ϵ -constraint method was adopted in order to build curves of Pareto optimal solutions under several scenarios, thus assessing systematically the effect of decision variables, i.e. operating conditions and design features. The optimization tool included in the gPROMS Model Builder[®] software package was used. This optimization study showed that optimized operating conditions and design features may be chosen to maximize the net Round Trip Efficiency up to a value of 64% and Net Power Density to 19.5 W m^{-2} in a closed-loop configuration. Moreover, improved membrane properties led to net Round Trip Efficiency and Power Density of 76.2% and 23.2 W m^{-2} respectively, thus showing promising performance for future developments of the AB-FB.

7.1 Literature review

In the last years, many studies on BMED systems have been focused mainly on the experimental analysis under several operating conditions (e.g. current and voltage, mean flow velocities, temperature, etc.) and with the stack dimensions (i.e. length, width, number of repeating units, etc.) for a large variety of applications. Few efforts have been devoted to the experimental characterization of BMRED and AB-FB systems. Overall, no attempts have been made for the optimization of these systems.

Only a few of works presented in literature are focused on the conventional electro dialysis and reversal electro dialysis processes. Regarding the conventional electro dialysis, a multi-objective optimization study was performed by Chindapan et al. [260] for the desalination of fish sauce. In their work, the genetic algorithm method was used (MOGA). Particularly, they obtained the Pareto frontiers using the final product concentrations and the energy consumption as objective functions. Bian et al. [261] performed an ED optimization aiming at minimizing the overall costs of an electro dialysis unit coupled with photovoltaic energy. The Particle Swarm Optimization (PSO) algorithm [262] was implemented in a previously developed ED model [222]. Guesmi et al. [263] performed an experimentally-based optimization study on the removal of boron via ED. The Response Surface Methodology (RSM)

was used with the Central Composite Design (CCD) to optimize the experiments, searching for the maximum boron removal by varying the operating conditions. Rohman and Aziz [264] evaluated the optimal operating conditions for the HCl recovery by batch ED. A dynamic optimization technique, i.e. the orthogonal collocation method, was used with a lumped parameters ED model. The optimization was performed with different single objectives regarding process time, energy consumption, degree of separation, dilute concentration and process profit. These objective functions exhibited contrasting requirements. Therefore, the same authors developed a multi-objective optimization [265]. In particular, an ED process was optimized by minimizing the energy consumption and maximizing the acid concentration. A Non-dominated Sorting Genetic Algorithm II (NSGA-II) was used, and the decision variables were the external current and the flow rates of the electrolyte solutions.

In regard to conventional reverse electrodialysis (RED) processes, Veerman et al. [266] performed simulations with a RED one-dimensional process model to optimize three variables, i.e. the Net Power Density, or the net Energy Density or the product of them, by varying channel thicknesses and flow rates as decision variables with different stack length as scenario variable. Long et al. [160] optimized the maximum Net Power Density with a single-objective approach for a conventional RED stack of given total size by changing channel's thicknesses and solution's flow rates. The method of the Genetic Algorithm (GA) based on the evolution algorithm was used. In another work, Long et al. [159] observed the existence of optimal flow rates of the electrolyte solutions that maximize the Net Power Density in a single-objective optimization problem. However, these optimal conditions resulted in reduced values of the energy efficiency (i.e. ratio of the actual power extracted and the energy that could be extracted in the reversible process). Therefore, they performed also a multi-objective optimization study based on the NSGA-II approach, in order to obtain the Pareto frontier of Net Power Density and Energy efficiency. Ciofalo et al. [161] performed an optimization study with the gradient-ascent algorithm implemented on a previously developed RED model [106]. The Net Power Density was maximized by using channel's thicknesses and inlet fluid velocities as decision variables, while other features were varied as scenario variables (solution's concentrations, stack length, flow arrangement and presence of spacers).

The optimization of the AB-FB is an essential step to increase the competitiveness of the battery. Different combinations of operating and design features affect significantly the performance of the system during both phases (i.e. charge and discharge). These parameters may eventually have contrasting effects on the performance. The main performance indicators of an Acid-Base Flow Battery are

the Round Trip Efficiency and the average power density obtained during the discharge. However, a high efficiency could be associated with a low power density. In fact, the latter is a parabolic function of the applied external current. Therefore, depending on the external load (i.e. a direct function of the external current) the power density may be maximized when the increased ohmic losses lead to a RTE decrease. Moreover, pumping power may play an important role in terms of energy consumption, particularly in the discharge phase, when the maximization of the collected energy is crucial. Therefore, power losses must be limited. In this chapter, the developed AB-FB multi-scale model was used to perform a dynamic multi-objective optimization study of the system in several scenarios. Up to eight operating and design decision variables were varied, thus maximizing the Net Round Trip Efficiency and the Net Power Density in the discharge phase. The objective functions were chosen to be the net rather than the gross quantities, in order to take into account for the effect of different pumping powers.

7.2 Optimization method

The Net Power Density was already defined in chapters 3 and 4 (see Eqs. 90 and 109). The net Round Trip Efficiency is defined as follows,

$$RTE_{net} = \frac{\int_0^{t_d} (GPD_d - PPD_d) dt}{\int_0^{t_c} (GPD_c + PPD_c) dt} \quad (168)$$

A multi-objective optimization problem may be generally defined as the minimization (or the maximization) of a vector of objective functions [267]:

$$\max\{f(\mathbf{x})\} \leftrightarrow \min\{-f(\mathbf{x})\} \quad (169)$$

$$f(\mathbf{x}) = [f_1(\mathbf{x}), f_2(\mathbf{x}), \dots, f_m(\mathbf{x})]^T \quad (170)$$

$$g_i(\mathbf{x}) \leq 0 \quad (j = 1, 2, \dots, p) \quad (171)$$

$$h_k(\mathbf{x}) = 0 \quad (k = 1, 2, \dots, q) \quad (172)$$

$$x_i^{min} \leq x_i \leq x_i^{max} \quad (i = 1, 2, \dots, n) \quad (173)$$

where f is the objective functions vector, \mathbf{x} is the vector of the decision variables falling within the interval between the lower and upper limits as in Eq. 173. Eqs. 171 and 172 denote p - inequalities and q -equalities constraints.

In this chapter, the multi-objective optimization problem was solved by using the optimization tool of gPROMS Model Builder®. Since this software allows only to solve single-objective optimization problems, the two-objective optimization was performed by using the ε -constraint method. This method was proposed in 1971 by

Haimes et al. [268]. The ε -constraint method allows to maintain a single-objective function, transforming the other functions in inequality constraints, in which ε represents the constraints vector with its upper (or lower) bounds. In the present case, the objective functions are the RTE_{net} (Net Round Trip Efficiency) and the average NPD_d (Net Power Density during the discharge phase), thus the problem is bi-objective [269] and may be described as follows,

$$\text{Objective: } \quad \text{Max } RTE_{net}(\mathbf{x}) \quad (174)$$

$$\text{Subject to: } \quad Av. NPD_d(\mathbf{x}) \geq \varepsilon \quad (175)$$

$$g(\mathbf{x}) \leq 0 \quad (176)$$

$$h(\mathbf{x}) = 0 \quad (177)$$

The results of the present optimization study were expressed in terms of Pareto optimal front, which consists of a curve of best trade-off points between the two chosen objective functions (optimal or *non-dominated* solutions [267]). Any point of the Pareto frontier represents an optimal solution that maximizes RTE_{net} under a constraint on the value of NPD_d . The extreme points represent the two single-objective optimizations without any constraint. Note that the optimized battery is in a closed-loop configuration, with solutions recirculated in the tanks assumed with perfect mixing. Therefore, this problem is intrinsically dynamic. The RTE_{net} is a performance parameter which can be calculated only at the end of each battery cycle. Likewise, the average NPD_d is computable at the end of the discharge phase. These quantities may be regarded as “cycle” variables rather than time variables. A battery phase (i.e. charge or discharge) ends when a certain target is reached. This target was assumed to be a specific HCl concentration in the acid tank, namely $C_{target,c}$ and $C_{target,d}$ for the concentration reached at the end of the charge and discharge, respectively. The acid concentration target was chosen as representative of the State of Charge of the battery. Specifically, the State of Charge is 0% when it reaches $C_{target,d}$ and 100% when it reaches $C_{target,c}$. The decision variables were of two types: operating and design (Table 23).

Table 23. List of the decision variables with their respective lower and upper bounds.

| Operating variables | | | |
|---------------------------|------------|------------------------|-----------------------|
| Variable name | symbol | lower bound | upper bound |
| charge current density | i_c | 30 A m ⁻² | 500 A m ⁻² |
| discharge current density | i_d | 30 A m ⁻² | 200 A m ⁻² |
| charge mean flow velocity | $u_{ch,c}$ | 0.5 cm s ⁻¹ | 5 cm s ⁻¹ |

Acid/Base Flow Battery optimization

| | | | |
|--------------------------------|----------------|-------------------------|--------------------------|
| discharge mean flow velocity | $u_{ch,d}$ | 0.5 cm s ⁻¹ | 5 cm s ⁻¹ |
| charge target concentration | $C_{target,c}$ | 500 mol m ⁻³ | 1000 mol m ⁻³ |
| Discharge target concentration | $C_{target,d}$ | 50 mol m ⁻³ | 200 mol m ⁻³ |
| Design variables | | | |
| Spacer length | L | 5 cm | 200 cm |
| Spacer thickness | b | 50 μm | 1000 μm |

Other variables were regarded as scenario variables. The scenario variables were: the number of decision variables, the initial volume ratio (in term of $V_{t,a}:V_{t,b}:V_{t,s}$) of the electrolyte solutions in the three external tanks, i.e. acid, base and salt tank, the lower bound of $C_{target,c}$ and improved membrane properties (in terms of ohmic resistances, ion diffusivities and water permeability). These scenarios are reported in Table 24.

Table 24. List of the optimization scenarios.

| decision variables | scenario |
|--|---|
| i_c, i_d | |
| $i_c, i_d, u_{ch,c}, u_{ch,d}$ | |
| $i_c, i_d, u_{ch,c}, u_{ch,d}, C_{target,c}, C_{target,d}$ | |
| $i_c, i_d, u_{ch,c}, u_{ch,d}, C_{target,c}, C_{target,d}$ | $C_{target,c}=500 \text{ mol m}^{-3}$ |
| $i_c, i_d, u_{ch,c}, u_{ch,d}, C_{target,c}, C_{target,d}, L, b$ | |
| $i_c, i_d, u_{ch,c}, u_{ch,d}, C_{target,c}, C_{target,d}, L, b$ | $V_{t,a}:V_{t,b}:V_{t,s}= 1:1:1$ |
| $i_c, i_d, u_{ch,c}, u_{ch,d}, C_{target,c}, C_{target,d}, L, b$ | improved membrane properties ¹ |

¹ by halving electrical resistances, ion diffusivities and water permeability of the IEMs.

Table 25 reports all the model input used in the reference case. Depending on the decision and scenario variables these input may differ. Every time that the model inputs are different, it will be declared. Each simulation was performed for a single battery cycle, i.e. a charge followed by a discharge.

Finally, the Yo-Yo (see 6.3.3.2) simulations were performed at the Pareto set conditions obtained in the scenario with 8 decision variables and with $V_{t,a}:V_{t,b}:V_{t,s}=1$.

Acid/Base Flow Battery optimization

Table 25. Model inputs of the reference case for the optimization study.

| Geometrical features | | | | | |
|-------------------------------------|---|---------|---------|---------|---------|
| Spacer length | cm | 44 | | | |
| Spacer width | cm | 47.6 | | | |
| Spacer thickness | μm | 500 | | | |
| N° triplet | - | 10 | | | |
| N° spacer holes | - | 1 | | | |
| Spacer hole area | mm^2 | 400 | | | |
| Membrane properties | | | | | |
| | | AEM | CEM | AEL | CEL |
| Thickness | μm | 75 | 75 | 60 | 60 |
| Electrical resistance | ohm cm^2 | 4 | 3.5 | 2.5 | 2.5 |
| H+ diffusivity | $\text{m}^2 \text{s}^{-1}$ | 2.0E-11 | 0.7E-11 | 2.0E-11 | 0.7E-11 |
| Na+ diffusivity | $\text{m}^2 \text{s}^{-1}$ | 1.6E-11 | 0.5E-11 | 1.6E-11 | 0.5E-11 |
| Cl- diffusivity | $\text{m}^2 \text{s}^{-1}$ | 1.7E-11 | 0.6E-11 | 1.7E-11 | 0.6E-11 |
| OH- diffusivity | $\text{m}^2 \text{s}^{-1}$ | 1.9E-11 | 0.6E-11 | 1.9E-11 | 0.6E-11 |
| Water permeability | ml bar^{-1} $\text{h}^{-1} \text{m}^{-2}$ | 8 | 8 | - | - |
| Fixed charge group | mol m^{-3} | 5000 | 5000 | 5000 | 5000 |
| Initial conditions of the solutions | | | | | |
| $C_{t,HCl,a,out}$ | mol m^{-3} | 50 | | | |
| $C_{t,NaCl,a,out}$ | mol m^{-3} | 250 | | | |
| $V_{t,a}$ | l | 10 | | | |
| $C_{t,NaOH,b,out}$ | mol m^{-3} | 50 | | | |

| | | |
|-----------------------------------|--------------------------|-----|
| $C_{t,NaCl,b,out}$ | mol m ⁻³ | 250 |
| $V_{t,b}$ | l | 10 |
| $C_{t,HCl,s,out}$ | mol m ⁻³ | 10 |
| $C_{t,NaCl,s,out}$ | mol m ⁻³ | 250 |
| $V_{t,s}$ | l | 60 |
| Mean flow velocity (charge) | cm s ⁻¹ | 1 |
| Mean flow velocity (discharge) | cm s ⁻¹ | 1 |
| R_{bl} | Ω cm ² | 12 |

7.3 Optimization results

The first investigated case concerns the use of the charge and discharge current densities as decision variables. The predicted Pareto frontier is shown in Figure 125.

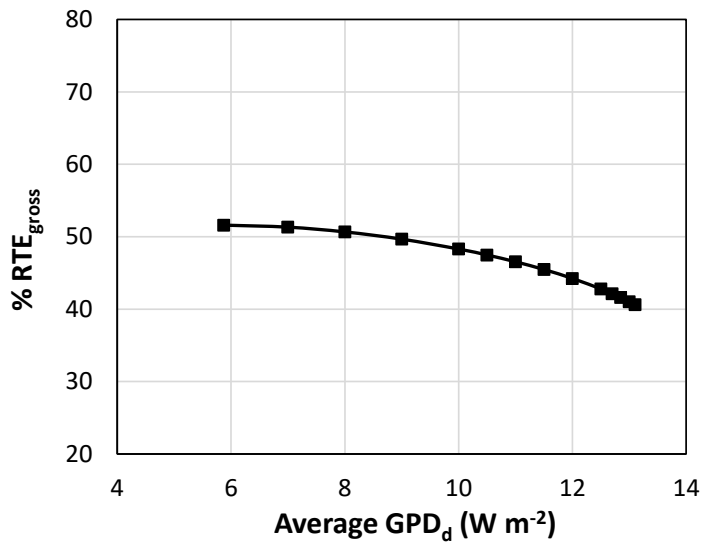


Figure 125. Pareto frontier of gross RTE as a function of the average discharge GPD. Decision variables: i_c , i_d .

Only in this case, the Pareto frontier was reported as function of the gross RTE and GPD because the net values showed negligible variations with current densities.

The Pareto curve shows a maximum of RTE of 51.6%, which corresponds to the minimum of the constraint GPD, which is equal to 5.87 W m^{-2} . At the maximum constraint GPD, equal to 13.1 W m^{-2} , the RTE was found to be 40.6%. The theoretical energy density difference from $C_{target,d}$ to the $C_{target,c}$ is 20.1 kWh m^{-3} and this value was always equal across the Pareto set because the target concentrations of charge and discharge were fixed and equal to 1 M and 0.05 M of HCl, respectively.

Figure 126 shows the results obtained in the scenario with four decision variables. The channel mean flow velocities in the two battery phases were added as decision variables.

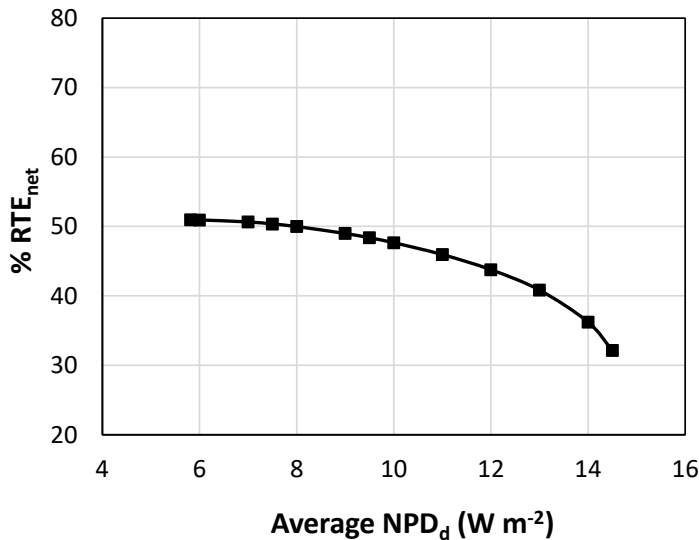


Figure 126. Pareto frontier of net RTE as a function of the average discharge NPD. Decision variables: i_c , i_d , $u_{ch,c}$ and $u_{ch,d}$.

The Pareto curve reports a maximum RTE_{net} of 50.9%, while NPD was 5.82 W m^{-2} . At the maximum constraint of average NPD equal to 14.5 W m^{-2} the resulting RTE_{net} was 32.1%. Again the energy density was 20.1 kWh m^{-3} as the one recorded in the previous case with 2 decision variables. This occurred because also in this case the target concentrations were fixed.

Figure 127 illustrates the results for the case with 6 decision variables. Particularly, target concentration of charge and discharge were added.

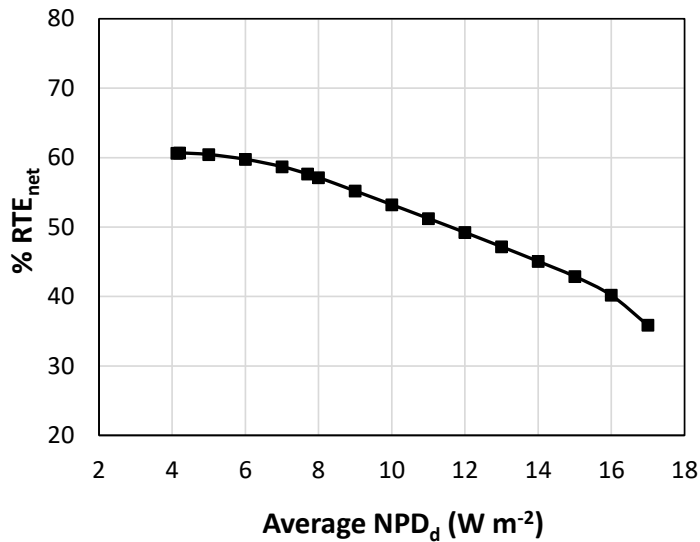


Figure 127. Pareto frontier of net RTE as a function of the average discharge NPD. Decision variables: i_c , i_d , $u_{ch,c}$, $u_{ch,d}$, $C_{target,c}$ and $C_{target,d}$. Lower limit of $C_{target,c}$ = 600 mol m^{-3} .

In this case, a significant improvement of the optimal solution was obtained. The Pareto front, in fact, covers a larger range of both variables. The maximum RTE_{net} is 60.6%, whereas the corresponding average discharge NPD was 4.13 W m^{-2} . The obtained maximum RTE_{net} is almost 10% higher (in absolute value) than the one observed in the previous cases. Therefore, a significant improvement occurs when changing the concentration targets. When adding target concentrations as decision variables, the resulting energy density differs at the two ends of the curve, namely 9.81 and 17.1 kWh m^{-3} . In this scenario, the interval of charge target concentration varied from 0.6 M to 1 M . Moreover, the concentration at which the maximum RTE_{net} was found corresponded to 0.6 M , thus the effect of a variation of the lower limit of $C_{target,c}$ was considered as a possible scenario. Specifically, in the next results the lower limit of the charge concentration was fixed at 0.5 M . Figure 128 shows a comparison between the optimization analysis with 6 decision variables performed with the lower limit of $C_{target,c}$ equal to 0.5 M and 0.6 M .

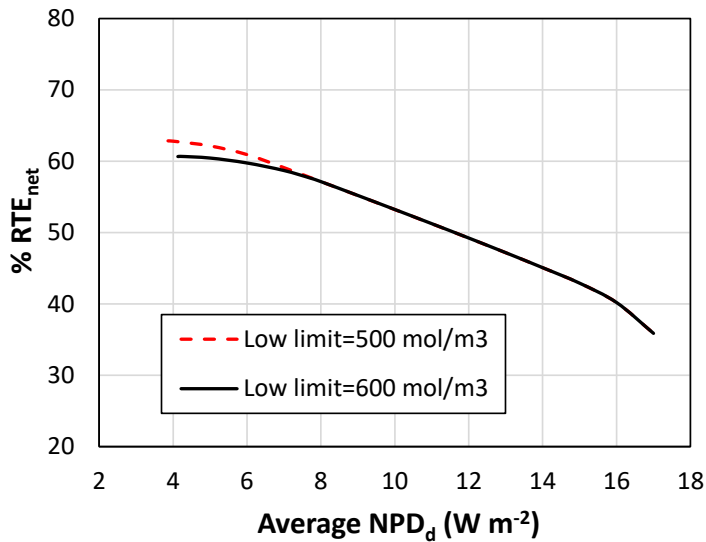


Figure 128. Comparison between the Pareto frontiers of net RTE as a function of the average discharge NPD. Decision variables: i_c , i_d , $u_{ch,c}$, $u_{ch,d}$, $C_{target,c}$ and $C_{target,d}$. Black line: Lower limit of $C_{target,c}=600 \text{ mol m}^{-3}$. Red dashed line: Lower limit of $C_{target,c}=500 \text{ mol m}^{-3}$.

As shown in Figure 128, a better performance in terms of maximum RTE_{net} (~3% higher) may be obtained by applying a lower $C_{target,c}$ limit. However, from a constraint average NPD of $\approx 7 \text{ W m}^{-2}$, the resulting optimal RTE was almost equal to the one obtained with the higher limit of $C_{target,c}$. Therefore, this lower limit only affects the first tract of the Pareto frontier.

Figure 129 illustrates the optimization scenario with 8 decision variables. In this case, two design features were added, namely spacer thickness and length.

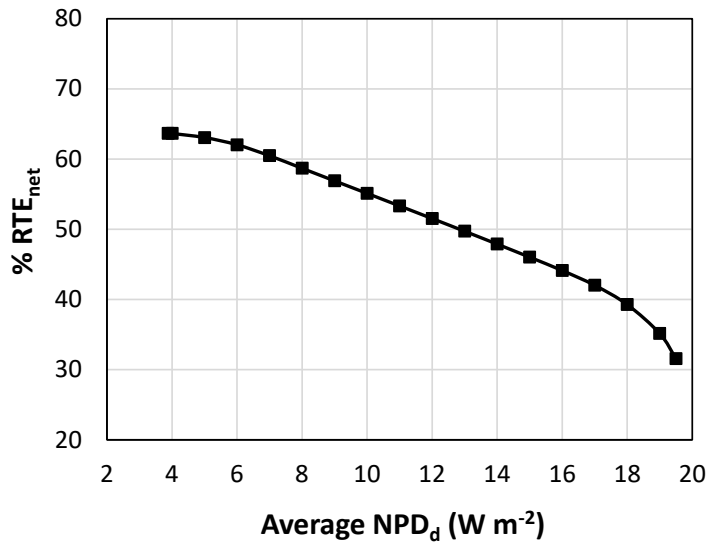


Figure 129. Pareto frontier of net RTE as a function of the average discharge NPD. Decision variables: i_c , i_d , $u_{ch,c}$, $u_{ch,d}$, $C_{target,c}$, $C_{target,d}$, L and b . Lower limit of $C_{target,c}=500 \text{ mol m}^{-3}$.

By comparing Figure 129 with Figure 128, it can be drawn that when adding the design variables only small improvements were predicted.

Concerning the optimization case illustrated in Figure 129, the profiles of the decision variables as functions of the average discharge NPD are reported in Figure 130.

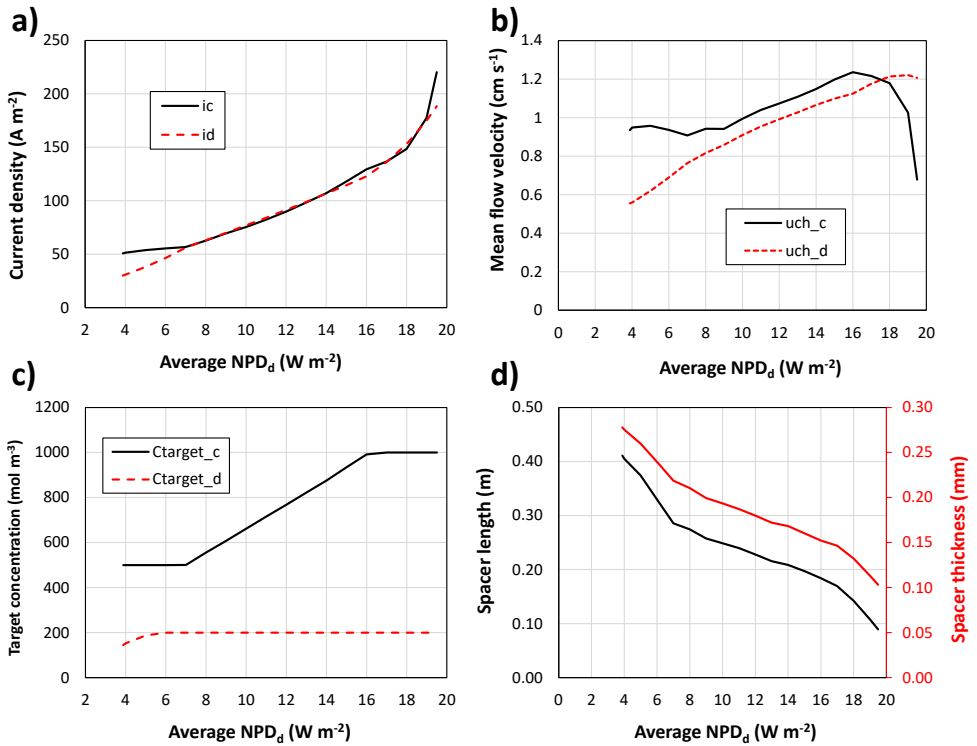


Figure 130. Decision variables profiles as functions of the average discharge NPD. Decision variables: i_c , i_d , $u_{ch,c}$, $u_{ch,d}$, $C_{target,c}$, $C_{target,d}$, L and b . Lower limit of $C_{target,c} = 500 \text{ mol m}^{-3}$.

The predicted values of current densities show an increasing trend with the NPD, that means a decreasing trend with the RTE. At lower current densities, the resulting voltage efficiency is higher as the external voltage tends towards the open circuit condition in both charge and discharge phases. Particularly, the maximum RTE was obtained when the discharge and charge current densities were 30 and 50 A m^{-2} respectively. The mean flow velocities across the Pareto frontier (Figure 130b) ranged from 0.67 to 1.2 cm s^{-1} for the charge and from 0.55 to 1.2 cm s^{-1} for the discharge. Concerning the target concentration profiles (Figure 130c), apart for a short stretch, the discharge target concentration shows a constant profile against the NPD, meaning that the upper limit of $C_{target,d}$ was reached. On the other hand, $C_{target,c}$ resulted in a greater variation along the NPD axis, ranging from the whole interval of the decision variable. Although higher or lower limits of the charge target concentrations could be beneficial for reaching higher values of the objective functions, these may not be of practical use. In fact, the actual Ion Exchange Membranes cannot be used with high acid and base concentrations due to unsuitable

properties of selectivity. On the other hand, too low acid and base concentrations would decrease the electromotive force and thus the obtainable energy density. Finally, spacer length and thickness (Figure 130d) show both a similar (at least qualitatively) decreasing trend with NPD.

Figure 131 illustrates the optimization scenario with 8 decision variables but by adopting different volume ratios, namely 1:1:1 and 1:1:6.

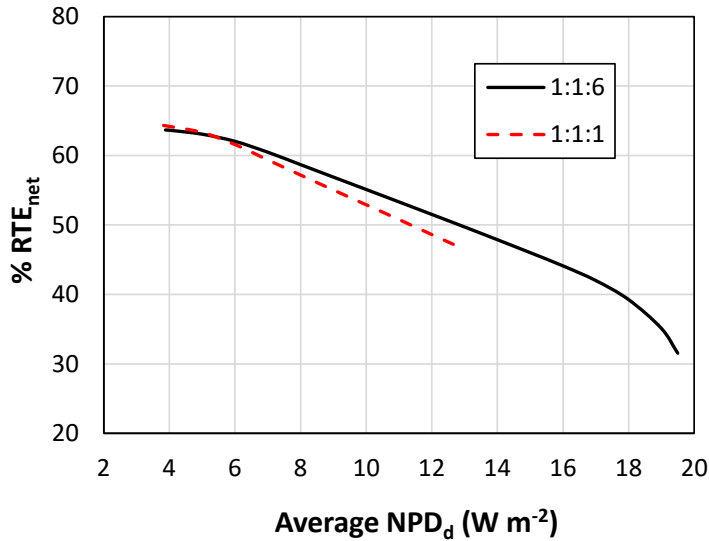


Figure 131. Comparison between the Pareto frontiers of net RTE as a function of the average discharge NPD. Decision variables: i_c , i_d , $u_{ch,c}$, $u_{ch,d}$, $C_{target,c}$, $C_{target,d}$, L and b . Black line: volumes ratio 1:1:6 and initial $C_{t,NaCl,s,out}=500 \text{ mol m}^{-3}$. Dashed red line: volumes ratio 1:1:1 and initial $C_{t,NaCl,s,out}=100 \text{ mol m}^{-3}$. Limit of $C_{target,c}=500 \text{ mol m}^{-3}$.

In the case of a volumes ratio of 1:1:1, an increase of the initial NaCl concentration in the salt tank was required, due to the stoichiometric acid/base formation. The volumes ratio 1:1:6 guaranteed better performance in terms of average RTE_{net}, as it was $\approx 3.5\%$ higher than the one obtained with volumes ratio 1:1:1. The maximum constraint NPD was limited at 13 W m^{-2} in order to avoid a failure of the convergence of the optimization tool for excessive reduction of the outlet NaCl concentration from the stack. Finally, Figure 132 showed the comparison between the Pareto frontier in the membrane reference case, and the results obtained by using improved membrane properties. The improvement concerned the halving of the electrical resistance, ion diffusivities and water permeability of the membranes.

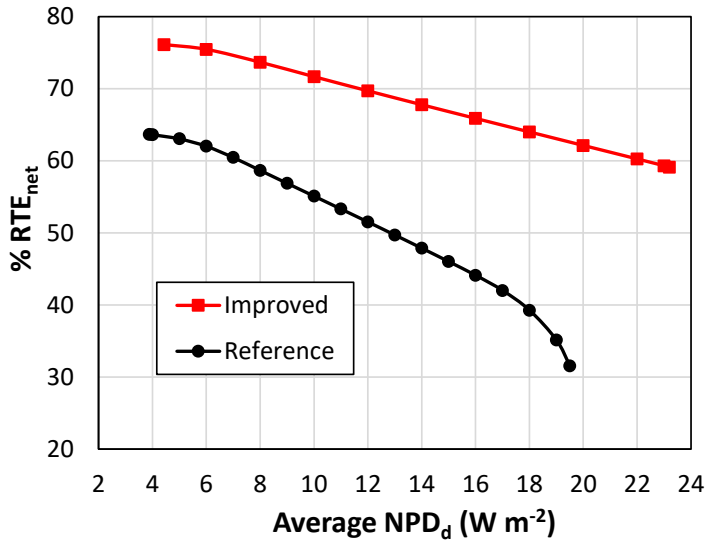


Figure 132. Comparison between the Pareto frontiers of net RTE as a function of the average discharge NPD. Decision variables: i_c , i_d , $u_{ch,c}$, $u_{ch,d}$, $C_{target,c}$, $C_{target,d}$, L and b . Black line: Reference membrane properties. Red line: Improved membrane properties. Limit of $C_{target,c}=500 \text{ mol m}^{-3}$. Volumes ratio = 1:1:6. Initial $C_{t,NaCl,s,out}=500 \text{ mol m}^{-3}$.

The Pareto frontier for the improved membrane properties is intended to provide a possible future scenario for the AB-FB technology. Improved membranes may lead to significant better performance as shown by the great deviation between the two curves in Figure 132 (higher average values over the Pareto front for both RTE and NPD). The improved scenario resulted in an increase of 12.4% of the maximum RTE_{net}, reaching 76.1%, whereas the NPD was 4.43 W m⁻². At the maximum constraint NPD of 23.2 W m⁻², the resulting RTE_{net} was 59.1%. The energy density in this improved case was 6.31 kWh m⁻³ at the minimum NPD, whereas 17.1 kWh m⁻³ at the maximum NPD. The energy density values were obtained at the two ends of the Pareto frontier. However, the maximum or minimum values may correspond at intermediate values of NPD. Therefore, a future optimization study could also include the effect of the energy density as third objective function.

7.4 Results of the Yo-Yo configuration at the Pareto frontier closed-loop conditions

In this final section, a comparison between closed-loop and yo-yo configurations is shown. In order to maintain coherence between the two configurations in terms of the volume ratios, the results have been compared using

volume ratios equal to 1:1:1. Specifically, the Yo-Yo configuration was simulated at the Pareto frontier conditions obtained for the closed-loop operation, with 8 decision variables (shown in Figure 131).

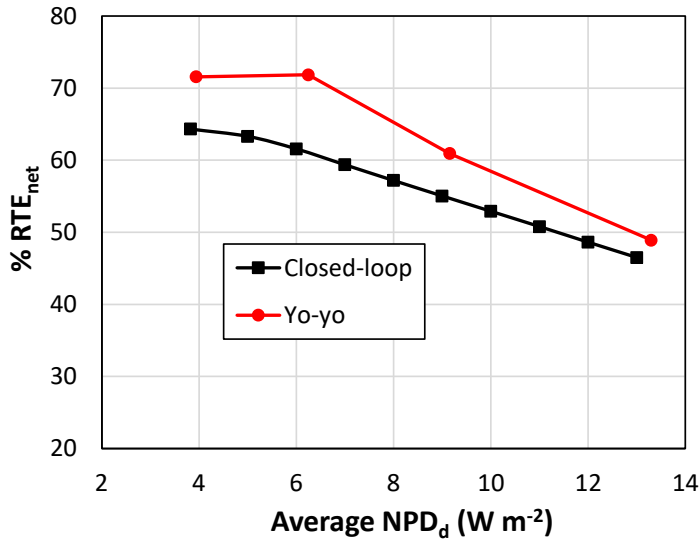


Figure 133. Comparison between the closed-loop configuration and the Yo-Yo configuration simulated by imposing the conditions of the Pareto frontier of the closed-loop operation with 8 decision variables and volumes ratio= 1:1:1.

Note that the results obtained in Yo-Yo operation represent dominated, non-optimal solutions, as in this configuration the Pareto frontier was not obtained. Indeed, it would require large complications in the model that are not justified by the aims of this work. Nevertheless, even better performance was obtained with the yo-yo configuration. At the closed-loop Pareto set conditions, the Yo-Yo configuration gave a maximum RTE_{net} of 71.9%, whereas NPD was 6.25 W m⁻². Overall, in relative terms, the RTE_{net} and NPD were found to be on average $\approx 13.4\%$ and $\approx 28.6\%$ higher respectively compared to the closed-loop ones. Therefore, these results represent a further proof of the better performance provided by the Yo-Yo operation, as already discussed in section 6.6.1.

Conclusions

This PhD thesis aimed to develop and validate an original, mathematical, multi-scale model of the BMED and BMRED, in order to simulate an innovative and sustainable Acid/Base Flow Battery by analysing the main phenomena occurring during its functioning and finding the optimal operating conditions and design features.

Firstly, a general overview of the energy storage systems was presented. Following this, the relevant literature regarding the bipolar membranes was discussed, in order to collate current knowledge concerning the fundamental aspects of the functioning of these special membranes.

In Chapter 3, the BMED technology was firstly presented through a critical literature review. Following this, for the first time, a fully integrated BMED process model with distributed parameters was developed, adopting a multi-scale simulation strategy. At the lowest dimensional scale, the channel model is able to calculate the physical properties of the solutions, and it is also supported by external information regarding flow and mass transfer, which was provided by Computational Fluid Dynamics modelling. Moreover, within the model, a level was purposely developed to predict the behavior of the bipolar membrane. A 1-D cell triplet level was developed to compute the solutes and water fluxes across all of the IEMs, the mass balances, the electromotive force and cell resistance. Additionally, an electrical equivalent circuit model was developed for the whole stack. The model requires membrane properties which are available or easily accessible by experiments. Through this, different stack designs and operating conditions can be simulated. The process model was shown to be robust and reliable by validation against experiments conducted in a steady-state mode. Afterwards, it was used to perform a preliminary sensitivity analysis with once-through simulations. Model outcomes suggested that high conversion rates (about 70%) of hydrochloric acid can be reached by increasing the applied current density to 500 A m^{-2} in stacks with $75 \times 75 \text{ cm}^2$ of active membrane area. However, with higher current densities, the resulting current efficiency and BMED efficiency were lower. In addition, it was found that mean flow velocities within a typical range ($1\text{-}5 \text{ cm s}^{-1}$) do not significantly affect the module performance.

Chapter 4 presented the BMRED technology, which represents a promising system to harvest energy from the neutralization of acid and base streams. The BMED model developed in Chapter 3 was partially modified in Chapter 4, in order to simulate the BMRED process. Most of the modifications focused on the Bipolar Membrane level, whereas the other sub-models remained the same with only a few

differences. As with the BMED model, the BMRED process model was shown to be reliable by validation against experiments conducted in a steady-state mode. A sensitivity analysis was performed to evaluate the BMRED performance with once-through simulations, and as a function of several process parameters. These included the external current density, flow velocity inside the channels, and the acid and base inlet concentrations. Significantly, this sensitivity analysis showed promising results. Indeed, it was found that the gross energy density can be greatly enhanced by developing high-performance membranes able to reduce water permeability, co-ion leakage and the electrical resistance. Moreover, an example of an industrial scheme was simulated to show the potentiality of BMRED for harvesting of energy by neutralizing acid and base wastes.

In Chapter 5, the parasitic phenomena of the shunt currents in electro-membrane units were deeply investigated. An electrical model for the calculation of the ionic shortcut currents was implemented. This model was based on the solution of Ohm's and Kirchhoff's laws in the equivalent electrical circuit of the stack and the external load or generator, including the pathways of the electrolyte solutions (i.e. collectors and distributors). The model was validated under several design features and operating conditions through comparisons with both original experimental results collected with lab-scale stacks and data from the literature, showing good agreement. Compared to simple Ohmic models, the presented process simulator exhibited higher predictive capabilities, being a more effective, powerful and flexible tool for the simulation of electro-membrane units, with the inclusion of shortcut current effects. A large number of simulations were performed by varying the design features and operating conditions, in order to comprehensively characterize the shortcut currents, and to assess their impact in applications of electro-membrane processes. In conventional ED and RED processes, as well as in BMED and BMRED processes, the presence of parasitic pathways via manifolds led to a distribution of the cell current (electric current flowing perpendicularly to the membranes). Particularly, for RED/BMRED processes parasitic currents led to an increase of the average cell current value with respect to the external current (useful current delivered to the load). For ED/BMED processes, these parasitic pathways led to a reduction of the average cell current value with respect to the external current.

The sensitivity analysis, along with the experimental campaign, highlighted that stacks with a large number of cells, like those expected for industrial applications, may suffer from a significant drop in performance due to high shunt currents. The higher the number of repetitive units, the higher the number of ion shortcuts and the larger the amount and impact of shunt currents. In particular, they play a crucial role when the electrical resistance of the parasitic pathways is relatively low compared to

the cell resistance in the (desired) direction perpendicular to the membranes. Overall, the current leakage and its relative weight with respect to the cell current were maximum under open circuit conditions and decreased at higher external currents. Moreover, parasitic currents were negligible in channels of low conductivities. Typical configurations which have conditions that cause high shunt currents include stacks fed by highly conductive solutions, or equipped with high resistance membranes, short channels or large manifolds.

Chapter 6 presents for the first time a process model able to predict the performance of Acid/Base flow batteries based on the reversible electro-dialytic conversion of energy in stacks equipped with monopolar ion-exchange membranes and bipolar membranes. The AB-FB model integrates the BMED and BMRED models presented in Chapters 3 and 4 and it was successfully validated under dynamic operations. Within the range of the geometrical features and operating conditions investigated (i) energy spent on pumping had a small effect on the Net Power Density, (ii) concentration polarization in the boundary layer was not an issue, while (iii) the ionic short circuit currents via manifolds appeared to be the most detrimental phenomenon. On the other hand, pressure drops may be larger in real systems, due to geometrical irregularities, stack tightening, and other “non-ideal” features not included in the simulations. Moreover, concentration polarization phenomena in improved systems operated at higher current densities may have more significant effects. Interestingly, some geometrical features may affect different aspects. For example, the manifolds diameter can be crucial for the electrical resistance of the parasitic pathways. However, the use of small manifolds diameters to reduce the amount of shunt currents and their energy dissipation may pose other issues in terms of pressure drops and flow maldistribution within the channel width.

Simulation results showed also that the Round Trip Efficiency may be dramatically reduced in scaled-up stacks with a high number of triplets for the storage of large amounts of energy. Therefore, some measures have to be taken in the design of such systems in order to achieve acceptable efficiencies of the battery. For example, the use of isolated blocks with a small number of triplets can be suggested.

Furthermore, compared to closed-loop operation, the Yo-Yo configuration allowed better results in term of charge and discharge energy density.

Moreover, to evaluate the feasibility of the AB-FB technology at larger scale, different scenarios of multi-stage (from 4 to 17) operation were simulated by fixing the same concentration target at the last stage. The results showed average values of discharge power density decreasing from 30.6 to 11.7 W m⁻² membrane, while the energy density increased from 10.7 to 17.4 kWh m⁻³ acid. This means a total

membrane area of $\sim 30\text{-}86\text{ m}^2\text{ kW}^{-1}$ discharge power and a volume of each electrolyte solution of $0.09\text{-}0.06\text{ m}^3\text{ kWh}^{-1}$. The Round Trip Efficiency increased from 31% to 63%. Improved membranes and optimized systems can lead to enhanced performances, thus reducing the electrolyte volumes and the membrane area.

Finally, in Chapter 7, the original simulation tool for the AB-FB was used to identify the optimal design and the best operating conditions for maximizing both the net Round Trip Efficiency and the average net discharge power density, under a closed-loop configuration. Therefore, a multi-objective optimization study was performed by adopting the ϵ -constraint method, with a various number of decision variables and for different process scenarios. Optimized operating conditions and design features may be chosen to maximize the net Round Trip Efficiency up to a value of 64%, when the average discharge net power density is $\approx 4\text{ W m}^{-2}$. On the other hand, by constraining the average NPD at 19.5 W m^{-2} , the Pareto set gave a RTE_{net} of $\approx 32\%$. Considering a future scenario when we have the development of improved membrane properties, by halving membrane electrical resistances, ion diffusivities and water permeability, the maximum RTE_{net} could be 76.2%, when the constraint NPD is 4.4 W m^{-2} . However, by constraining the NPD at 23.2 W m^{-2} the resulting RTE_{net} is 59.1%.

The results presented in this PhD thesis have shown the potential of the Acid/Base Flow Battery in the field of energy storage. Further studies, especially on special tailored membranes, will be necessary to boost the development of this technology, and to promote its spread within the market.

Nomenclature

Symbols

| | |
|---|--|
| a (mol m ⁻³) | ion activity |
| a_1 (-) | first Darcy friction factor correlation coefficient |
| a_2 (-) | second Darcy friction factor correlation coefficient |
| a_3 (-) | third Darcy friction factor correlation coefficient |
| a_4 (-) | fourth Darcy friction factor correlation coefficient |
| b (m) | spacer width |
| b_1 (-) | first Sherwood number correlation coefficient |
| b_2 (-) | second Sherwood number correlation coefficient |
| c_1 (-) | first local loss coefficient correlation |
| c_2 (-) | second local loss coefficient correlation |
| C (mol m ⁻³) | molar concentration |
| CE (-) | Coulombic Efficiency |
| d (m) | membrane/channel thickness |
| d_{ext} (m) | pipeline diameter |
| d_{man} (m) | manifold diameter |
| D (m ² s ⁻¹) | diffusion coefficient |
| E (V) | triplet electromotive force corrected for concentration polarization |
| EMF (V) | triplet electromotive force |
| f (-) | frictional coefficient |
| f_s (-) | spacer shadow factor |
| F (C mol ⁻¹) | Faraday constant |
| G (kg m ⁻² s ⁻¹) | mass flux |
| GED_m (kWh kg ⁻³) | gross energy density per unit mass |
| GED_v (kWh m ⁻³) | gross energy density per unit volume |
| GPD (W m ⁻²) | gross power density |
| GPD_c (W m ⁻²) | gross power density of charge |
| GPD_d (W m ⁻²) | gross power density of discharge |
| i (A m ⁻²) | current density |
| i_c (A m ⁻²) | current density of charge |
| i_d (A m ⁻²) | current density of discharge |
| I (A) | current intensity |
| J (mol m ⁻² s ⁻¹) | molar flux |
| J_{diff}^* (mol m ⁻² s ⁻¹) | molar flux for each BPL taken individually |
| k (-) | generic local loss coefficient |
| k_ζ (-) | regression coefficient |

| | |
|--|--|
| K_w (-) | Self-ionization constant of water |
| l_{man} (m) | triplet thickness |
| l_{oma} (m) | length of the spacer regions out of the active area |
| L (m) | spacer length |
| L_{ext} (m) | pipeline length |
| L_p (ml m ⁻² h ⁻¹ bar) | osmotic permeability |
| L_x (m) | half channel length |
| m^0 (mol kg ⁻¹) | standard molality |
| M (g mol ⁻¹) | molar mass |
| n (-) | number of ion species |
| n_c (-) | ion coordination number |
| n_h (-) | hydration number |
| N (-) | number of triplets |
| NPD_d (W m ⁻²) | net power density of discharge |
| N_{holes} (-) | number of inlet spacer holes |
| N_p (-) | number of stacks hydraulically in parallel |
| N_s (-) | number of sequential stages |
| NPD (W m ⁻²) | net power density |
| p_1 (-) | first gross power regression coefficient |
| p_2 (-) | second gross power regression coefficient |
| p_3 (-) | third gross power regression coefficient |
| P (W) | gross power |
| PPD (W m ⁻²) | pumping power density |
| Q (m ³ s ⁻¹) | volume flow rate |
| R (Ω) | generic electric resistance |
| R^* (Ω) | electric resistance of additional parasitic pathway |
| R_g (J mol ⁻¹ k ⁻¹) | gas constant |
| Re (-) | Reynolds number |
| RSE (kWh kg ⁻¹) | Recovered Specific Energy |
| RTE (-) | Round Trip Efficiency |
| Sc (-) | Schmidt number |
| SEC_m (kWh kg ⁻¹) | Specific Energy Consumption per unit mass |
| SEC_v (kWh m ⁻³) | Specific Energy Consumption per unit volume |
| Sh (-) | Sherwood number |
| t (s) | time |
| t_c (s) | charge time |
| t_d (s) | discharge time |
| t_i^* (-) | ion transport number for each BPL taken individually |
| t_i (-) | ion transport number |
| T (K) | temperature |
| u (m s ⁻¹) | mean flow velocity |
| $u_{ch,c}$ (m s ⁻¹) | mean flow velocity of charge |

Nomenclature

| | |
|---------------------------------|--|
| $u_{ch,d}$ (m s ⁻¹) | mean flow velocity of discharge |
| U | potential difference over the series of resistances R_u and R_{bl} |
| U_{ext} | potential difference over the external load R_u |
| V (V) | generic voltage |
| V_t (m ³) | solution volume in the tank |
| V_{tr} (m ³) | BPM transition region volume |
| VE (-) | Voltage Efficiency |
| x (m) | coordinate along the flow direction |
| X (mol m ⁻³) | membrane fixed charge groups |
| z (-) | ion charge |

Greek letters

| | |
|-------------------------------|---|
| α (-) | empirical parameter |
| β (-) | empirical parameter |
| β_r (-) | calibration parameter |
| γ (-) | empirical parameter |
| ΔG (J) | Gibbs Enthalpy |
| ΔP (Pa) | Pressure drop |
| ζ (-) | generic physical property |
| η_{BL} (V) | boundary layer potential drop |
| η_c (-) | current efficiency |
| η_{cell} (-) | cell efficiency |
| η_d (-) | discharge energy efficiency |
| η_{BMED} (-) | BMED efficiency |
| θ (-) | polarization coefficient |
| I_{loss} (-) | parasitic current loss |
| μ (Pa s) | dynamic viscosity |
| π_{osm} (bar) | osmotic pressure |
| ρ (kg m ⁻³) | mass density |
| σ (S m ⁻¹) | electric conductivity |
| τ (-) | conversion rate |
| χ (-) | pump efficiency |
| ψ_p (-) | Loss of GPD due to the presence of parasitic currents |

Subscripts/superscripts

| | |
|-------|-----------------------------|
| a | acid |
| ac | acid solution/CEL interface |
| av | average |
| AEM | anionic exchange membrane |
| AEL | anionic exchange layer |

| | |
|---------------|--|
| <i>b</i> | base |
| <i>ba</i> | alkaline solution/AEL interface |
| <i>bl</i> | blank |
| <i>BPL</i> | bipolar membrane layer |
| <i>BPM</i> | bipolar membrane |
| <i>c</i> | collector |
| <i>ch</i> | channel |
| <i>co</i> | co-ion |
| <i>ct</i> | counter-ion |
| <i>CEM</i> | cationic exchange membrane |
| <i>CEL</i> | cationic exchange layer |
| <i>d</i> | distributor |
| <i>diff</i> | diffusive |
| <i>down</i> | lower branch |
| <i>e. osm</i> | electro-osmotic |
| <i>ext</i> | external |
| <i>ext, c</i> | external during the charge |
| <i>ext, d</i> | external during the discharge |
| <i>fd</i> | fully developed |
| <i>G</i> | constant |
| <i>h</i> | electric current |
| <i>MPM</i> | monopolar membrane |
| <i>i</i> | ion species |
| <i>in</i> | inlet |
| <i>int</i> | interface |
| <i>IEL</i> | ionic exchange layer |
| <i>IEM</i> | ionic exchange membrane |
| <i>j</i> | ion species |
| <i>k</i> | generic cell-triplet in the stack |
| <i>l</i> | local |
| <i>lim</i> | BPM diffusion limitation |
| <i>loss</i> | loss |
| <i>m</i> | membrane |
| <i>man</i> | manifold |
| <i>net</i> | net |
| <i>no par</i> | reference case neglecting shunt currents |
| <i>ohm</i> | Ohmic |
| <i>out</i> | outlet |
| <i>oma</i> | out of the membrane active area |
| <i>osm</i> | osmotic |
| <i>s</i> | salt |
| <i>sol</i> | solution |
| <i>spacer</i> | spacer |

Nomenclature

| | |
|---------------------|--|
| <i>split/recomb</i> | Water flux through the BPM |
| <i>t</i> | tank |
| <i>target, c</i> | target of charge |
| <i>target, d</i> | target of discharge |
| <i>th</i> | theoretical |
| <i>tot</i> | total |
| <i>u</i> | external load |
| <i>up</i> | upper branch |
| <i>w</i> | water |
| <i>x</i> | longitudinal branch (<i>up</i> or <i>down</i>) |

Acronyms/abbreviations

| | |
|-------|--|
| AB-FB | Acid Base-Flow Battery |
| AC | Alternating Current |
| AEL | Anion-Exchange Layer |
| AEM | Anion-Exchange Membrane |
| BMED | Bipolar-Electrodialysis |
| BMRED | Bipolar-Reverse Electrodialysis |
| BPM | BiPolar Membrane |
| CAES | Compressed Air Energy Storage |
| CCD | Central Composite Design |
| CE | Coulombic Efficiency |
| CED | Conventional ElectroDialysis |
| CEL | Cation-Exchange Layer |
| CEM | Cation-Exchange Membrane |
| CFD | Computational Fluid Dynamic |
| CGFB | Concentration Gradient Flow battery |
| CHR | Chemical Reaction Model |
| DC | Direct current |
| ED | Electrodialysis |
| EES | Electrical Energy Storage |
| EIS | Electrochemical Impedance Spectroscopy |
| ERS | Electrode Rinse Solution |
| GA | Genetic Algorithm |
| GED | Gross Energy Density |
| IEC | Ion-Exchange Capacity |
| IEM | Ionic-Exchange Membrane |
| LCOS | Levelized Cost Of Storage |
| LCOE | Levelized Cost Of Electricity |

| | |
|---------|--|
| MOGA | Multi-Objective Genetic Algorithm |
| NET | Non-Equilibrium Thermodynamic |
| N-P | Nernst Planck |
| NSGA-II | Non-dominated Sorting Genetic Algorithm II |
| OCV | Open Circuit Voltage |
| PHS | Pumped Hydro Storage |
| PSO | Particle Swarm Optimization |
| RED | Reverse Electrodialysis |
| RO | Reverse Osmosis |
| RSE | Recovered Specific Energy |
| RSM | Response Surface Methodology |
| RTE | Round Trip Efficiency |
| SEC | Specific Energy Consumption |
| SOC | State Of Charge |
| SWE | Second Wien Effect |
| VE | Voltage Efficiency |
| VRFB | Vanadium Redox Flow Battery |
| ZLD | Zero Liquid Discharge |

Appendix A –

Table A.1. List of the physical properties in the acid (a), base (b) and salt (s) solution and the regression coefficients used to compute them by Equation (A.1).

| | ζ | sol | i | j | $k_{\zeta,sol,1}$ | $k_{\zeta,sol,2}$ | $k_{\zeta,sol,3}$ |
|---|----------|--------|--------|--------|-------------------|-------------------|-------------------|
| Electrical conductivity (S m ⁻¹) | σ | a | H^+ | Na^+ | 0.0341 | 0.00646 | 0.908 |
| | σ | s | H^+ | - | 0.0353 | 0 | 2.52 |
| | σ | b | OH^- | Cl^- | 0.0184 | 0.00697 | 0.772 |
| Dynamic viscosity (Pa s) | μ | a | H^+ | - | 2.8E-9 | 0 | 0.928E-3 |
| | μ | s | H^+ | - | 2.8E-9 | 0 | 0.928E-3 |
| | μ | b | OH^- | - | 0.215E-6 | 0 | 0.927E-3 |
| Ion diffusivity (m s ⁻²) | D_H | a | H^+ | - | -1E-13 | 0 | 2E-9 |
| | D_{Na} | a | Na^+ | - | -5E-14 | 0 | 1E-9 |
| | D_{OH} | a | OH^- | - | 0 | 0 | 4E-9 |
| | D_{Cl} | a | Cl^- | - | -7E-14 | 0 | 2E-9 |
| | D_H | s | H^+ | - | -1E-13 | 0 | 2E-9 |
| | D_{Na} | s | Na^+ | - | -5E-14 | 0 | 1E-9 |
| | D_{OH} | s | OH^- | - | -1E-13 | 0 | 5E-9 |
| | D_{Cl} | s | Cl^- | - | -7E-14 | 0 | 2E-9 |
| | D_H | b | H^+ | - | 0 | 0 | 8E-9 |
| | D_{Na} | b | Na^+ | - | -2E-13 | 0 | 1E-9 |
| D_{OH} | b | OH^- | - | -5E-13 | 0 | 5E-9 | |
| D_{Cl} | b | Cl^- | - | -2E-13 | 0 | 2E-9 | |

List of ISI publications

- R. Pärnamäe, L. Gurreri, J. Post, W.J. van Egmond, A. Culcasi, M. Saakes, J. Cen, E. Goosen, A. Tamburini, D.A. Vermaas, M. Tedesco, The Acid–Base Flow Battery: Sustainable Energy Storage via Reversible Water Dissociation with Bipolar Membranes, *Membranes (Basel)*. 10 (2020) 409. <https://doi.org/10.3390/membranes10120409>.
- A. Zaffora, A. Culcasi, L. Gurreri, A. Cosenza, A. Tamburini, M. Santamaria, G. Micale, Energy harvesting by waste acid/base neutralization via bipolar membrane reverse electrodialysis, *Energies*. 13 (2020). <https://doi.org/10.3390/en13205510>.
- A. Culcasi, L. Gurreri, A. Zaffora, A. Cosenza, A. Tamburini, G. Micale, On the modelling of an Acid/Base Flow Battery: An innovative electrical energy storage device based on pH and salinity gradients, *Appl. Energy*. 277 (2020) 115576. <https://doi.org/10.1016/j.apenergy.2020.115576>.
- A. Culcasi, L. Gurreri, A. Zaffora, A. Cosenza, A. Tamburini, A. Cipollina, G. Micale, Ionic shortcut currents via manifolds in reverse electrodialysis stacks, *Desalination*. 485 (2020) 114450. <https://doi.org/10.1016/j.desal.2020.114450>.
- A. Culcasi, R. Gueccia, S. Randazzo, A. Cipollina, G. Micale, Design of a novel membrane-integrated waste acid recovery process from pickling solution, *J. Clean. Prod.* 236 (2019) 117623. <https://doi.org/10.1016/j.jclepro.2019.117623>.

Submitted papers

- A. Culcasi, L. Gurreri, G. Micale, A. Tamburini, Bipolar Membrane Reverse Electrodialysis for the sustainable recovery of energy from pH gradients of industrial wastewater: performance prediction by a validated process model, submitted to *Journal of Environmental Management*.
- A. Culcasi, L. Gurreri, A. Tamburini, A. Cipollina, G. Micale, Effect of Design Features and Operating Conditions on the Performance of a Bipolar Membrane-Based Acid/Base Flow Battery, submitted to *Chemical Engineering Transactions*.

Papers in preparation

- A. Culcasi, L. Gurreri, A. Zaffora, A. Cosenza, A. Tamburini, G. Micale, A comprehensive multi-scale process model of bipolar membrane electro dialysis (BMED) systems, in preparation
- A. Culcasi, L. Gurreri, A. Zaffora, A. Cosenza, A. Tamburini, G. Micale, Ionic shortcut currents in electro-membrane processes, in preparation

Abstracts at international conferences

- A. Culcasi, A. Zaffora, A. Cosenza, M. Di Liberto, L. Gurreri, A. Tamburini, A. Cipollina, G. Micale, Process modelling of a novel acid-base flow battery based on bipolar-membranes, Regional congress on membrane technology 2020 and Regional conference environmental engineering 2020, 16-17 January 2021, online.
- A. Culcasi, A. Zaffora, L. Gurreri, A. Cipollina, A. Tamburini, G. Micale, A comprehensive multi-scale process model of bipolar membrane electro dialysis (BMED) systems, 12th International Congress on Membranes and Membrane Processes, 7-11 December 2020, online.
- A. Culcasi, A. Zaffora, L. Gurreri, A. Cipollina, A. Tamburini, G. Micale, On the modelling of an Acid/Base Flow battery: an innovative electrical energy storage device based on pH and salinity gradients, 14th SDEWES conference, 1-6 October 2019, Dubrovnik, Croatia.
- A. Culcasi, A. Zaffora, L. Gurreri, A. Cipollina, A. Tamburini, G. Micale, A mathematical multi-scale model of an Acid/Base Flow Battery: a promising way to store renewable energy, ECCE12 conference, 15-19 September 2019, Florence, Italy.

Submitted abstracts for oral presentations

- A. Culcasi, L. Gurreri, A. Tamburini, G. Micale, Optimization study of acid-base flow battery stacks with monopolar and bipolar membranes, 12th European Symposium on Electrochemical Engineering, 13-17 June 2021, Leeuwarden, the Netherlands.
- A. Culcasi, L. Gurreri, A. Tamburini, A. Cipollina, G. Micale, Effect of Design Features and Operating Conditions on the Performance of a Bipolar Membrane-Based Acid/Base Flow Battery, 15th International Conference on Chemical and Process Engineering, 23-26 May 2021, Naples, Italy.

References

- [1] BAoBaB project, (2020). <http://www.baobabproject.eu/>.
- [2] N. Mikova, W. Eichhammer, B. Pfluger, Low-carbon energy scenarios 2050 in north-west European countries: Towards a more harmonised approach to achieve the EU targets, *Energy Policy*. (2019). <https://doi.org/10.1016/j.enpol.2019.03.047>.
- [3] J.R. Martinez-Bolanos, M.E.M. Udaeta, A.L.V. Gimenes, V.O. da Silva, Economic feasibility of battery energy storage systems for replacing peak power plants for commercial consumers under energy time of use tariffs, *J. Energy Storage*. (2020). <https://doi.org/10.1016/j.est.2020.101373>.
- [4] A. Baldinelli, L. Barelli, G. Bidini, G. Discepoli, Economics of innovative high capacity-to-power energy storage technologies pointing at 100% renewable micro-grids, *J. Energy Storage*. (2020). <https://doi.org/10.1016/j.est.2020.101198>.
- [5] P.N.D. Premadasa, D.P. Chandima, An innovative approach of optimizing size and cost of hybrid energy storage system with state of charge regulation for stand-alone direct current microgrids, *J. Energy Storage*. (2020). <https://doi.org/10.1016/j.est.2020.101703>.
- [6] C. Jankowiak, A. Zacharopoulos, C. Brandoni, P. Keatley, P. MacArtain, N. Hewitt, Assessing the benefits of decentralised residential batteries for load peak shaving, *J. Energy Storage*. (2020). <https://doi.org/10.1016/j.est.2020.101779>.
- [7] International Eletrotechnical Commission, *Electrical Energy Storage White Paper*, 2011. <https://doi.org/10.1002/bse.3280020501>.
- [8] H. Chen, T.N. Cong, W. Yang, C. Tan, Y. Li, Y. Ding, Progress in electrical energy storage system: A critical review, *Prog. Nat. Sci.* 19 (2009) 291–312. <https://doi.org/10.1016/j.pnsc.2008.07.014>.
- [9] G.J. May, A. Davidson, B. Monahov, Lead batteries for utility energy storage: A review, *J. Energy Storage*. (2018). <https://doi.org/10.1016/j.est.2017.11.008>.
- [10] S. Ould Amrouche, D. Rekioua, T. Rekioua, S. Bacha, Overview of energy storage in renewable energy systems, *Int. J. Hydrogen Energy*. (2016). <https://doi.org/10.1016/j.ijhydene.2016.06.243>.
- [11] F. Díaz-González, A. Sumper, O. Gomis-Bellmunt, R. Villafafila-Robles, A review of energy storage technologies for wind power applications, *Renew. Sustain. Energy Rev.* (2012). <https://doi.org/10.1016/j.rser.2012.01.029>.
- [12] E. Bullich-Massagué, F.-J. Cifuentes-García, I. Glenney-Crende, M. Cheah-

- Mañé, M. Aragüés-Peñalba, F. Díaz-González, O. Gomis-Bellmunt, A review of energy storage technologies for large scale photovoltaic power plants, *Appl. Energy*. 274 (2020) 115213. <https://doi.org/10.1016/j.apenergy.2020.115213>.
- [13] M.K. Shobana, Metal oxide coated cathode materials for Li ion batteries – A review, *J. Alloys Compd.* (2019). <https://doi.org/10.1016/j.jallcom.2019.06.194>.
- [14] M.S. Whittingham, History, evolution, and future status of energy storage, in: *Proc. IEEE*, 2012. <https://doi.org/10.1109/JPROC.2012.2190170>.
- [15] H. Kamath, S. Rajagopalan, M. Zwillenberg, *Vanadium Redox Flow Batteries - An In-Depth Analysis*, 2007.
- [16] G. Kear, A.A. Shah, F.C. Walsh, Development of the all-vanadium redox flow battery for energy storage: A review of technological, Financial and policy aspects, *Int. J. Energy Res.* (2012). <https://doi.org/10.1002/er.1863>.
- [17] D.O. Akinyele, R.K. Rayudu, Review of energy storage technologies for sustainable power networks, *Sustain. Energy Technol. Assessments*. 8 (2014) 74–91. <https://doi.org/10.1016/j.seta.2014.07.004>.
- [18] G.P. Rajarathnam, A.M. Vassallo, *The Zinc/Bromine Flow Battery*, SpringerBriefs in Energy. (2016). <https://doi.org/10.1007/978-981-287-646-1>.
- [19] A. Castillo, D.F. Gayme, Grid-scale energy storage applications in renewable energy integration: A survey, *Energy Convers. Manag.* 87 (2014) 885–894. <https://doi.org/10.1016/j.enconman.2014.07.063>.
- [20] O. Schmidt, S. Melchior, A. Hawkes, I. Staffell, Projecting the Future Levelized Cost of Electricity Storage Technologies, *Joule*. (2019). <https://doi.org/10.1016/j.joule.2018.12.008>.
- [21] S. Boulmrharj, R. Ouladsine, Y. NaitMalek, M. Bakhouya, K. Zine-dine, M. Khaidar, M. Siniti, Online battery state-of-charge estimation methods in micro-grid systems, *J. Energy Storage*. 30 (2020) 101518. <https://doi.org/10.1016/j.est.2020.101518>.
- [22] B. Bauer, F.J.J. Gerner, H. Strathmann, Development of bipolar membranes, *Desalination*. 68 (1988) 279–292. [https://doi.org/10.1016/0011-9164\(88\)80061-4](https://doi.org/10.1016/0011-9164(88)80061-4).
- [23] K. Sollner et al., *Ion Transport Across Membranes*, Elsevier, 1954. <https://doi.org/10.1016/C2013-0-12056-9>.
- [24] V.J. Frilette, Preparation and characterization of bipolar ion-exchange membranes, *J. Phys. Chem.* (1956). <https://doi.org/10.1021/j150538a013>.

References

- [25] K.N. Mani, F.P. Chlanda, C.H. Byszewski, Aquatech membrane technology for recovery of acid/base values for salt streams, *Desalination*. (1988). [https://doi.org/10.1016/0011-9164\(88\)80051-1](https://doi.org/10.1016/0011-9164(88)80051-1).
- [26] P. Ramírez, H.J. Rapp, S. Mafé, B. Bauer, Bipolar membranes under forward and reverse bias conditions. Theory vs. experiment, *J. Electroanal. Chem.* 375 (1994) 101–108. [https://doi.org/10.1016/0022-0728\(94\)03379-X](https://doi.org/10.1016/0022-0728(94)03379-X).
- [27] R. Simons, G. Khanarian, Water dissociation in bipolar membranes: Experiments and theory, *J. Membr. Biol.* 38 (1978) 11–30. <https://doi.org/10.1007/BF01875160>.
- [28] H.G.L. Coster, A Quantitative Analysis of the Voltage-Current Relationships of Fixed Charge Membranes and the Associated Property of “Punch-Through,” *Biophys. J.* 5 (1965) 669–686. [https://doi.org/10.1016/S0006-3495\(65\)86745-5](https://doi.org/10.1016/S0006-3495(65)86745-5).
- [29] S. Mafé, J.A. Manzanares, P. Ramirez, Model for ion transport in bipolar membranes, *Phys. Rev. A.* 42 (1990) 6245–6248. <https://doi.org/10.1103/PhysRevA.42.6245>.
- [30] R. Simons, Electric field effects on proton transfer between ionizable groups and water in ion exchange membranes, *Electrochim. Acta.* 29 (1984) 151–158. [https://doi.org/10.1016/0013-4686\(84\)87040-1](https://doi.org/10.1016/0013-4686(84)87040-1).
- [31] R. Simons, Water splitting in ion exchange membranes, *Electrochim. Acta.* 30 (1985) 275–282. [https://doi.org/10.1016/0013-4686\(85\)80184-5](https://doi.org/10.1016/0013-4686(85)80184-5).
- [32] P. Ramirez, V.M. Aguilera, J.A. Manzanares, Effects of temperature and ion transport on water splitting in bipolar membranes, *J. Memb. Sci.* 73 (1992) 191–201.
- [33] H. Strathmann, J.J. Krol, H.J. Rapp, G. Eigenberger, Limiting current density and water dissociation in bipolar membranes, *J. Memb. Sci.* 125 (1997) 123–142. [https://doi.org/10.1016/S0376-7388\(96\)00185-8](https://doi.org/10.1016/S0376-7388(96)00185-8).
- [34] G.Z. Greben, V P, Pivovarov, N Ya, Kovarskii, N Ya, Nefedova, Influence of ion-exchange resin nature on physic-chemical properties of bipolar membrane, *Zh. Fiz. Khim.* (1978) 2641–2645.
- [35] V.Z. R. Pärnamäe, S. Mareev, V. Nikonenko, S. Melnikov, N. Sheldeshov, M.T. H.V.M. Hamelers, Bipolar membranes: A review on principles, latest developments, and applications, *J. Memb. Sci.* (2020) 118538.
- [36] A.M. Rajesh, M. Kumar, V.K. Shahi, Functionalized biopolymer based bipolar membrane with poly ethylene glycol interfacial layer for improved water splitting, *J. Memb. Sci.* (2011). <https://doi.org/10.1016/j.memsci.2011.02.009>.
- [37] Y. Oda, T. Yawataya, Neutrality-disturbance phenomenon of membrane-

- solution systems, *Desalination*. (1968). [https://doi.org/10.1016/S0011-9164\(00\)80208-8](https://doi.org/10.1016/S0011-9164(00)80208-8).
- [38] R. Simons, High performance bipolar membrane, US5227040, 1993. <https://doi.org/US005485919A>.
- [39] Y. Liu, J. Chen, R. Chen, T. Zhou, C. Ke, X. Chen, Effects of multi-walled carbon nanotubes on bipolar membrane properties, *Mater. Chem. Phys.* (2018). <https://doi.org/10.1016/j.matchemphys.2017.09.068>.
- [40] J.M. Ahlfield, L. Liu, P.A. Kohl, PEM/AEM Junction Design for Bipolar Membrane Fuel Cells, *J. Electrochem. Soc.* (2017). <https://doi.org/10.1149/2.1041712jes>.
- [41] M.S. Kang, Y.J. Choi, H.J. Lee, S.H. Moon, Effects of inorganic substances on water splitting in ion-exchange membranes: I. Electrochemical characteristics of ion-exchange membranes coated with iron hydroxide/oxide and silica sol, *J. Colloid Interface Sci.* (2004). <https://doi.org/10.1016/j.jcis.2004.01.050>.
- [42] A. V. Bandura, S.N. Lvov, The ionization constant of water over wide ranges of temperature and density, *J. Phys. Chem. Ref. Data.* (2006). <https://doi.org/10.1063/1.1928231>.
- [43] J.H. Hao, C. Chen, L. Li, L. Yu, W. Jiang, Preparation of bipolar membranes (I), *J. Appl. Polym. Sci.* (2001). <https://doi.org/10.1002/app.1260>.
- [44] J.H. Hao, L. Yu, C. Chen, N. Li, W. Jiang, Preparation of bipolar membranes. II, *J. Appl. Polym. Sci.* (2001). <https://doi.org/10.1002/app.2014>.
- [45] K.-J.L. Frederick P. Chlanda, Lester T. C. Lee, Bipolar membranes and method of making same, US4116889, 1976.
- [46] B. Yang, H. Zhang, Preparation of a bipolar membrane by photografting polymerization, *Front. Chem. China.* (2008). <https://doi.org/10.1007/s11458-008-0002-7>.
- [47] C. Shen, R. Wycisk, P.N. Pintauro, High performance electrospun bipolar membrane with a 3D junction, *Energy Environ. Sci.* (2017). <https://doi.org/10.1039/c7ee00345e>.
- [48] G.M. Geise, H.J. Cassady, D.R. Paul, B.E. Logan, M.A. Hickner, E. Logan, M.A. Hickner, Specific ion effects on membrane potential and the permselectivity of ion exchange membranes, *Phys. Chem. Chem. Phys.* 16 (2014) 21673–21681. <https://doi.org/10.1039/C4CP03076A>.
- [49] T. Sata, T. Sata, W. Yang, Studies on cation-exchange membranes having permselectivity between cations in electrodialysis, *J. Memb. Sci.* 206 (2002) 31–60. [https://doi.org/10.1016/S0376-7388\(01\)00491-4](https://doi.org/10.1016/S0376-7388(01)00491-4).

References

- [50] Y. Ji, H. Luo, G.M. Geise, Specific co-ion sorption and diffusion properties influence membrane permselectivity, *J. Memb. Sci.* 563 (2018) 492–504. <https://doi.org/10.1016/j.memsci.2018.06.010>.
- [51] C. Larchet, L. Dammak, B. Auclair, S. Parchikov, V. Nikonenko, A simplified procedure for ion-exchange membrane characterisation, *New J. Chem.* (2004). <https://doi.org/10.1039/b316725a>.
- [52] K. Kontturi, A. Ekman, P. Forssell, I. Persson, F. Salvatore, A Method for Determination of Transport Numbers in Ion Exchange Membranes., *Acta Chem. Scand.* 39a (1985) 273–277. <https://doi.org/10.3891/acta.chem.scand.39a-0273>.
- [53] N. Lakshminarayanaiah, *Transport phenomena in membranes*, New York, 1969.
- [54] J.A. Manzanares, G. Vergara, S. Mafé, K. Kontturi, P. Viinikka, Potentiometric determination of transport numbers of ternary electrolyte systems in charged membranes, *J. Phys. Chem. B.* 102 (1998) 1301–1307. <https://doi.org/10.1021/jp970216w>.
- [55] R. Pärnamäe, S. Mareev, V. Nikonenko, S. Melnikov, N. Sheldeshov, V. Zabolotskii, H.V.M. Hamelers, M. Tedesco, Bipolar membranes: A review on principles, latest developments, and applications, *J. Memb. Sci.* (2021). <https://doi.org/10.1016/j.memsci.2020.118538>.
- [56] Y. Tanaka, *Ion Exchange Membranes - Fundamentals and Applications*, Elsevier, Amsterdam, 2007. [https://doi.org/10.1016/S0927-5193\(07\)12022-2](https://doi.org/10.1016/S0927-5193(07)12022-2).
- [57] V. Zabolotskii, N. Sheldeshov, S. Melnikov, Heterogeneous bipolar membranes and their application in electrodialysis, *Desalination.* (2014). <https://doi.org/10.1016/j.desal.2013.11.043>.
- [58] Brochure of Fujifilm Membrane Technology, Ion Exchange Membranes for water purification, Version 1.0, 2018. (2018) 6. https://fujifilmmembranes.com/images/IEM_brochure_1_1_-final_small_size.pdf.
- [59] Q. Li, C. Huang, T. Xu, Ethanol splitting in bipolar membranes: Evidence from NMR analysis, *J. Memb. Sci.* (2008). <https://doi.org/10.1016/j.memsci.2008.08.014>.
- [60] A. Cipollina, G. Micale, *Sustainable Energy from Salinity Gradients*, 2016. <https://doi.org/10.1016/C2014-0-03709-4>.
- [61] N. Liang, Y. Liu, X. Liao, Z. Luo, D. Chen, X. Liu, H. Zhang, Preparation and characterization of anion-exchange membranes derived from poly(vinylbenzyl chloride-co-styrene) and intercalated montmorillonite,

- Polym. Adv. Technol. (2017). <https://doi.org/10.1002/pat.3959>.
- [62] N. Ataollahi, K. Vezzù, G. Nawn, G. Pace, G. Cavinato, F. Girardi, P. Scardi, V. Di Noto, R. Di Maggio, A Polyketone-based Anion Exchange Membrane for Electrochemical Applications: Synthesis and Characterization, *Electrochim. Acta.* (2017). <https://doi.org/10.1016/j.electacta.2016.12.150>.
- [63] G.S. Trivedi, B.G. Shah, S.K. Adhikary, V.K. Indusekhar, R. Rangarajan, Studies on bipolar membranes, *React. Funct. Polym.* (1996). [https://doi.org/10.1016/1381-5148\(95\)00088-7](https://doi.org/10.1016/1381-5148(95)00088-7).
- [64] F.G. Wilhelm, N.F.A. Van der Vegt, M. Wessling, H. Strathmann, Chronopotentiometry for the advanced current-voltage characterisation of bipolar membranes, *J. Electroanal. Chem.* (2001). [https://doi.org/10.1016/S0022-0728\(01\)00348-5](https://doi.org/10.1016/S0022-0728(01)00348-5).
- [65] I.C. Bassignana, H. Reiss, Ion transport and water dissociation in bipolar ion exchange membranes, *J. Memb. Sci.* 15 (1983) 27–41. [https://doi.org/10.1016/S0376-7388\(00\)81360-5](https://doi.org/10.1016/S0376-7388(00)81360-5).
- [66] W.H. Rose, I.F. Miller, A Model for Bipolar Membranes in an Acid-Base Environment, *Ind. Eng. Chem. Fundam.* 25 (1986) 360–367. <https://doi.org/10.1021/i100023a010>.
- [67] K. Kontturi, L. Murtomäki, J.A. Manzanares, *Ionic Transport Processes*, Oxford University Press, 2008. <https://doi.org/10.1093/acprof:oso/9780199533817.001.0001>.
- [68] V.M. Volgin, A.D. Davydov, Ionic transport through ion-exchange and bipolar membranes, *J. Memb. Sci.* 259 (2005) 110–121. <https://doi.org/10.1016/j.memsci.2005.03.010>.
- [69] A.D. MacGillivray, Nernst-Planck Equations and the Electroneutrality and Donnan Equilibrium Assumptions, *J. Chem. Phys.* 48 (1968) 2903–2907. <https://doi.org/10.1063/1.1669549>.
- [70] F.G. Wilhelm, I. Pünt, N.F.A. Van Der Vegt, M. Wessling, H. Strathmann, Optimisation strategies for the preparation of bipolar membranes with reduced salt ion leakage in acid-base electro dialysis, *J. Memb. Sci.* 182 (2001) 13–28. [https://doi.org/10.1016/S0376-7388\(00\)00519-6](https://doi.org/10.1016/S0376-7388(00)00519-6).
- [71] R. El Moussaoui, G. Pourcelly, M. Maeck, H.D. Hurwitz, C. Gavach, Co-ion leakage through bipolar membranes Influence on I-V responses and water-splitting efficiency, *J. Memb. Sci.* 90 (1994) 283–292. [https://doi.org/10.1016/0376-7388\(94\)80078-2](https://doi.org/10.1016/0376-7388(94)80078-2).
- [72] J.L. Gineste, G. Pourcelly, Y. Lorrain, F. Persin, C. Gavach, Analysis of factors limiting the use of bipolar membranes: A simplified model to determine trends, *J. Memb. Sci.* 112 (1996) 199–208.

References

- [https://doi.org/10.1016/0376-7388\(95\)00284-7](https://doi.org/10.1016/0376-7388(95)00284-7).
- [73] V.I. Kovalchuk, E.K. Zholkovskij, E. V. Aksenenko, F. Gonzalez-Caballero, S.S. Dukhin, Ionic transport across bipolar membrane and adjacent Nernst layers, *J. Memb. Sci.* 284 (2006) 255–266. <https://doi.org/10.1016/j.memsci.2006.07.038>.
- [74] C. Huang, T. Xu, Electrodialysis with Bipolar Membranes for Sustainable Development, *Environ. Sci. Technol.* 40 (2006) 5233–5243. <https://doi.org/10.1021/es060039p>.
- [75] V.A. Shaposhnik, K. Kesore, An early history of electrodialysis with permselective membranes, *J. Memb. Sci.* 136 (1997) 35–39. [https://doi.org/10.1016/S0376-7388\(97\)00149-X](https://doi.org/10.1016/S0376-7388(97)00149-X).
- [76] L. Bazinet, T.R. Geoffroy, Electrodialytic processes: Market overview, membrane phenomena, recent developments and sustainable strategies, *Membranes* (Basel). (2020). <https://doi.org/10.3390/membranes10090221>.
- [77] F. Fu, Q. Wang, Removal of heavy metal ions from wastewaters: A review, *J. Environ. Manage.* 92 (2011) 407–418. <https://doi.org/10.1016/j.jenvman.2010.11.011>.
- [78] L. Gurreri, A. Tamburini, A. Cipollina, G. Micale, Electrodialysis Applications in Wastewater Treatment for Environmental Protection and Resources Recovery: A Systematic Review on Progress and Perspectives, *Membranes* (Basel). 10 (2020) 146. <https://doi.org/10.3390/membranes10070146>.
- [79] C.R. Gally, T. Benvenuti, C.D.M. Da Trindade, M.A.S. Rodrigues, J. Zoppas-Ferreira, V. Pérez-Herranz, A.M. Bernardes, Electrodialysis for the tertiary treatment of municipal wastewater: Efficiency of ion removal and ageing of ion exchange membranes, *J. Environ. Chem. Eng.* 6 (2018) 5855–5869. <https://doi.org/10.1016/j.jece.2018.07.052>.
- [80] N. van Linden, G.L. Bandinu, D.A. Vermaas, H. Spanjers, J.B. van Lier, Bipolar membrane electrodialysis for energetically competitive ammonium removal and dissolved ammonia production, *J. Clean. Prod.* 259 (2020) 120788. <https://doi.org/https://doi.org/10.1016/j.jclepro.2020.120788>.
- [81] J. Lin, W. Ye, J. Huang, B. Ricard, M.C. Baltaru, B. Greydanus, S. Balta, J. Shen, M. Vlad, A. Sotto, P. Luis, B. Van Der Bruggen, Toward Resource Recovery from Textile Wastewater: Dye Extraction, Water and Base/Acid Regeneration Using a Hybrid NF-BMED Process, *ACS Sustain. Chem. Eng.* (2015). <https://doi.org/10.1021/acssuschemeng.5b00234>.
- [82] M. Fidaleo, M. Moresi, Electrodialysis Applications in The Food Industry, *Adv. Food Nutr. Res.* 51 (2006) 265–360. [https://doi.org/10.1016/S1043-4526\(06\)51005-8](https://doi.org/10.1016/S1043-4526(06)51005-8).

- [83] A. Campione, L. Gurreri, M. Ciofalo, G. Micale, A. Tamburini, A. Cipollina, Electrodesalination for water desalination: A critical assessment of recent developments on process fundamentals, models and applications, *Desalination*. 434 (2018) 121–160. <https://doi.org/10.1016/j.desal.2017.12.044>.
- [84] A.H. Galama, J.W. Post, M.A. Cohen Stuart, P.M. Biesheuvel, Validity of the Boltzmann equation to describe Donnan equilibrium at the membrane-solution interface, *J. Memb. Sci.* 442 (2013) 131–139. <https://doi.org/10.1016/j.memsci.2013.04.022>.
- [85] X. Tongwen, Electrodesalination processes with bipolar membranes (EDBM) in environmental protection - A review, *Resour. Conserv. Recycl.* 37 (2002) 1–22. [https://doi.org/10.1016/S0921-3449\(02\)00032-0](https://doi.org/10.1016/S0921-3449(02)00032-0).
- [86] M. Mier, R. Ibanez, I. Ortiz, Influence of ion concentration on the kinetics of electrodesalination with bipolar membranes, *Sep. Purif. Technol.* 59 (2008) 197–205. <https://doi.org/10.1016/j.seppur.2007.06.015>.
- [87] H. Luo, X. Cheng, G. Liu, Y. Zhou, Y. Lu, R. Zhang, X. Li, W. Teng, Citric acid production using a biological electrodesalination with bipolar membrane, *J. Memb. Sci.* 523 (2017) 122–128. <https://doi.org/10.1016/j.memsci.2016.09.063>.
- [88] W. Tian, X. Wang, C. Fan, Z. Cui, Optimal treatment of hypersaline industrial wastewater via bipolar membrane electrodesalination, *ACS Sustain. Chem. Eng.* 7 (2019) 12358–12368. <https://doi.org/10.1021/acssuschemeng.9b01778>.
- [89] V. Kravtsov, I. Kulikova, S. Mikhaylin, L. Bazinet, Alkalinization of acid whey by means of electrodesalination with bipolar membranes and analysis of induced membrane fouling, *J. Food Eng.* 277 (2020) 109891. <https://doi.org/10.1016/j.jfoodeng.2019.109891>.
- [90] A.T. Cherif, J. Molenat, A. Elmidaoui, Nitric acid and sodium hydroxide generation by electrodesalination using bipolar membranes, *J. Appl. Electrochem.* 27 (1997) 1069–1074. <https://doi.org/10.1023/A:1018438710451>.
- [91] M.T. de Groot, R.M. de Rooij, A.A.C.M. Bos, G. Bargeman, Bipolar membrane electrodesalination for the alkalinization of ethanolamine salts, *J. Memb. Sci.* 378 (2011) 415–424. <https://doi.org/10.1016/j.memsci.2011.05.024>.
- [92] J.R. Davis, Y. Chen, J.C. Baygents, J. Farrell, Production of Acids and Bases for Ion Exchange Regeneration from Dilute Salt Solutions Using Bipolar Membrane Electrodesalination, *ACS Sustain. Chem. Eng.* 3 (2015) 2337–2342. <https://doi.org/10.1021/acssuschemeng.5b00654>.
- [93] M. Wang, K. kai Wang, Y. xiang Jia, Q. chun Ren, The reclamation of brine generated from desalination process by bipolar membrane electrodesalination, *J.*

References

- Memb. Sci. (2014). <https://doi.org/10.1016/j.memsci.2013.10.029>.
- [94] E. Vera, J. Ruales, M. Dornier, J. Sandeaux, R. Sandeaux, G. Pourcelly, Deacidification of clarified passion fruit juice using different configurations of electro dialysis, *J. Chem. Technol. Biotechnol.* 78 (2003) 918–925. <https://doi.org/10.1002/jctb.827>.
- [95] L. Yao, Y. Qiu, Y. Zhao, C. Tang, J. Shen, A continuous mode operation of bipolar membrane electro dialysis (BMED) for the production of high-pure choline hydroxide from choline chloride, *Sep. Purif. Technol.* 233 (2020) 116054. <https://doi.org/10.1016/j.seppur.2019.116054>.
- [96] M. Szczygiełda, K. Prochaska, Alpha-ketoglutaric acid production using electro dialysis with bipolar membrane, *J. Memb. Sci.* 536 (2017) 37–43. <https://doi.org/10.1016/j.memsci.2017.04.059>.
- [97] S. Koter, A. Warszawski, A new model for characterization of bipolar membrane electro dialysis of brine, *Desalination.* 198 (2006) 111–123. <https://doi.org/10.1016/j.desal.2006.09.016>.
- [98] E. Vera, J. Sandeaux, F. Persin, G. Pourcelly, M. Dornier, J. Ruales, Modeling of clarified tropical fruit juice deacidification by electro dialysis, *J. Memb. Sci.* 326 (2009) 472–483. <https://doi.org/10.1016/j.memsci.2008.10.034>.
- [99] S. Koter, Modeling of weak acid production by the EDB method, *Sep. Purif. Technol.* 57 (2007) 406–412. <https://doi.org/10.1016/j.seppur.2006.03.005>.
- [100] H. Roux-de Balman, M. Bailly, F. Lutin, P. Aimar, Modelling of the conversion of weak organic acids by bipolar membrane electro dialysis, *Desalination.* 149 (2002) 399–404. [https://doi.org/10.1016/S0011-9164\(02\)00863-9](https://doi.org/10.1016/S0011-9164(02)00863-9).
- [101] L. Shi, Y. Hu, S. Xie, G. Wu, Z. Hu, X. Zhan, Recovery of nutrients and volatile fatty acids from pig manure hydrolysate using two-stage bipolar membrane electro dialysis, *Chem. Eng. J.* 334 (2018) 134–142. <https://doi.org/10.1016/j.cej.2017.10.010>.
- [102] Y. Wang, A. Wang, X. Zhang, T. Xu, Simulation of Electro dialysis with Bipolar Membranes: Estimation of Process Performance and Energy Consumption, *Ind. Eng. Chem. Res.* 50 (2011) 13911–13921. <https://doi.org/10.1021/ie200467s>.
- [103] S.S. Melnikov, O.A. Mugtarnov, V.I. Zabolotsky, Study of electro dialysis concentration process of inorganic acids and salts for the two-stage conversion of salts into acids utilizing bipolar electro dialysis, *Sep. Purif. Technol.* 235 (2020) 116198. <https://doi.org/10.1016/j.seppur.2019.116198>.
- [104] H. Roux-de Balman, M. Bailly, F. Lutin, P. Aimar, Modelling of the conversion of weak organic acids by bipolar membrane electro dialysis,

- Desalination. 149 (2002) 399–404. [https://doi.org/10.1016/S0011-9164\(02\)00863-9](https://doi.org/10.1016/S0011-9164(02)00863-9).
- [105] S. Koter, A. Warszawski, A new model for characterization of bipolar membrane electro dialysis of brine, *Desalination*. 198 (2006) 111–123. <https://doi.org/10.1016/j.desal.2006.09.016>.
- [106] M.L. La Cerva, M. Di Liberto, L. Gurreri, A. Tamburini, A. Cipollina, G. Micale, M. Ciofalo, Coupling CFD with a one-dimensional model to predict the performance of reverse electro dialysis stacks, *J. Memb. Sci.* 541 (2017) 595–610. <https://doi.org/10.1016/j.memsci.2017.07.030>.
- [107] M. La Cerva, L. Gurreri, M. Tedesco, A. Cipollina, M. Ciofalo, A. Tamburini, G. Micale, Determination of limiting current density and current efficiency in electro dialysis units, *Desalination*. 445 (2018) 138–148. <https://doi.org/10.1016/j.desal.2018.07.028>.
- [108] N.A. Mishchuk, Concentration polarization of interface and non-linear electrokinetic phenomena, *Adv. Colloid Interface Sci.* 160 (2010) 16–39. <https://doi.org/10.1016/j.cis.2010.07.001>.
- [109] V. V. Nikonenko, N.D. Pismenskaya, E.I. Belova, P. Sistas, P. Huguet, G. Pourcelly, C. Larchet, Intensive current transfer in membrane systems: Modelling, mechanisms and application in electro dialysis, *Adv. Colloid Interface Sci.* 160 (2010) 101–123. <https://doi.org/10.1016/j.cis.2010.08.001>.
- [110] J. Veerman, J.W. Post, M. Saakes, S.J. Metz, G.J. Harmsen, Reducing power losses caused by ionic shortcut currents in reverse electro dialysis stacks by a validated model, *J. Memb. Sci.* 310 (2008) 418–430. <https://doi.org/10.1016/j.memsci.2007.11.032>.
- [111] A. Culcasi, L. Gurreri, A. Zaffora, A. Cosenza, A. Tamburini, A. Cipollina, G. Micale, Ionic shortcut currents via manifolds in reverse electro dialysis stacks, *Desalination*. 485 (2020) 114450. <https://doi.org/10.1016/j.desal.2020.114450>.
- [112] M. Tedesco, A. Cipollina, A. Tamburini, I.D.L. Bogle, G. Micale, A simulation tool for analysis and design of reverse electro dialysis using concentrated brines, *Chem. Eng. Res. Des.* 93 (2015) 441–456. <https://doi.org/10.1016/j.cherd.2014.05.009>.
- [113] R.S. Jupudi, G. Zappi, R. Bourgeois, Prediction of shunt currents in a bipolar electrolyzer stack by difference calculus, *J. Appl. Electrochem.* (2007). <https://doi.org/10.1007/s10800-007-9330-4>.
- [114] Z. Peng, Y. Sun, Leakage circuit characteristics of a bipolar membrane electro dialyzer with 5 BP-A-C units, *J. Memb. Sci.* (2020). <https://doi.org/10.1016/j.memsci.2019.117762>.

References

- [115] X. Sun, H. Lu, J. Wang, Recovery of citric acid from fermented liquid by bipolar membrane electrodialysis, *J. Clean. Prod.* 143 (2017) 250–256. <https://doi.org/10.1016/j.jclepro.2016.12.118>.
- [116] P. Pinacci, M. Radaelli, Recovery of citric acid from fermentation broths by electrodialysis with bipolar membranes, *Desalination.* (2002). [https://doi.org/10.1016/S0011-9164\(02\)00674-4](https://doi.org/10.1016/S0011-9164(02)00674-4).
- [117] J.S.J. Ferrer, S. Laborie, G. Durand, M. Rakib, Formic acid regeneration by electromembrane processes, *J. Memb. Sci.* (2006). <https://doi.org/10.1016/j.memsci.2006.02.012>.
- [118] C. Lei, Z. Li, Q. Gao, R. Fu, W. Wang, Q. Li, Z. Liu, Comparative study on the production of gluconic acid by electrodialysis and bipolar membrane electrodialysis: Effects of cell configurations, *J. Memb. Sci.* (2020). <https://doi.org/10.1016/j.memsci.2020.118192>.
- [119] M. Herrero-Gonzalez, N. Admon, A. Dominguez-Ramos, R. Ibañez, A. Wolfson, A. Irabien, Environmental sustainability assessment of seawater reverse osmosis brine valorization by means of electrodialysis with bipolar membranes, *Environ. Sci. Pollut. Res.* 27 (2020) 1256–1266. <https://doi.org/10.1007/s11356-019-04788-w>.
- [120] C. Fernandez-Gonzalez, A. Dominguez-Ramos, R. Ibañez, A. Irabien, Electrodialysis with Bipolar Membranes for Valorization of Brines, *Sep. Purif. Rev.* 45 (2016) 275–287. <https://doi.org/10.1080/15422119.2015.1128951>.
- [121] M. Herrero-Gonzalez, P. Diaz-Guridi, A. Dominguez-Ramos, A. Irabien, R. Ibañez, Highly concentrated HCl and NaOH from brines using electrodialysis with bipolar membranes, *Sep. Purif. Technol.* 242 (2020) 116785. <https://doi.org/10.1016/j.seppur.2020.116785>.
- [122] T. Tong, M. Elimelech, The Global Rise of Zero Liquid Discharge for Wastewater Management: Drivers, Technologies, and Future Directions, *Environ. Sci. Technol.* (2016). <https://doi.org/10.1021/acs.est.6b01000>.
- [123] Muhammad Yaqub, W. Lee, Zero-liquid discharge (ZLD) technology for resource recovery from wastewater: A review, *Sci. Total Environ.* (2019). <https://doi.org/10.1016/j.scitotenv.2019.05.062>.
- [124] M. Badruzzaman, J. Oppenheimer, S. Adham, M. Kumar, Innovative beneficial reuse of reverse osmosis concentrate using bipolar membrane electrodialysis and electrochlorination processes, *J. Memb. Sci.* (2009). <https://doi.org/10.1016/j.memsci.2008.10.018>.
- [125] S. Bunani, K. Yoshizuka, S. Nishihama, M. Arda, N. Kabay, Application of bipolar membrane electrodialysis (BMED) for simultaneous separation and recovery of boron and lithium from aqueous solutions, *Desalination.* 424

- (2017) 37–44. <https://doi.org/10.1016/j.desal.2017.09.029>.
- [126] D. İpekçi, N. Kabay, S. Bunani, E. Altıok, M. Arda, K. Yoshizuka, S. Nishihama, Application of heterogeneous ion exchange membranes for simultaneous separation and recovery of lithium and boron from aqueous solution with bipolar membrane electro dialysis (EDBM), *Desalination*. 479 (2020) 114313. <https://doi.org/10.1016/j.desal.2020.114313>.
- [127] S. Bunani, M. Arda, N. Kabay, K. Yoshizuka, S. Nishihama, Effect of process conditions on recovery of lithium and boron from water using bipolar membrane electro dialysis (BMED), *Desalination*. 416 (2017) 10–15. <https://doi.org/10.1016/j.desal.2017.04.017>.
- [128] A. Merkel, A.M. Ashrafi, J. Ečer, Bipolar membrane electro dialysis assisted pH correction of milk whey, *J. Memb. Sci.* 555 (2018) 185–196. <https://doi.org/10.1016/j.memsci.2018.03.035>.
- [129] V.A. Kravtsov, I.K. Kulikova, A.S. Bessonov, I.A. Evdokimov, Feasibility of using electro dialysis with bipolar membranes to deacidify acid whey, *Int. J. Dairy Technol.* 73 (2020) 261–269. <https://doi.org/10.1111/1471-0307.12637>.
- [130] G. Dufton, S. Mikhaylin, S. Gaaloul, L. Bazinet, How electro dialysis configuration influences acid whey deacidification and membrane scaling, *J. Dairy Sci.* 101 (2018) 7833–7850. <https://doi.org/10.3168/jds.2018-14639>.
- [131] C. Aspirault, A. Doyen, L. Bazinet, Impact of Preheating Temperature on the Separation of Whey Proteins When Combined with Chemical or Bipolar Membrane Electrochemical Acidification, *Int. J. Mol. Sci.* 21 (2020) 2792. <https://doi.org/10.3390/ijms21082792>.
- [132] L. Gurreri, A. Tamburini, A. Cipollina, G. Micale, M. Ciofalo, Flow and mass transfer in spacer-filled channels for reverse electro dialysis: a CFD parametrical study, *J. Memb. Sci.* (2016). <https://doi.org/10.1016/j.memsci.2015.09.006>.
- [133] M. Laliberté, W.E. Cooper, Model for calculating the density of aqueous electrolyte solutions, *J. Chem. Eng. Data*. 49 (2004) 1141–1151. <https://doi.org/10.1021/je0498659>.
- [134] K.S. Pitzer, G. Mayorga, Thermodynamics of electrolytes. II. Activity and osmotic coefficients for strong electrolytes with one or both ions univalent, *J. Phys. Chem.* 77 (1973) 2300–2308. <https://doi.org/10.1021/j100638a009>.
- [135] K.S. Pitzer, J.J. Kim, Thermodynamics of Electrolytes. IV. Activity and Osmotic Coefficients for Mixed Electrolytes, 1426 (1974) 5701–5707. <https://doi.org/10.1021/ja00825a004>.
- [136] M. Tedesco, H.V.M. Hamelers, P.M. Biesheuvel, Nernst-Planck transport

References

- theory for (reverse) electrodialysis: I. Effect of co-ion transport through the membranes, *J. Memb. Sci.* 510 (2016) 370–381. <https://doi.org/10.1016/j.memsci.2016.03.012>.
- [137] J.N. Israelachvili, *Intermolecular and Surface Forces: Third Edition*, 2011. <https://doi.org/10.1016/C2011-0-05119-0>.
- [138] K. Jiao, X. Li, Water transport in polymer electrolyte membrane fuel cells, *Prog. Energy Combust. Sci.* 37 (2011) 221–291. <https://doi.org/10.1016/j.peecs.2010.06.002>.
- [139] L. Han, S. Galier, H. Roux-de Balman, Ion hydration number and electro-osmosis during electrodialysis of mixed salt solution, *Desalination*. 373 (2015) 38–46. <https://doi.org/10.1016/j.desal.2015.06.023>.
- [140] M. La Cerva, M. Di Liberto, L. Gurreri, A. Tamburini, A. Cipollina, G. Micale, M. Ciofalo, Coupling CFD with a one-dimensional model to predict the performance of reverse electrodialysis stacks, *J. Memb. Sci.* 541 (2017) 595–610. <https://doi.org/10.1016/j.memsci.2017.07.030>.
- [141] L. Gurreri, A. Tamburini, A. Cipollina, G. Micale, M. Ciofalo, Pressure drop at low Reynolds numbers in woven-spacer-filled channels for membrane processes: CFD prediction and experimental validation, *Desalin. Water Treat.* 61 (2017) 170–182. <https://doi.org/10.5004/dwt.2016.11279>.
- [142] N.Y. Yip, D. Brogioli, H.V.M. Hamelers, K. Nijmeijer, *Salinity Gradients for Sustainable Energy: Primer, Progress, and Prospects*, (2016). <https://doi.org/10.1021/acs.est.6b03448>.
- [143] R.A. Tufa, S. Pawlowski, J. Veerman, K. Bouzek, E. Fontananova, G. di Profio, S. Velizarov, J. Goulão Crespo, K. Nijmeijer, E. Curcio, Progress and prospects in reverse electrodialysis for salinity gradient energy conversion and storage, *Appl. Energy*. 225 (2018) 290–331. <https://doi.org/10.1016/j.apenergy.2018.04.111>.
- [144] A. Cipollina, G. Micale, A. Tamburini, M. Tedesco, L. Gurreri, J. Veerman, S. Grasman, Reverse electrodialysis: Applications, in: A. Cipollina, G. Micale (Eds.), *Sustain. Energy from Salin. Gradients*, 1st Ed., Woodhead Publishing, Elsevier, Amsterdam, 2016: pp. 135–180. <https://doi.org/10.1016/B978-0-08-100312-1.00005-5>.
- [145] J. Veerman, D.A. Vermaas, Reverse electrodialysis: Fundamentals, in: A. Cipollina, G. Micale (Eds.), *Sustain. Energy from Salin. Gradients*, 1st Ed., Woodhead Publishing, Elsevier, Amsterdam, 2016: pp. 77–133. <https://doi.org/10.1016/B978-0-08-100312-1.00004-3>.
- [146] H. Strathmann, *Ion-Exchange Membrane Separation Processes*, First ed., Elsevier, Amsterdam, 2004. <https://doi.org/10.1007/s13398-014-0173-7.2>.

- [147] O. Scialdone, C. Guarisco, S. Grispo, A.D. Angelo, A. Galia, Investigation of electrode material - Redox couple systems for reverse electro dialysis processes. Part I: Iron redox couples, *J. Electroanal. Chem.* (2012). <https://doi.org/10.1016/j.jelechem.2012.05.017>.
- [148] R.E. Pattle, Production of electric power by mixing fresh and salt water in the hydroelectric pile [19], *Nature*. 174 (1954) 660. <https://doi.org/10.1038/174660a0>.
- [149] D.A. Vermaas, M. Saakes, K. Nijmeijer, Doubled Power Density from Salinity Gradients at Reduced Intermembrane Distance, *Environ. Sci. Technol.* 45 (2011) 7089–7095. <https://doi.org/10.1021/es2012758>.
- [150] H.K. Kim, M.S. Lee, S. Y. Lee, Y.W. Choi, N.J. Jeong, C.S. Kim, High power density of reverse electro dialysis with pore-filling ion exchange membranes and a high-open-area spacer, *J. Mater. Chem. A*. 3 (2015) 16302–16306. <https://doi.org/10.1039/c5ta03571f>.
- [151] M. Tedesco, A. Cipollina, A. Tamburini, I.D.L. Bogle, G. Micale, A simulation tool for analysis and design of reverse electro dialysis using concentrated brines, *Chem. Eng. Res. Des.* 93 (2015) 441–456. <https://doi.org/10.1016/j.cherd.2014.05.009>.
- [152] R.A. Tufa, E. Rugiero, D. Chanda, J. Hnàt, W. van Baak, J. Veerman, E. Fontananova, G. Di Profio, E. Drioli, K. Bouzek, E. Curcio, Salinity gradient power-reverse electro dialysis and alkaline polymer electrolyte water electrolysis for hydrogen production, *J. Memb. Sci.* 514 (2016) 155–164. <https://doi.org/10.1016/j.memsci.2016.04.067>.
- [153] R.S. Kingsbury, F. Liu, S. Zhu, C. Boggs, M.D. Armstrong, D.F. Call, O. Coronell, Impact of natural organic matter and inorganic solutes on energy recovery from five real salinity gradients using reverse electro dialysis, *J. Memb. Sci.* 541 (2017) 621–632. <https://doi.org/10.1016/j.memsci.2017.07.038>.
- [154] F. Giacalone, M. Papapetrou, G. Kosmadakis, A. Tamburini, G. Micale, A. Cipollina, Application of reverse electro dialysis to site-specific types of saline solutions: A techno-economic assessment, *Energy*. (2019). <https://doi.org/10.1016/j.energy.2019.05.161>.
- [155] A. Tamburini, A. Cipollina, M. Tedesco, L. Gurreri, M. Ciofalo, G. Micale, The REAPower Project: Power Production From Saline Waters and Concentrated Brines, in: A. Basile, E. Curcio, I. Inamuddin (Eds.), *Curr. Trends Futur. Dev. Membr.*, Elsevier, Amsterdam, 2019: pp. 407–448. <https://doi.org/https://doi.org/10.1016/B978-0-12-813551-8.00017-6>.
- [156] M. Tedesco, C. Scalici, D. Vaccari, A. Cipollina, A. Tamburini, G. Micale, Performance of the first reverse electro dialysis pilot plant for power

- production from saline waters and concentrated brines, *J. Memb. Sci.* 500 (2016) 33–45. <https://doi.org/10.1016/j.memsci.2015.10.057>.
- [157] A. Daniilidis, D.A. Vermaas, R. Herber, K. Nijmeijer, Experimentally obtainable energy from mixing river water, seawater or brines with reverse electro dialysis, *Renew. Energy.* 64 (2014) 123–131. <https://doi.org/10.1016/j.renene.2013.11.001>.
- [158] J. Veerman, M. Saakes, S.J. Metz, G.J. Harmsen, Reverse electro dialysis: A validated process model for design and optimization, *Chem. Eng. J.* 166 (2011) 256–268. <https://doi.org/10.1016/j.cej.2010.10.071>.
- [159] R. Long, B. Li, Z. Liu, W. Liu, Reverse electro dialysis: Modelling and performance analysis based on multi-objective optimization, *Energy.* 151 (2018) 1–10. <https://doi.org/10.1016/j.energy.2018.03.003>.
- [160] R. Long, B. Li, Z. Liu, W. Liu, Performance analysis of reverse electro dialysis stacks: Channel geometry and flow rate optimization, *Energy.* 158 (2018) 427–436. <https://doi.org/10.1016/j.energy.2018.06.067>.
- [161] M. Ciofalo, M. La Cerva, M. Di Liberto, L. Gurreri, A. Cipollina, G. Micale, Optimization of net power density in Reverse Electro dialysis, *Energy.* 181 (2019) 576–588. <https://doi.org/https://doi.org/10.1016/j.energy.2019.05.183>.
- [162] M. Tedesco, H.V.M. Hamelers, P.M. Biesheuvel, Nernst-Planck transport theory for (reverse) electro dialysis: I. Effect of co-ion transport through the membranes, *J. Memb. Sci.* 510 (2016) 370–381. <https://doi.org/10.1016/j.memsci.2016.03.012>.
- [163] M. Tedesco, H.V.M. Hamelers, P.M. Biesheuvel, Nernst-Planck transport theory for (reverse) electro dialysis: II. Effect of water transport through ion-exchange membranes, *J. Memb. Sci.* (2017). <https://doi.org/10.1016/j.memsci.2017.02.031>.
- [164] M. Ciofalo, M. Di Liberto, L. Gurreri, M. La Cerva, L. Scelsi, G. Micale, Mass transfer in ducts with transpiring walls, *Int. J. Heat Mass Transf.* (2019). <https://doi.org/10.1016/j.ijheatmasstransfer.2018.12.059>.
- [165] T. Rijnaarts, E. Huerta, W. Van Baak, K. Nijmeijer, Effect of Divalent Cations on RED Performance and Cation Exchange Membrane Selection to Enhance Power Densities, *Environ. Sci. Technol.* 51 (2017) 13028–13035. <https://doi.org/10.1021/acs.est.7b03858>.
- [166] A.H. Avci, R.A. Tufa, E. Fontananova, G. Di Profio, E. Curcio, Reverse Electro dialysis for energy production from natural river water and seawater, *Energy.* 165 (2018) 512–521. <https://doi.org/10.1016/j.energy.2018.09.111>.
- [167] M.L. La Cerva, M. Di Liberto, L. Gurreri, A. Tamburini, A. Cipollina, G.

- Micale, M. Ciofalo, Coupling CFD with a one-dimensional model to predict the performance of reverse electro dialysis stacks, *J. Memb. Sci.* (2017). <https://doi.org/10.1016/j.memsci.2017.07.030>.
- [168] D.A. Vermaas, E. Guler, M. Saakes, K. Nijmeijer, Theoretical power density from salinity gradients using reverse electro dialysis, in: *Energy Procedia*, 2012. <https://doi.org/10.1016/j.egypro.2012.03.018>.
- [169] S. Pawlowski, T. Rijnaarts, M. Saakes, K. Nijmeijer, J.G. Crespo, S. Velizarov, Improved fluid mixing and power density in reverse electro dialysis stacks with chevron-profiled membranes, *J. Memb. Sci.* (2017). <https://doi.org/10.1016/j.memsci.2017.03.003>.
- [170] V. V. Waghlikar, H. Zhuang, Y. Jiao, N.E. Moe, H. Ramanan, L.M. Goh, J. Barber, K.S. Lee, H.P. Lee, J.Y.H. Fuh, Modeling cell pair resistance and spacer shadow factors in electro-separation processes, *J. Memb. Sci.* (2017). <https://doi.org/10.1016/j.memsci.2017.08.054>.
- [171] S. Mehdizadeh, M. Yasukawa, T. Abo, Y. Kakihana, M. Higa, Effect of spacer geometry on membrane and solution compartment resistances in reverse electro dialysis, *J. Memb. Sci.* (2019). <https://doi.org/10.1016/j.memsci.2018.09.051>.
- [172] G. Battaglia, L. Gurreri, G. Airòfarulla, A. Cipollina, A. Pirrotta, G. Micale, M. Ciofalo, Membrane deformation and its effects on flow and mass transfer in the electromembrane processes, *Int. J. Mol. Sci.* 20 (2019) 11–15. <https://doi.org/10.3390/ijms20081840>.
- [173] G. Battaglia, L. Gurreri, G.A. Farulla, A. Cipollina, A. Pirrotta, G. Micale, M. Ciofalo, Pressure-induced deformation of pillar-type profiled membranes and its effects on flow and mass transfer, *Computation*. 7 (2019) 1–14. <https://doi.org/10.3390/computation7020032>.
- [174] G. Battaglia, L. Gurreri, A. Cipollina, A. Pirrotta, S. Velizarov, M. Ciofalo, G. Micale, Fluid–Structure Interaction and Flow Redistribution in Membrane-Bounded Channels, *Energies*. (2019). <https://doi.org/10.3390/EN12224259>.
- [175] Y. Mei, L. Liu, Y.C. Lu, C.Y. Tang, Reverse Electro dialysis Chemical Cell for Energy Harvesting from Controlled Acid-Base Neutralization, *Environ. Sci. Technol.* 53 (2019) 4640–4647. <https://doi.org/10.1021/acs.est.8b06361>.
- [176] N.Y. Walther, James F., Skaneateles, Process for production of electrical energy from the neutralization of acid and base in a bipolar membrane cell, 1982.
- [177] W.J. van Egmond, M. Saakes, I. Noor, S. Porada, C.J.N. Buisman, H.V.M. Hamelers, Performance of an environmentally benign acid base flow battery at high energy density, *Int. J. Energy Res.* 42 (2018) 1524–1535.

- <https://doi.org/10.1002/er.3941>.
- [178] J. Xia, G. Eigenberger, H. Strathmann, U. Niekens, Flow battery based on reverse electro dialysis with bipolar membranes: Single cell experiments, *J. Memb. Sci.* 565 (2018) 157–168. <https://doi.org/10.1016/j.memsci.2018.07.073>.
- [179] A.T. Emrén, V.J.M. Holmström, Energy storage in a fuel cell with bipolar membranes burning acid and hydroxide, *Energy*. 8 (1983) 277–282. [https://doi.org/10.1016/0360-5442\(83\)90103-2](https://doi.org/10.1016/0360-5442(83)90103-2).
- [180] J. Pretz, E. Staude, Reverse electro dialysis (RED) with bipolar membranes, an energy storage system, *Berichte Der Bunsengesellschaft Für Phys. Chemie.* 102 (1998) 676–685. <https://doi.org/10.1002/bbpc.19981020412>.
- [181] E.K. Zholkovskij, M.C. Müller, E. Staude, The storage battery with bipolar membranes, *J. Memb. Sci.* 141 (1998) 231–243. [https://doi.org/10.1016/S0376-7388\(97\)00306-2](https://doi.org/10.1016/S0376-7388(97)00306-2).
- [182] J.H. Kim, J.H. Lee, S. Maurya, S.H. Shin, J.Y. Lee, I.S. Chang, S.H. Moon, Proof-of-concept experiments of an acid-base junction flow battery by reverse bipolar electro dialysis for an energy conversion system, *Electrochem. Commun.* 72 (2016) 157–161. <https://doi.org/10.1016/j.elecom.2016.09.025>.
- [183] J. Xia, G. Eigenberger, H. Strathmann, U. Niekens, Acid-Base Flow Battery, Based on Reverse Electro dialysis with Bi-Polar Membranes: Stack Experiments, *Processes*. 8 (2020) 99. <https://doi.org/10.3390/pr8010099>.
- [184] A. Agrawal, K.K. Sahu, An overview of the recovery of acid from spent acidic solutions from steel and electroplating industries, *J. Hazard. Mater.* (2009). <https://doi.org/10.1016/j.jhazmat.2009.06.099>.
- [185] R. Guccia, A.R. Aguirre, S. Randazzo, A. Cipollina, G. Micale, Diffusion dialysis for separation of hydrochloric acid, iron and zinc ions from highly concentrated pickling solutions, *Membranes (Basel)*. (2020). <https://doi.org/10.3390/membranes10060129>.
- [186] C. Sundberg, D. Yu, I. Franke-Whittle, S. Kauppi, S. Smårs, H. Insam, M. Romantschuk, H. Jönsson, Effects of pH and microbial composition on odour in food waste composting, *Waste Manag.* (2013). <https://doi.org/10.1016/j.wasman.2012.09.017>.
- [187] A. Culcasi, R. Guccia, S. Randazzo, A. Cipollina, G. Micale, Design of a novel membrane-integrated waste acid recovery process from pickling solution, *J. Clean. Prod.* 236 (2019) 117623. <https://doi.org/10.1016/j.jclepro.2019.117623>.
- [188] R.K. Goel, J.R. V. Flora, J.P. Chen, Flow Equalization and Neutralization, in: L.K. Wang, Y.-T. Hung, N.K. Shamas (Eds.), *Physicochem. Treat.*

- Process., Humana Press, Totowa, NJ, NJ, 2005: pp. 21–45. <https://doi.org/10.1385/1-59259-820-x:021>.
- [189] U. Kesieme, A. Chrysanthou, M. Catulli, C.Y. Cheng, A review of acid recovery from acidic mining waste solutions using solvent extraction, *J. Chem. Technol. Biotechnol.* 93 (2018) 3374–3385. <https://doi.org/10.1002/jctb.5728>.
- [190] L. Gurreri, A. Cipollina, A. Tamburini, G. Micale, Electrodialysis for wastewater treatment—Part II: Industrial effluents, in: A. Basile, A. Comite (Eds.), *Curr. Trends Futur. Dev. Bio-Membranes Membr. Technol. Water Wastewater Treat. - Adv. Emerg. Process.*, Elsevier, Amsterdam, 2020: pp. 195–241. <https://doi.org/10.1016/B978-0-12-816823-3.00008-3>.
- [191] P. Tansens, A.T. Rodal, C.M.M. Machado, H.M.V.M. Soares, Recycling of aluminum and caustic soda solution from waste effluents generated during the cleaning of the extruder matrixes of the aluminum industry, *J. Hazard. Mater.* 187 (2011) 459–465. <https://doi.org/10.1016/j.jhazmat.2011.01.048>.
- [192] P. Aprea, B. de Gennaro, C. Colella, An unconventional method for the recovery of caustic soda from spent Al-rich pickling solutions, *J. Environ. Manage.* 92 (2011) 1821–1827. <https://doi.org/10.1016/j.jenvman.2011.03.012>.
- [193] K. Md. Atikur, Rahman, Nymul Ehsan, Study of an evaporation system for sodium hydroxide solution, *J. Chem. Eng.* 24 (2006) 35–36.
- [194] I. Ben Hariz, A. Halleb, N. Adhoum, L. Monser, Treatment of petroleum refinery sulfidic spent caustic wastes by electrocoagulation, *Sep. Purif. Technol.* 107 (2013) 150–157. <https://doi.org/10.1016/j.seppur.2013.01.051>.
- [195] B. Imran, S.J. Khan, I.A. Qazi, M. Arshad, Removal and recovery of sodium hydroxide (NaOH) from industrial wastewater by two-stage diffusion dialysis (DD) and electrodialysis (ED) processes, *Desalin. Water Treat.* 57 (2016) 7926–7932. <https://doi.org/10.1080/19443994.2015.1048742>.
- [196] S. Sarkar, A.K. SenGupta, J.E. Greenleaf, M. El-Moselhy, Energy Recovery from Acid–Base Neutralization Process through pH-Sensitive Polymeric Ion Exchangers, *Ind. Eng. Chem. Res.* 50 (2011) 12293–12298. <https://doi.org/10.1021/ie201652p>.
- [197] M. German, A.K. SenGupta, J. Greenleaf, Hydrogen Ion (H⁺) in Waste Acid as a Driver for Environmentally Sustainable Processes: Opportunities and Challenges, *Environ. Sci. Technol.* 47 (2013) 2145–2150. <https://doi.org/10.1021/es304260u>.
- [198] X. Zhu, W. Yang, M.C. Hatzell, B.E. Logan, Energy Recovery from Solutions with Different Salinities Based on Swelling and Shrinking of Hydrogels, *Environ. Sci. Technol.* 48 (2014) 7157–7163.

References

- <https://doi.org/10.1021/es500909q>.
- [199] T. Facci, W.J.A.S. Gomes, B. Bravin, D.M. Araújo, F. Huguenin, Proton Electroinsertion in Self-Assembled Materials for Neutralization Pseudocapacitors, *Langmuir*. 30 (2014) 426–431. <https://doi.org/10.1021/la4037524>.
- [200] A. D'Angelo, M. Tedesco, A. Cipollina, A. Galia, G. Micale, O. Scialdone, Reverse electro dialysis performed at pilot plant scale: Evaluation of redox processes and simultaneous generation of electric energy and treatment of wastewater, *Water Res.* 125 (2017) 123–131. <https://doi.org/10.1016/j.watres.2017.08.008>.
- [201] J. Luque Di Salvo, A. Cosenza, A. Tamburini, G. Micale, A. Cipollina, Long-run operation of a reverse electro dialysis system fed with wastewaters, *J. Environ. Manage.* 217 (2018) 871–887. <https://doi.org/10.1016/j.jenvman.2018.03.110>.
- [202] M.C. Hatzell, X. Zhu, B.E. Logan, Simultaneous hydrogen generation and waste acid neutralization in a reverse electro dialysis system, *ACS Sustain. Chem. Eng.* 2 (2014) 2211–2216. <https://doi.org/10.1021/sc5004133>.
- [203] G. Kraaijeveld, V. Sumberova, S. Kuindersma, H. Wesselingh, Modelling electro dialysis using the Maxwell-Stefan description, *Chem. Eng. J. Biochem. Eng. J.* (1995). [https://doi.org/10.1016/0923-0467\(94\)02940-7](https://doi.org/10.1016/0923-0467(94)02940-7).
- [204] A. Campione, A. Cipollina, I.D.L. Bogle, L. Gurreri, A. Tamburini, M. Tedesco, G. Micale, A hierarchical model for novel schemes of electro dialysis desalination, *Desalination*. 465 (2019) 79–93. <https://doi.org/10.1016/j.desal.2019.04.020>.
- [205] J. Veerman, M. Saakes, S.J. Metz, G.J. Harmsen, Reverse electro dialysis: Evaluation of suitable electrode systems, *J. Appl. Electrochem.* 40 (2010) 1461–1474. <https://doi.org/10.1007/s10800-010-0124-8>.
- [206] W.G.B. Mandersloot, R.E. Hicks, Leakage currents in electro dialytic desalting and brine production, *Desalination*. (1966). [https://doi.org/10.1016/S0011-9164\(00\)84017-5](https://doi.org/10.1016/S0011-9164(00)84017-5).
- [207] I. Choi, J.Y. Han, S.J. Yoo, D. Henkensmeier, J.Y. Kim, S.Y. Lee, J. Han, S.W. Nam, H.J. Kim, J.H. Jang, Experimental investigation of operating parameters in power generation by lab-scale reverse electro-dialysis (RED), *Bull. Korean Chem. Soc.* 37 (2016) 1010–1019. <https://doi.org/10.1002/bkcs.10810>.
- [208] N. Václavíková, L. Zich, M. Doležel, Pilot module for electro dialysis-metathesis protected against shunt currents, *Desalin. Water Treat.* 75 (2017) 320–324. <https://doi.org/10.5004/dwt.2017.20446>.

- [209] R. Kodým, P. Pánek, D. Šnita, D. Tvrzník, K. Bouzek, Macrohomogeneous approach to a two-dimensional mathematical model of an industrial-scale electro dialysis unit, *J. Appl. Electrochem.* 42 (2012) 645–666. <https://doi.org/10.1007/s10800-012-0457-6>.
- [210] M. Doležela, K. Keslerová, Measurement of non-effective electric current in electro dialysis stacks, *J. Electrochem. Soc.* 164 (2017) E276–E282. <https://doi.org/10.1149/2.1481709jes>.
- [211] R. Yamane, M. Ichikawa, Y. Mizutani, Y. Onoue, Concentrated brine production from sea water by electro dialysis using ion exchange membranes, *Ind. Eng. Chem. Process Des. Dev.* 8 (1969) 159–165. <https://doi.org/10.1021/i260030a003>.
- [212] B.R. Bligh, Reverse electro dialysis, Patent GB2197116A, 1988.
- [213] M. Sadrzadeh, T. Mohammadi, Treatment of sea water using electro dialysis: Current efficiency evaluation, *Desalination.* (2009). <https://doi.org/10.1016/j.desal.2008.10.029>.
- [214] A. Tamburini, M. Tedesco, A. Cipollina, G. Micale, M. Ciofalo, M. Papapetrou, W. Van Baak, A. Piacentino, Reverse electro dialysis heat engine for sustainable power production, *Appl. Energy.* 206 (2017) 1334–1353. <https://doi.org/10.1016/j.apenergy.2017.10.008>.
- [215] F. Giacalone, P. Catrini, A. Tamburini, A. Cipollina, A. Piacentino, G. Micale, Exergy analysis of reverse electro dialysis, *Energy Convers. Manag.* 164 (2018) 588–602. <https://doi.org/10.1016/j.enconman.2018.03.014>.
- [216] I. Rubinstein, J. Pretz, E. Staude, Open circuit voltage in a reverse electro dialysis cell, *Phys. Chem. Chem. Phys.* 3 (2001) 1666–1667. <https://doi.org/10.1039/b010030g>.
- [217] G.M. Andreadis, A.K.M. Podias, P.E. Tsiakaras, The effect of the parasitic current on the Direct Ethanol PEM Fuel Cell Operation, *J. Power Sources.* 181 (2008) 214–227. <https://doi.org/10.1016/j.jpowsour.2008.01.060>.
- [218] W.R. Bennett, M.A. Hoberecht, V.F. Lvovich, Analysis of shunt currents and associated corrosion of bipolar plates in PEM fuel cells, *J. Electroanal. Chem.* 737 (2015) 162–173. <https://doi.org/10.1016/j.jelechem.2014.09.009>.
- [219] H.S. Burney, R.N. Beaver, Predicting Shunt Currents in Stacks of Bipolar Plate Cells, *J. Electrochem. Soc.* 133 (1986) 485–492. <https://doi.org/10.1149/1.2108606>.
- [220] C. Yin, S. Guo, H. Fang, J. Liu, Y. Li, H. Tang, Numerical and experimental studies of stack shunt current for vanadium redox flow battery, *Appl. Energy.* 151 (2015) 237–248. <https://doi.org/10.1016/j.apenergy.2015.04.080>.
- [221] J.R. Wilson, Demineralization by Electro dialysis, Butterworths Sci. Publ.

References

- London. (1960). <https://doi.org/https://doi.org/10.1002/bbpc.19600641022>.
- [222] N.C. Wright, S.R. Shah, S.E. Amrose, A.G. Winter, A robust model of brackish water electro dialysis desalination with experimental comparison at different size scales, *Desalination*. 443 (2018) 27–43. <https://doi.org/10.1016/j.desal.2018.04.018>.
- [223] E. Brauns, Salinity gradient power by reverse electro dialysis: effect of model parameters on electrical power output, *Desalination*. (2009). <https://doi.org/10.1016/j.desal.2008.10.003>.
- [224] Fumatech Bwt GmbH, Brochure on Ion Exchange Membranes, (n.d.). https://www.fumatech.com/NR/rdonlyres/3DF915E1-47B5-4F43-B18A-D23F9CD9FC9D/0/FUMATECH_BWT_GmbHIon_Exchange_Membranes.pdf.
- [225] W. Zappa, M. Junginger, M. van den Broek, Is a 100% renewable European power system feasible by 2050?, *Appl. Energy*. 233–234 (2019) 1027–1050. <https://doi.org/10.1016/j.apenergy.2018.08.109>.
- [226] M. Aneke, M. Wang, Energy storage technologies and real life applications – A state of the art review, *Appl. Energy*. 179 (2016) 350–377. <https://doi.org/10.1016/j.apenergy.2016.06.097>.
- [227] B. V. Mathiesen, H. Lund, D. Connolly, H. Wenzel, P.A. Ostergaard, B. Möller, S. Nielsen, I. Ridjan, P. KarnOe, K. Sperling, F.K. Hvelplund, Smart Energy Systems for coherent 100% renewable energy and transport solutions, *Appl. Energy*. 145 (2015) 139–154. <https://doi.org/10.1016/j.apenergy.2015.01.075>.
- [228] X. Luo, J. Wang, M. Dooner, J. Clarke, Overview of current development in electrical energy storage technologies and the application potential in power system operation, *Appl. Energy*. 137 (2015) 511–536. <https://doi.org/10.1016/j.apenergy.2014.09.081>.
- [229] B. Dunn, H. Kamath, J.M. Tarascon, Electrical energy storage for the grid: A battery of choices, *Science* (80-.). 334 (2011) 928–935. <https://doi.org/10.1126/science.1212741>.
- [230] Z. Yang, J. Zhang, M.C.W. Kintner-Meyer, X. Lu, D. Choi, J.P. Lemmon, J. Liu, Electrochemical energy storage for green grid, *Chem. Rev.* 111 (2011) 3577–3613. <https://doi.org/10.1021/cr100290v>.
- [231] K. Amini, M.D. Pritzker, Improvement of zinc-cerium redox flow batteries using mixed methanesulfonate-chloride negative electrolyte, *Appl. Energy*. 255 (2019). <https://doi.org/10.1016/j.apenergy.2019.113894>.
- [232] Y. Zeng, Z. Yang, F. Lu, Y. Xie, A novel tin-bromine redox flow battery for large-scale energy storage, *Appl. Energy*. 255 (2019) 113756.

- <https://doi.org/10.1016/j.apenergy.2019.113756>.
- [233] M. Pugach, V. Vyshinsky, A. Bischi, Energy efficiency analysis for a kilowatt class vanadium redox flow battery system, *Appl. Energy*. 253 (2019). <https://doi.org/10.1016/j.apenergy.2019.113533>.
- [234] H. Chen, X. Li, H. Gao, J. Liu, C. Yan, A. Tang, Numerical modelling and in-depth analysis of multi-stack vanadium flow battery module incorporating transport delay, *Appl. Energy*. 247 (2019) 13–23. <https://doi.org/10.1016/j.apenergy.2019.04.034>.
- [235] L. Wei, L. Zeng, M.C. Wu, X.Z. Fan, T.S. Zhao, Seawater as an alternative to deionized water for electrolyte preparations in vanadium redox flow batteries, *Appl. Energy*. 251 (2019) 113344. <https://doi.org/10.1016/j.apenergy.2019.113344>.
- [236] H.R. Jiang, Y.K. Zeng, M.C. Wu, W. Shyy, T.S. Zhao, A uniformly distributed bismuth nanoparticle-modified carbon cloth electrode for vanadium redox flow batteries, *Appl. Energy*. 240 (2019) 226–235. <https://doi.org/10.1016/j.apenergy.2019.02.051>.
- [237] Y. Shi, C. Eze, B. Xiong, W. He, H. Zhang, T.M. Lim, A. Ukil, J. Zhao, Recent development of membrane for vanadium redox flow battery applications: A review, *Appl. Energy*. 238 (2019) 202–224. <https://doi.org/10.1016/j.apenergy.2018.12.087>.
- [238] H. Prifti, A. Parasuraman, S. Winardi, T.M. Lim, M. Skyllas-Kazacos, Membranes for redox flow battery applications, *Membranes (Basel)*. 2 (2012) 275–306. <https://doi.org/10.3390/membranes2020275>.
- [239] P. Alotto, M. Guarnieri, F. Moro, Redox flow batteries for the storage of renewable energy: A review, *Renew. Sustain. Energy Rev.* 29 (2014) 325–335. <https://doi.org/10.1016/j.rser.2013.08.001>.
- [240] G.L. Soloveichik, Flow Batteries: Current Status and Trends, *Chem. Rev.* 115 (2015) 11533–11558. <https://doi.org/10.1021/cr500720t>.
- [241] M.C. Díaz-Ramírez, V.J. Ferreira, T. García-Armingol, A.M. López-Sabirón, G. Ferreira, Environmental Assessment of Electrochemical Energy Storage Device Manufacturing to Identify Drivers for Attaining Goals of Sustainable Materials 4.0, *Sustainability*. 12 (2020) 342. <https://doi.org/10.3390/su12010342>.
- [242] R.S. Kingsbury, K. Chu, O. Coronell, Energy storage by reversible electro dialysis: The concentration battery, *J. Memb. Sci.* 495 (2015) 502–516. <https://doi.org/10.1016/j.memsci.2015.06.050>.
- [243] W.J. van Egmond, M. Saakes, S. Porada, T. Meuwissen, C.J.N. Buisman, H.V.M. Hamelers, The concentration gradient flow battery as electricity

- storage system: Technology potential and energy dissipation, *J. Power Sources*, 325 (2016) 129–139. <https://doi.org/10.1016/j.jpowsour.2016.05.130>.
- [244] A. Campione, L. Gurreri, M. Ciofalo, G. Micale, A. Tamburini, A. Cipollina, Electrodialysis for water desalination: A critical assessment of recent developments on process fundamentals, models and applications, *Desalination*, 434 (2018) 121–160. <https://doi.org/10.1016/j.desal.2017.12.044>.
- [245] L. Gurreri, A. Cipollina, A. Tamburini, G. Micale, Electrodialysis for wastewater treatment—Part I: Fundamentals and municipal effluents, in: A. Basile, A. Comite (Eds.), *Curr. Trends Futur. Dev. Membr.*, Elsevier, Amsterdam, 2020: pp. 141–192. <https://doi.org/10.1016/B978-0-12-816823-3.00007-1>.
- [246] L. Gurreri, A. Cipollina, A. Tamburini, G. Micale, Electrodialysis for wastewater treatment—Part II: Industrial effluents, in: A. Basile, A. Comite (Eds.), *Curr. Trends Futur. Dev. Membr.*, Elsevier, Amsterdam, 2020: pp. 195–241. <https://doi.org/10.1016/B978-0-12-816823-3.00008-3>.
- [247] R.A. Tufa, S. Pawlowski, J. Veerman, K. Bouzek, E. Fontananova, G. di Profio, S. Velizarov, J. Goulão Crespo, K. Nijmeijer, E. Curcio, Progress and prospects in reverse electrodialysis for salinity gradient energy conversion and storage, *Appl. Energy*, 225 (2018) 290–331. <https://doi.org/10.1016/j.apenergy.2018.04.111>.
- [248] A. Tamburini, A. Cipollina, M. Tedesco, L. Gurreri, M. Ciofalo, G. Micale, The REAPower Project, in: A. Basile, E. Curcio, I. Inamuddin (Eds.), *Curr. Trends Futur. Dev. Membr.*, Elsevier, Amsterdam, 2019: pp. 407–448. <https://doi.org/10.1016/B978-0-12-813551-8.00017-6>.
- [249] AquaBattery – We give power to water., (n.d.). <https://aquabattery.nl/> (accessed January 10, 2020).
- [250] W.J. van Egmond, M. Saakes, I. Noor, S. Porada, C.J.N. Buisman, H.V.M. Hamelers, Performance of an environmentally benign acid base flow battery at high energy density, *Int. J. Energy Res.* 42 (2018) 1524–1535. <https://doi.org/10.1002/er.3941>.
- [251] M.S. Guney, Y. Tepe, Classification and assessment of energy storage systems, *Renew. Sustain. Energy Rev.* 75 (2017) 1187–1197. <https://doi.org/10.1016/j.rser.2016.11.102>.
- [252] W.J. van Egmond, Concentration Gradient Flow Batteries: salinity gradient energy systems as environmentally benign large scale electricity storage, 2018. <https://doi.org/10.1192/bjp.111.479.1009-a>.
- [253] E.K. Zholkovskij, M.C. Müller, E. Staude, The storage battery with bipolar

- membranes, *J. Memb. Sci.* 141 (1998) 231–243. [https://doi.org/10.1016/S0376-7388\(97\)00306-2](https://doi.org/10.1016/S0376-7388(97)00306-2).
- [254] J. Pretz, E. Staude, Reverse electrodialysis (RED) with bipolar membranes, an energy storage system, *Berichte Der Bunsengesellschaft Für Phys. Chemie.* 102 (1998) 676–685. <https://doi.org/10.1002/bbpc.19981020412>.
- [255] J.H. Kim, J.H. Lee, S. Maurya, S.H. Shin, J.Y. Lee, I.S. Chang, S.H. Moon, Proof-of-concept experiments of an acid-base junction flow battery by reverse bipolar electrodialysis for an energy conversion system, *Electrochem. Commun.* 72 (2016) 157–161. <https://doi.org/10.1016/j.elecom.2016.09.025>.
- [256] J. Xia, G. Eigenberger, H. Strathmann, U. Nieken, Flow battery based on reverse electrodialysis with bipolar membranes: Single cell experiments, *J. Memb. Sci.* 565 (2018) 157–168. <https://doi.org/10.1016/j.memsci.2018.07.073>.
- [257] J. Xia, G. Eigenberger, H. Strathmann, U. Nieken, Acid-base flow battery, based on reverse electrodialysis with bi-polar membranes: Stack experiments, *Processes.* 8 (2020) 99. <https://doi.org/10.3390/pr8010099>.
- [258] A. Campione, A. Cipollina, I.D.L. Bogle, L. Gurreri, A. Tamburini, M. Tedesco, G. Micale, A hierarchical model for novel schemes of electrodialysis desalination, *Desalination.* 465 (2019) 79–93. <https://doi.org/10.1016/J.DESAL.2019.04.020>.
- [259] L. Gurreri, A. Tamburini, A. Cipollina, G. Micale, M. Ciofalo, CFD prediction of concentration polarization phenomena in spacer-filled channels for reverse electrodialysis, *J. Memb. Sci.* 468 (2014) 133–148. <https://doi.org/10.1016/j.memsci.2014.05.058>.
- [260] N. Chindapan, S.S. Sablani, N. Chiewchan, S. Devahastin, Modeling and Optimization of Electrodialytic Desalination of Fish Sauce Using Artificial Neural Networks and Genetic Algorithm, *Food Bioprocess Technol.* 6 (2013) 2695–2707. <https://doi.org/10.1007/s11947-012-0914-6>.
- [261] D.W. Bian, S.M. Watson, N.C. Wright, S.R. Shah, T. Buonassisi, D. Ramanujan, I.M. Peters, A.G. Winter, Optimization and design of a low-cost, village-scale, photovoltaic-powered, electrodialysis reversal desalination system for rural India, *Desalination.* (2019). <https://doi.org/10.1016/j.desal.2018.09.004>.
- [262] J. Kennedy, R. Eberhart, Particle swarm optimization, in: *IEEE Int. Conf. Neural Networks - Conf. Proc.*, 1995. <https://doi.org/10.4018/ijmfmp.2015010104>.
- [263] F. Guesmi, I. Louati, C. Hannachi, B. Hamrouni, Optimization of boron removal from water by electrodialysis using response surface methodology, *Water Sci. Technol.* (2020). <https://doi.org/10.2166/wst.2020.105>.

References

- [264] F.S. Rohman, N. Aziz, Optimization of batch electro dialysis for hydrochloric acid recovery using orthogonal collocation method, *Desalination*. (2011). <https://doi.org/10.1016/j.desal.2011.02.025>.
- [265] F.S. Rohman, N. Aziz, Performance metrics analysis of dynamic multi-objective optimization for energy consumption and productivity improvement in batch electro dialysis, *Chem. Eng. Commun.* 0 (2019) 1–13. <https://doi.org/10.1080/00986445.2019.1674817>.
- [266] J. Veerman, M. Saakes, S.J. Metz, G.J. Harmsen, Reverse electro dialysis: A validated process model for design and optimization, *Chem. Eng. J.* (2011). <https://doi.org/10.1016/j.cej.2010.10.071>.
- [267] Y. Cui, Z. Geng, Q. Zhu, Y. Han, Review: Multi-objective optimization methods and application in energy saving, *Energy*. 125 (2017) 681–704. <https://doi.org/10.1016/j.energy.2017.02.174>.
- [268] HAIMES YV, LASDON LS, WISMER DA, On a bicriterion formation of the problems of integrated system identification and system optimization, *IEEE Trans. Syst. Man Cybern.* (1971). <https://doi.org/10.1109/TSMC.1971.4308298>.
- [269] G.P. Rangaiah, A. Bonilla-Petriciolet, *Multi-Objective Optimization in Chemical Engineering: Developments and Applications*, 2013. <https://doi.org/10.1002/9781118341704>.

Acknowledgements

First and foremost I would like to express my sincere gratitude to Prof. Giorgio Micale and Dr. Alessandro Tamburini for their invaluable advice, unwavering support and patience during my PhD. I am also very grateful to Prof. David Bogle, who gave me the opportunity to study at University College London. I wish to offer my special thanks to Prof. Andrea Cipollina for all his suggestions, and for always encouraging me in all of my academic research and in daily life. I also extend my thanks to the colleagues of the BAoBaB project for all the fruitful discussions during the project meetings.

I would like to thank Dr. Luigi Gurreri for his input, knowledge and countless brainstorming sessions.

I wish to acknowledge Dr. Andrea Zaffora, Alessandro Cosenza, Luca Muratore and Antonino Agnello for having performed the experiments on the laboratory test-rig.

Furthermore, I would like to thank my colleagues Fabrizio, Daniele, Mariagiorgia, Peppe, Mimma, Antonella, Carmelo, Javier, Francesco, Serena Lima, Nunzio of the chemical engineering department with whom I shared wonderful moments during these last three years.

A special thanks to my colleagues and friends Ninni, Marina and Rosa, whom I have both studied with and made great memories with since the early years of university.

My sincere gratitude also goes out to my closest friends Giangio, Alvisè and Andrea.

Last but not least, I thank my family, particularly my parents Salvatore and Donatella and my sister Roberta, who supported and encouraged me in every moment.

Andrea Culcasi